

NASA Technical Paper 1100

**Dynamic Stall Experiments
on the NACA 0012 Airfoil**

**CASE FILE
COPY**

**Kenneth W. McAlister, Lawrence W. Carr,
and William J. McCroskey**

JANUARY 1978

NASA

NASA Technical Paper 1100

Dynamic Stall Experiments on the NACA 0012 Airfoil

Kenneth W. McAlister, Lawrence W. Carr,
and William J. McCroskey

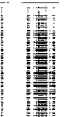
Aeromechanics Laboratory
U.S. Army Aviation R&D Command
Ames Research Center
Moffett Field, California

NASA

National Aeronautics
and Space Administration

**Scientific and Technical
Information Office**

1978



TABLES OF CONTENTS

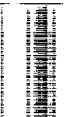
	Page
SYMBOLS	iii
SUMMARY	1
INTRODUCTION	2
DESCRIPTION OF EXPERIMENT	4
Model and Drive Mechanism	4
Instrumentation	5
Data Acquisition	5
RESULTS AND DISCUSSION	6
Steady Comparison	6
Averaging	7
Transition Near the Leading Edge	7
Separation Bubble	8
Flow Separation Near the Leading Edge	9
Moment Stall Indicator	10
Vortex Passage	11
Pressure Integration	12
Reduced Frequency	13
Mean Angle and Amplitude	15
End Plates	15
Leading-Edge Modifications	16
Coefficient Extrema	16
CONCLUSIONS	19
TABLES	21
FIGURES	24
APPENDIX – SUMMARY OF PRESSURE DISTRIBUTIONS AND INTEGRATIONS	116
FIGURES	117
REFERENCES	161

1
2
3
4
5
6
7
8
9
10
11
12
13
14
15
16
17
18
19
20
21
22
23
24
25
26
27
28
29
30
31
32
33
34
35
36
37
38
39
40
41
42
43
44
45
46
47
48
49
50
51
52
53
54
55
56
57
58
59
60
61
62
63
64
65
66
67
68
69
70
71
72
73
74
75
76
77
78
79
80
81
82
83
84
85
86
87
88
89
90
91
92
93
94
95
96
97
98
99
100

1
2
3
4
5
6
7
8
9
10
11
12
13
14
15
16
17
18
19
20
21
22
23
24
25
26
27
28
29
30
31
32
33
34
35
36
37
38
39
40
41
42
43
44
45
46
47
48
49
50
51
52
53
54
55
56
57
58
59
60
61
62
63
64
65
66
67
68
69
70
71
72
73
74
75
76
77
78
79
80
81
82
83
84
85
86
87
88
89
90
91
92
93
94
95
96
97
98
99
100

1
2
3
4
5
6
7
8
9
10
11
12
13
14
15
16
17
18
19
20
21
22
23
24
25
26
27
28
29
30
31
32
33
34
35
36
37
38
39
40
41
42
43
44
45
46
47
48
49
50
51
52
53
54
55
56
57
58
59
60
61
62
63
64
65
66
67
68
69
70
71
72
73
74
75
76
77
78
79
80
81
82
83
84
85
86
87
88
89
90
91
92
93
94
95
96
97
98
99
100

1
2
3
4
5
6
7
8
9
10
11
12
13
14
15
16
17
18
19
20
21
22
23
24
25
26
27
28
29
30
31
32
33
34
35
36
37
38
39
40
41
42
43
44
45
46
47
48
49
50
51
52
53
54
55
56
57
58
59
60
61
62
63
64
65
66
67
68
69
70
71
72
73
74
75
76
77
78
79
80
81
82
83
84
85
86
87
88
89
90
91
92
93
94
95
96
97
98
99
100



SYMBOLS

A	area of airfoil, m^2
C	chord force, N
C_c	chord-force coefficient, $\frac{C}{qA}$, nondimensional
C_D	drag-force coefficient, $\frac{D}{qA}$, nondimensional
C_L	lift-force coefficient, $\frac{L}{qA}$, nondimensional
C_M	pitching-moment coefficient, $\frac{M}{qAc}$, nondimensional
$C.P.$	center of pressure, $\frac{X}{c} - \frac{C_M}{C_N}$, nondimensional
C_p	pressure coefficient, $\frac{p - p_\infty}{q}$, nondimensional
C_{p_3}	pressure coefficient evaluated at $\frac{s}{c} = 0.014$
c	chord of airfoil, m
D	drag force, N
k	reduced frequency, $\frac{\omega c}{2U_\infty}$, nondimensional
L	lift force, N
M	pitching moment, about quarter chord, N-m
N	normal force, N
p	static pressure on airfoil, N/m^2
p_∞	static freestream pressure, N/m^2
p_t	total freestream pressure, N/m^2
q	freestream dynamic pressure, N/m^2
Re	Reynolds number, $\frac{U_\infty c}{\nu}$, nondimensional
s	distance measured on surface of airfoil, m
t	time, sec

U_∞	freestream velocity, m/sec
X	location of pitch axis, m
x	distance measured along chord of airfoil, m
α	airfoil incidence, deg
α_{ss}	static-stall incidence, deg
α_0	mean incidence, deg
α_1	oscillatory amplitude, deg
$\dot{\alpha}$	time rate of change of incidence, rad/sec
ζ	pitch damping, $-\frac{\oint C_m d\alpha}{4\alpha_1^2}$ with α expressed in rad, nondimensional
ν	kinematic viscosity, m^2/sec
ξ	normal force defect, $\frac{\oint C_N d\alpha}{\int_{-\pi/2}^{\pi/2} C_N d\alpha}$, nondimensional
τ	time constant, nondimensional
ω	rotational frequency, rad/sec

DYNAMIC STALL EXPERIMENTS ON THE NACA 0012 AIRFOIL

Kenneth W. McAlister, Lawrence W. Carr, and William J. McCroskey

Ames Research Center
and
Aeromechanics Laboratory, U.S. Army Aviation R&D Command

SUMMARY

The flow over a NACA 0012 airfoil oscillating in pitch was experimentally investigated at a Reynolds number of 2.5×10^6 , a Mach number of 0.09, and over a range of frequencies and amplitudes. Hot-wire probes and surface-pressure transducers were used to clarify the role of the laminar separation bubble, to delineate the growth and shedding of the stall vortex and to quantify the resultant aerodynamic loads.

It was found that the leading-edge separation bubble has no direct effect on the gross stall character and that it even persists during the onset of the suction collapse. The familiar elements of dynamic stall are also shown to be qualitatively unchanged by modifications to the airfoil leading edge. That is, the predominant features continue to be the development of unusually high forces and the shedding of a vortex. The present results make clear that following the initial lift overshoot arising from unsteady effects which delay boundary layer separation, the strong surge in lift (which continues the overshoot) is an induced effect from the shed vortex during its period of residence over the airfoil. The imprint made on the pressure distribution by the vortex is observed to become more concentrated and pronounced as the frequency is increased, indicating that the strength of the shed vortex is related to the circulation around the airfoil at the time the vortex is formed.

A symptomatic pattern was detected in the pressure response near the leading edge. It was found that the general shape of the curve and the azimuthal location of the peak could be used for determining the presence of moment stall as well as for judging its relative severity. It appears that a more abrupt stall results when the vortex is shed while the airfoil is still pitching up rather than when the airfoil is at the top of the cycle. These two categories are defined as fully developed and partially developed stalls, respectively.

Another area examined in this study was the dispersion of measured quantities from one cycle to another. It was found that to obtain a stabilized representation of the aerodynamic loads required the ensemble averaging (based on ωt) of 50 or more cycles of data. These average pressure data were then integrated to obtain the pitching moment and the normal-force and chord-force coefficients. Although containing only the contribution due to pressure forces, loads developed during the dynamic cases indicate that a reasonable estimate of unsteady drag forces has been achieved. This is especially valid over the stalled portion of the cycle where viscous shear is expected to be relatively less significant. It should be emphasized that the pressure drag can only be obtained from single-surface measurements and not from differential (upper-lower surface) measurements. The present study constitutes the first time that single-surface pressure measurements have been used to provide an estimate of the unsteady drag on an airfoil.

Leading-edge modifications are shown to precipitate an earlier stall onset and, with the exception of greater pitch damping, generally do not offer an improvement in performance. End plates were employed in an attempt to reduce the interference between the model and the wind tunnel walls, and these were found to delay the onset of stall and produce a stronger vortex only at the lower frequencies. However, they generally improve the performance and stability characteristics over the entire frequency range.

INTRODUCTION

An airfoil that experiences an unsteady increase in incidence which carries it beyond its static stall angle is known to develop an increase in lift without any detectable change in the lift-curve slope. This has also been observed on helicopter rotors where changes in angle-of-attack are predominantly due to the sinusoidal variation in blade incidence imposed on the rotor as it moves around the azimuth. Although dependent on the rate and amplitude of the oscillation, it is generally observed that as the airfoil continues to pitch upward, a point is reached where a surge in the lift force and a negative roll-off in the pitching moment occurs. Simultaneously, a vortex can be seen to grow and be shed from the leading-edge region. As it moves over the surface its size grows and further increases in lift and negative moment are induced. As this vortex passes off the rear of the airfoil, a peak negative pitching moment is attained and a sudden loss in lift occurs. During the next portion of the cycle the airfoil will be in deep stall and under an extensive region of separated flow. This condition causes large hysteresis loops to develop in the lift, drag, and pitching moment curves when viewed as functions of angle-of-attack.

In general terms this describes the familiar features of dynamic stall as observed in two-dimensional flow experiments; however, to better understand the stall phenomenon it is necessary to examine these events in greater detail. The first distinguishing difference between the static and dynamic stall behavior of an airfoil is that the break in the lift and moment curves no longer occur at the same time, nor for the same reason. Moment stall, which is due to the growth and initial shedding of the vortex in the dynamic case, can be defined in general as the point where the pressure distribution is altered sufficiently to produce a noticeable negative divergence in the pitching moment. Lift stall, which is a necessary consequence of vortex shedding in most dynamic cases, can in general be defined as the point where the boundary layer has sufficiently separated so that the resulting pressure distribution no longer yields an increase in lift with further increases in incidence.

The second important difference between static and dynamic stall is the distinction between flow reversal and flow separation. In all cases, a boundary layer that is growing under an adverse pressure gradient will at some location weaken to a state where zero velocity appears near the surface, thus defining a condition of vanishing wall shear and the beginning of reversed flow. The region of reversed flow is part of a domain bounded by the surface and the dividing streamline which emanates from the point of zero shear and continues into the wake behind the airfoil. It is the relative shape of the dividing streamline boundary and hence the extent of the domain that it encloses that testifies to whether the point of zero shear is also the point of flow separation. In steady flow these two points are said to be coincident since the dividing streamline strongly diverges from the surface to encompass a large wake flow. However, in unsteady flow the dividing

streamline encloses a narrow boundary-layer-like zone that extends from the point of zero shear to some downstream location where it there separates.

Airfoil stall is known to occur in several different ways. If the laminar boundary layer enters an adverse pressure field and separates before transition occurs, the flow will either remain separated, thereby producing an immediate change in the lift, or become turbulent and reattach to the surface. The region enclosed by the resulting free-shear layer between the points of separation and reattachment is known as a laminar separation bubble; it extends over a distance that is primarily dependent on the shape of the airfoil. The flow then separates either due to a breakdown of the bubble or due to a downstream depletion of sustaining energy within the turbulent boundary layer. It has been shown, for the conditions of this test, that the NACA 0012 belongs in the latter category; that is, it stalls by the mechanism of unsteady turbulent boundary layer separation (ref. 1). Reported in reference 1, the NACA 0012 airfoil was the subject of a qualitative study in which major modifications to the leading-edge region were made in order to force the stall to result from either trailing-edge or leading-edge separation. It was during this investigation that a new stall type was discovered to occur on the basic airfoil — a stall which results from an abrupt turbulent leading-edge separation of the flow.

The purpose of this test was to examine in quantitative detail the flow as it developed through stall on the NACA 0012 airfoil oscillating in pitch. This was accomplished by using single-surface instrumentation over the entire airfoil, with sufficient density near the leading edge to disclose the existence and participation of the laminar separation bubble. An additional requirement was to quantify the resulting unsteady aerodynamic loads and to identify their dependence on the mean angle, amplitude, and frequency of oscillation. Another objective was to study the possibility of altering the timing and severity of the stall by using two candidate passive modifications to the leading edge which were intended to either eliminate or distort the separation bubble. A final objective was to determine the importance of end plates during large scale unsteady tests.

The significance of obtaining single-surface pressure data should be noted. In steady flow the drag force on a body may be readily determined by either balance or wake measurements; however, in unsteady experiments the balance approach must deal with large dynamic tare loads (see e.g., ref. 2) while the wake method would need to account for the time rate of change of momentum within the assumed control volume. A possible remedy is offered through the integration of the chordwise component of the force resulting from the surface-pressure distribution. This assumes that the pressure forces dominate those contributed by viscous shear, which should be especially valid over the stall portion of the cycle. Some error is anticipated at low angles of attack where little flow separation occurs and the difference between the contributions from the normal and chordwise components becomes small. This latter condition may be critical since the calculated drag in this case results from the difference between two nearly equal quantities, thereby exposing any existing deficiencies in the placement of the pressure transducers and the type of integration procedure utilized. However, since this situation does not exist over most of the cycle, it is expected that a meaningful drag force can be represented in the dynamic case.

Because the viscous contributions to the normal force can be justly neglected, the integrated pressure results will be presented in the body-fixed coordinate system. Both for completeness and to facilitate comparisons, the results of all test cases have been included in the appendix using a common set of scales. Each case is summarized graphically in terms of the upper-surface pressure distribution over a complete cycle of oscillation and the resultant integrated loads represented by

the pitching moment and the normal- and chord-force coefficients. Also presented for convenience is the center of pressure that is obtained from the pitching moment and the normal force. Some care is recommended in interpreting this quantity because relatively large values can result whenever the normal force is small.

DESCRIPTION OF EXPERIMENT

This experiment was conducted in the AMRDL-Ames 7- by 10-Foot Subsonic Wind Tunnel to obtain detailed information about the NACA 0012 airfoil operating under conditions that produce dynamic stall. The work was an extension of an earlier test (ref. 1) in which dynamic stall was qualitatively studied on a broader scale. The Reynolds number in the present test was held fixed at 2.5×10^6 and the dimensionless frequency, $\omega c/2U_\infty$ was varied up to values of 0.25. The airfoil was constrained so that sinusoidal oscillations in pitch could be imposed about an axis passing through the quarter-chord location. Although mean-angle and amplitude variations were included, most of the data recorded were for $\alpha = 15^\circ + 10^\circ \sin \omega t$. In addition to the basic airfoil, a limited amount of data was obtained for two modifications to the leading edge consisting of: (1) a boundary-layer trip and (2) a set of upstream-facing serrations. In order to show the existence of a separation bubble and to delineate its participation in the dynamic stall process, emphasis was initially placed on hot-wire anemometer and pressure transducer measurements over the leading-edge region. The second portion of the test was principally concerned with obtaining both upper- and lower-surface pressure measurements to document the passing imprint of the stall vortex and to provide data from which the dynamic loads could be calculated. During this phase of testing, selected cases were also examined using end plates to improve the two-dimensionality of the flow. The complete matrix of test conditions is summarized in table 1.

Model and Drive Mechanism

The basic airfoil measured 1.22 m (4 ft) chord, 1.98 m (6.5 ft) span and was mounted vertically across the test section (fig. 1). The model was fabricated around a tubular spar which was supported below a ground plane by a pivot bearing and above the ceiling by a sleeve bearing (fig. 2). One of the modifications studied was a boundary-layer trip consisting of a narrow strip of laminated tape, 0.46-mm wide and 0.16-mm high, running along the entire length of the airfoil-leading edge. The second modification to the leading edge was a serrated metal strip (denoted as B20BR in ref. 1) with the teeth bent to the local contour of the airfoil surface and pointed in an upstream direction (fig. 3).

The spar that passed through the quarter-chord axis of the airfoil was attached to a crank, connecting-rod, and flywheel mechanism located above the test section (fig. 2). This apparatus enabled the airfoil to be sinusoidally oscillated in pitch. The mean angle of oscillation was controlled by the length of the connecting rod and the amplitude was governed by the radial station on the flywheel to which the rod was attached. The higher frequency oscillations (0.15 to 2.0 Hz) were obtained using a compressed-air motor; the lower-frequency oscillations (0.017 to 0.15 Hz) were obtained using a belt and pulley system attached to a variable speed motor.

End plates were formed from 13-mm thick plywood sections which extended normal to the airfoil approximately 0.5 m on the pressure side and 1.2 m on the suction side. These plates were mounted 0.3 m inboard from the wind tunnel walls.

Instrumentation

Two identical pitot-static probes were located upstream of the model to provide an instantaneous measure of the dynamic pressure in the test section and to serve as a source of total pressure to be used as a reference for all differential pressure transducers. These independent probes were used in order to isolate any possible contamination of the dynamic-pressure measurement that might arise from the lengthy tubing required to reach the reference-pressure plenum located within the model. By mounting the differential-pressure transducers as close to the upper and lower surfaces of the model as possible, the tubing on the measuring side of the transducers could be minimized so that a nominally flat frequency response of 250 Hz could be obtained. The constant-temperature hot-wire anemometer probes which were installed over the leading-edge region of the airfoil were conventional two-prong, single-element units that projected vertically from the surface. Each wire was positioned above the surface at a distance not to exceed the estimated local minimum boundary-layer thickness during any cycle of oscillation for the range of test conditions planned. Since the purpose of hot-wire measurements was strictly qualitative, the recorded signals were neither calibrated nor linearized. The locations of all transducers mounted on the model are schematically presented in figures 4 and 5. The instrumentation locations shown in figure 4 apply to both the pressure transducers and the hot-wire probes – each pair being separated slightly along the span of the airfoil. The instrumentation layout shown in figure 5 consisted of only pressure transducers and they are numbered independently of those given in figure 4. Data obtained from a transducer located on the upper surface at the 75% location (not shown) were later found to be suspect and were therefore eliminated from calculations. The angle of incidence was obtained from a potentiometer that was keyed to the spar of the airfoil (fig. 2).

Data Acquisition

The output of each transducer was recorded in analog form on two 14-channel tape recorders under conditions assuring a flat frequency response up to 2500 Hz. Normally data from 100 cycles of airfoil oscillation were recorded for reduced frequencies above 0.05; however, the lowest recorded frequency required as much as 100 sec to complete one cycle and was necessarily limited to 5 cycles of data. Steady data were recorded over a period of 30 sec. In addition to the various combinations of pressure and hot-wire data taken on the model, certain other quantities were routinely recorded: (1) a 200/rev timing mark (modulated by a 1/rev dc step) generated by an optical system attached to the rotating flywheel of the drive mechanism; (2) a reference time code (generated electronically) for later identification of the run and frame number as well as for correlating the two data tapes; (3) the dynamic pressure in the test section; and (4) the angle of incidence of the airfoil. All pressure transducers were statically calibrated at the beginning and end of each tape and the time interval between data and a zero reference was limited to 15 min. The data were later digitized (based on the 200/rev timing marks), repacked, and analyzed on the computer, with each test case typically containing 0.5×10^6 words of data.

RESULTS AND DISCUSSION

The following sections identify and discuss those features of the test that are unique and contribute in some way to the understanding of dynamic stall. Results are first presented that establish the credibility of the data and give purpose to the process of conditional averaging. Discussed next are the detailed measurements made near the leading edge which were intended to detect transition and separation in that region as well as to help define the role of the laminar separation bubble. The characteristics of the shed vortex are examined in terms of the time of origin, the rate of passage and the dependence of these events on certain parameters. The resultant pressures are integrated to obtain familiar aerodynamic quantities such as pitching moment, normal and chord forces, and the center of pressure. Using these integrated quantities, a parametric study is presented to show the importance of frequency and amplitude as well as the significance of configuration changes. Finally, a summary is organized in terms of extremes of the aerodynamic coefficients and their derivatives.

Steady Comparison

Steady airfoil data have been traditionally presented as lift and drag forces defined in terms of an inertially-fixed coordinate system aligned with the wind axis. To compare with the present results, force data from a recent study by Gregory and O'Reilly (ref. 3) have been transformed to normal and chordwise components and are included in figure 6 for reference. All chordwise data are in excellent agreement for $\alpha < 12^\circ$; however, for higher angles of incidence the data taken with end plates show some deviation, and those taken without end plates appear to be seriously contaminated by three-dimensional separation. Although the normal force data taken with and without end plates differ by no more than 5% for $\alpha < 14^\circ$ they both exceed the referenced data by as much as 15%. Since the model chord-to-tunnel-width ratio was 0.4, the excess normal force observed in the present study is no doubt attributable to wind tunnel wall interference. The irregular patterns appearing in both the chord- and normal-force curves just prior to stall when end plates are not used indicate that a three-dimensional stall is being caused by the intersection of the flow over the airfoil with relatively thick boundary layers on the test section walls.

The present data have been transformed to yield lift and drag components and are compared in figure 7 with the results from references 3-9 at several Mach numbers and Reynolds numbers. This comparison indicates that the previous remarks about wall interference apply to lift as well as to normal force. This conclusion is supported by the solid symbols, which were obtained by applying the semi-empirical lift correction suggested by Pope and Harper (ref. 10). Although this corrective procedure can be successfully applied to the lift data, the error in drag, approximately 100% for $\alpha < 15^\circ$, is too large to be treated with confidence. This error is clearly not due to the omission of viscous forces because they would be additive. This large disagreement is instead believed to be merely a shortcoming of the algebraic mechanics of constructing a relatively small drag force from large and nearly equal normal- and chord-force contributions. Also, it is there that the distribution of pressure transducers and the preciseness of the integration technique are called into question. To improve the integration a variable power spline was fitted to the data, thereby achieving a smooth curve with occasional but slight oscillations. Unfortunately, the resulting integration yielded a manyfold increase in the drag error. Although further effort along these lines could provide a remedy, it was judged somewhat inconsequential in view of the much better agreement attained at

higher angles of incidence and because the values of drag realized in typical dynamic cases are an order of magnitude larger than the level of the inaccuracies being discussed.

Averaging

Because of unavoidable freestream irregularities, each cycle of pressure and hot-wire measurements was found to be distinctly different, especially during the stalled portion of the cycle. To facilitate parametric comparisons it was desirable to remove this randomness from the pressure data by ensemble averaging over a number of cycles, but without forfeiting any significant feature that might be symptomatic of stall onset. The most prominent prestall feature of individual pressure signals was the appearance of a pressure perturbation believed to be associated with the closure point of a separation bubble as it moves forward toward the leading edge (figs. 8(a-c)). Using this phenomenon as a measure of the level of detail to be preserved, figure 8 indicates that regardless of reduced frequency, averaging not only preserves but actually improves the clarity of this event.

The normal-force and pitching-moment coefficients are calculated by ensemble-averaging the total number of recorded cycles (usually 100) and then integrating these pressures over the airfoil. The arithmetic differences between these results and those obtained by using a lesser number of cycles in the ensemble average are shown in figures 9(a-c). These results show that significant departures from the total average exist when less than 25 cycles are averaged, but that a more representative presentation is realized using 50 or more cycles. Also included is the standard deviation, a diagnostic quantity which denotes within any given cycle where differences from the mean are most likely to occur. It can be seen that the maximum standard deviations for both the normal force and pitching moment occur at a point in the cycle immediately following lift stall for $k = 0.02$. The second less prominent deviation may be due to secondary vortex shedding. As the reduced frequency is increased, the maxima not only occur later in the cycle, but there is a progressive delay in azimuth from the respective points of stall.

The data were also subjected to various degrees of filtration prior to digitization to see if the required number of cycles could be reduced. It was found that after narrowing the frequency acceptance to less than 100 Hz, ensemble averaging over 50 or more cycles was still required. It appears that the low frequency randomness, on the order of the first harmonic, is what is most objectionable and must be removed. Since this can only be accomplished by conditional averaging, it is fortunate that it has the additional effect of filtering out the unwanted high frequency content.

Transition Near the Leading Edge

Hot wires placed along the leading-edge region were used to detect transition from laminar to turbulent flow during airfoil oscillations. An effective procedure for determining the occurrence of transition utilizes the standard deviation of 50 or more cycles of ensemble-averaged data. Based on the multi-cyclic average at each surface location (figs. 10(a-c)), the rectified deviation from this average by each contributing cycle can be calculated and the results accumulated over all cycles. This technique not only preserves the effects of randomness during separation, but more importantly it retains the effects caused by the presence of turbulence.

Since the deviations resulting from boundary-layer turbulence are much smaller than those occurring during the period of separation, the latter have been sacrificed in figures 11(a-c) in order to amplify the hot-wire response to the pre-stall turbulence. The existence of a period of turbulence prior to separation is clearly evident over a portion of the surface.

It is interesting to compare the standard deviation results with those obtained from direct observation of the analog traces. Since an abrupt change in the character of the analog trace of velocity is usually not observed, due to the presence of noise and the gradual development of turbulence during the period of transition (fig. 12), it was necessary to estimate the time of transition based on a sensible increase in the relative amplitude of the high frequency content in the hot-wire signal. Based on subjective estimates using analog data and the more definitive judgments using standard deviations, the azimuthal locations of transition over the surface near the leading edge are shown in figure 13.

Although within the indicated error band (fig. 13), transition at the forward locations ($s/c \leq 0.024$), when determined by the standard deviation approach, appears to lag those observations made directly from analog signals, the agreement is otherwise found to be quite good. In general, the forward rate of advance of transition is seen to be briefly decelerated as it moves through a zone centered around $s/c = 0.035$. As the reduced frequency is increased, transition at each surface location is observed to occur later in the cycle; however, the trend remains unchanged. Evidence will be presented in succeeding sections to confirm that this behavior reflects the emergence of a separation bubble and the additional constraint which this places on the point of transition.

It is interesting to note that there appears in figure 10 a consistent association between the points of transition and a subsequent slight depression in the mean responses. This decrease in the hot-wire voltage is believed to be due to the sequential movement of the probes through the stagnation region at the closure of the separation bubble. This assumption is collaborated by the local pressure rise (identified in fig. 8) occurring at each corresponding location.

Separation Bubble

The laminar boundary layer near the leading edge of certain airfoils is sometimes found to separate from the surface and continue as a narrow shear layer before transitioning to turbulent flow and reattaching to the surface a short distance downstream. This detached shear layer encloses a trapped fluid region commonly referred to as a laminar separation bubble. An examination of figures 14(a-e) shows that during the interval of azimuth between mean incidence and moment stall a pressure perturbation appears in the untripped case which is reminiscent of the classical bubble region (ref. 11). Specifically, those transducers located along the first 2% of the surface show a decelerated pressure recovery followed by a rapid return to a smooth trend. During this portion of the cycle (and independent of the reduced frequency) the bubble travels upstream a surface distance of approximately 1% and then persists intact well past the onset of the suction collapse over the leading-edge region. The term suction collapse refers to the first time in the cycle when the pressure over the entire leading-edge region exhibits a definite and often uneven decline relative to the previous time step.

The placement of a boundary-layer trip along the airfoil leading edge for the purpose of promoting premature transition is observed (fig. 14) to not only circumvent the development of a bubble region, but also to affect three distinguishing alterations. There is a substantial loss in suction over the entire leading-edge region; the suction collapse occurs earlier in the cycle (thus implying an earlier moment stall); and the point of minimum pressure moves away from the leading edge. Both sets of curves are plotted on a common scale which is determined by the maximum pressure detected in this region during the interval of the cycle shown.

If the pressure at discrete locations are viewed with respect to time (figs. 15(a-c)), the pressure perturbation takes the form of a double inflection that interrupts an otherwise smooth increase in suction, thereby creating the impression of a pause in the suction development. This pause is of the order $\Delta\omega t \approx 0.13$ and appears to be independent of reduced frequency. It is interesting that this perturbation is a great deal more pronounced in the unsteady case than that inferred from steady measurements by McCullough and Gault (ref. 11); this may only be due to a sparsity of data points in the referenced study. In comparing figures 13 and 16, the phase angle assigned to the initial pre-stall break in the pressure distribution is found to correlate with transition quite well. Thus the second inflection, which represents a local pressure maximum, no doubt locates the zone of reattachment. Whether the existence of a separation bubble is demonstrated in terms of space or time distributions, it is clear that a bubble is present and moves forward as the angle of incidence increases, but is not present when a trip is placed at the leading edge.

Although much higher values of suction are reached in the untripped case, it is interesting to note that the qualitative characteristics of the pressure distribution are quite similar. A common feature of both the tripped and untripped boundary layer cases is the general suction collapse over the leading-edge region (which signals the onset of moment stall) that is quickly followed by flow separation (figs. 17 and 18). In both cases these events are postponed to successively higher angles-of-incidence as the reduced frequency is increased.

Using the mean angle of incidence as the origin ($\omega t = 0$), a dimensionless time step of unity indicates that the freestream has traveled a distance of one chord length before a given event has taken place. Utilizing this terminology it can be seen that as the reduced frequency is increased, the number of dimensionless time steps is decreased. It is also evident that the trip accelerates the suction collapse and flow separation by as much as two time steps. It is significant to note that when expressed in terms of dimensionless time that an almost constant delay exists between the trip and untripped cases, whereas the delay in terms of azimuth is definitely nonuniform.

Flow Separation Near the Leading Edge

During the high-pitch amplitude cases given by $\alpha = 15^\circ + 10^\circ \sin \omega t$, there were no reduced frequencies studied for which the flow did not separate over a portion of the cycle. Flow separation was assigned on the basis of a divergence to large sustained values of the standard deviation of the hot-wire fluctuations (fig. 11). The relatively large deviations encountered during separation are mainly attributable to the large scale turbulent fluctuations about a nearly quiescent mean flow within the separation domain.

The point of flow separation was found to accelerate as it progressed toward the leading edge. This was equally true for both the tripped and untripped cases over the frequency range from

$k = 0.05$ to 0.25 . However, since the separation over this region was nearly simultaneous, the value given was based on the responses of the hot-wire probes nearest the 3% location. The resulting trend shows that as the reduced frequency increases, the number of elapsed dimensionless time steps decreases before separation occurs (fig. 18). This decrease appears to be approaching a limit which is no doubt governed by the growing importance of the time scale of the airfoil oscillation compared with that of the freestream (e.g., the ratio of the period of airfoil oscillation to the time required for a freestream element to travel one chord length is decreasing).

Moment Stall Indicator

Because it is primarily due to the severe negative divergence of the pitching moment that dynamic stall has come under study, it is reasonable to seek a simple indicator (short of a detailed pressure integration) that would signal the onset of moment stall. Not only would such information be useful for keying a control device during rotor operation, but it might prove paramount in correlating detailed boundary-layer events which are not only dependent upon many cycles of data for conditional averaging, but also depend on the precise beginning of a precipitating phenomenon.

For the purpose of quantification, moment stall will refer to that point in the cycle where the pitching moment exhibits a definite negative roll-off with respect to ωt . The suction collapse over the leading-edge region represents a sufficiently serious alteration of the total pressure distribution to cause pitching-moment stall. The phase angle at which the leading-edge suction is judged to collapse is shown in figure 19 for numerous pitch schedules and reduced frequencies. Also included are the times when C_{p_3} (positioned at $s/c = 0.014$) reached peak suction values. It is evident that there is a correlation between the suction collapse and the peak suction for $\omega t < \pi/2$; however, there are also peaks for $\omega t > \pi/2$ where no suction collapse was observed. To better understand the significance of the suction peak, it is useful to refer to figure 20 where C_M and C_{p_3} are shown over a full cycle. The pitching moment curves extend from two nonstalled cases to progressively stronger or deeper stalls, the worst stall being for $k = 0.15$. Referring to the lower set of curves, it is realized that the shape of C_{p_3} and the phase angle of the peak are sufficient characteristics to identify the presence and degree of moment stall.

A sinusoidal shape of the curve for C_{p_3} indicates that the flow about the airfoil is essentially potential and that any observable moment hysteresis is primarily due to wake-induced effects on the local velocity field. In this instance the suction peak will normally occur after maximum airfoil incidence ($\omega t > \pi/2$), and is typical for oscillations below the static stall angle.

If the shape of C_{p_3} is nonsinusoidal and the peak occurs after maximum incidence, then a partially-developed moment stall is being forced by the change in the direction of pitch. This condition usually occurs only for a limited range of oscillation amplitude and frequency combinations. For these cases the static stall angle is exceeded while oscillating at a frequency which produces an insufficient store of energy within the turbulent boundary layer, yet yields a relatively mild boundary-layer breakdown without a vortex being evident in the pressure distribution. It has been shown for the case where the static stall angle was exceeded by 2° during a low frequency oscillation (ref. 1) that unstalled conditions can be reinstated by increasing the oscillation frequency sufficiently. It will be shown later that the same trend can be obtained by reducing the mean angle of oscillation while maintaining a constant reduced frequency.

Finally, if the shape of the curve for C_{p_3} is nonsinusoidal and the peak occurs prior to maximum incidence, then a fully developed moment stall is in progress. As the reduced frequency is decreased, the retardation of the peak smoothly relaxes to the static stall azimuthal position. For these cases the peak in the curve for C_{p_3} consistently precedes the onset of the suction collapse over the leading-edge region by an average of 0.075 rad and is accompanied by definite evidence for the passage of a vortex over the upper surface.

Vortex Passage

Simultaneous with the suction collapse over the leading-edge region is the emergence of a secondary low-pressure zone that is first discernable at between 10 and 20% chord. This zone continues to grow in strength and then begins to travel over the upper surface as a suction wave with a velocity averaging less than one-half that of the freestream. It has been shown experimentally (ref. 12) that this is the imprint made by the passage of the dynamic-stall vortex, a phenomenon originally identified by Han and Garelick (ref. 13).

To demonstrate the effect of reduced frequency on the stall vortex, consider the unmodified airfoil case presented in figures 21(a-c) for that portion of the cycle during which the vortex passage takes place. Although there is no evidence of a suction wave for $k = 0.05$, waves are seen to become more detectable as the oscillation frequency is increased. The initial growth of this low-pressure zone immediately follows the point of minimum pressure.

The cases with leading-edge modifications (figs. 22(a-c) and 23(a-c)) exhibit suction imprints that are substantially more pronounced. For a given frequency, the suction wave appears to both elongate and weaken as it moves over the airfoil surface. A feature which is common to all cases with and without modification is that the magnitude of the suction imprint increases with increasing reduced frequency, thereby suggesting that the intensity of the stall vortex is related to the increase in maximum lift developed for the cycle.

The influence of the stall vortex cannot be based on an estimate of the suction imprint alone. To do so would discredit the importance of the physically large vortex occurring in the unmodified airfoil case (ref. 1) where the suction imprint is comparatively faint. Although the perturbation itself is slight, the influence of the vortex over the entire surface is significant. Hence, for the modified cases, proportionately more lift must be contributed from the immediate region of the suction wave.

Based on subjective judgments about the chordwise location of the center of the suction wave in terms of dimensionless time, a comparison of results with and without modification is given in figures 24 and 25. Because of an unresolved phase lag error of approximately 0.1 rad, some caution is recommended when interpreting the full pressure distribution results obtained for the unmodified airfoil without end plates. With the exception of this discrepancy, these data show that the time of initial detection is latest for the unmodified case and earliest for the serration case. However, the corresponding chordwise locations for the unmodified and serration cases at the time of detection is further aft than for the trip case. This would imply that the size of the vortex is smallest (because of its proximity to the leading edge) at the time of its detection for the trip case; and this is consistent with the fact that a stronger and more concentrated suction perturbation is produced for the trip case as the vortex passes over the surface (fig. 22).

Another important parameter affecting the stall vortex is the oscillation amplitude. Figures 26(a-b) show a comparison between $\alpha_1 = 10^\circ$ and 14° for a reduced frequency $k = 0.1$. These results indicate that an ordered flow around the airfoil is maintained for several additional degrees of incidence in the higher amplitude case. As the flow breaks down there appears a much stronger suction perturbation, once again suggesting that the lift contributed by the leading-edge region is being transferred to the shed vortex. Although postponed about five dimensionless time steps in the higher amplitude case, there does not appear to be any significant difference in the rate of movement of the suction wave over the surface (fig. 27).

End plates also seem to have an effect on the shedding characteristics of the stall vortex. A comparison of figures 22(a-c) and 28(a-c) will show that without end plates, higher suction values are attained over the leading-edge region and are followed by suction waves that are initially stronger and more concentrated. Figure 29 shows that for the higher frequency cases without end plates, the suction wave originates later in time but then moves more rapidly over the surface. Although the imprint is difficult to detect in either case, end plates seem to have the greatest effect at the lowest frequency, $k = 0.05$. Without end plates the suction wave apparently degenerates before reaching midchord, possibly as the result of a weaker vortex.

An important result of this study is that the strength of the stall vortex may be related to the circulation on the airfoil at the time the vortex is formed. Combining this estimate of the strength of the vortex with the data presented for the time of origin and the shedding velocity of the vortex, it appears that the missing elements for a semi-empirical model for the basic NACA 0012 airfoil oscillating through stall are now at hand.

Pressure Integration

Recall that up to this point the more significant events making up the dynamic stall process have been discussed on an individual and somewhat unconnected basis. Viewed collectively, an airfoil undergoing high amplitude pitch oscillations is generally said to experience a well-behaved period of suction increase over the upper surface, followed by a strong distortion of this pressure distribution caused by the shedding of a vortex from the leading-edge region, and a completion of the cycle beneath a large domain of separated flow. The resultant importance of these various flow states is realized by integrating the pressure over the upper and lower surface to obtain the more familiar aerodynamic quantities. The majority of the following results are given in terms of (1) the pitching moment about the quarterchord, (2) the normal force, (3) the chord force, and (4) the center of pressure. For convenience, a few select cases have been presented in terms of lift and drag coefficients. Certain of these aerodynamic coefficients have also been summarized for all test cases in table 2. It should be kept in mind that all aerodynamic coefficients are calculated on the basis of pressure forces only and do not include viscous shear. Some care is therefore advisable when interpreting low frequency chord- and drag-force data.

A variable power spline was applied to the discrete points of data in anticipation that a smooth representation of the pressure distribution would yield better integration accuracy. Although this was a definite improvement over a cubic spline fit, overshoots were still found that made the method unacceptable on a general application basis. Instead, all integrations given herein are based on the trapezoidal rule.

With quantifiable data for the normal force and pitching moment available, numerical values can now be assigned to the results reported in reference 1. A comparison was made at various reduced frequencies and the results were found to be in good qualitative agreement. The principal difference appears in the prestall negative trend in the pitching moment which does not exist in the present data. This is attributable to the present inclusion of second-order terms in the quadrature formulation for the moment.

Reduced Frequency

The most significant parameter in this study was found to be the frequency at which the airfoil was pitched about its quarter-chord axis. It was common to find 100% increases in force and moment coefficients as the reduced frequency, $k = \omega c / 2U_\infty$ was varied from 0.004 to 0.25 (figs. 30(a-d)). Because the coefficients in these figures have been displayed as a function of α , it is readily apparent that the recovery from stall is further delayed and the extent of the hysteresis loops enlarged as the reduced frequency is increased. It is observed for $k = 0.02$ that prior to reaching maximum lift there appears to be a surge in the lift which occurs very near the point of negative roll-off in pitching moment that marks the beginning of moment stall (refer to fig. 31(a) for the subjective definitions of C_N surge and C_M roll-off). If quasi-steady is defined as the condition where coefficients do not deviate from steady values, then $k = 0.004$ would appear to be a dividing line for quasi-steady, at least for those cases without end plates. It is, therefore, surprising to find a sizable overshoot existing at this low frequency for the case with end plates (fig. 30(d)). The frequency is too low for the lift-induced benefits of the shed vortex to account for the long period of lift overshoot observed. It is possible, however, that the presence of end plates has reduced the amount of three-dimensional separation (mentioned earlier). In any case, it is clear that $k = 0.004$ cannot be considered as quasi-steady when end plates are used.

If the integrated pressure results are instead plotted concurrently as a function of ωt , several new distinguishing features can be more easily discussed. In figure 31(a), not only does an increase in frequency generally bring about an increase in maximum normal force, but that portion of the cycle during which this increase takes place is measurably extended. This is a significant factor since it represents a substantial improvement in the cyclic load carrying capability of the airfoil. It should be remembered, however, that the contribution to drag is also proportionately increased. The chord force indicates that progressively larger amounts of thrust are experienced as the reduced frequency is increased. The pitching moment seems to follow the trend established by the normal force with regard to stall delay and cyclic extremes. In addition, there appears to be a clear relationship between the secondary perturbations in the normal force and pitching moment; these perturbations are believed to be due to the subsequent shedding of less prominent vortices from the airfoil. Finally, the center of pressure represents the point about which the moment is zero and is obtained by dividing the pitching moment by the normal force. The importance of this quantity is that it indicates the suitability of the location chosen for the pitch axis as far as minimizing the pitch-link loads on rotors.

The results indicate that the center of pressure moves away from the pitch axis and toward the midchord as the stall begins. During the stall recovery the moment becomes positive and the center of pressure moves forward of the pitch axis and is occasionally located ahead of the airfoil. In general, however, the excursions that occur during the stalled portion of the cycle seem to be

equally divided about the quarter-chord location, which demonstrates that this position continues to be a suitable pitch axis in the dynamic case. Figures 31(b-c) indicate that while leading-edge modifications do yield different results, the trend produced over the frequency range is found to be similar to the unmodified case discussed above.

In summary, figure 32 correlates the reduced frequency with a chronology of significant events which accompany the formation of the leading-edge vortex. At all frequencies there occurs a definite and ordered sequence of identifiable events as the airfoil pitches past the static stall angle. The suction over the upper surface continues to increase and then collectively yields a surge in the normal force which causes the lift-curve slope to as much as double in value (cf. fig. 31(a)). There next appears a slight negative growth in the pitching moment which is rapidly followed by the attainment of a maximum in negative chord force and a minimum in pressure over the leading-edge region. As the pitching moment continues to grow, the initial imprint of the suction wave appears in the pressure distribution and is quickly followed by a definite roll-off in the pitching moment. This divergence of the moment to large negative values is due to the movement of the shed vortex over the upper surface and is responsible for the extent of the increase in the normal force. Finally, the normal force reaches its maximum value and the sequence is concluded with the attainment of maximum negative moment. Although the order is unaffected, increasing the reduced frequency is seen to postpone the occurrence of each event as well as to generally expand the phase intervals between each event (also see table 3).

Numerous attempts have been made to correlate dynamic stall delay with key unsteady parameters in order to obtain some sort of universal law (ref. 14). A promising approach appeared to be based on a time constant that was linearly dependent on the static-stall phase angle and the reduced frequency,

$$\tau = \left[\omega t_* - \sin^{-1} \left(\frac{\alpha_{ss} - \alpha_0}{\alpha_1} \right) \right] / 2k$$

where ωt_* denotes the phase angle corresponding to a given stall event. By using data obtained at several frequencies, this quantity did not yield a universally constant value for the onset of lift stall; however an acceptable correlation did result for the initial negative growth in pitching moment. When examining the validity of this time constant in light of the present data, it appears that neither this event nor other less subjective events render constant values in this time frame. By replacing the denominator in the expression for τ with $\sqrt{2k}$, it is found that nearly constant values are obtained for $C_{N_{surge}}$, $-C_{c_{max}}$ and $C_{N_{max}}$ over the frequency range from 0.05 to 0.25. Although this slight modification does produce encouraging results, data representing a broader range of amplitudes and airfoil shapes are believed needed before a new time constant can be proposed with confidence. In the process of studying additional data, care should be taken to distinguish between partially- and fully-developed stall cases. Only fully developed stall data are expected to yield to a time constant classification of this type. A second point to bear in mind is that although the surge in normal force and the initial negative growth in pitching moment appear to be the first dynamic stall events to occur, they are subjective characteristics that are difficult to specify precisely. It may, therefore, be prudent to recognize the more quantifiable negative peak in the chord force as a key correlating quantity for various stall data.

Mean Angle and Amplitude

The mean angle and pitch amplitude are important since they determine the degree of penetration beyond the static stall angle and the associated unsteadiness for a given oscillation frequency. Most of the results presented thus far have been for $\alpha = 15^\circ + 10^\circ \sin \omega t$ where the flow breaks down between the static stall angle and the top of the cycle; however, by reducing the amplitude to 6° there are frequencies at which the stall is delayed to maximum incidence and the resultant loadings are found to be less pronounced (Figs. 33(a-b)). In spite of the impressive overshoot in normal force obtained in the 10° amplitude case, it can be calculated from figure 33(b) that the average over the cycle is actually higher in the 6° amplitude case. When this is coupled with the facts that the magnitude of the pitching moment is substantially reduced, that the center of pressure deviates less from the quarter-chord position, and that a greater average thrust is developed, the benefits from operating slightly below the fully stalled condition are realized to be considerable.

If the amplitude of oscillation is held fixed at 6° and the mean angle reduced from 15° to 6° , the normal force hysteresis is progressively reduced (fig. 34(a)) and the pitching moment passes from negative to positive damping. When the effects of mean angle reduction are examined as a function of ωt (fig. 34(b)), it is seen that the first reduction in mean angle to 11° eliminates the development of moment stall even though the static stall angle and static $C_{N_{\max}}$ are exceeded. However, a further reduction in mean angle to 6° only brings about an expected decrease in the cyclic averages of normal force and thrust.

Consider now the results where the pitch amplitude is increased from 10° to 14° while maintaining the reduced frequency at $k = 0.10$ (figs. 35(a-c)). In both cases fully-developed stall is observed to take place; that is, the flow breaks down and the vorticity is shed prior to reaching maximum incidence rather than the stall being forced to occur at the top of the cycle. The important difference between the 10° and 14° amplitude cases is that each stall occurs while undergoing different rates of change in incidence. Yet, in spite of the fact that the local $\dot{\alpha}$ is higher in the 14° amplitude case and that moment stall begins at a much higher incidence, the corresponding phase angle is only slightly lower. This behavior suggests that there may be a characteristic time, governing the interval of lift overshoot between the static stall angle and moment stall, that is a weak function of $\dot{\alpha}$ at the static stall angle.

End Plates

The results obtained from testing an airfoil that is large relative to the test section will necessarily be contaminated by a certain amount of erroneous loading due to the proximity of the test-section walls. For example, the walls that intersect with the model span give rise to a three-dimensional interaction of the respective boundary-layer sheets. This is known to cause a variation, in the local angle of attack along the span, that affects the stall process (ref. 10). This particular source of error can be minimized by the addition of a pair of end plates on the airfoil, thereby creating between them a region of flow that is more nearly two dimensional. Hot-wire probes placed at several spanwise locations along the airfoil showed (ref. 1) that for $k < 0.1$, where three-dimensional effects were found to be significant, the addition of end plates caused the flow to behave uniformly along the span.

Examining the results shown in figure 36(a) for $k = 0.02$, it is clear that the use of end plates delays the stall considerably. It has already been shown that end plates measurably affected the flow near the static stall angle (fig. 6). In the dynamic case the end plates appear to preserve a more nearly two-dimensional vortex as it passes over the airfoil. Once the reduced frequency has been increased to 0.10 and beyond, differences in the integrated pressure results become less distinguishable (figs. 36(b-e)). It is interesting that the results with trip also show the same trend at the lower frequencies (figs. 37(a-b)); however, the disagreement returns as the frequency is increased further (figs. 37(c-d)). The absence of end plates in the tripped case causes the vortex to develop slightly later in the cycle (fig. 29) and to produce a more evident imprint in the pressure distribution as it passes over the surface of the airfoil (figs. 22(a) and 28(a)). In the case without end plates there is apparently some beneficial three-dimensional relief that permits the vortex development to be postponed until later in the cycle when it then assumes a greater amount of circulation.

Leading-Edge Modifications

The existence of a leading-edge separation bubble on the NACA 0012 airfoil is known (ref. 1) to have no direct effect on the stall process for the conditions in this test; in fact, the pressure perturbation caused by the presence of the bubble was shown (fig. 14) to persist even during the initial phase of the suction collapse over the leading-edge region. Yet the precise character of the boundary layer in this region does play an important role in preparing the flow for its travel through an adverse pressure gradient over the remainder of the airfoil. Modifications were therefore applied to the leading edge that were specifically intended to either eliminate or drastically alter the separation bubble. Flow visualizations performed during static tests (ref. 1) confirmed that a boundary-layer trip placed along the leading edge was successful in promoting early transition to turbulence so that a laminar separation bubble was prevented. Upstream-facing serrations were also examined and found to produce a distorted flow pattern in the bubble vicinity; this indicated a possible alteration of that flow into horseshoe-shaped vortices.

While both modifications were observed to produce definite changes in the resulting loads, neither effort showed any deviation from the classical dynamic stall pattern (figs. 38(a-c)). Both the trip and serration cases are seen to trigger an earlier stall onset over the complete frequency range. Although the trip does produce a higher peak value for C_N in the $k = 0.25$ case, the mean average over the cycle is only slightly increased while the magnitude of the pitching moment is substantially increased. The peak pressures are considerably lower in the modified cases, but the integrated loads remain approximately equal until well beyond the static stall angle. Subsequent departures are the result of an early release of vorticity on the modified airfoils (figs. 24 and 25). The important point to note in attempting a modification to improve performance is that a higher peak value of lift is generally accompanied by higher negative values of pitching moment, but not necessarily by a higher mean average in lift.

Coefficient Extrema

After studying the various parameters affecting airfoil performance, it was realized that some measure of "goodness" can be represented by the extremes and averages of the integrated pressure

coefficients and their derivatives. This section summarizes this information and also includes several quantities that reflect the unsteady effects present in a given oscillation.

It should be kept in mind that in the process of digitizing the original analog test data at a finite number of discrete locations, it seems inevitable that the actual peak values may have been omitted. It is not practical to assign a meaningful value to the resulting error band for the extremes presented since the scaling and integration of the data were not performed until after digitization. Because each cycle of data did vary in phase relative to the digitizing locations, the error associated with the average extremes can be expected to be less than for any individual cycle.

It is evident from figures 39 and 40 that independent of the presence of end plates and leading-edge modifications, an increase in reduced frequency generally causes an increase in the average values of lift, drag, thrust, and negative pitching moment. The center of pressure also moves forward toward the quarter-chord location for the basic NACA 0012, but not for the modified cases. The reason that the center of pressure does not move to the quarter chord as the reduced frequency approaches zero is that the angle of incidence ranges from 0° to 25° so that the average center of pressure must include values from the stall regime. Due to the relative magnitudes of the normal and chord forces and the incidence range, the resulting lift force closely resembles the normal force; however, the chord and drag components are seen to be quite dissimilar. It is also found (fig. 39) that higher lift, lower drag, and lower negative pitching-moment averages are obtained for the basic airfoil. The addition of end plates to the basic airfoil (fig. 40) yields even higher values of lift, but at the expense of higher drag and higher negative pitching moment.

While mean values are important factors in determining the load-carrying capability and power requirements at a given condition, the maximum and minimum excursions of these loads and where they occur during the cycle may be even more important quantities since they provide a measure of the dynamic environment. For the present data there generally appears to be an increasing spread between the maximum and minimum values as the reduced frequency is increased over the lower range (fig. 41); however, the peak loads are observed to either reach a plateau or decrease in magnitude over the upper frequency range. The basic airfoil tends to produce higher lift, drag, and negative-pitching-moment peaks at the lower frequencies, but is bracketed by the trip and serration results at the higher frequencies (fig. 41). It appears that there is a greater amount of variation in the peak loads as a function of reduced frequency for the basic airfoil than for either of the two modifications. With the exception of the maximum lift and normal-force peaks, end plates are seen to generally reduce the maximum and minimum peak loads (fig. 42).

The interpretation of the azimuthal values assigned to the occurrence of peak loads is somewhat more difficult due to the erratic nature of the stall domain where these extremes are usually found. For example, the peculiar step in the azimuthal location of minimum C_L (Fig. 43) is indicative of the growing significance of the dynamic effects in the separated region at the higher frequencies (e.g., see fig. 30). Generally speaking, however, increasing the reduced frequency tends to retard the occurrence of maximum and minimum loads over the upper frequency range. It can also be seen that maximum drag precedes only slightly the point of maximum negative pitching moment, and that both occur after maximum lift has been reached. Without changing the order of these events, the addition of leading-edge modifications causes each event to occur earlier in the cycle. End plates, however, are shown in figure 44 to have little effect on these three quantities.

Two quantities which summarize the degree of hysteresis are given by the normal force defect and the pitch damping. The normal-force defect term, ξ , is obtained from the closed line integral around the cycle of the normal force and the pitch-damping term, ζ , is obtained from the closed line integral of the pitching moment; in both cases the variable of integration is α .

$$\xi = \oint C_N d\alpha / \int_{-\pi/2}^{\pi/2} C_N d\alpha \quad \zeta = -\oint C_M d\alpha / 4\alpha^2$$

The normal-force defect represents the loss in load-carrying ability arising from the fact that the normal force experienced during the pitch-down is usually less than that during the pitch-up. If there is no hysteresis, both portions of the cycle trace out an identical curve and the defect is zero. The numerical value assigned to this hysteresis is therefore based on that percentage of the integral contributed during the upstroke which is lost during the downstroke. The pitch-damping term, which is more frequently reported, has a different interpretation. Since the pitching moment acts in the direction of motion of the airfoil, the closed-line integral of the pitching moment with respect to α provides a measure of the net accumulation of energy from the flow. Hence, if the normal force and pitching moment trace out clockwise patterns when viewed as a function of α , then the normal-force defect will be positive and the pitch damping will be negative.

It is evident in figure 45 that in all cases the greatest increase in the normal-force defect takes place over the lower frequency range. The basic airfoil, however, shows a trend back to lower values of defect at the higher frequencies, otherwise the distinction between the airfoil-modification results is less obvious. The pitch damping is generally found to be stabilizing over the midfrequency range and destabilizing at high and very low frequencies. It is noted here that the modifications have a profound stabilizing effect over the entire frequency range and the airfoil is almost always stable when the serrations are used. End plates can be seen to generally decrease the normal force defect and increase the damping-in pitch (fig. 46). To better understand the inflection in pitch damping, it is useful to examine the integrand of the damping integral, $d\zeta/d\omega t \propto C_M d\alpha/d\omega t$, where ωt is taken to be the variable of integration (fig. 46). As the frequency is increased, the large negative pitching-moment values characterizing the moment stall not only increase in magnitude but also occur later in the cycle (fig. 30). When coupled with the local $d\alpha/d\omega t$, there results at the lower frequencies two large and opposing contributions to $d\zeta/d\omega t$, the upstroke being positive and the downstroke negative (fig. 47). As the frequency is increased further the major effects of moment stall move to the downstroke portion of the cycle, therefore favoring the net production of negative damping.

As suggested earlier, the onset of moment stall can be identified by either C_M roll-off or C_N surge as well as by the character of the pressure at some point near the leading edge. These indicators attest to the presence of moment stall in all cases for which $\alpha = 15^\circ + 10^\circ \sin \omega t$; in particular, the occurrence of a suction peak prior to reaching the top of the cycle means that a fully developed stall vortex is being shed. An increase in frequency causes each of these phenomena to occur later in the cycle while the addition of leading-edge modifications decreases the amount of this delay throughout the frequency range. The use of end plates generally causes a further delay in moment stall at the lower frequencies; however, at the higher frequencies it appears that the flow disturbance which causes the favorable surge in C_N (i.e., an increase in $dC_L/d\alpha$) has a longer residence time before the penalty of C_M roll-off is encountered (fig. 47).

The final area to be addressed is the unsteadiness of the time derivatives of the various aerodynamic coefficients over the complete cycle of oscillation (figs. 48(a-d) and 49(a-d)). The significant features to be observed are (1) that the more dominant fluctuations are confined to the

period of stall, and hence they are experienced during progressively later portions of the cycle; (2) that usually only one or two predominant excursions are observed to occur; and (3) that while one peak value may only slightly exceed another, they may occur at widely different values of ωt . Being familiar with these qualities and the general erratic nature of the coefficient derivatives, the frequently ill-behaved trends displayed in the summary figures of maxima and minima (figs. 50-53) can be better appreciated. Generally speaking, there appears to be a greater variation in extremes due to leading-edge modifications than due to reduced frequency; however, there is a common tendency for the data to exhibit an inflection over the mid-frequency range. It also seems that the strongest derivatives are those representing unfavorable changes in loading (e.g., lift loss and drag rise). The effect of end plates is to generally reduce the severity of these derivatives over the frequency range (fig. 51). The phase angles at which these extremes occur show, except in the case of pitching moment, that the peak increases usually precede peak decreases and that each can be delayed by increasing the frequency of oscillation (fig. 52). Although the effect of end plates is minor, there is a slight retardation in phase angle when they are present.

It is concluded that the various measures of "goodness" discussed in this section can be useful in weighing the impact of parametric changes on numerous performance quantities. It is noted that changes that produce higher values of maximum lift usually incur higher penalties in terms of drag and pitching moment while not necessarily improving the mean cycle average in lift. In addition, the impulsive loading qualities represented by the coefficient derivatives also need to be considered before all of the important design trade-offs can be reconciled.

CONCLUSIONS

The following conclusions are made about the data presented for the NACA 0012 airfoil at a Reynolds number of 2.5×10^6 .

1. Under the conditions stated for this test, the laminar separation bubble has no direct effect on the stall process and can be seen to persist even during the onset of the suction collapse over the leading-edge region.
2. It appears that a reasonable estimate of the unsteady drag forces can be achieved using only those contributions due to pressure forces. This procedure is especially valid over the stalled portion of the cycle where viscous shear is relatively less significant. These results demonstrate the importance of single-surface pressure measurements rather than differential ones.
3. Based on the pressure sensed at a point near the leading edge, the shape of the pressure response and the peak-suction phase angle are sufficient for determining the presence of moment stall and its relative severity.
4. The strength of the stall vortex seems to be related to the circulation on the airfoil at the time the vortex is formed. When combined with the data presented for the time of origin and the shedding velocity of the vortex, a semi-empirical model for this airfoil oscillating through stall is now possible.
5. The sequence of stall events is found to be (1) a positive surge in normal force, (2) negative moment growth, (3) maximum negative chord force, (4) maximum leading-edge suction, (5) suction

wave appears, (6) negative roll-off in pitching moment, (7) maximum normal force, and (g) maximum negative pitching moment.

6. The frequency of oscillation has an important influence in the delay of stall and the maximum aerodynamic loads that result. Stall may be delayed by as much as $\Delta\omega t = \pi/2$ with loads reaching $C_p = -30$, $C_L = 3.5$, $C_D = 1.5$, and $C_M = -0.75$.

7. Aside from improving the pitch damping and reducing the peak drag derivative, the leading-edge modifications considered were not found to offer a general improvement in performance throughout the frequency range.

8. End plates are found to have an effect on the stall onset and the strength of the shed vortex only at low frequencies, although they appear to offer some improvement in the stability and performance characteristics over the entire frequency range. It is recommended that end plates be considered when conducting similar tests of a relatively large airfoil.

Ames Research Center
National Aeronautics and Space Administration
and
Aeromechanics Laboratory, U.S. Army Aviation R&D Command
Ames Research Center, Moffett Field, Calif. 94035, June 23, 1977

TABLE 2.— SUMMARY OF AERODYNAMIC QUANTITIES

Case (figure)	Modification/ end plates	α_0	α_1	k	Average				Maximum				C_N defect, %	Pitch damping		
					C_N	$-C_c$	C_L	C_D	$-C_M$	$C.P.$	$-C_p$	C_L			C_D	$-C_M$
54(a)	None/No	15	10	0.004	1.06	0.09	1.03	0.20	0.05	0.30	9.	1.56	0.57	0.15	7	-0.014
54(b)				.020	1.07	.11	1.05	.18	.05	.29	14.	1.93	.51	.18	21	-.010
54(c)				.050	1.12	.12	1.09	.20	.04	.28	18.	2.44	.76	.32	40	.008
54(d)				.100	1.20	.15	1.18	.21	.04	.26	23.	2.74	1.11	.46	49	.011
54(e)				.150	1.25	.17	1.23	.22	.05	.25	26.	2.85	1.22	.52	52	-.019
54(f)				.200	1.32	.21	1.31	.22	.05	.25	27.	2.90	1.18	.50	47	-.029
54(g)				.250	1.34	.22	1.34	.23	.06	.24	28.	2.91	1.08	.48	41	-.056
54(h)				.150	0.68	.10	0.69	.00	.00	.29	7.	1.32	.03	.02	4	.045
54(i)				.240	0.69	.10	0.69	.01	.00	.27	7.	1.27	.04	.04	3	.073
54(j)				.240	1.20	.24	1.23	.02	.00	.25	13.	1.79	.08	.03	9	.083
54(k)				.240	1.42	.30	1.44	.12	.02	.26	20.	2.28	.42	.22	21	-.076
54(l)				.100	1.18	.10	1.12	.32	.10	.31	26.	3.09	1.50	.63	50	.012
55(a)	Trip/No			.003	1.07	.06	1.03	.23	.07	.31	8.	1.45	.60	.17	3	-.002
55(b)				.020	1.05	.06	1.01	.22	.06	.30	10.	1.79	.55	.17	22	.008
55(c)				.050	1.02	.07	0.98	.24	.07	.31	12.	2.13	.68	.30	43	.034
55(d)				.100	1.13	.07	1.08	.27	.08	.30	14.	2.62	1.06	.49	53	.041
55(e)				.150	1.31	.10	1.26	.31	.09	.29	15.	3.09	1.36	.62	51	.009
55(f)				.200	1.34	.11	1.29	.32	.09	.28	15.	3.15	1.43	.64	47	-.018
55(g)				.250	1.39	.11	1.34	.34	.09	.28	15.	3.13	1.42	.62	49	-.048
56(a)				.004	1.01	.05	0.97	.22	.03	.28	7.	1.29	.52	.12	3	.000
56(b)				.020	1.00	.05	0.96	.22	.04	.28	8.	1.45	.51	.14	14	.014
56(c)				.050	1.05	.06	1.01	.23	.06	.29	9.	1.84	.61	.28	29	.033
56(d)				.100	1.14	.06	1.10	.27	.07	.29	10.	2.25	.89	.42	47	.065
56(e)				.150	1.21	.07	1.16	.30	.08	.28	10.	2.48	1.04	.46	50	.043
56(f)				.200	1.23	.07	1.18	.33	.08	.28	11.	2.46	1.08	.47	52	.017
56(g)				.250	1.27	.08	1.22	.33	.08	.28	11.	2.54	1.10	.46	54	-.009
57(a)	None/Yes			.004	1.17	.11	1.15	.21	.06	.30	14.	2.12	.55	.16	19	-.022
57(b)				.020	1.25	.16	1.24	.20	.06	.30	15.	2.35	.63	.28	23	-.009
57(c)				.050	1.19	.15	1.17	.19	.05	.28	15.	2.39	.67	.30	34	.011
57(d)				.100	1.26	.14	1.24	.24	.06	.29	18.	2.83	1.01	.45	46	.011
57(e)				.150	1.30	.15	1.28	.26	.07	.28	20.	3.01	1.21	.48	49	-.017
57(f)				.200	1.35	.18	1.34	.26	.06	.27	22.	2.92	1.17	.44	44	-.021
57(g)				.250	1.38	.20	1.37	.26	.06	.27	22.	2.84	1.05	.36	39	-.027
57(h)				.240	1.41	.28	1.43	.13	.02	.25	17.	2.20	.34	.20	19	-.051
57(i)	Trip/Yes			.100	1.14	.10	1.09	.31	.08	.29	22.	3.09	1.44	.54	53	-.021
58(a)				.004	1.01	.05	0.97	.21	.05	.30	9.	1.60	.51	.12	12	-.013
58(b)				.020	1.01	.06	0.98	.22	.05	.30	10.	1.92	.51	.22	29	.004
58(c)				.050	1.04	.06	1.01	.23	.05	.29	11.	2.20	.73	.33	43	.025
58(d)				.100	1.13	.06	1.09	.27	.07	.29	12.	2.51	1.00	.46	52	.040
58(e)				.150	1.23	.08	1.19	.30	.08	.29	13.	2.76	1.19	.52	51	.024
58(f)				.200	1.29	.08	1.24	.33	.08	.28	13.	2.88	1.28	.52	49	-.006
58(g)				.250	1.34	.09	1.29	.34	.08	.28	13.	2.84	1.29	.52	52	-.017
58(h)				.250	1.39	.28	1.41	.10	.01	.25	15.	2.07	.18	.08	13	.008
59	Serr/Yes			.150	1.28	.08	1.23	.31	.08	.28	11.	2.78	1.18	.50	50	.042

TABLE 3.— CHRONOLOGY OF EVENTS ASSOCIATED WITH DYNAMIC STALL,
 $\alpha = 15^\circ + 10^\circ \sin \omega t$

Staff events	k				
	0.05	0.10	0.15	0.20	0.25
	ωt , rad				
$-C_{M_{\max}}$	0.91	1.26	1.63	1.98	2.26
$C_{N_{\max}}$.85	1.16	1.41	1.66	1.85
$C_{M_{\text{roll-off}}}$.72	.97	1.19	1.41	1.63
Suction wave detected	.75	.97	1.18	1.38	1.57
$-C_{p_3_{\max}}$.69	.94	1.13	1.32	1.45
$-C_{c_{\max}}$.66	.91	1.10	1.29	1.45
Negative-moment growth begins	.66	.85	1.04	1.25	1.38
$C_{N_{\text{surge}}}$.60	.79	.94	1.08	1.23

Note: Results obtained without airfoil modification and with end plates.

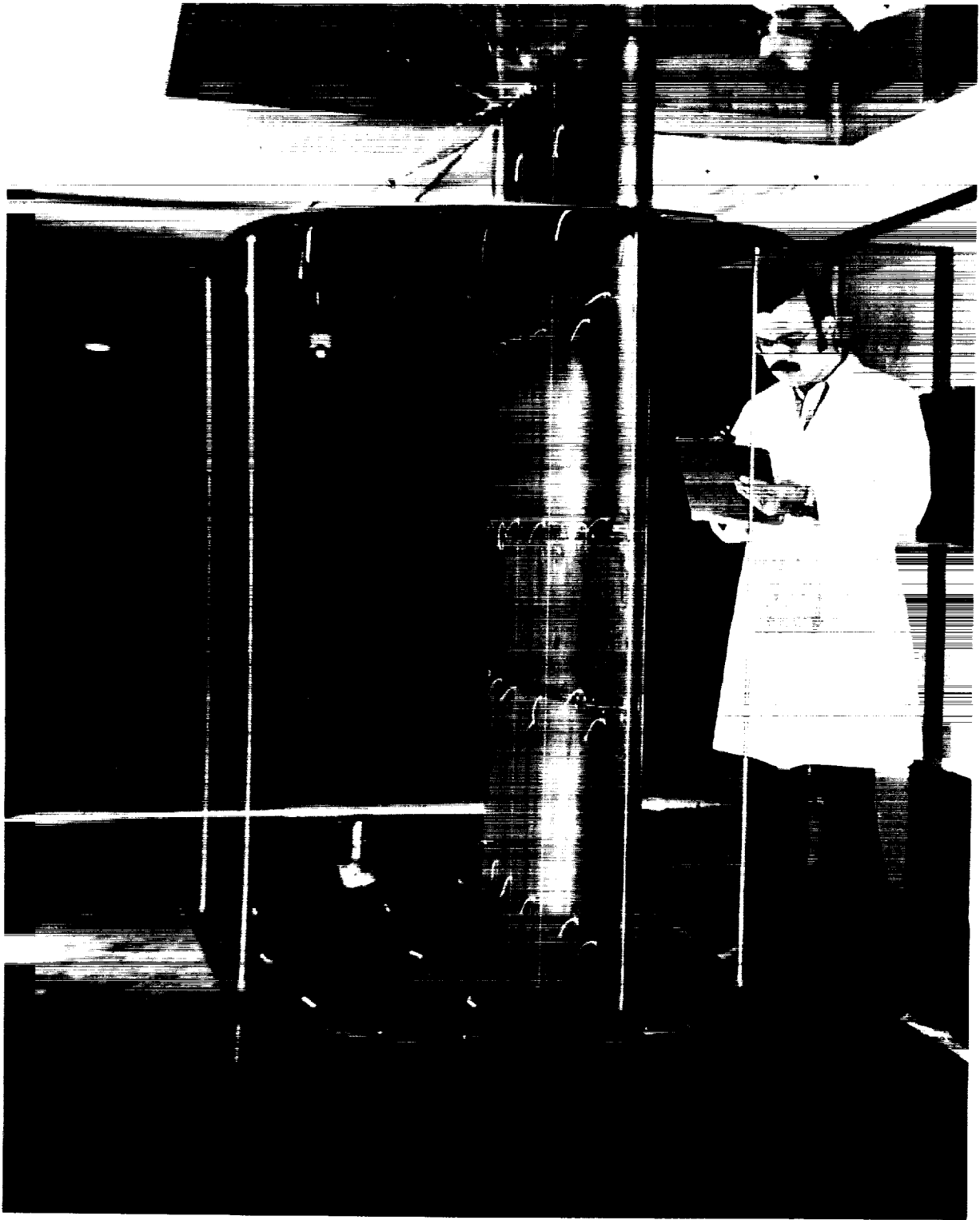


Figure 1.— View of airfoil with end plates.

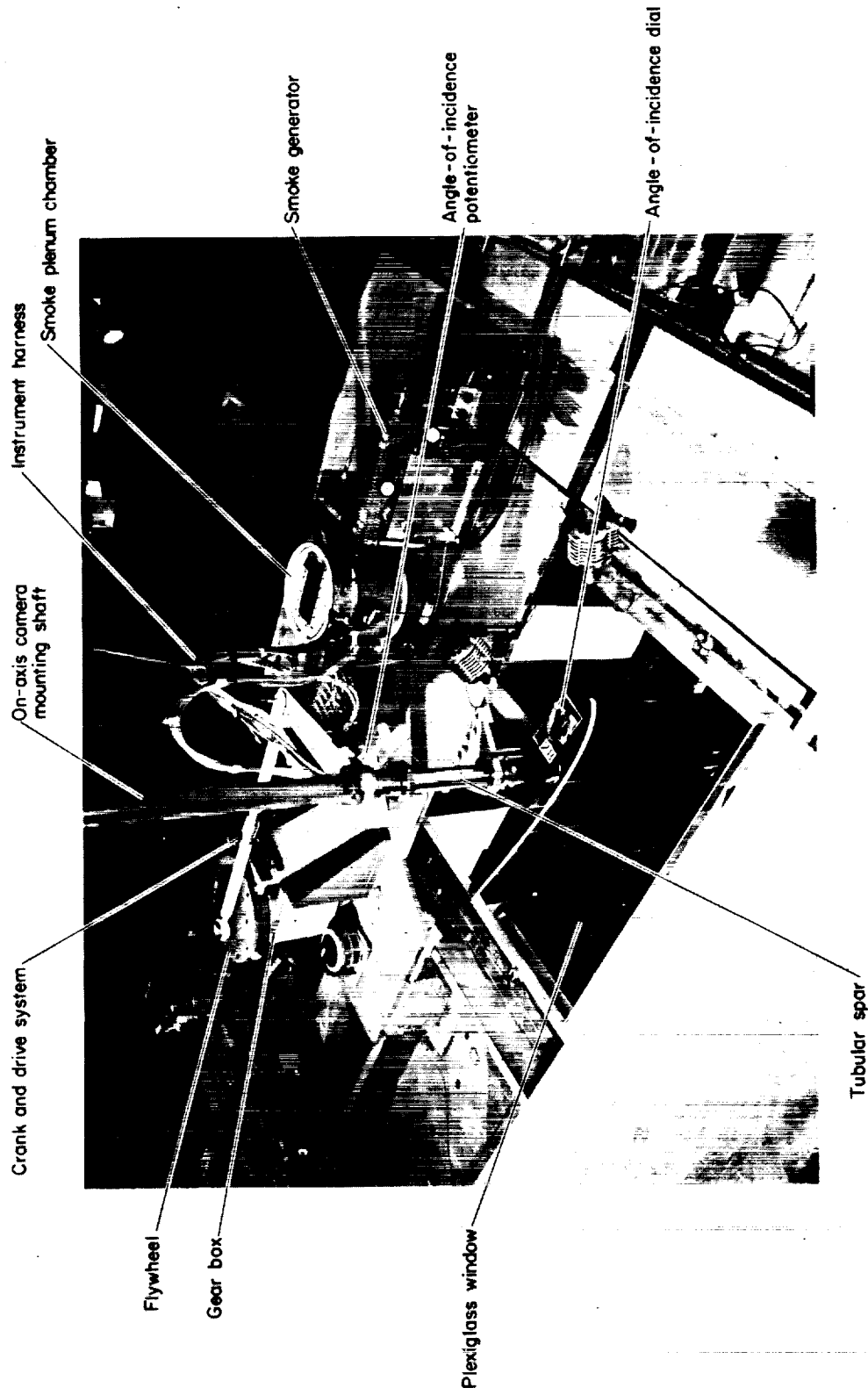


Figure 2.— Apparatus located above test section.

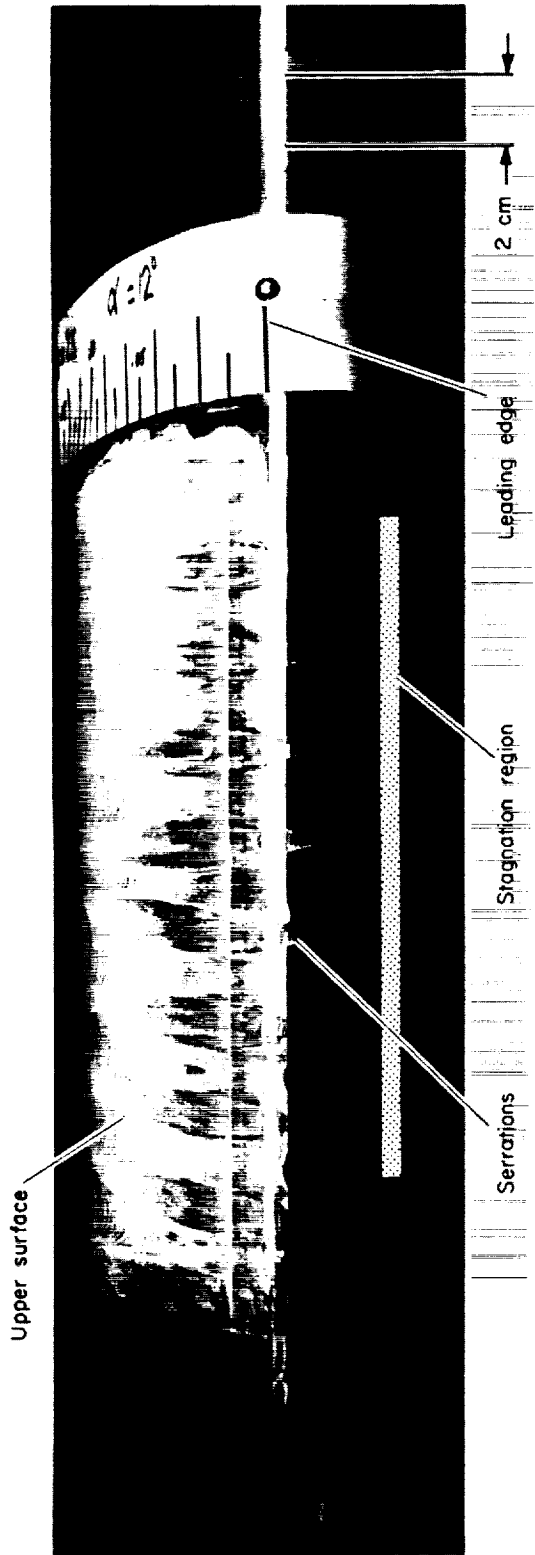


Figure 3.— NACA 0012 with leading-edge serrations.

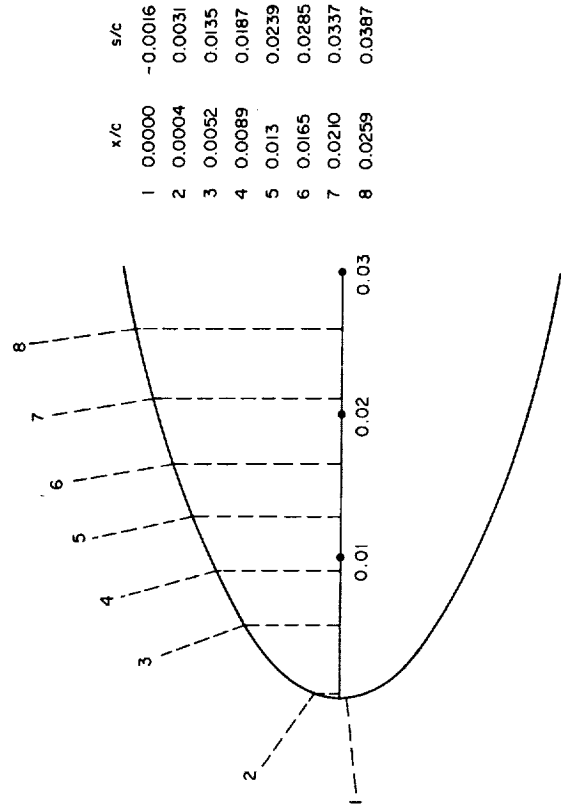


Figure 4.— Leading-edge pressure transducer and boundary-layer hot wire locations.

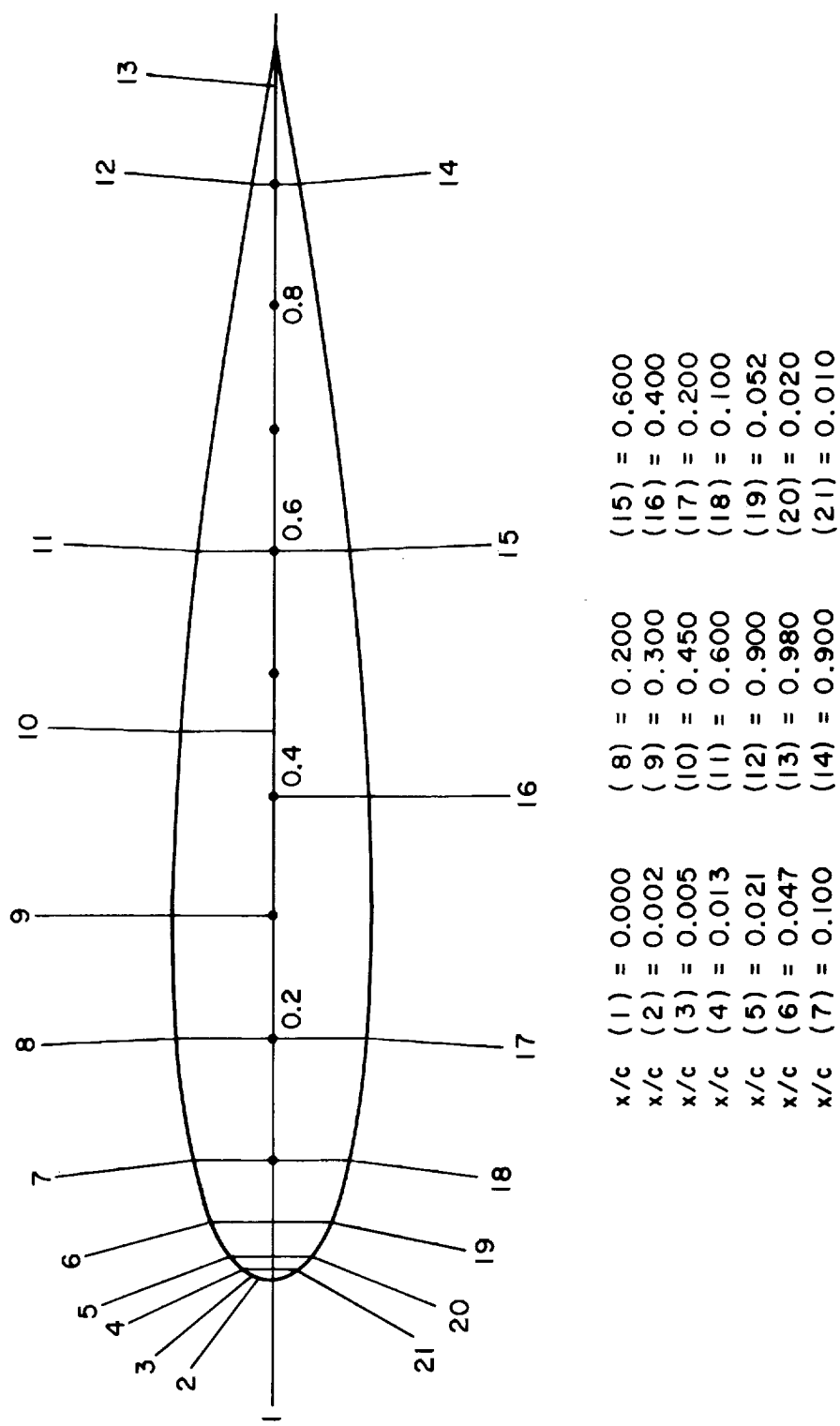


Figure 5.— Upper and lower surface pressure transducer locations.

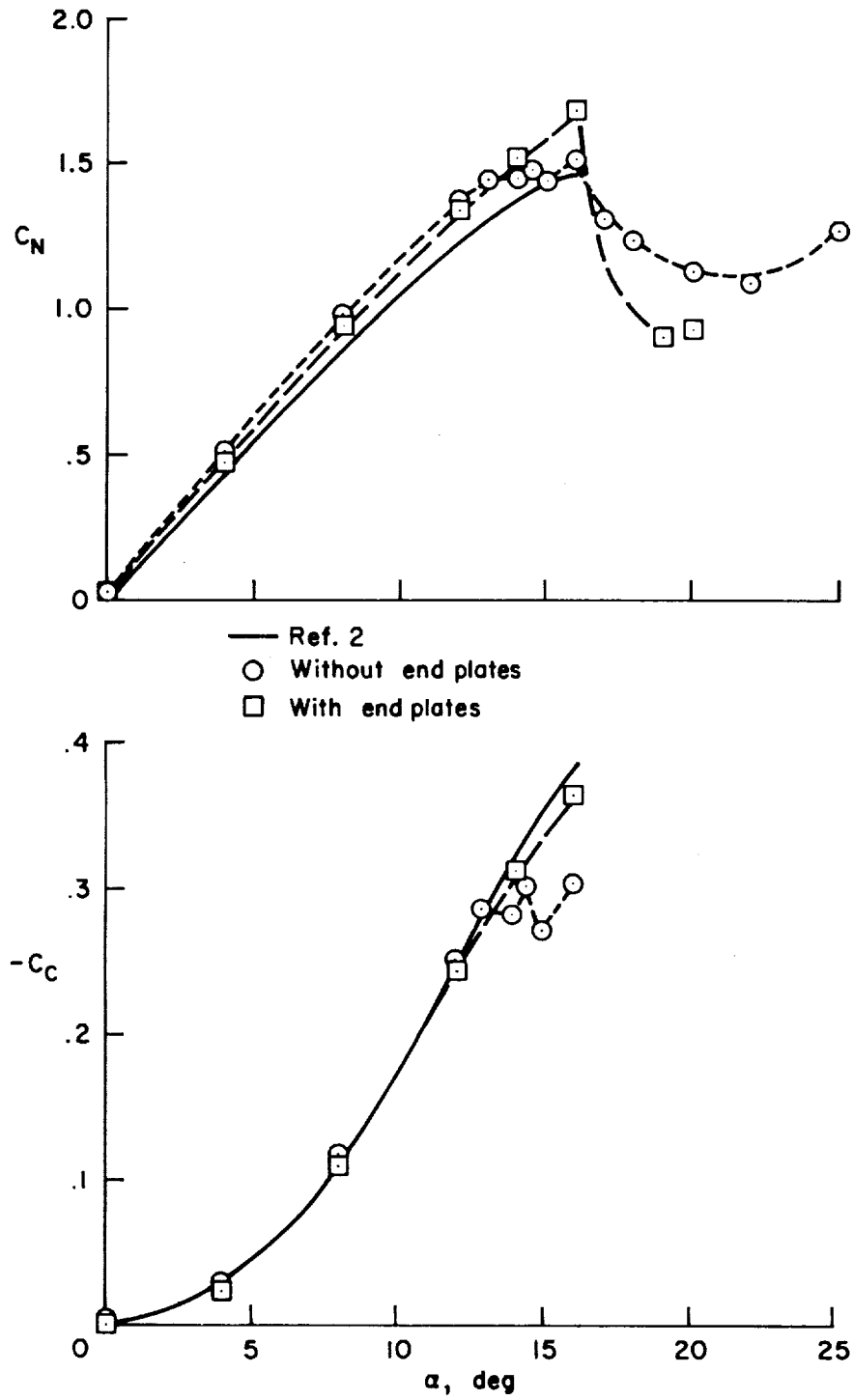


Figure 6.— Static normal- and chord-force coefficients.

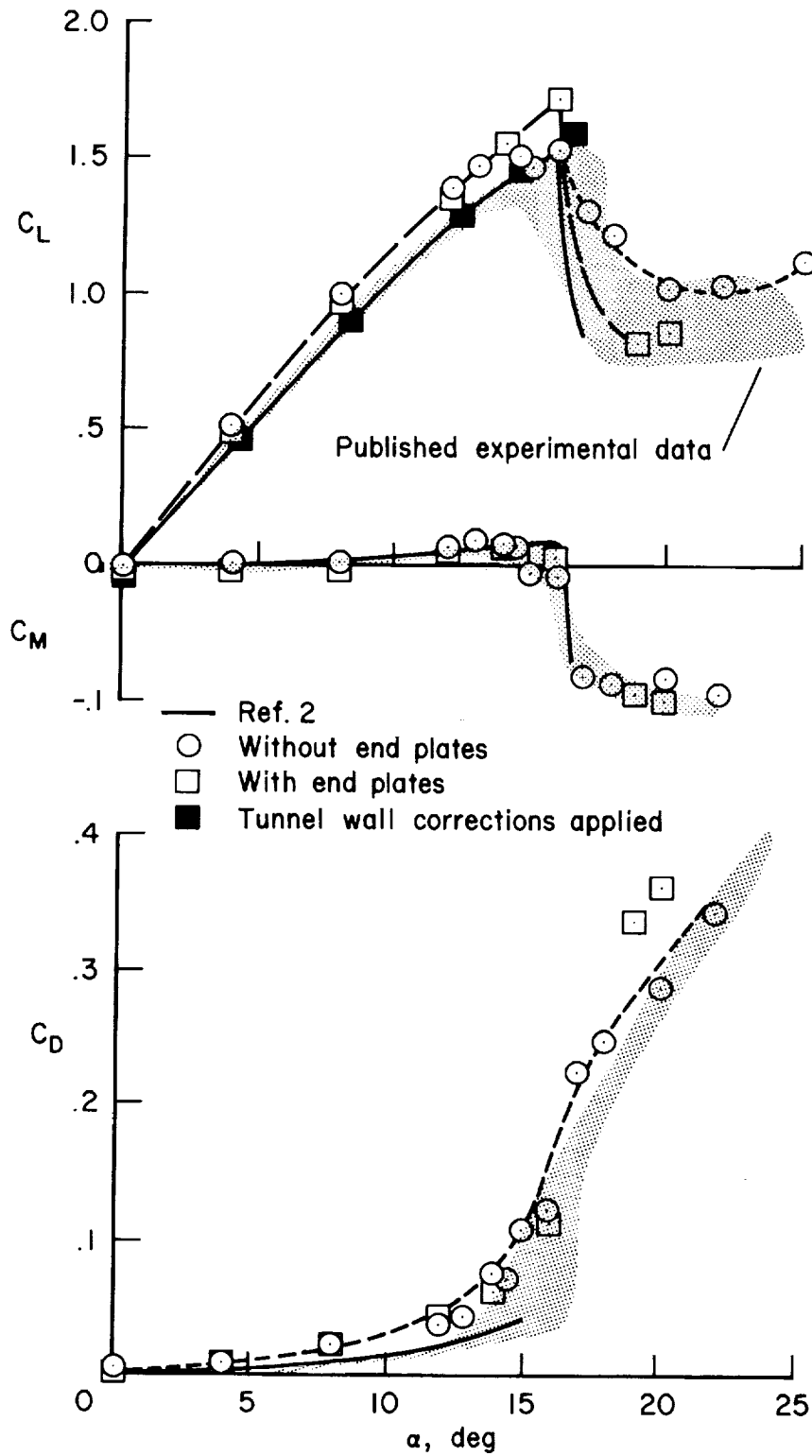
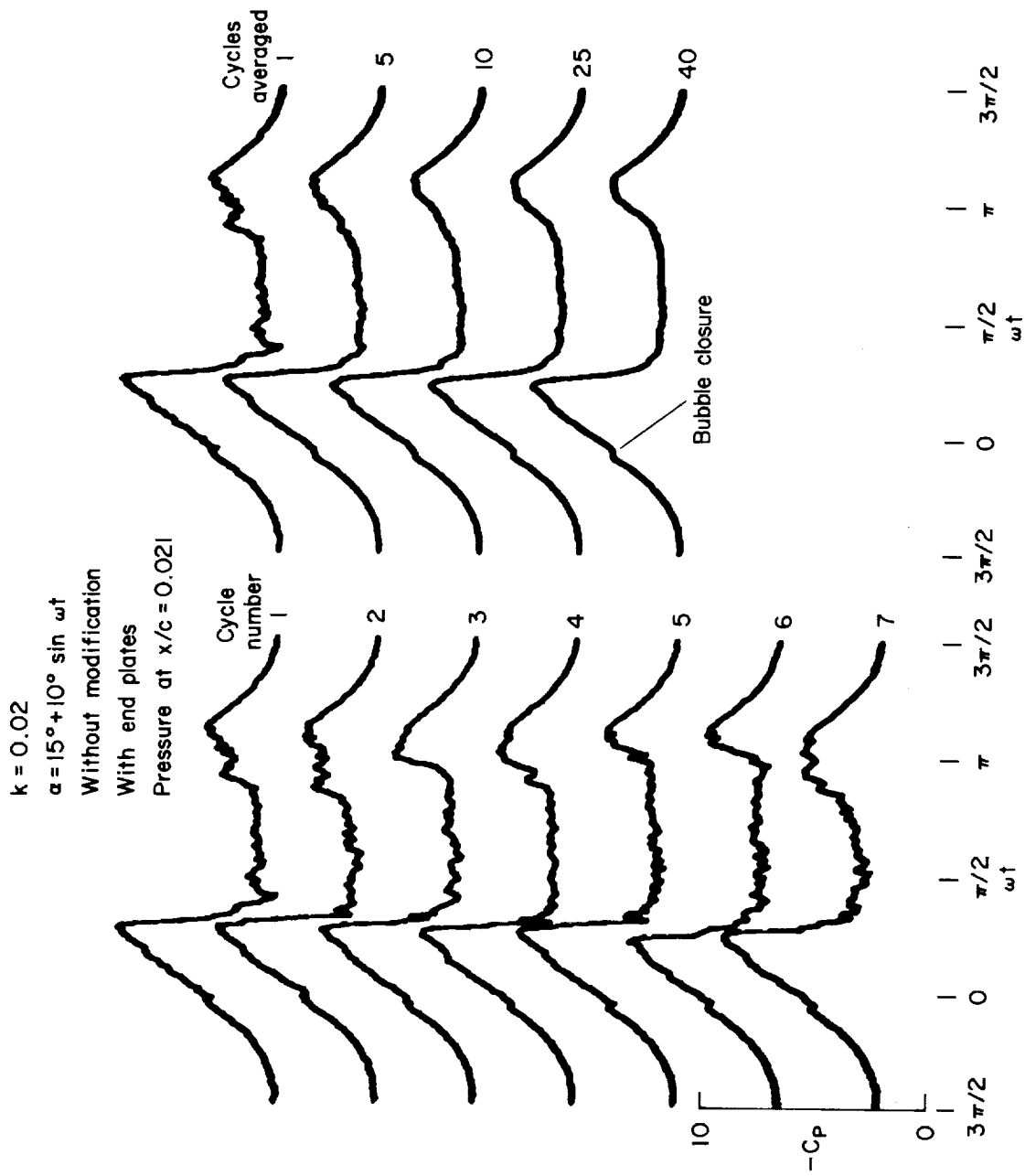
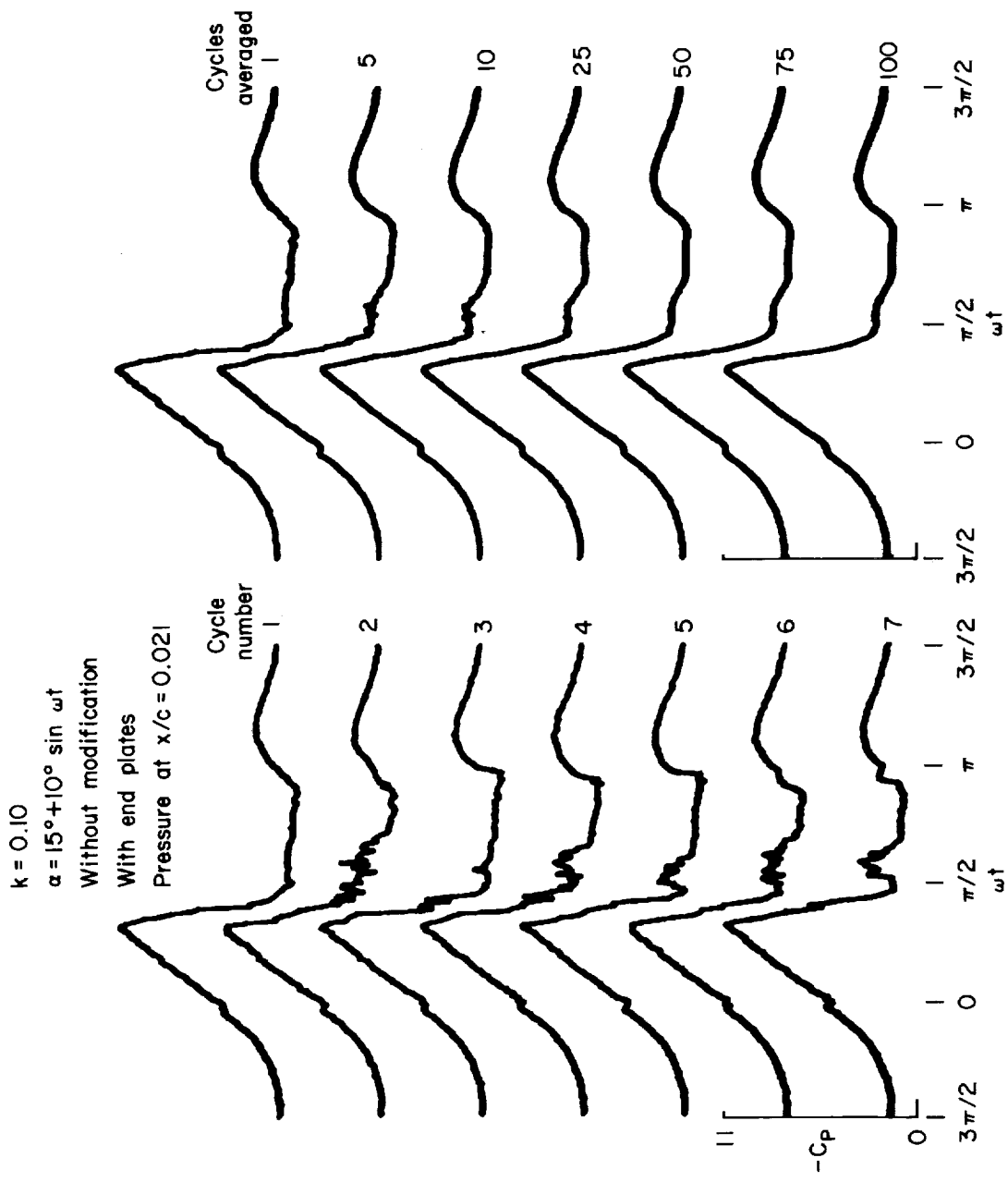


Figure 7.— Comparison with published static lift and drag data.



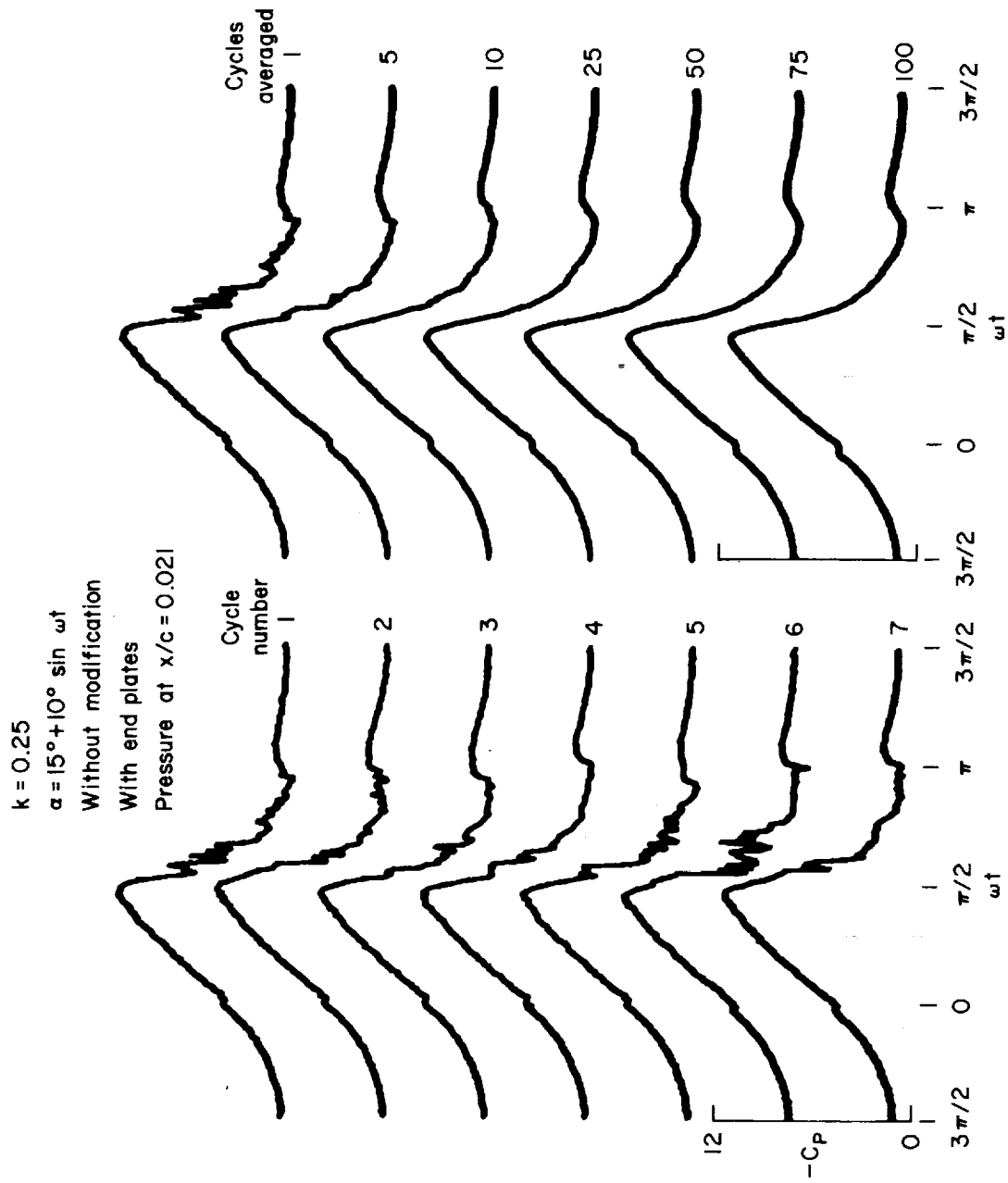
(a) $k = 0.02$.

Figure 8.— Appearance of pressure at $x/c = 0.021$ with and without conditional averaging.



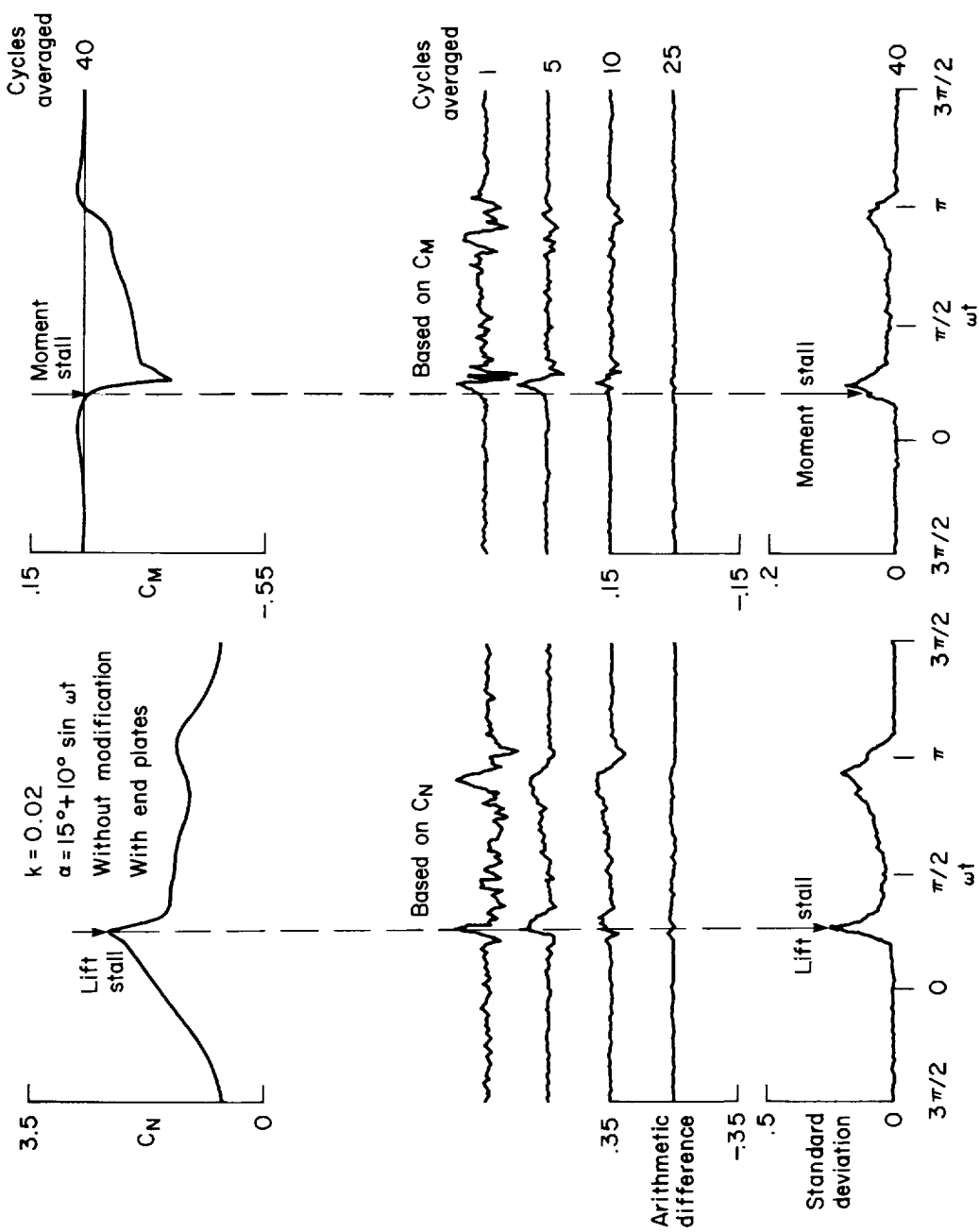
(b) $k = 0.10$.

Figure 8.— Continued.



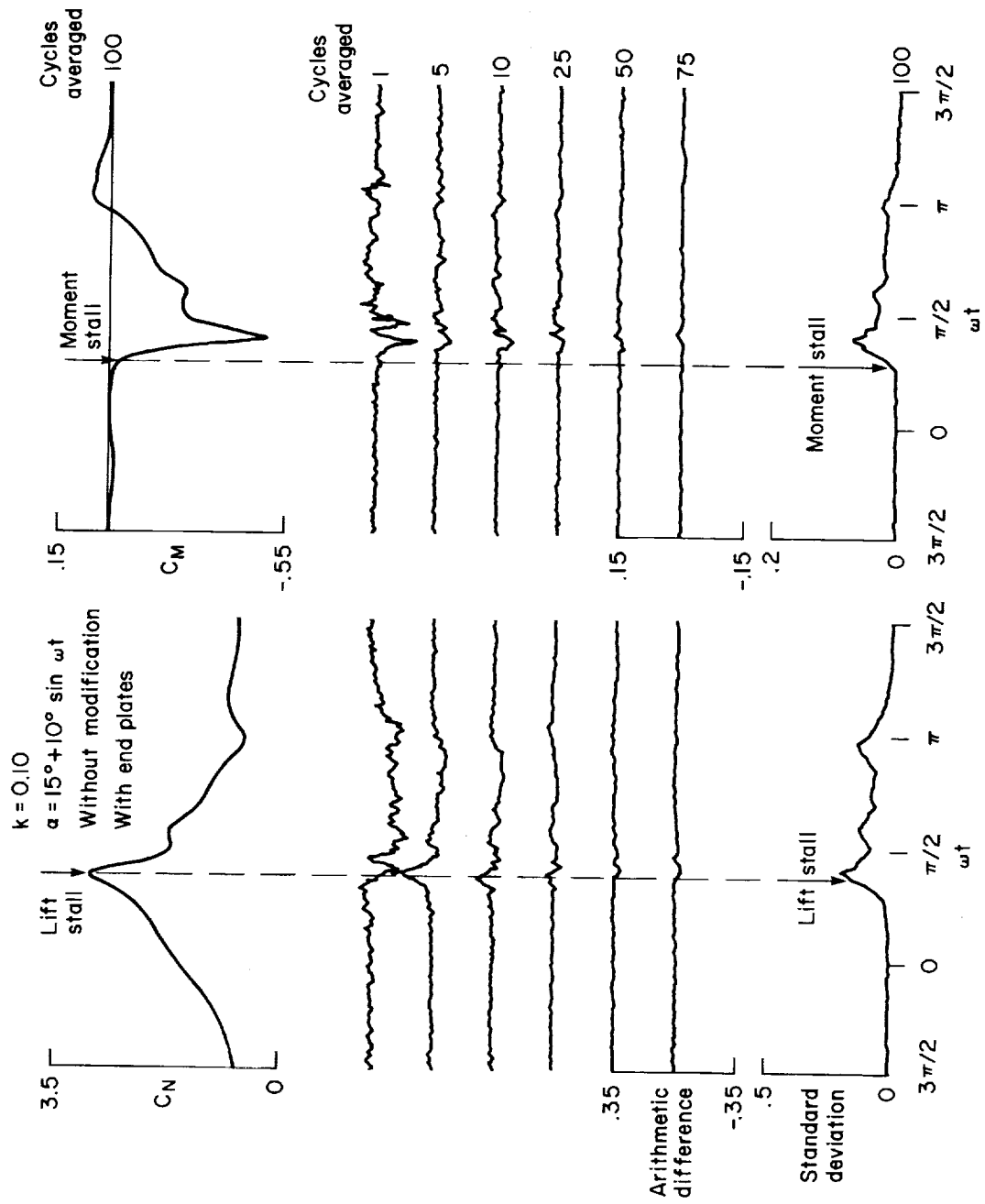
(c) $k = 0.25$.

Figure 8.— Concluded.



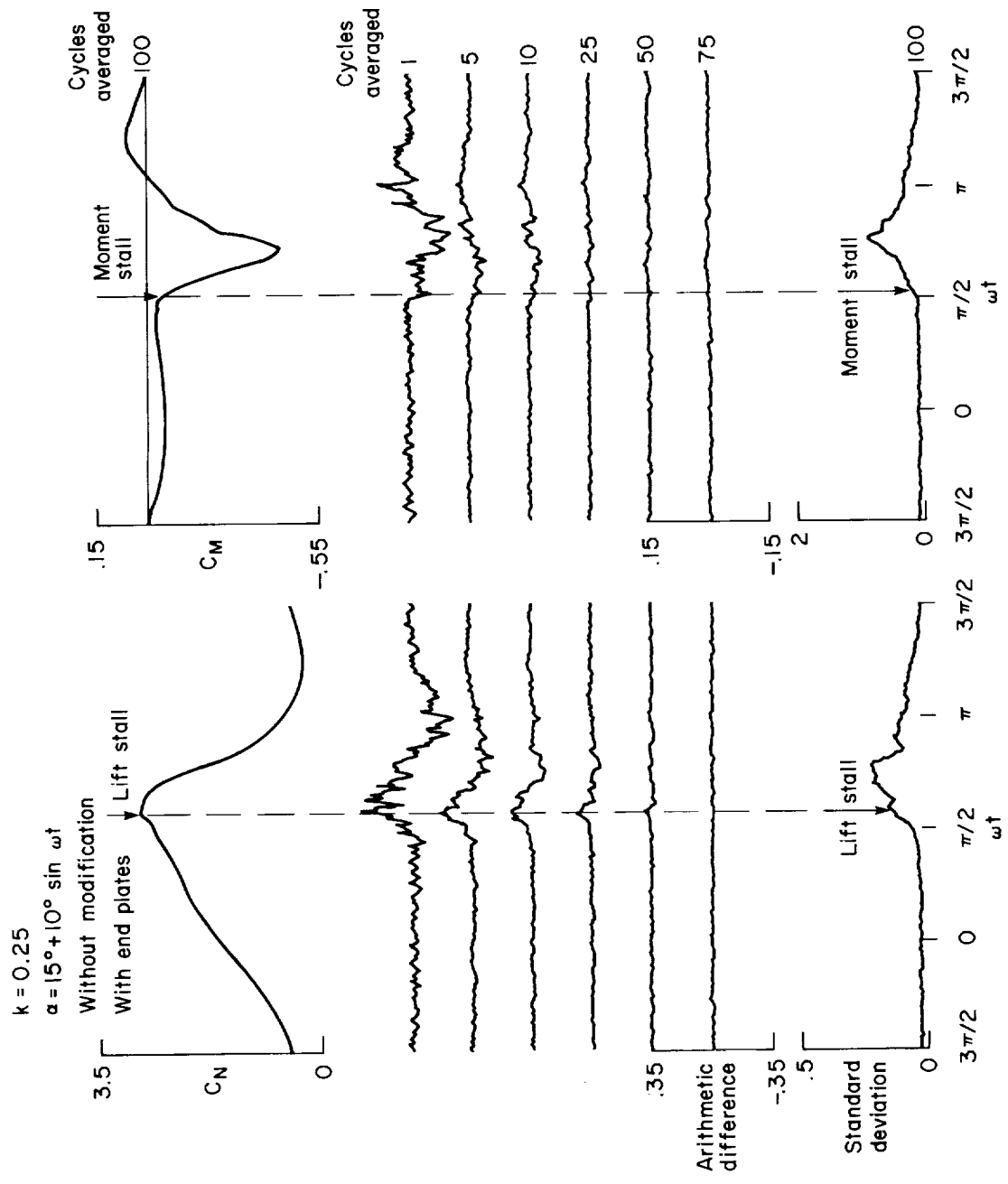
(a) $k = 0.02$.

Figure 9. — Normal force and pitching moment deviations from average of all cycles.



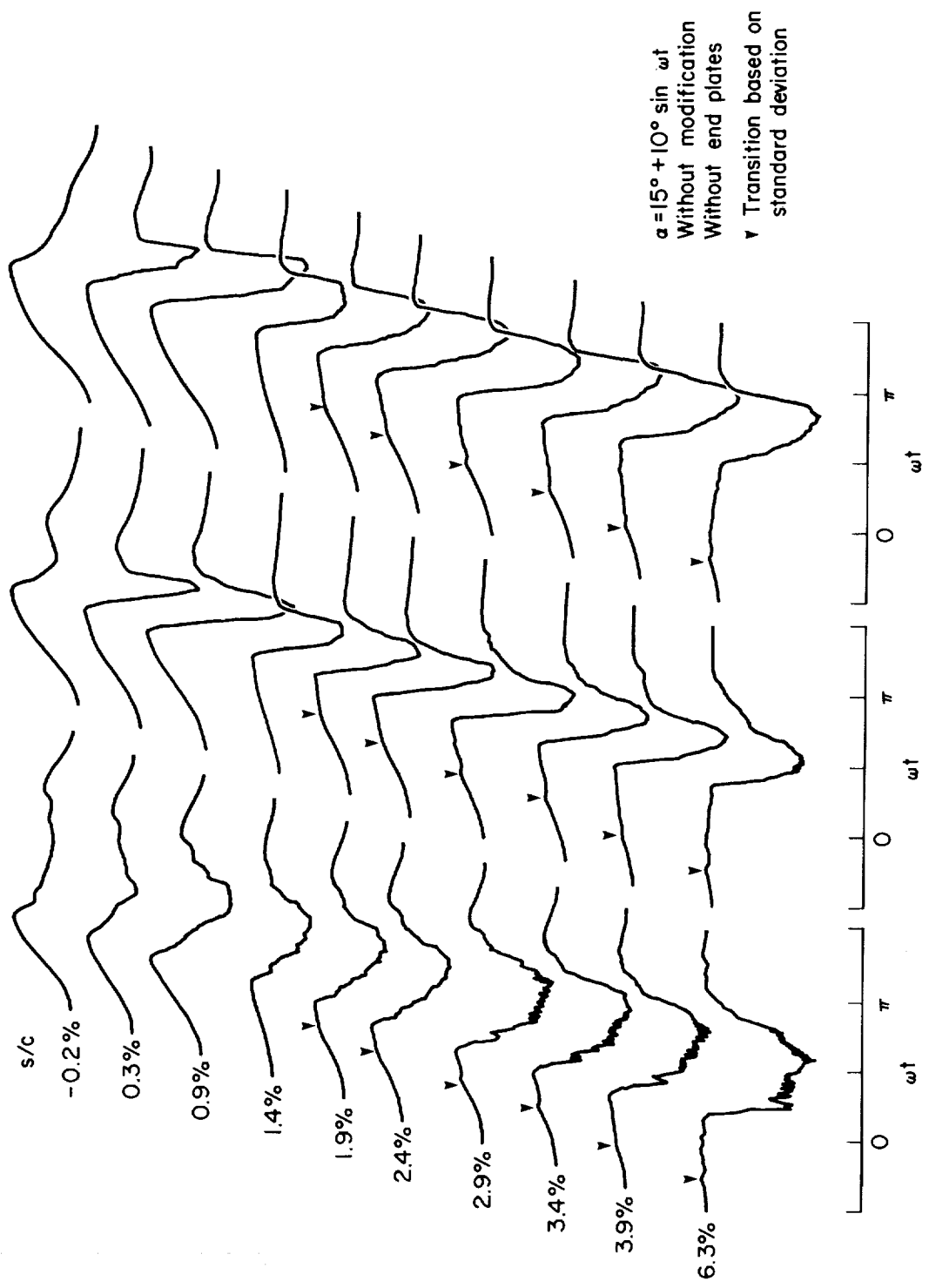
(b) $k = 0.10$.

Figure 9.-- Continued.



(c) $k = 0.25$.

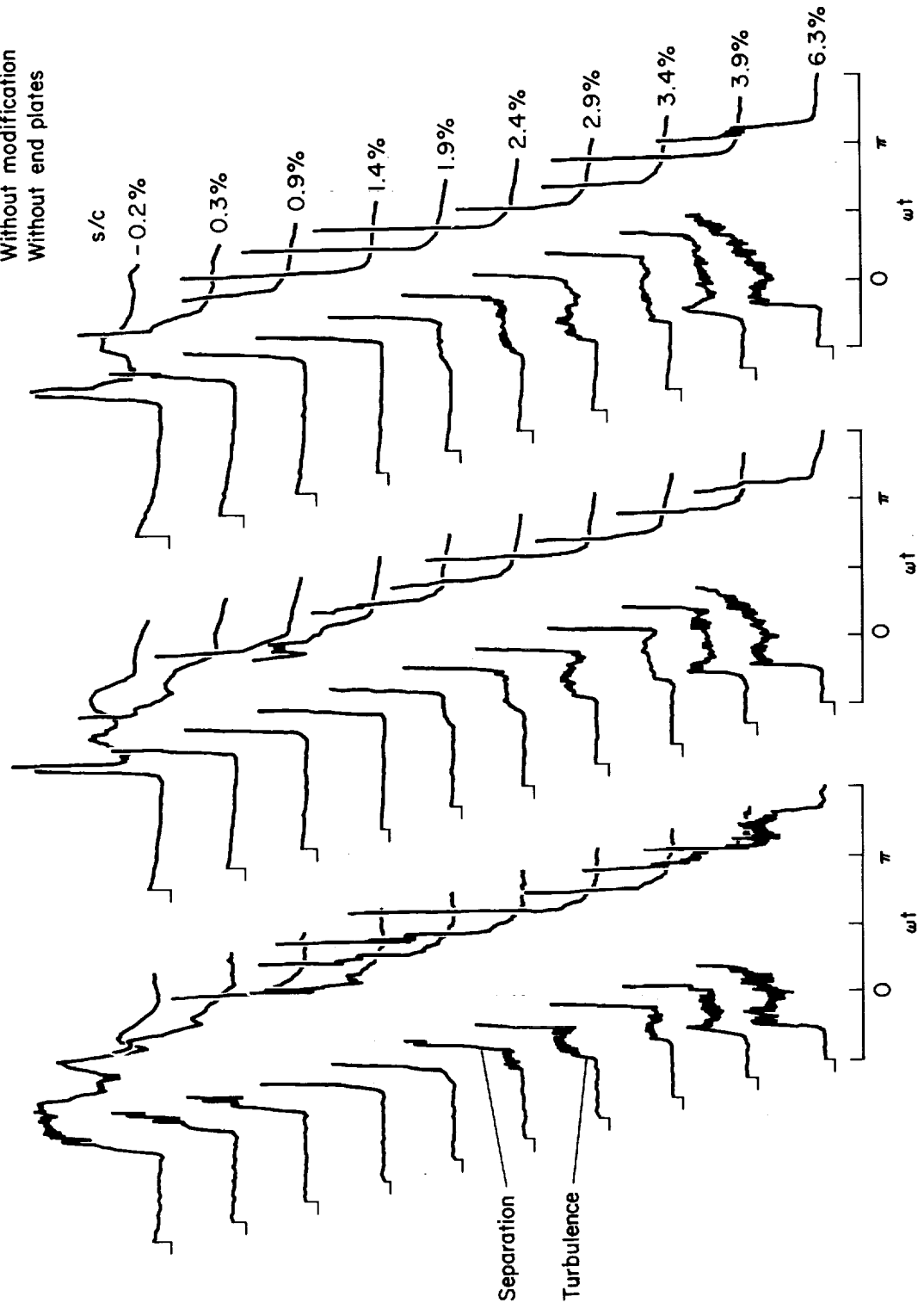
Figure 9. — Concluded.



(a) $k = 0.05$. (b) $k = 0.15$. (c) $k = 0.25$.

Figure 10.— Mean nonlinear hot-wire response near the leading edge.

$\alpha = 15^\circ + 10^\circ \sin \omega t$
 Without modification
 Without end plates



(a) $k = 0.05$.
 (b) $k = 0.15$.
 (c) $k = 0.25$.

Figure 11.— Standard deviation from averaged nonlinear hot-wire data measured near the leading edge.

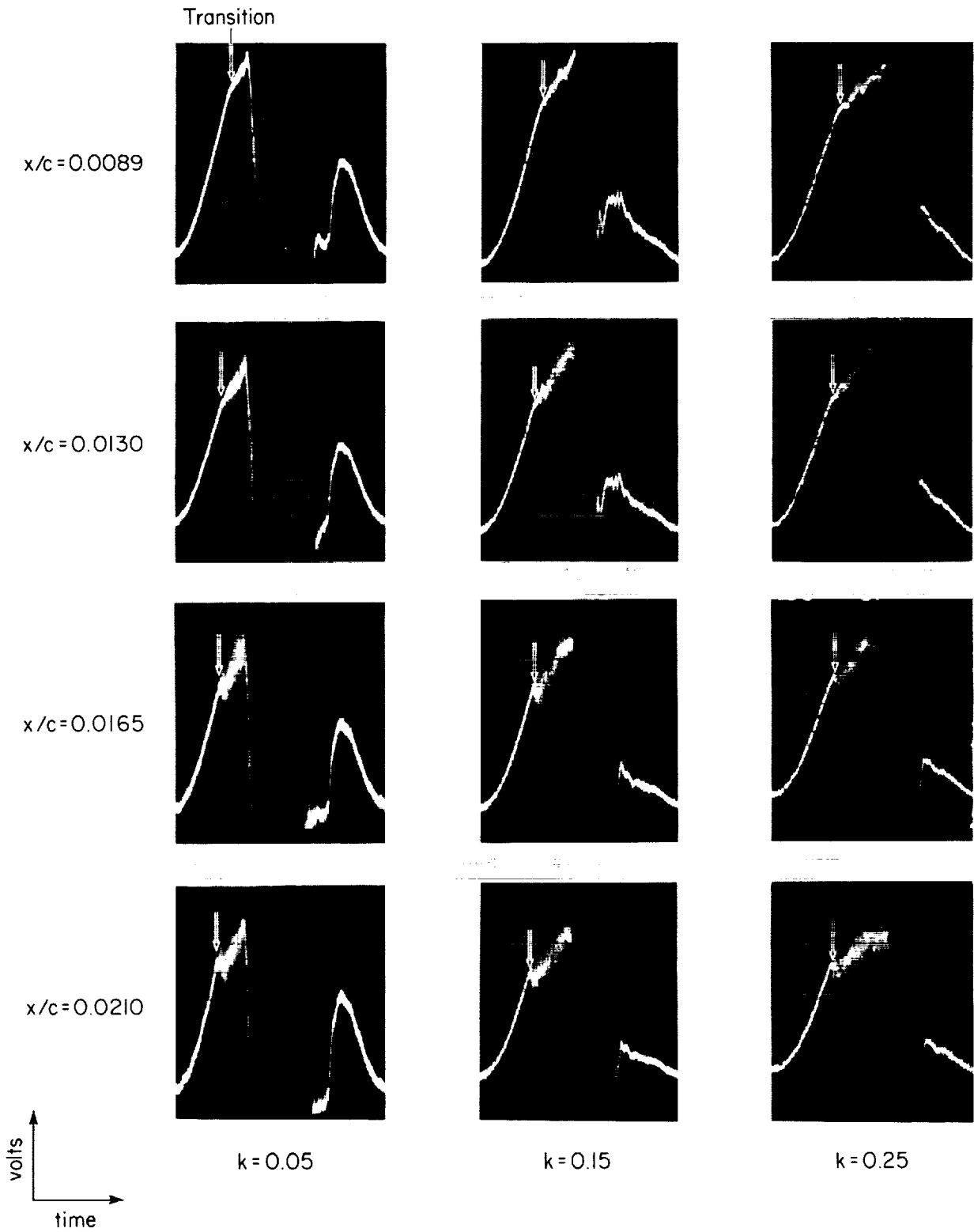


Figure 12.— Analog nonlinear hot-wire response near the leading edge.

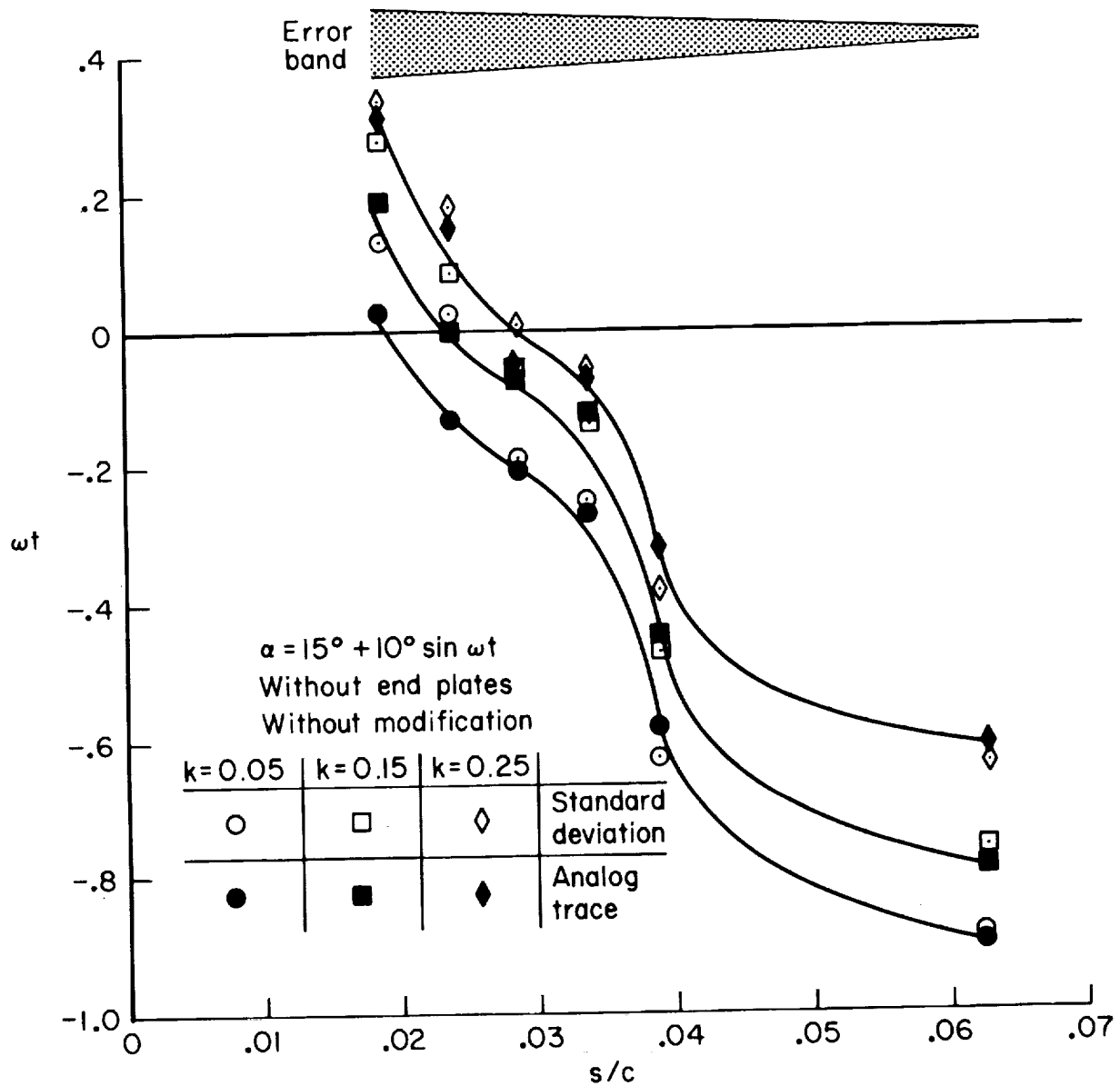
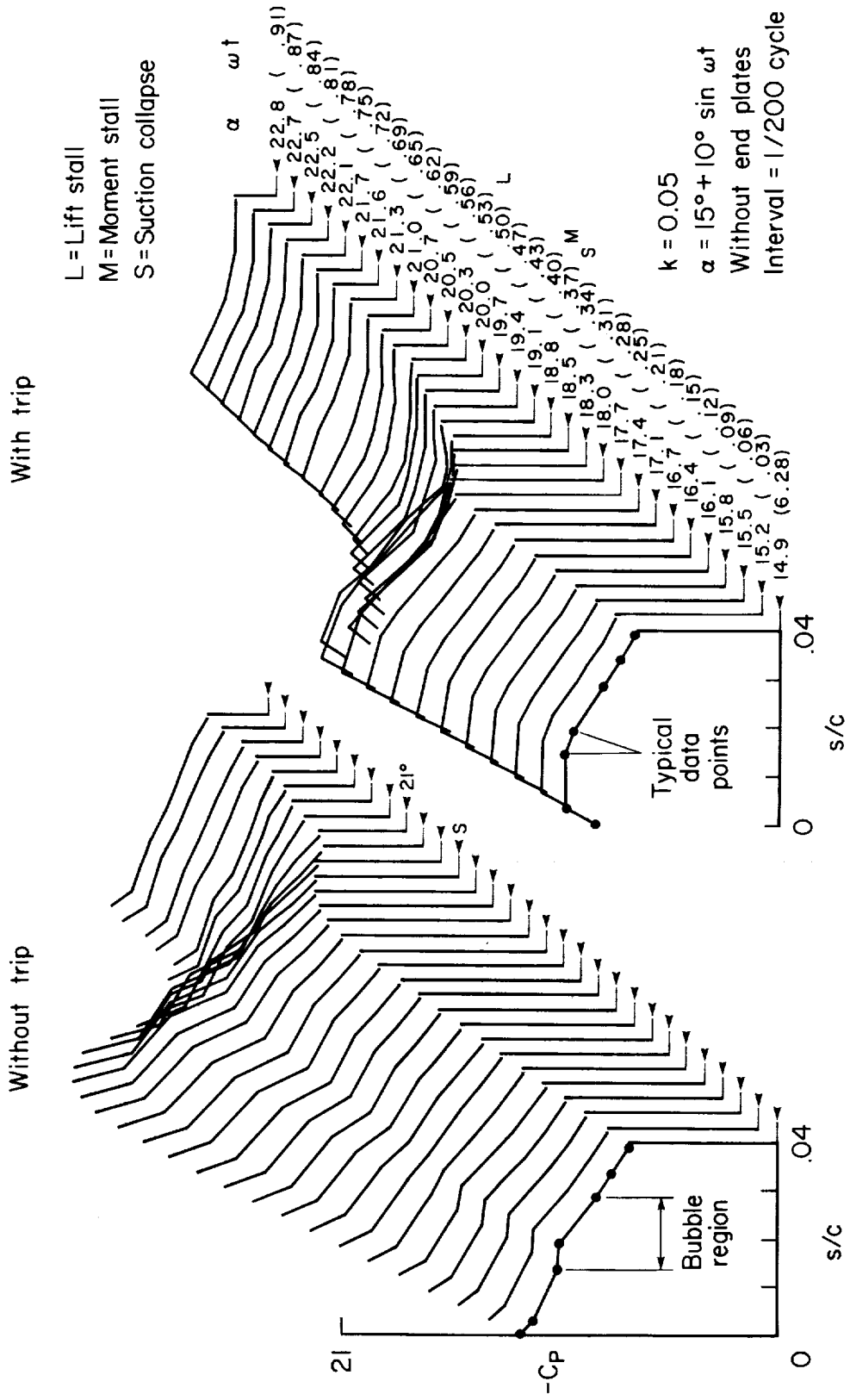
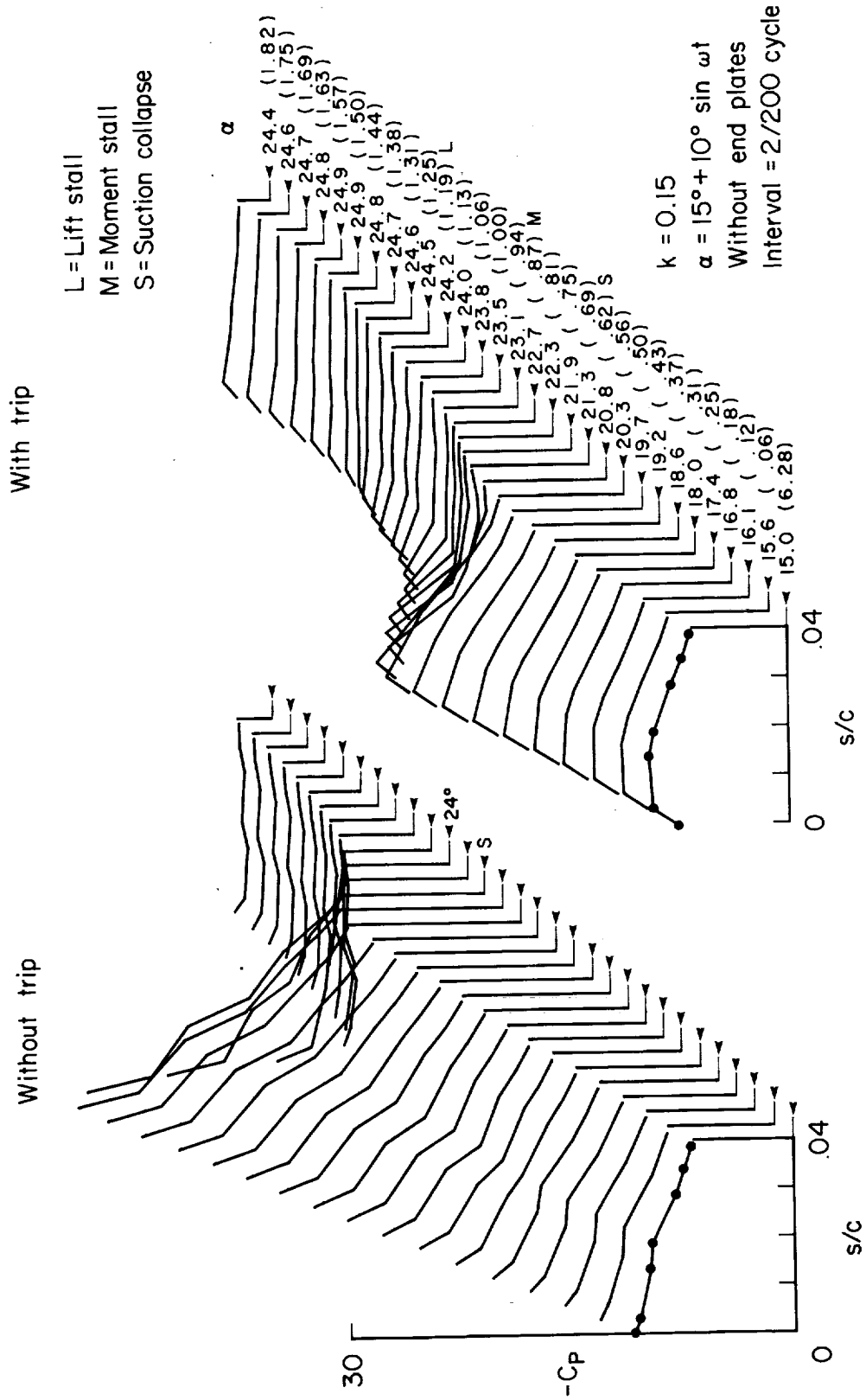


Figure 13.— Transition from laminar to turbulent flow over the upper leading-edge region.

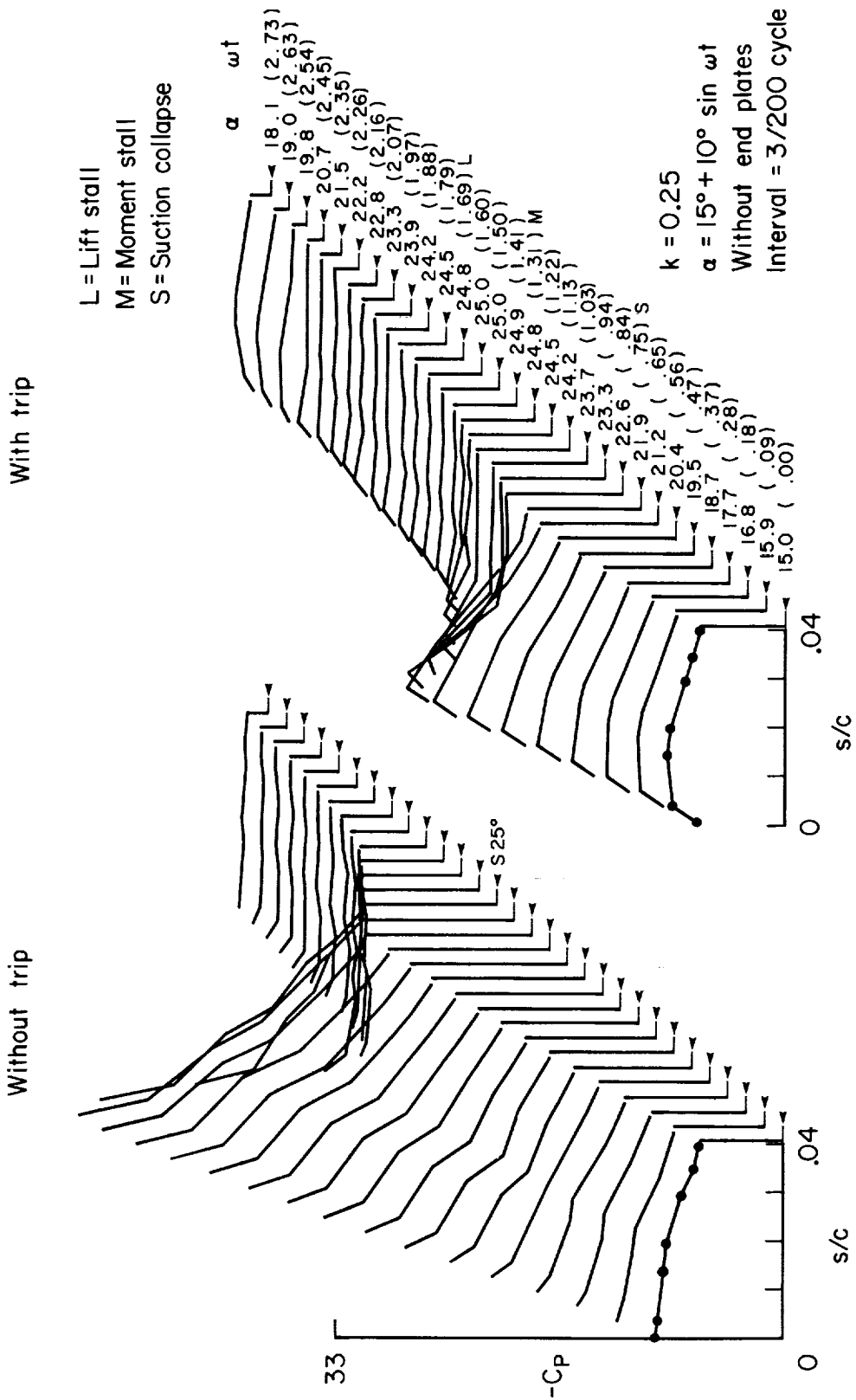


(a) $k = 0.05$.

Figure 14.— Pressure distribution over the upper leading-edge region at equidistant azimuthal positions.

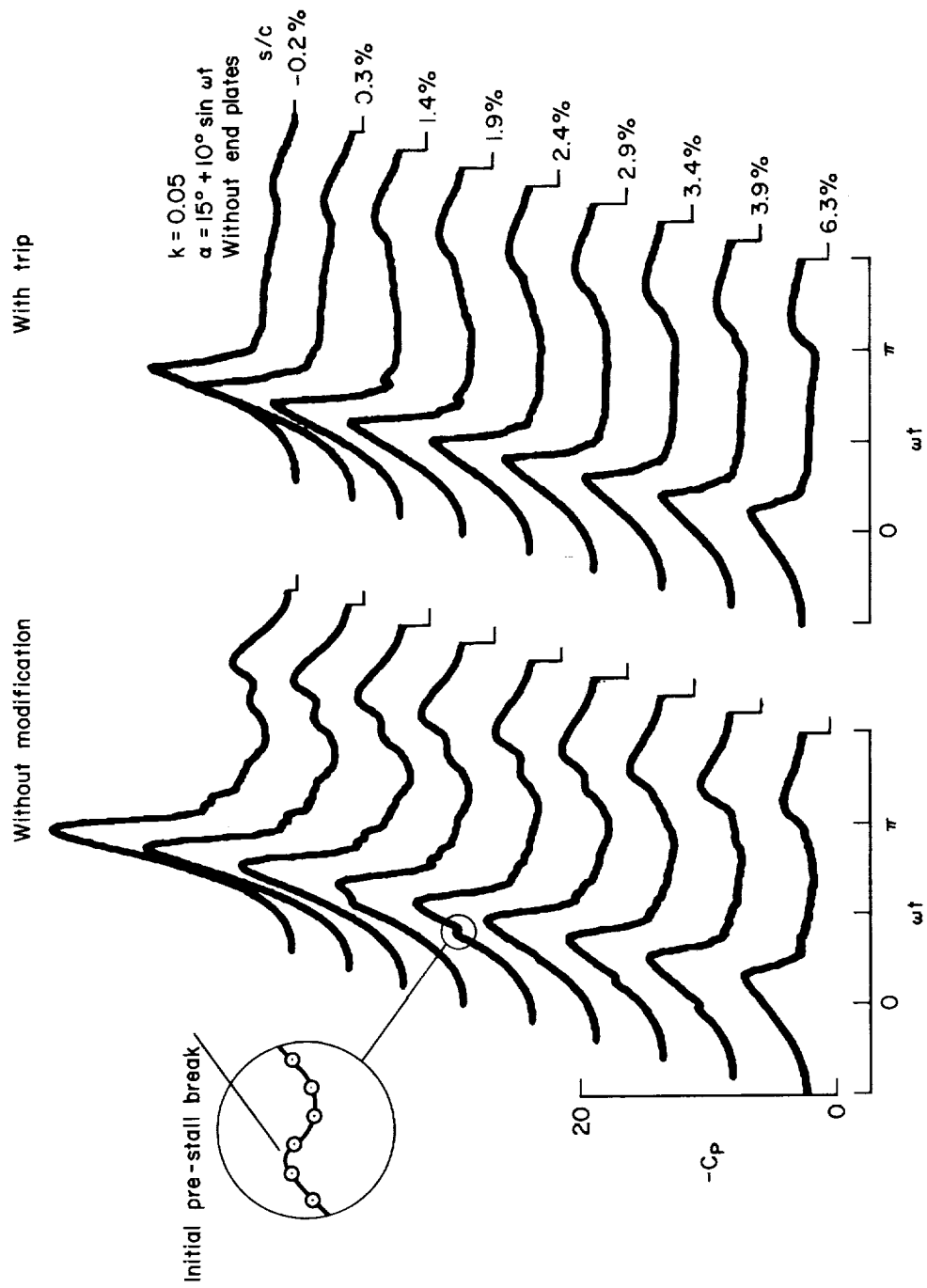


(b) $k = 0.15$.
Figure 14.— Continued.



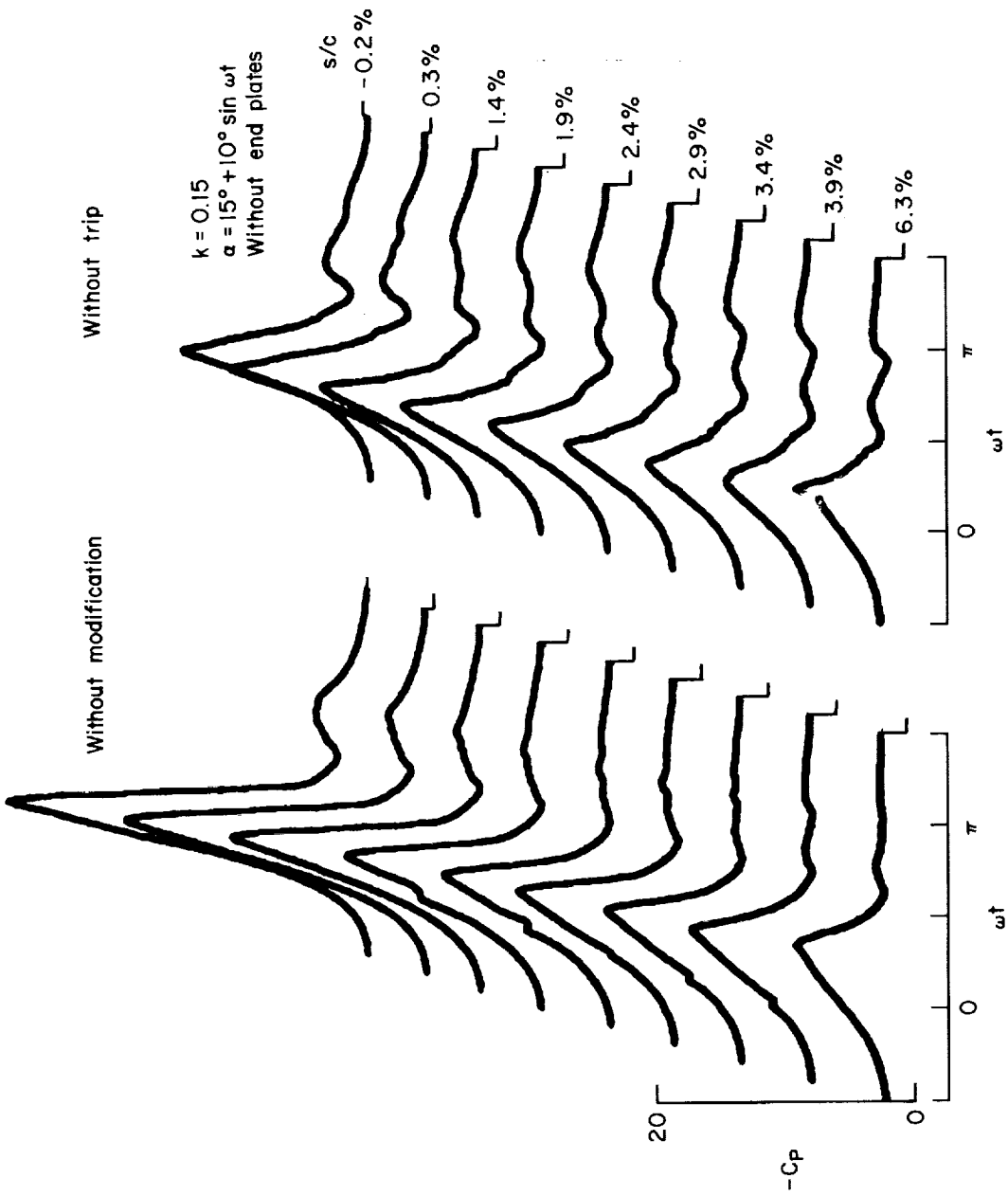
(c) $k = 0.25$.

Figure 14.— Concluded.



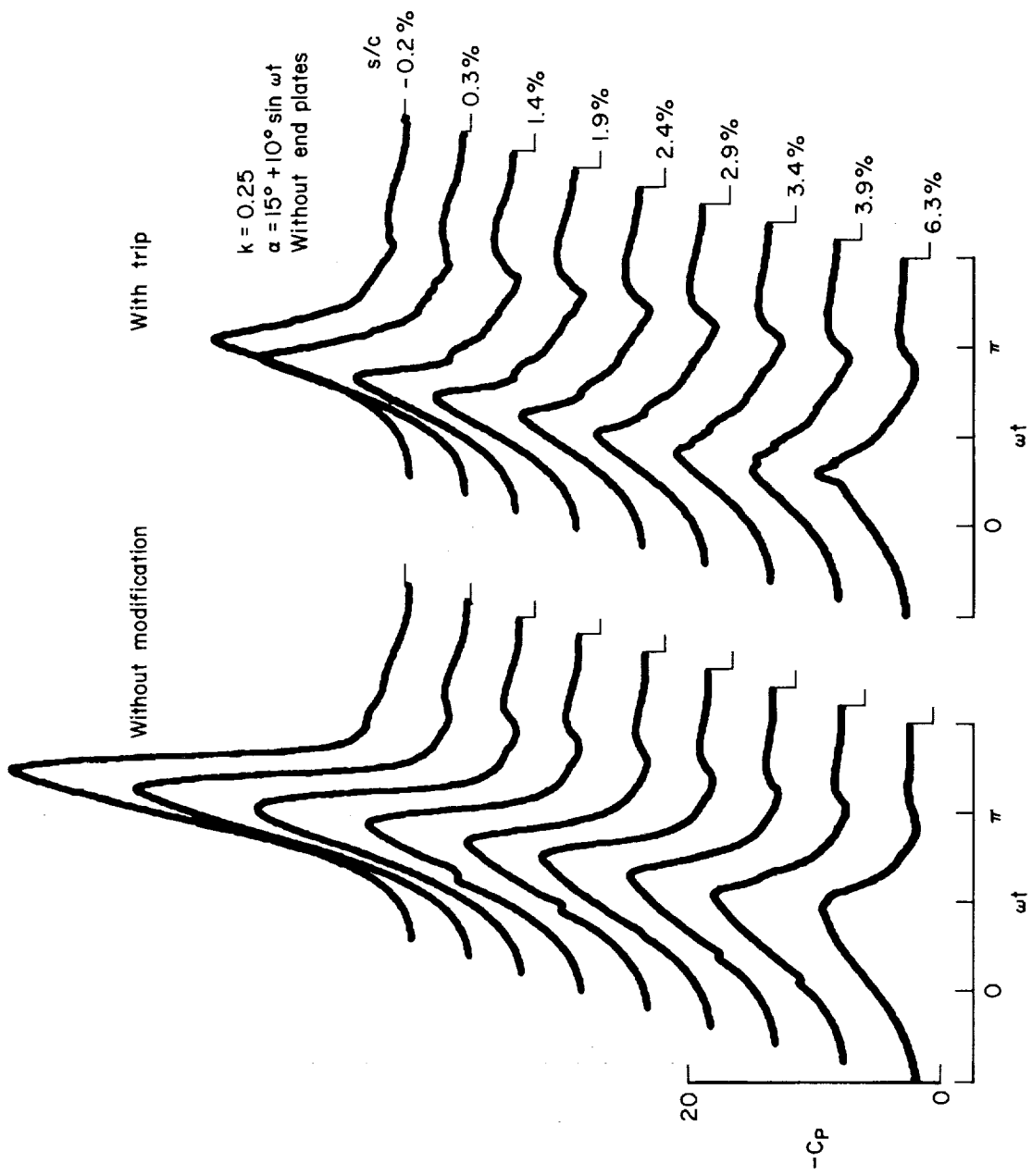
(a) $k = 0.05$.

Figure 15.— Cyclic pressure response at discrete locations near the leading edge.



(b) $k = 0.15$.

Figure 15.— Continued.



(c) $k = 0.25$.

Figure 15.— Concluded.

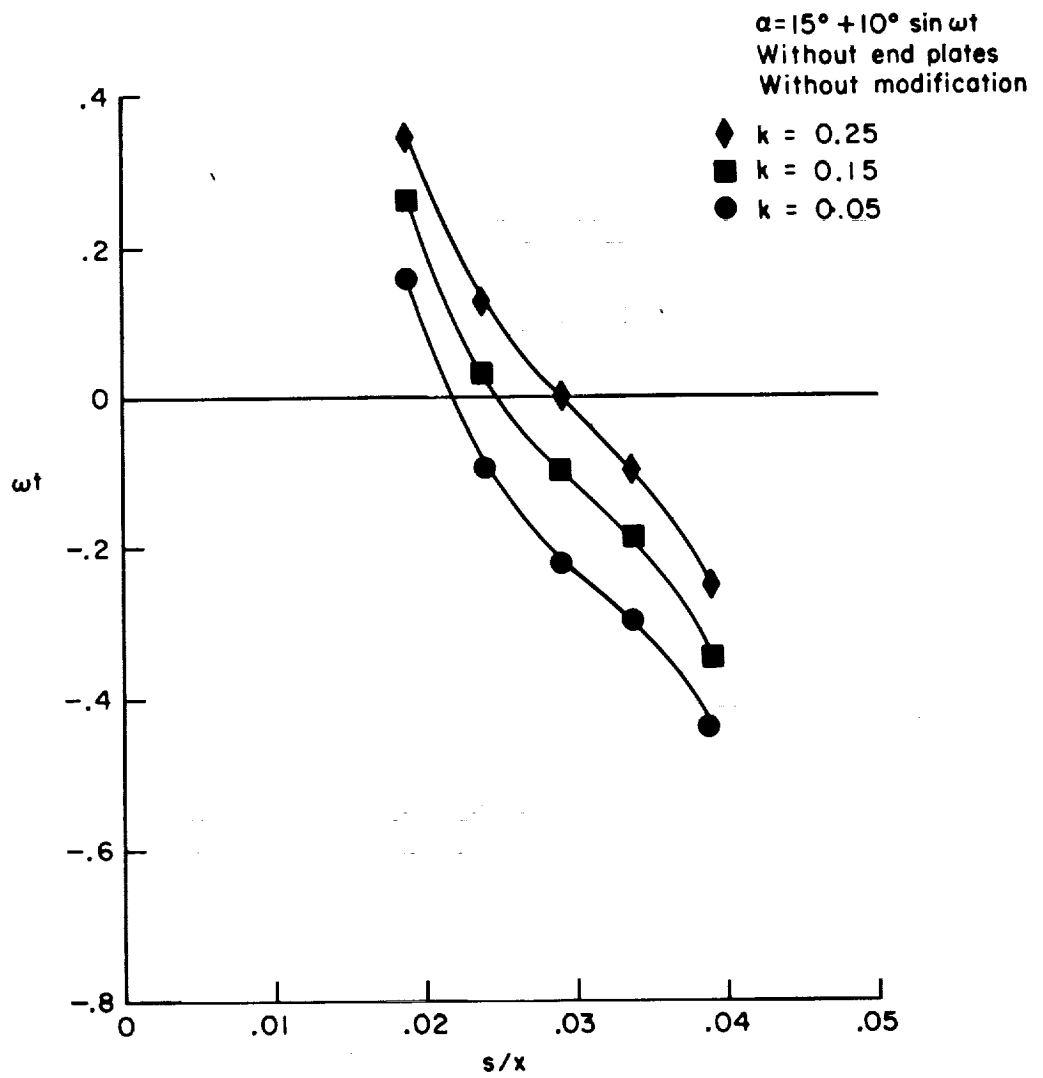


Figure 16.— Initial pre-stall break in the pressure distribution over the upper leading-edge region.

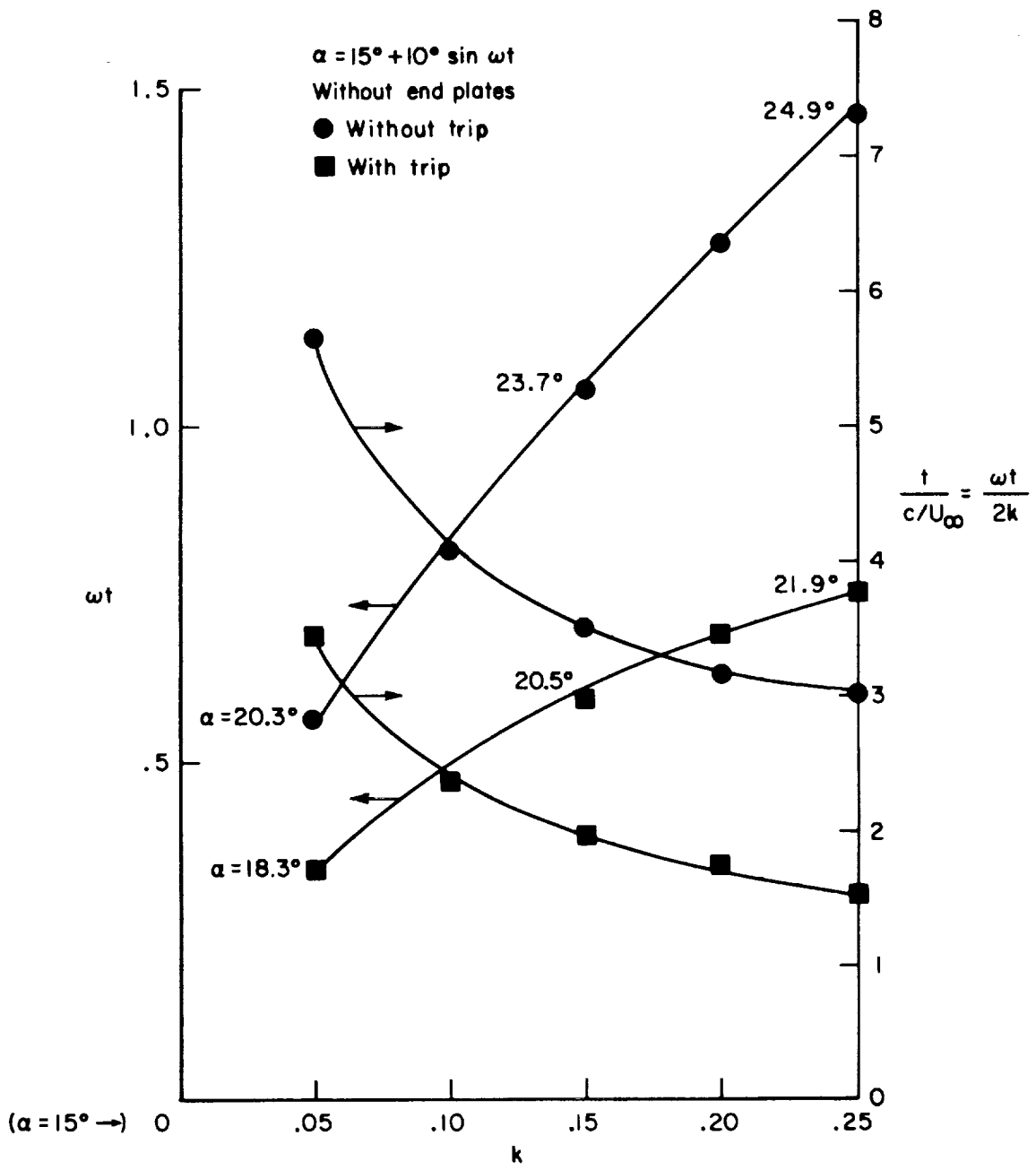


Figure 17.— Onset of the suction collapse over the upper leading-edge region.

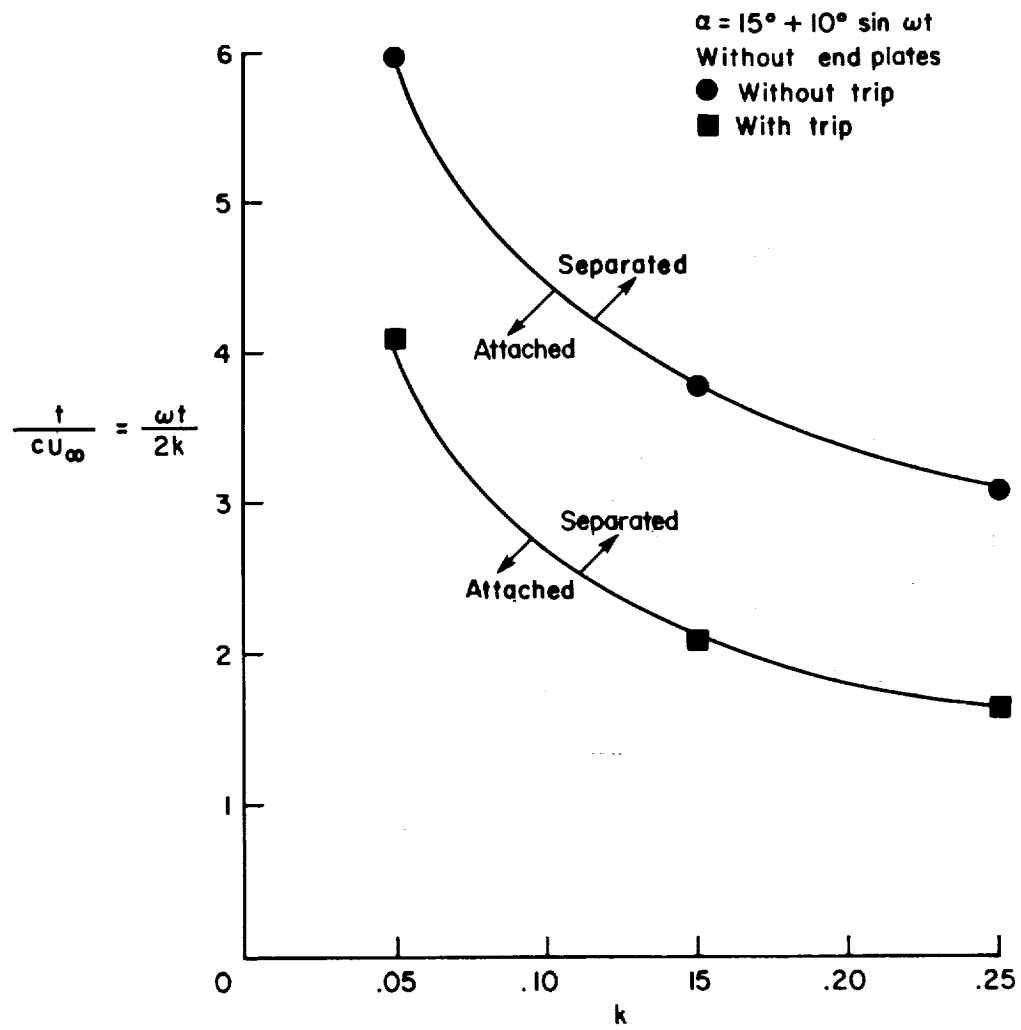
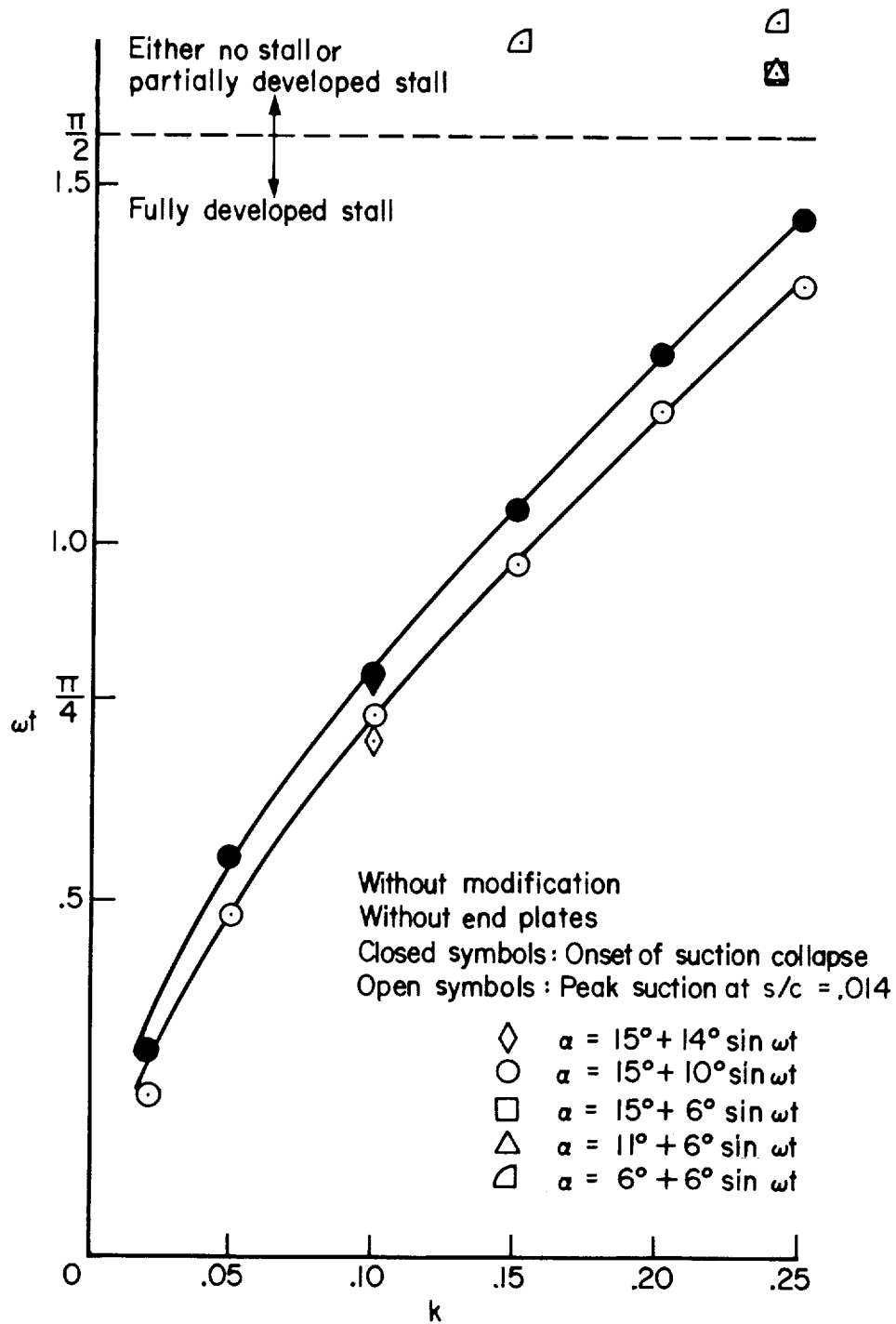


Figure 18.— Separation over the leading-edge region as determined from the standard deviation of hot-wire measurements.



Appropriateness of the peak suction at $s/c = .014$ as an indicator for the moment stall suction collapse over the leading-edge region

Figure 19.— Appropriateness of the peak suction at $s/c = 0.014$ as an indicator for the moment stall suction collapse over the leading-edge region.

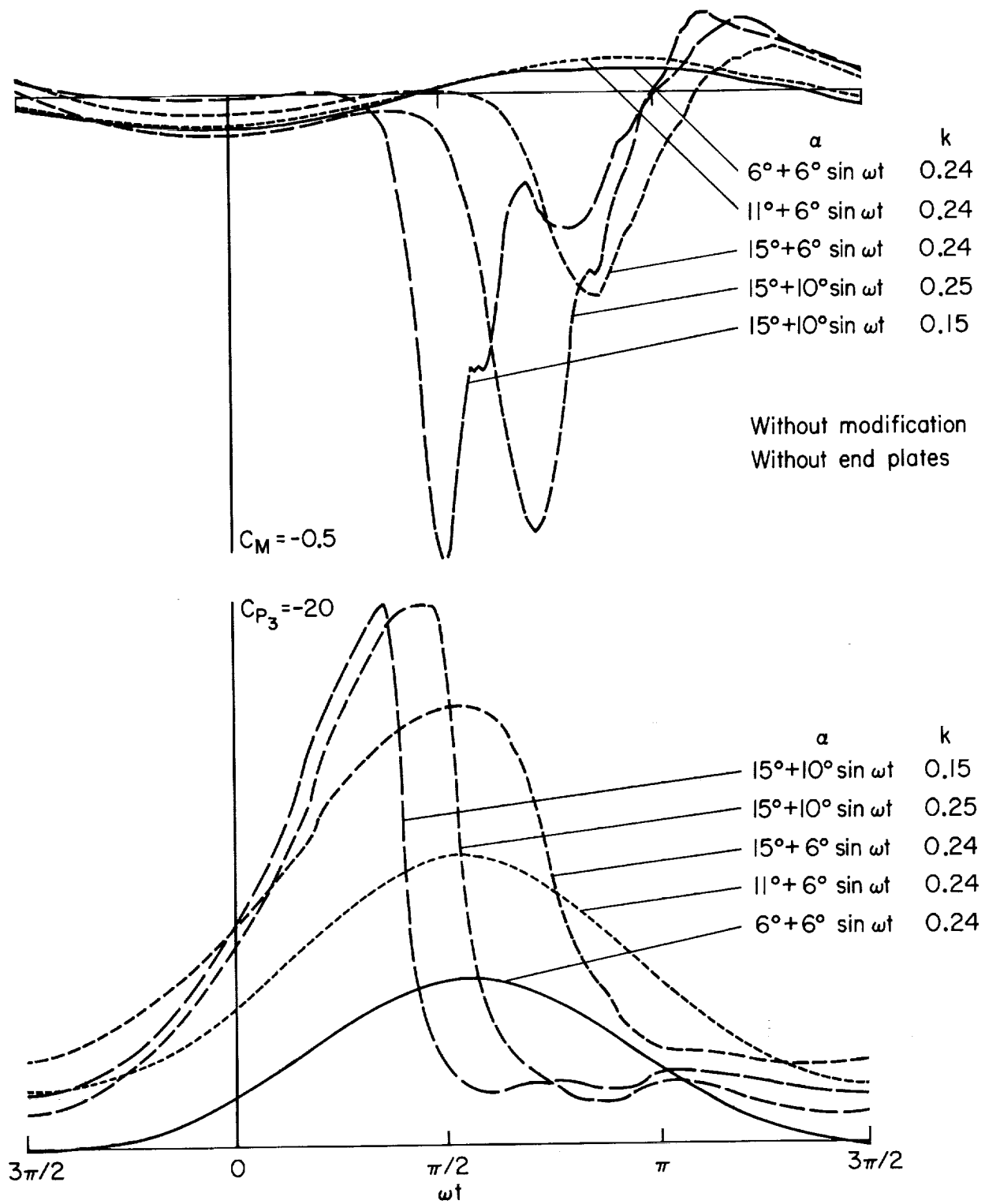
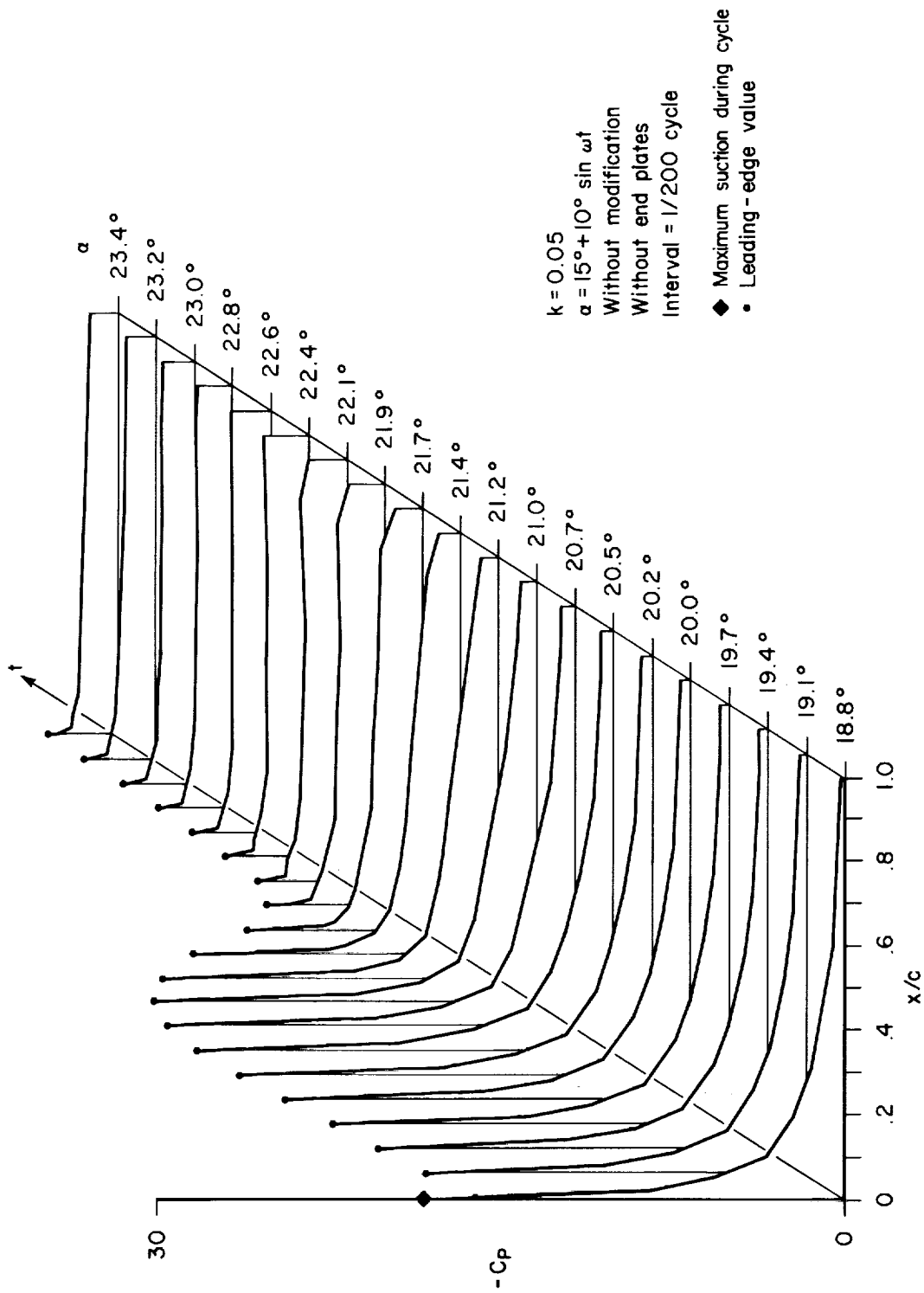
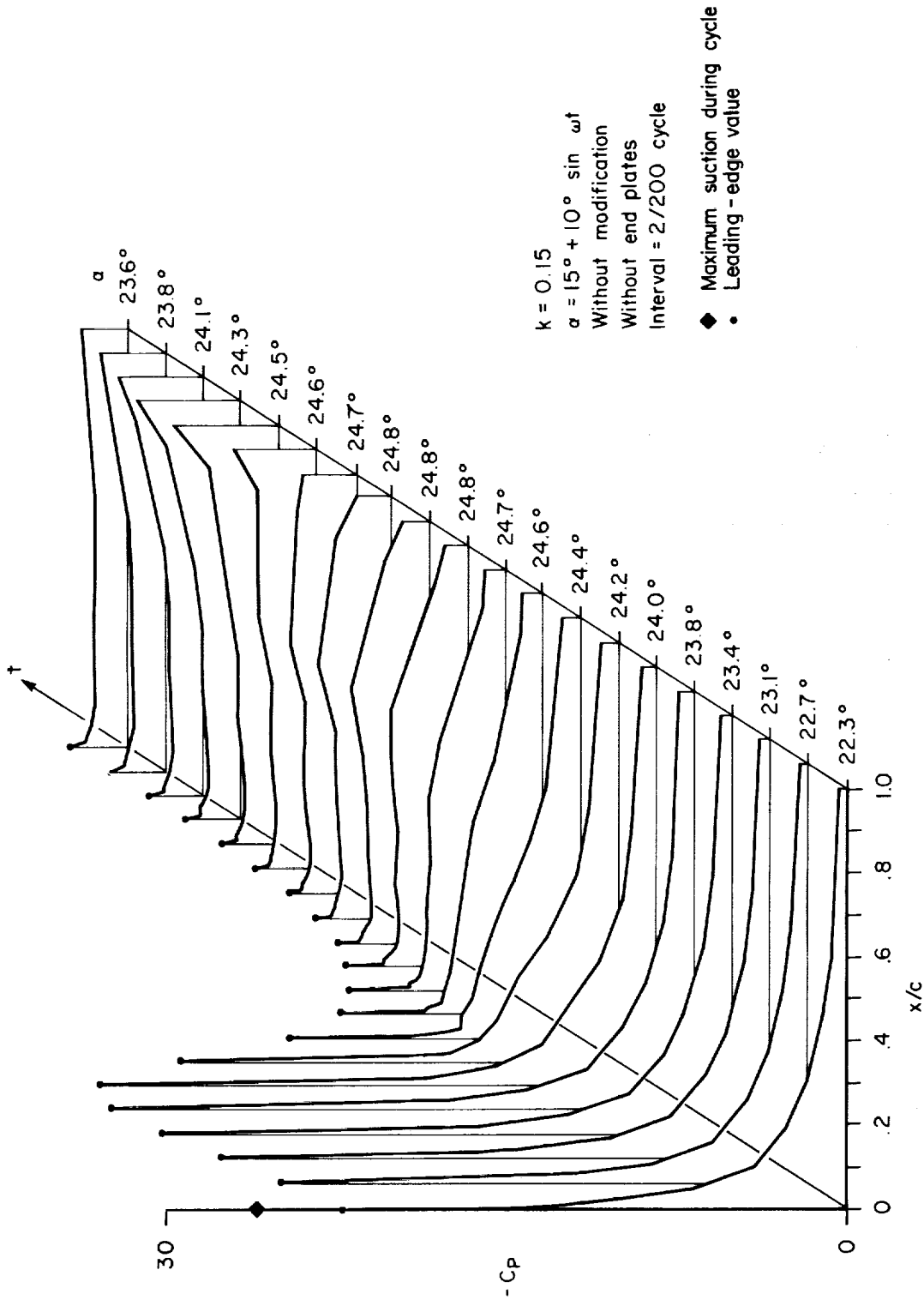


Figure 20.— Correlation between the cyclic pitching moment and the pressure response at $s/c = 0.014$.



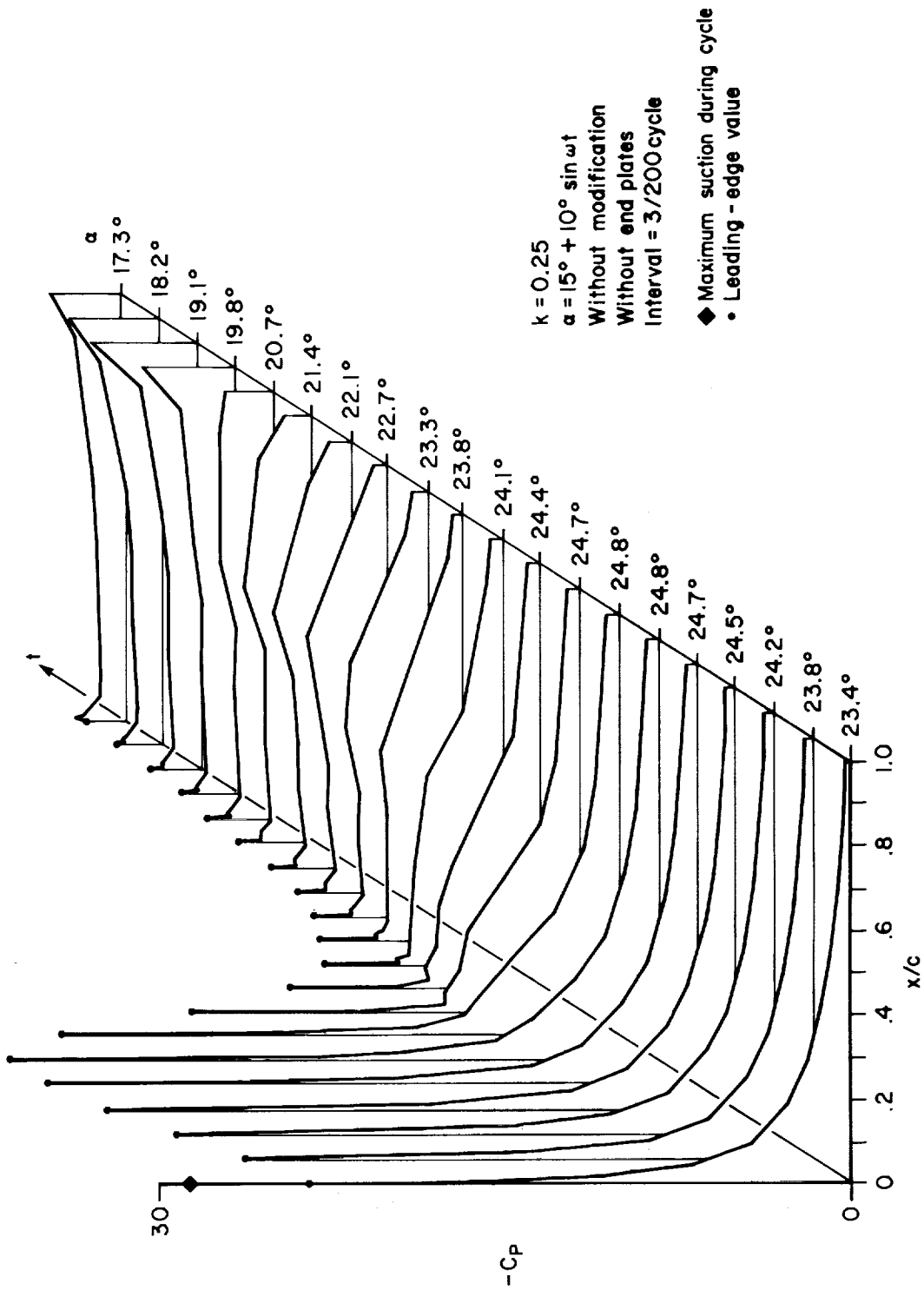
(a) $k = 0.05$.

Figure 21.— Suction wave development without airfoil modification and without end plates.



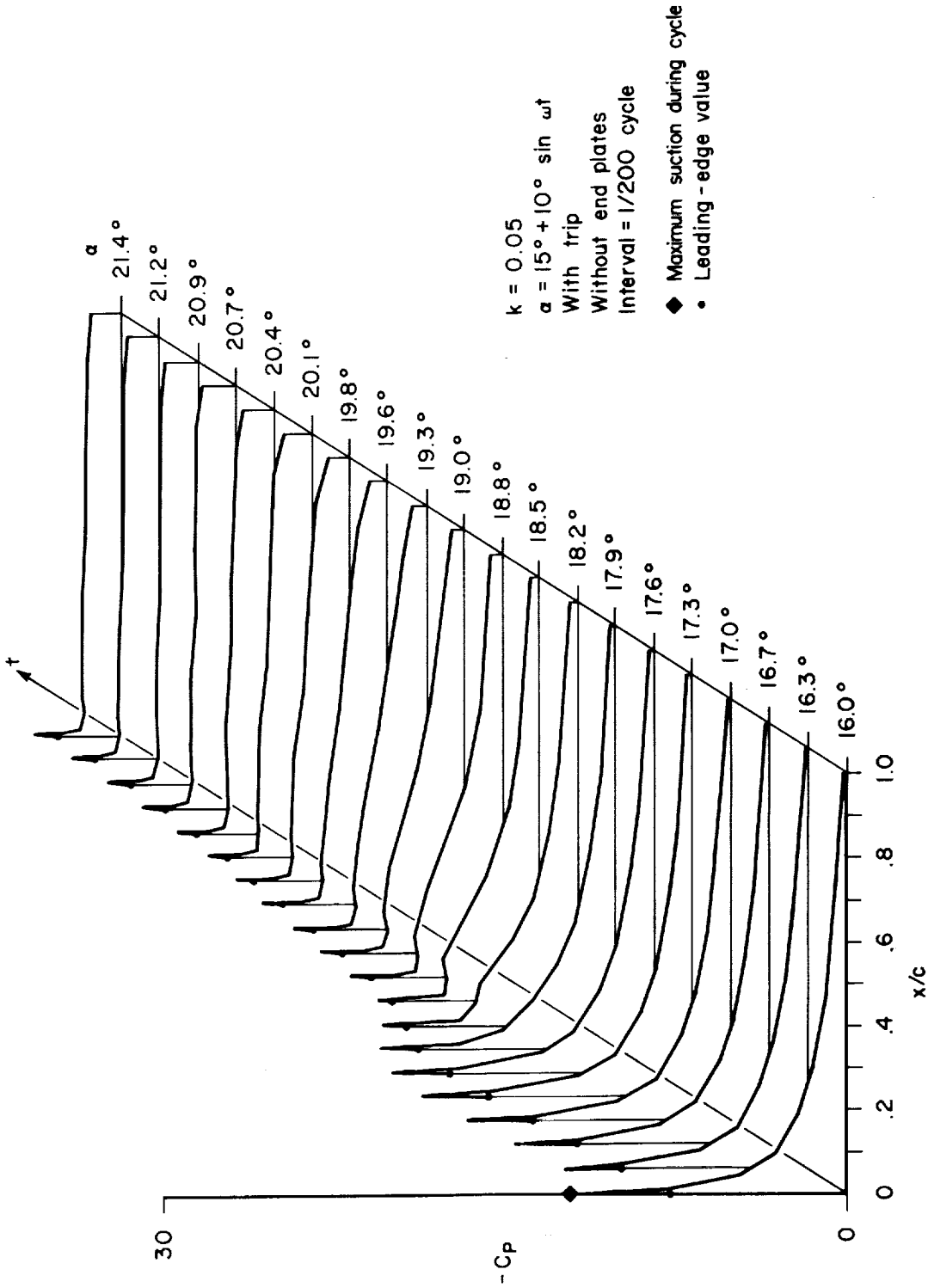
(b) $k = 0.15$.

Figure 21.- Continued.



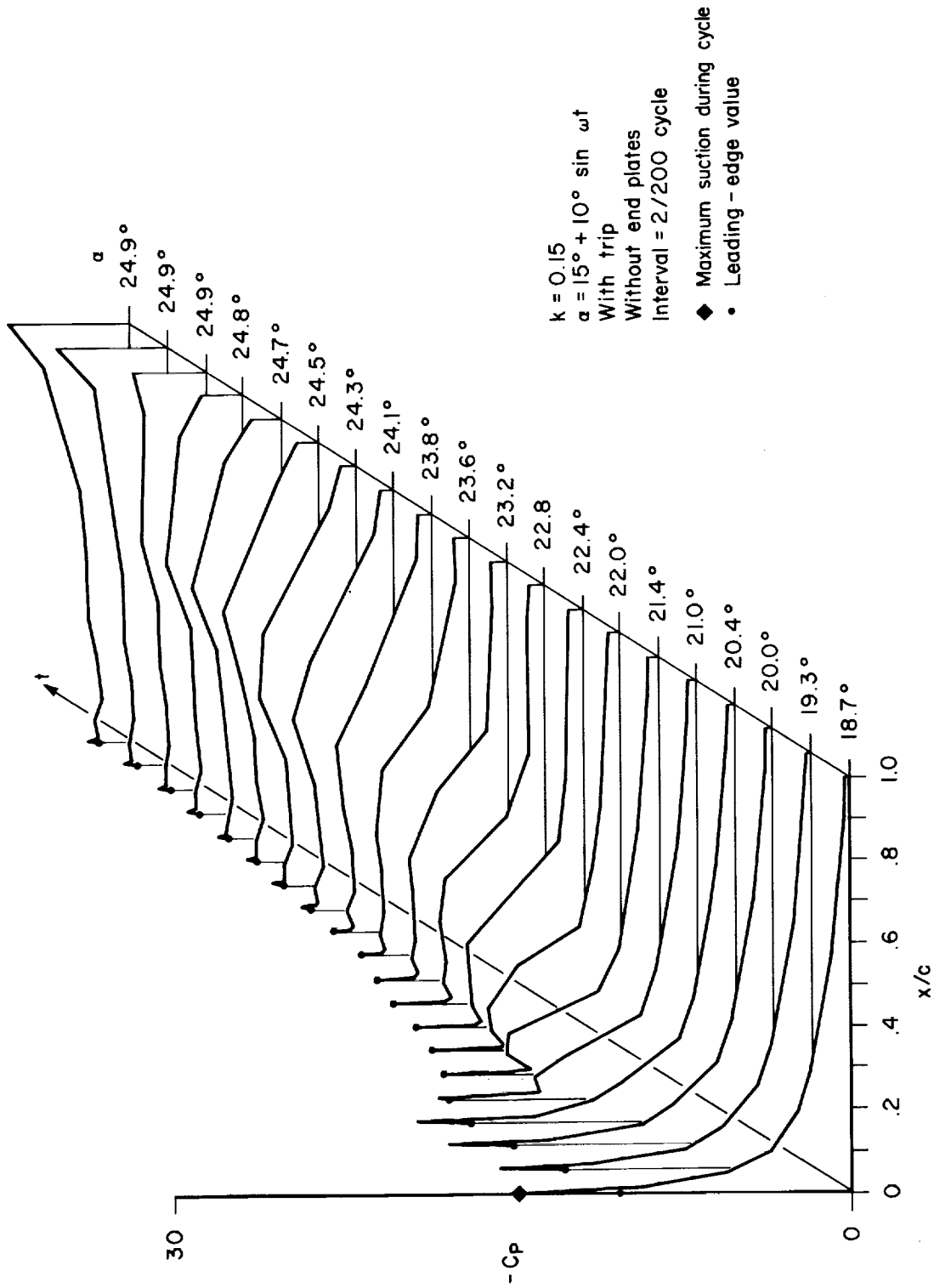
(c) $k = 0.25$.

Figure 21.— Concluded.



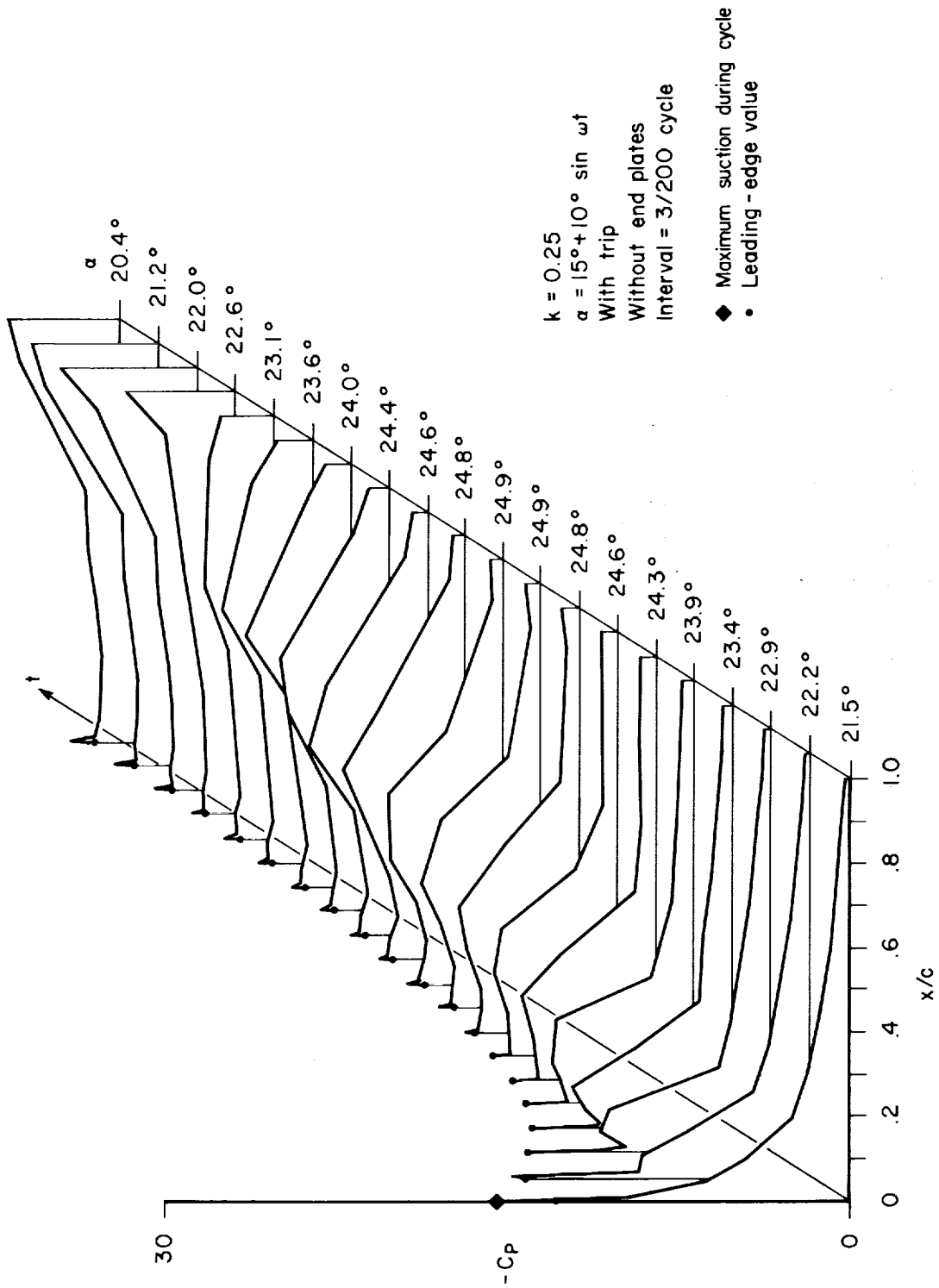
(a) $k = 0.05$.

Figure 22.— Suction wave development with trip and without end plates.



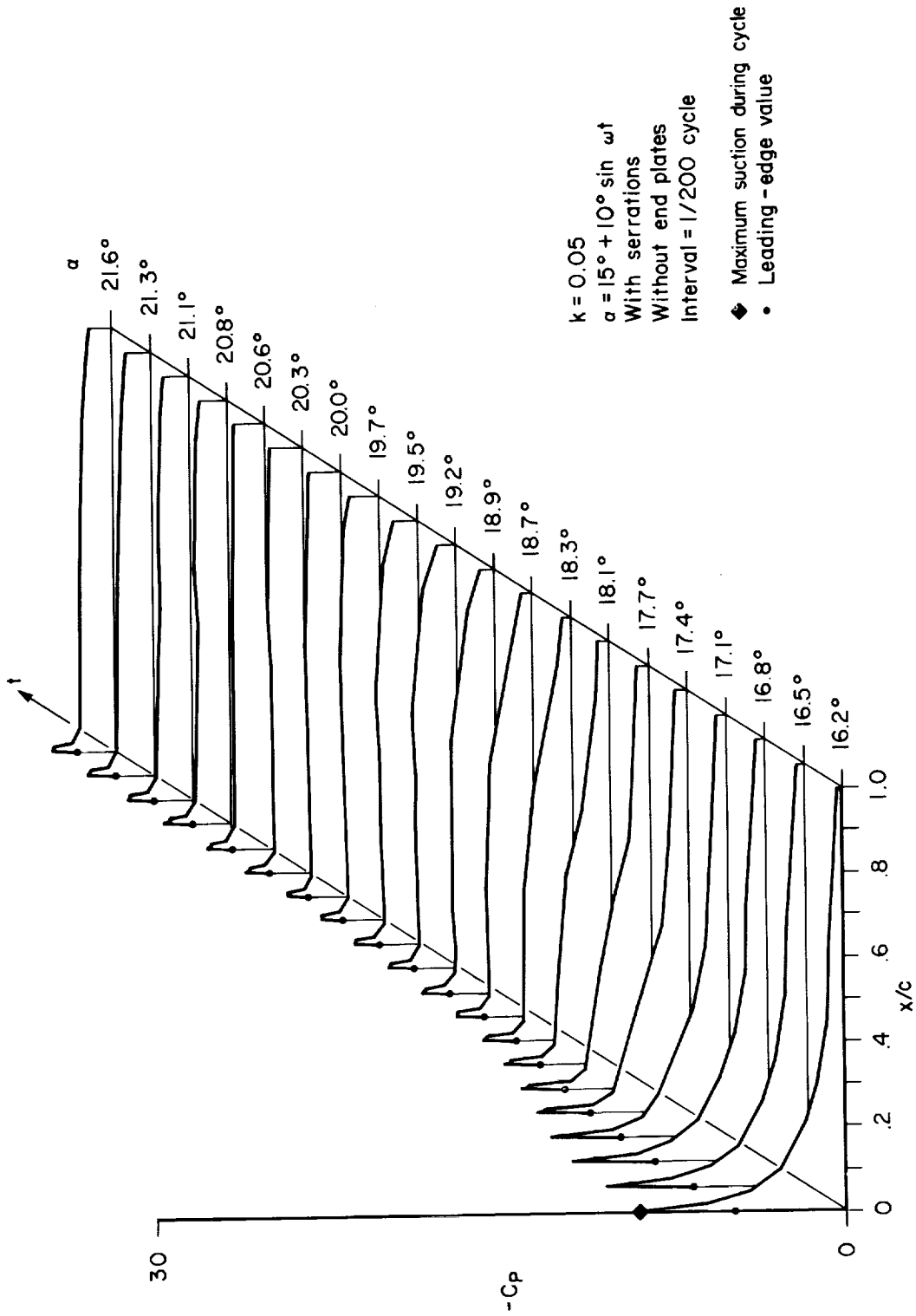
(b) $k = 0.15$.

Figure 22.— Continued.



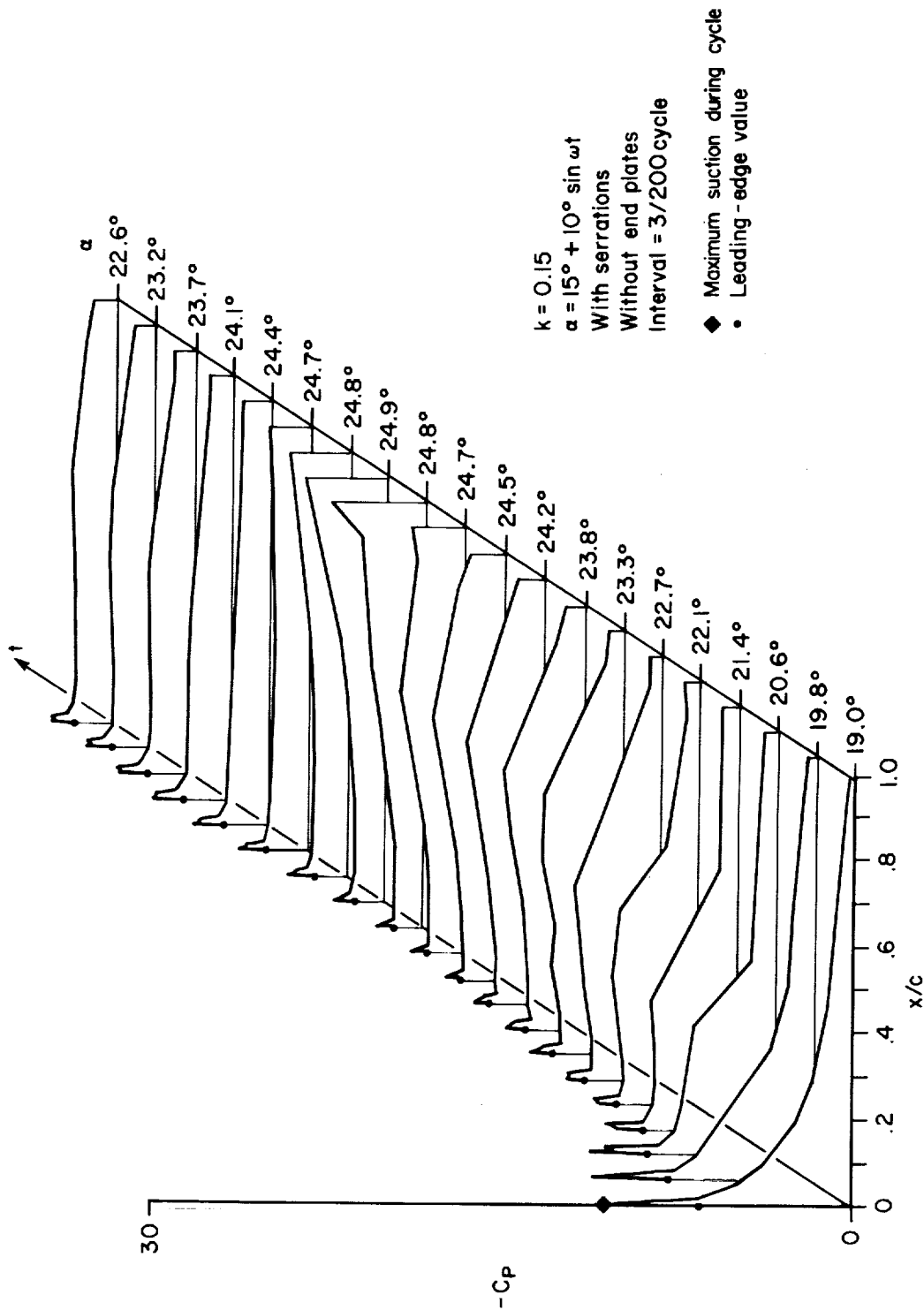
(c) $k = 0.25$.

Figure 22.— Concluded.



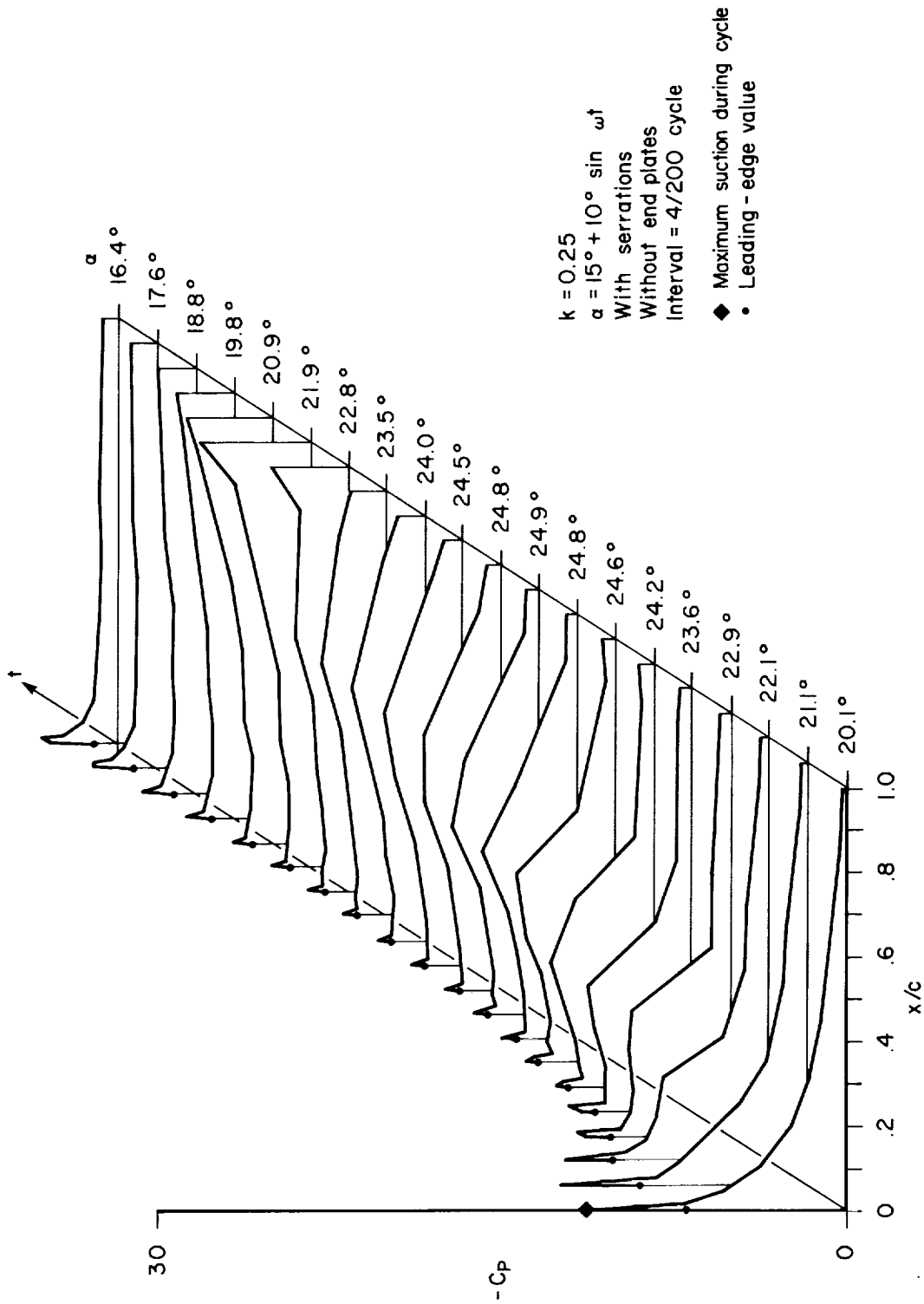
(a) $k = 0.05$.

Figure 23.— Suction wave development with serrations and without end plates.



(b) $k = 0.15$.

Figure 23.— Continued.



(c) $k = 0.25$.

Figure 23.- Concluded.

$$\alpha = 15^\circ + 10^\circ \sin \omega t$$

Without end plates

k=0.15	k=0.25	
□	◇	With trip
■	◆	Without trip

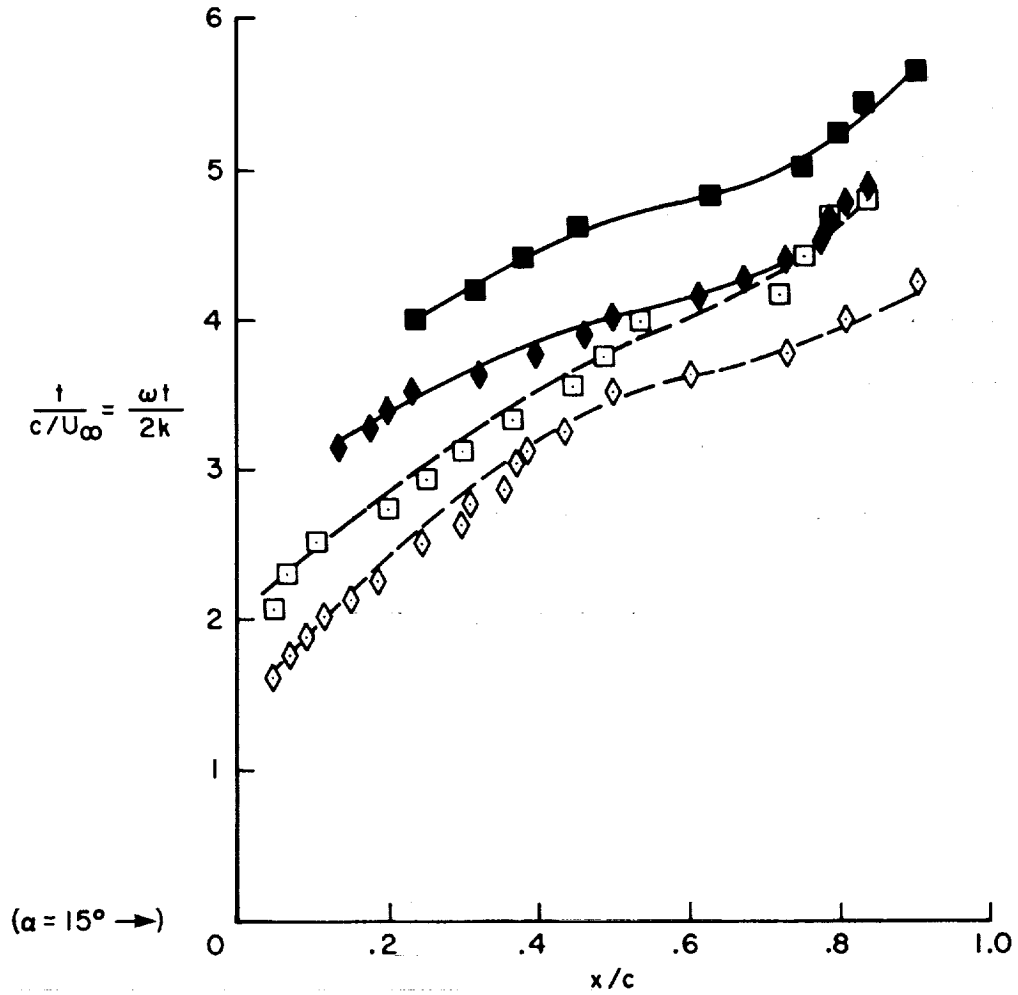


Figure 24.— Effect of leading-edge trip on the movement of the suction wave over the upper airfoil surface during moment stall.

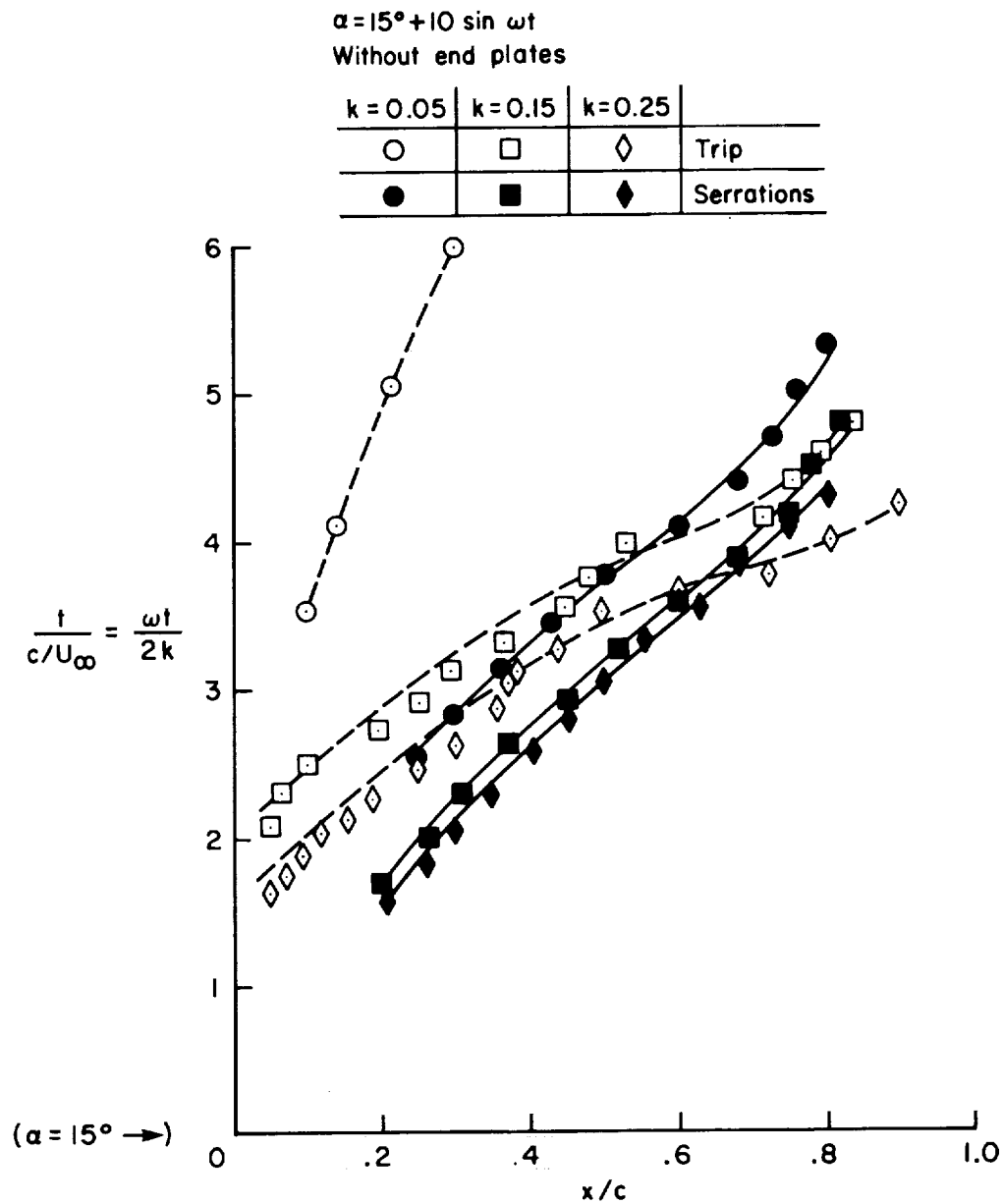
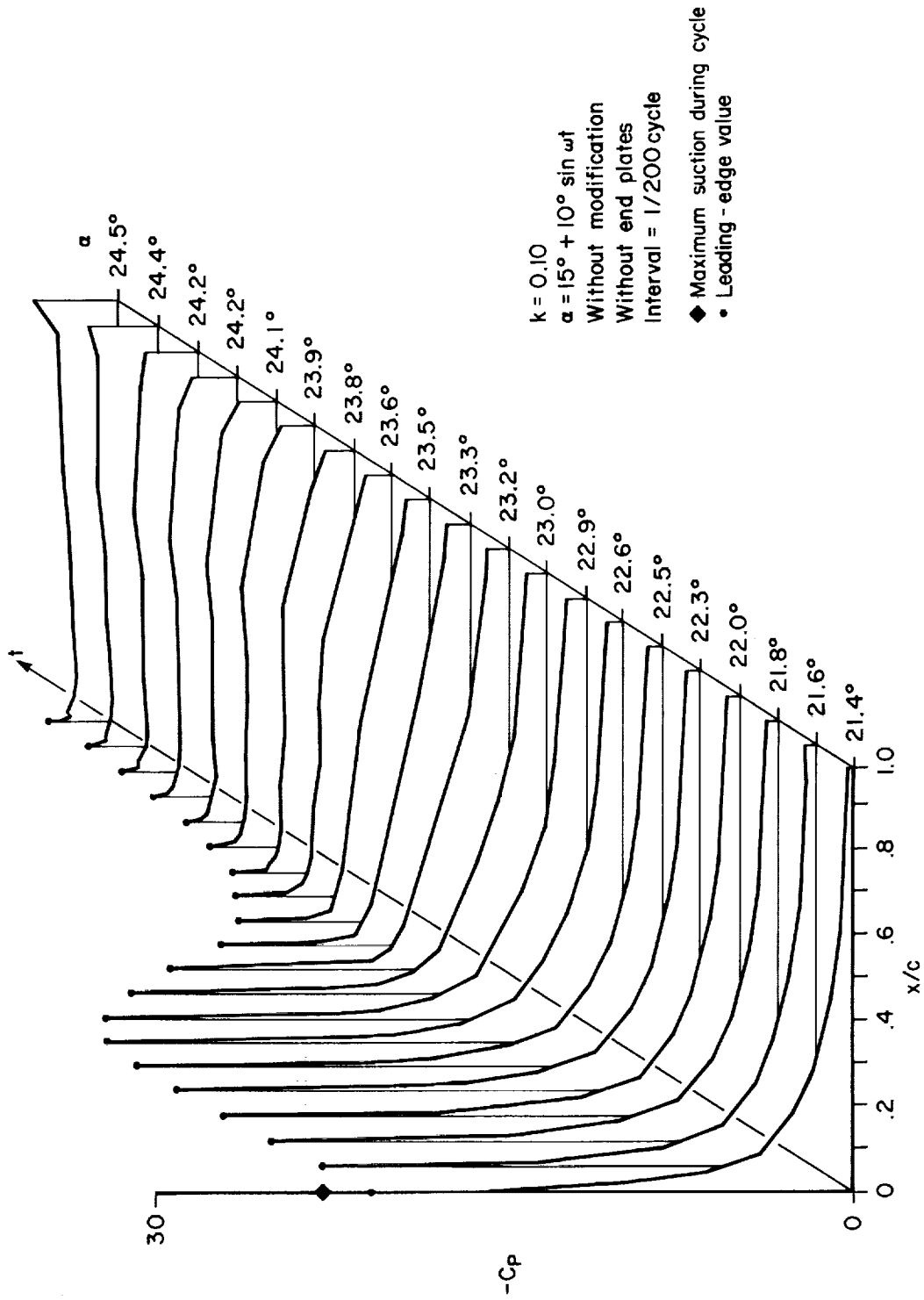
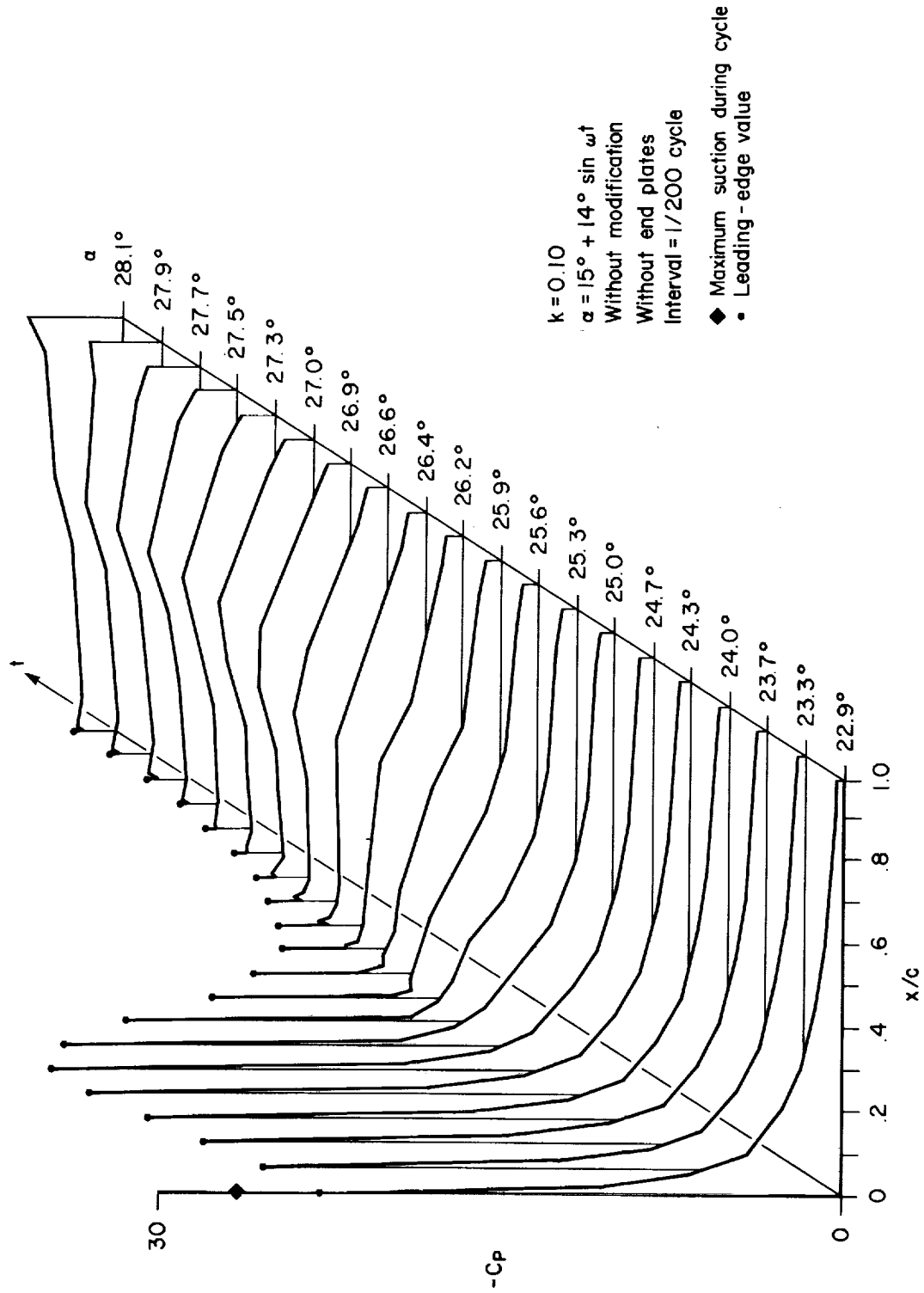


Figure 25.— Effect of leading-edge modifications on the movement of the suction wave over the upper airfoil surface during moment stall.



(a) $\alpha = 15^\circ + 10^\circ \sin \omega t$.

Figure 26.— Suction wave development without airfoil modification and without end plates.



(b) $\alpha = 15^\circ + 14^\circ \sin \omega t$.

Figure 26.— Concluded.

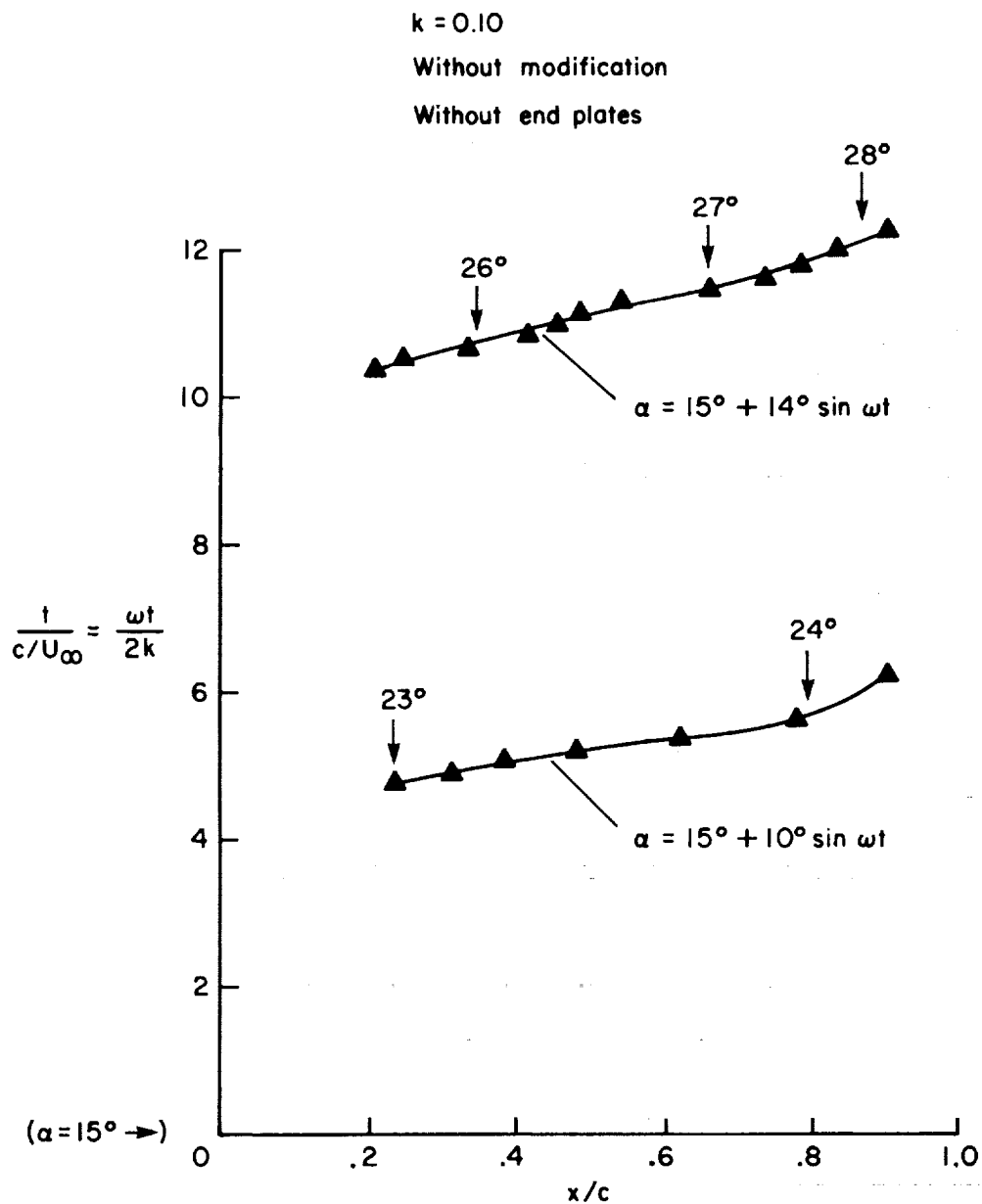
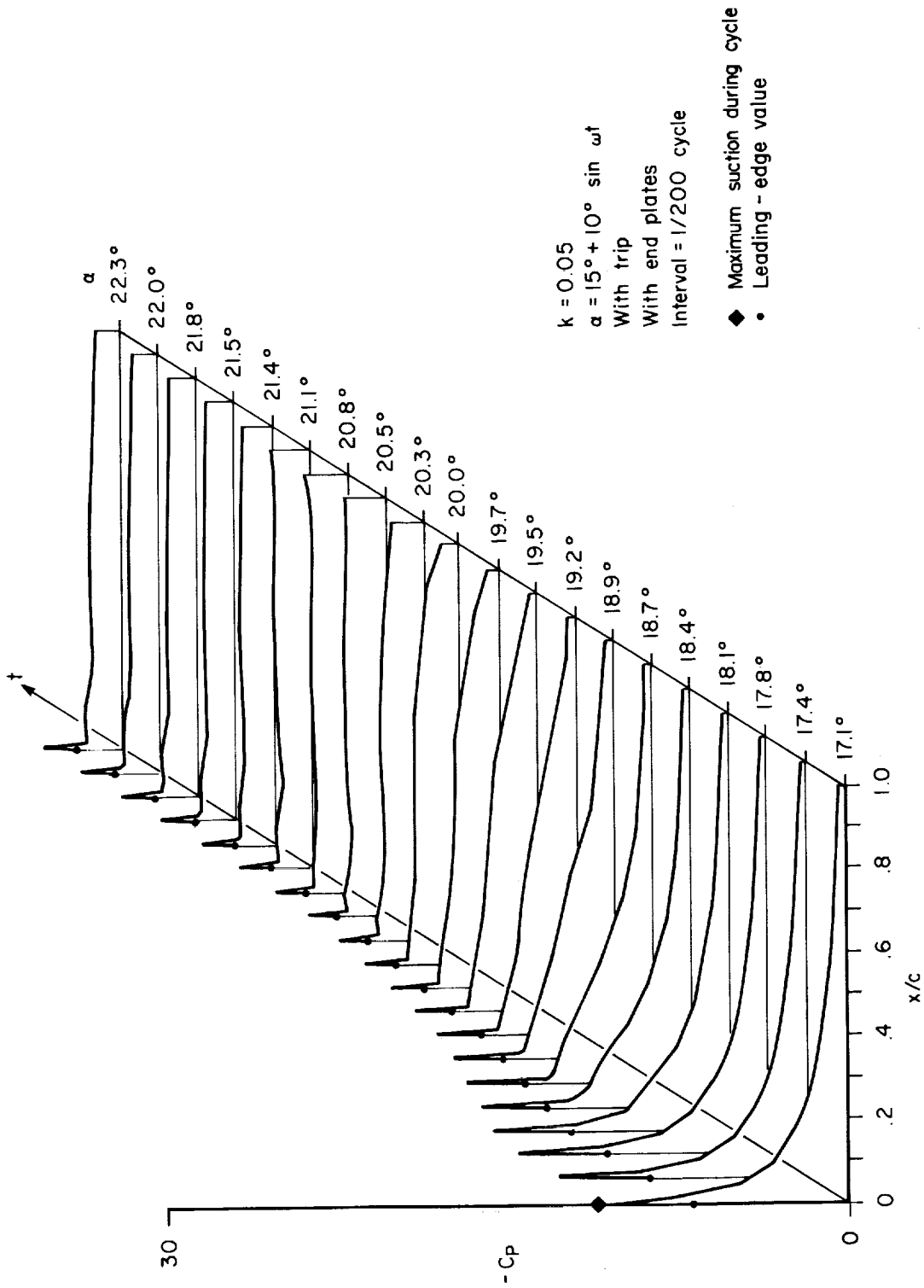
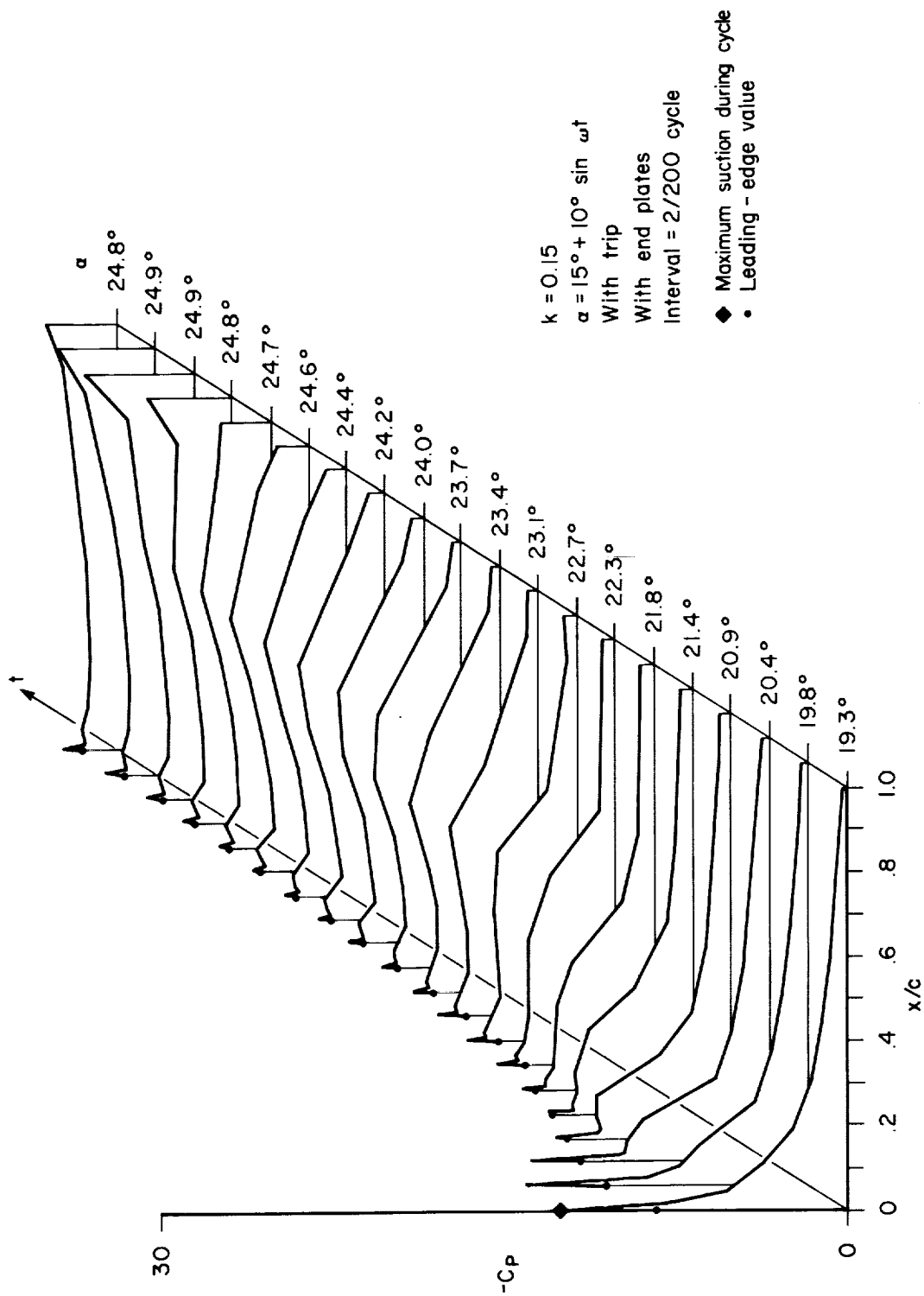


Figure 27.— Effect of oscillation amplitude on the movement of the suction wave over the upper airfoil surface during moment stall.



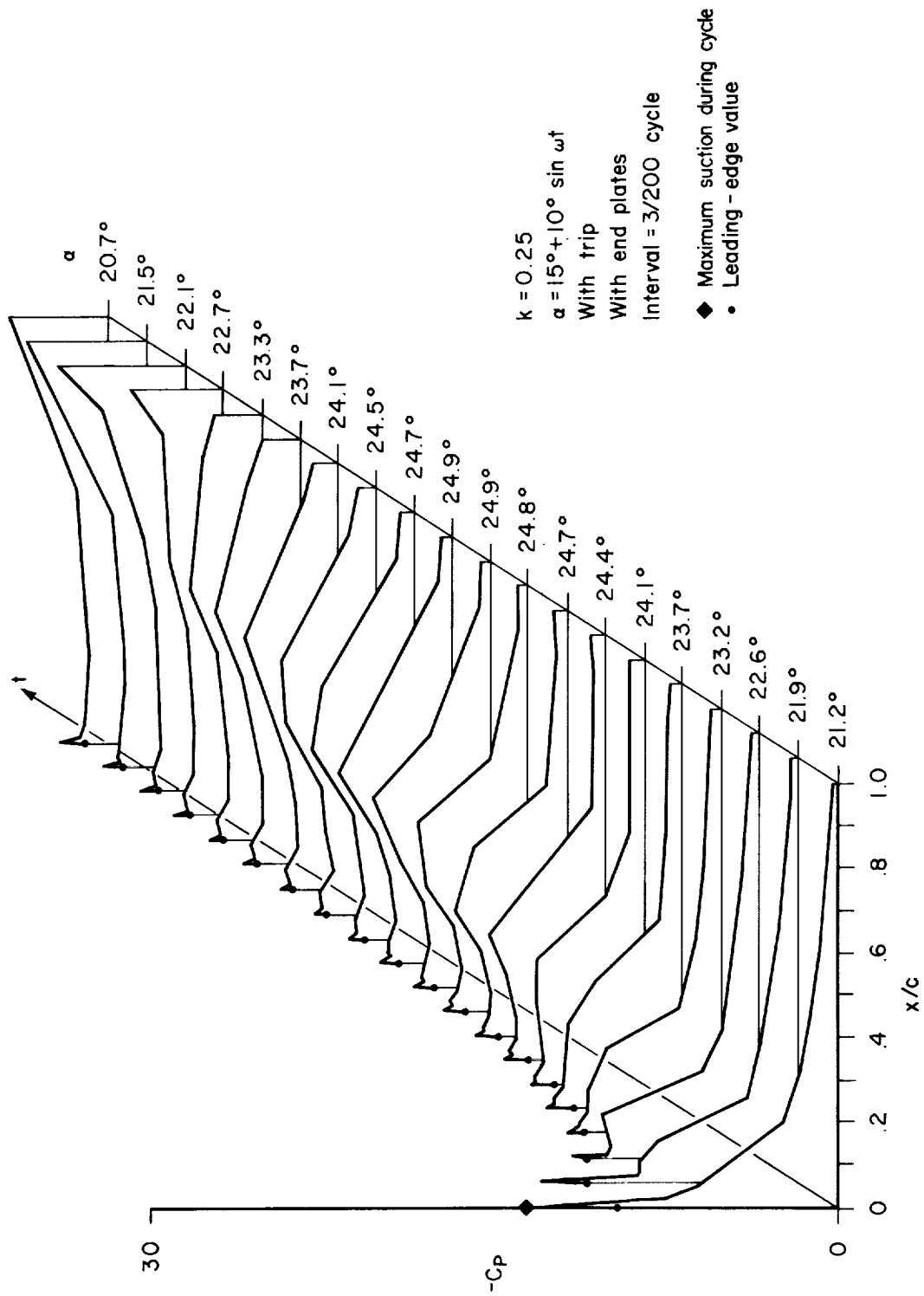
(a) $k = 0.05$.

Figure 28.— Suction wave development with trip and with end plates.



(b) $k = 0.15$.

Figure 28. - Continued.



(c) $k = 0.25$.

Figure 28.- Concluded.

$$\alpha = 15^\circ + 10^\circ \sin \omega t$$

With trip

k=0.05	k=0.15	k=0.25	
○	□	◇	With end plates
●	■	◆	Without end plates

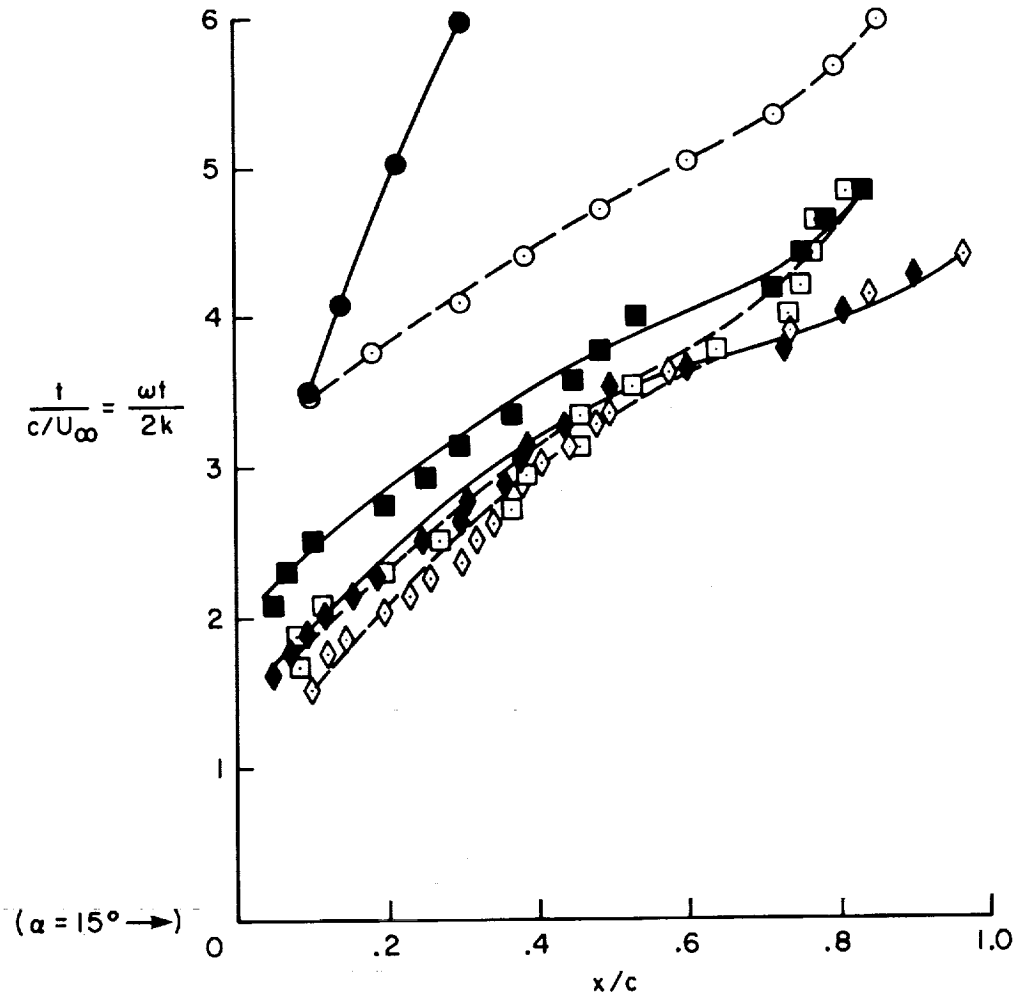


Figure 29.— Effect of end plates on the movement of the suction wave over the upper airfoil surface during moment stall.

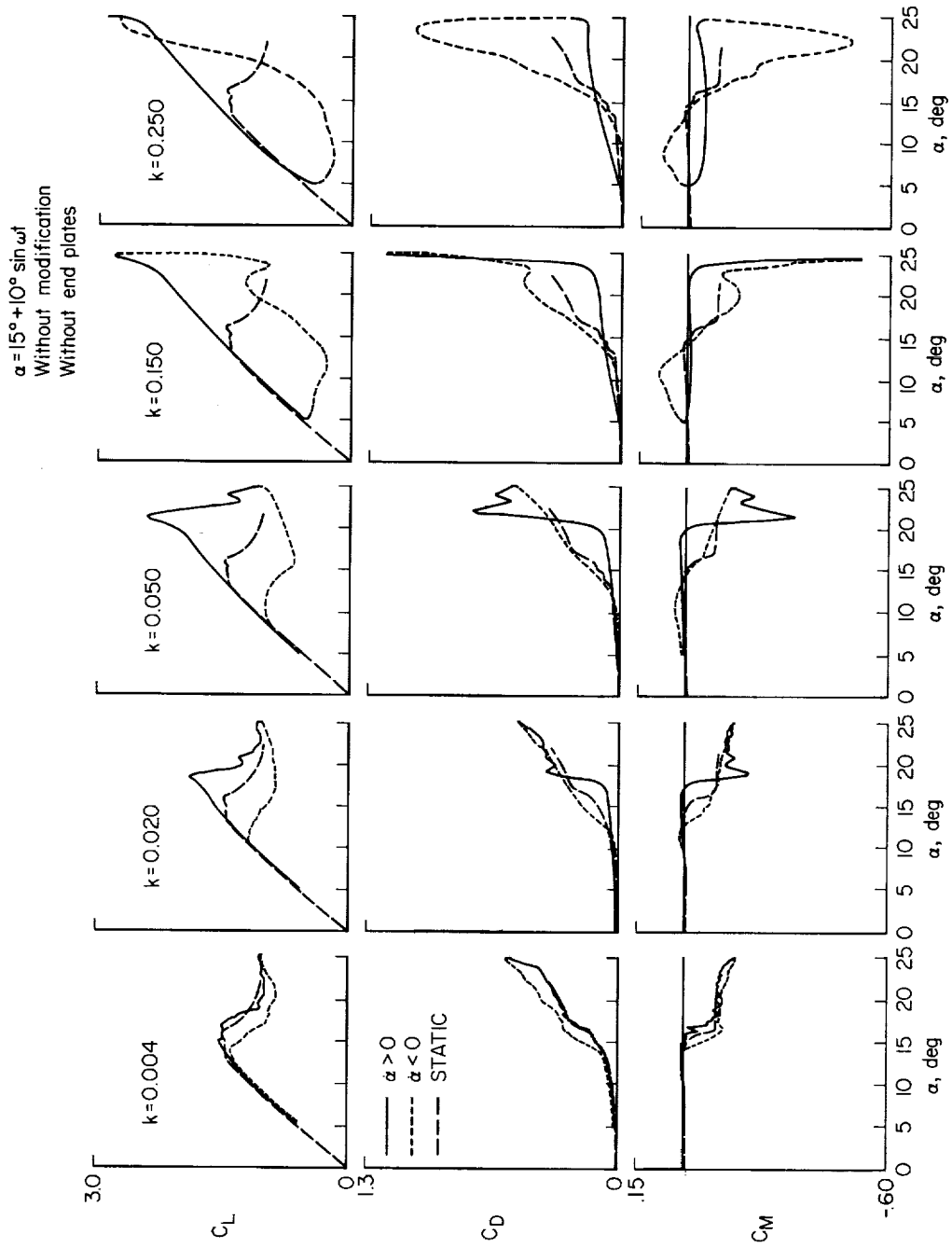
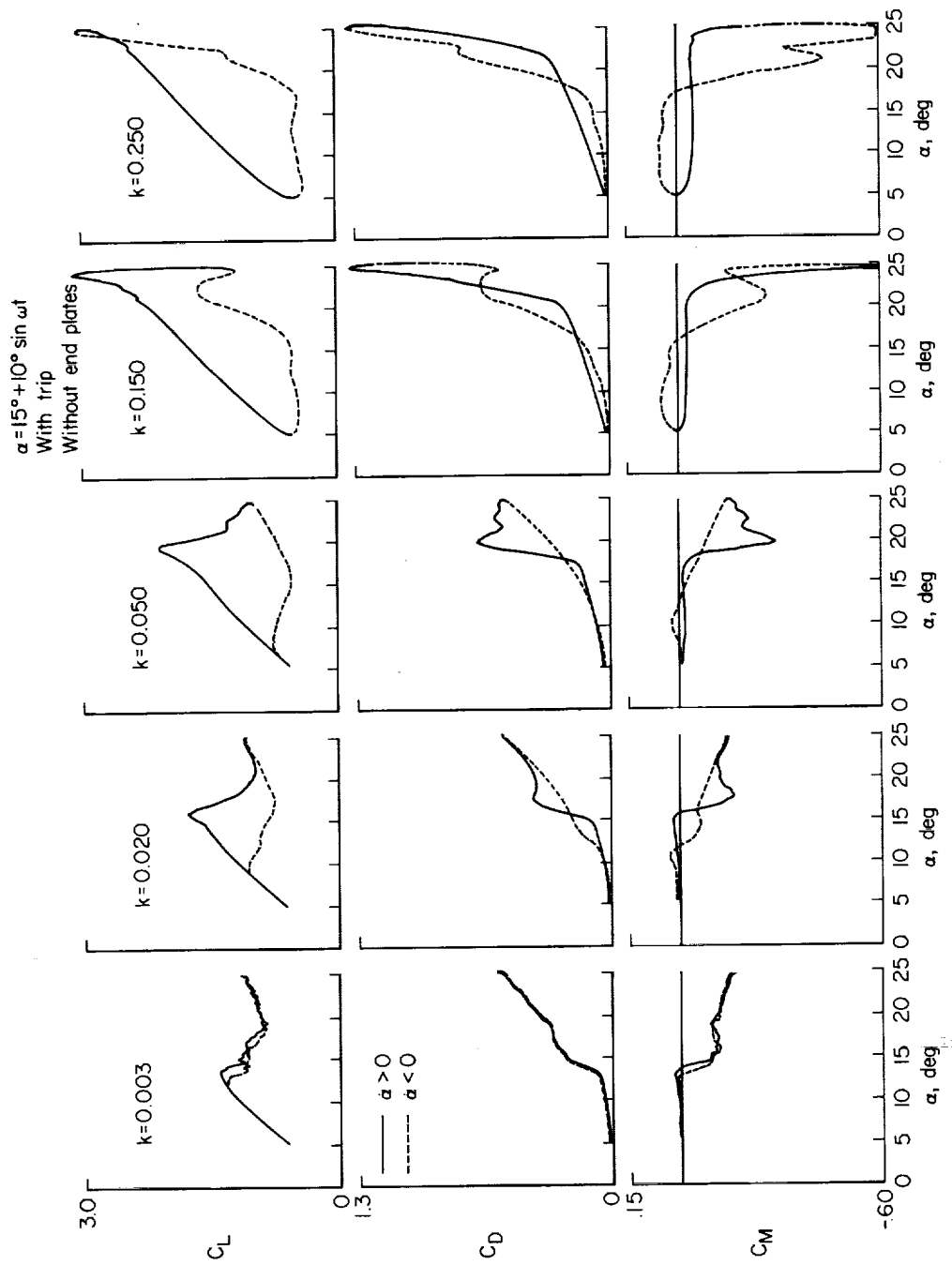
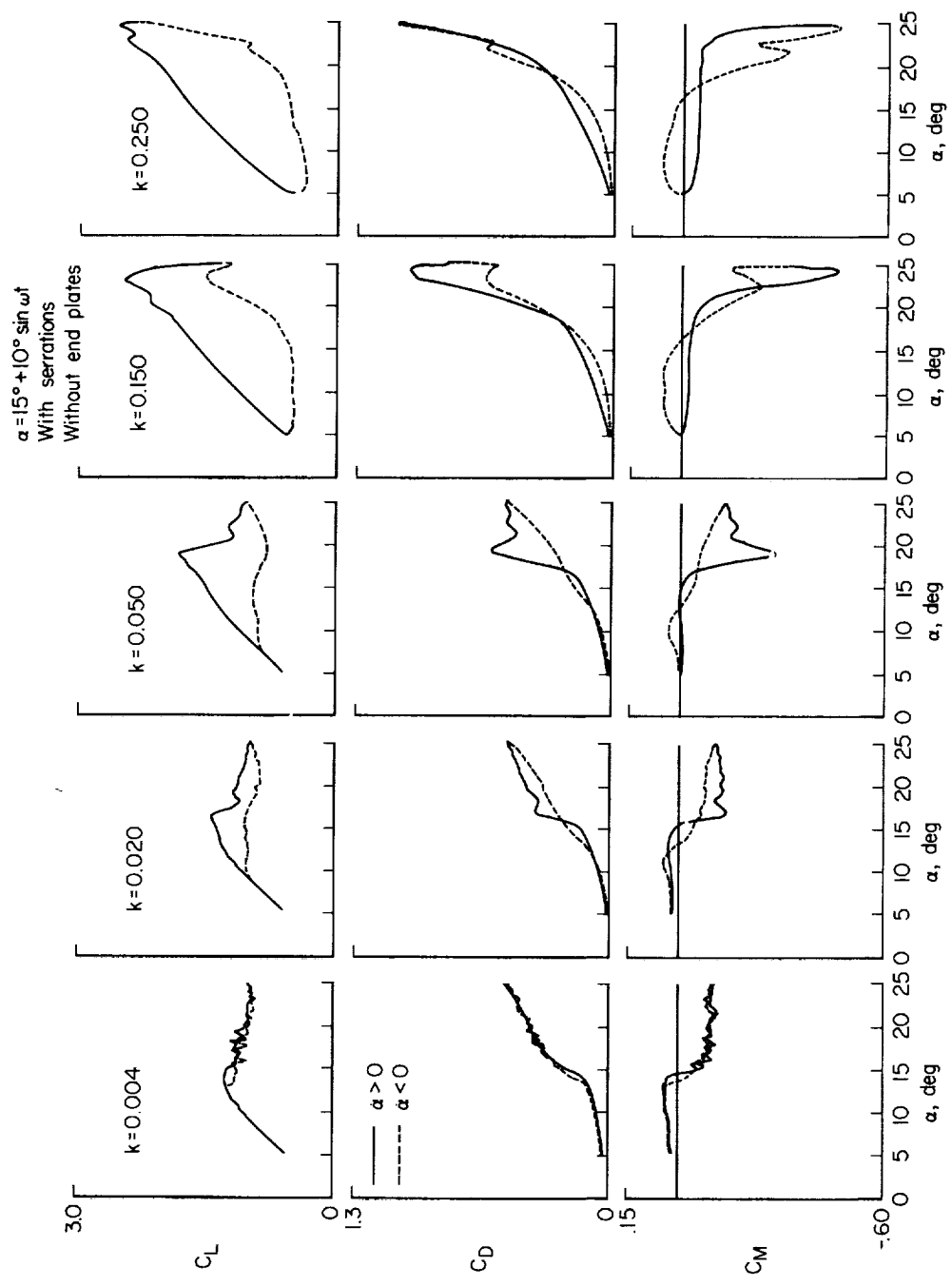


Figure 30.— Lift, drag, and pitching moment as a function of α at various reduced frequencies.



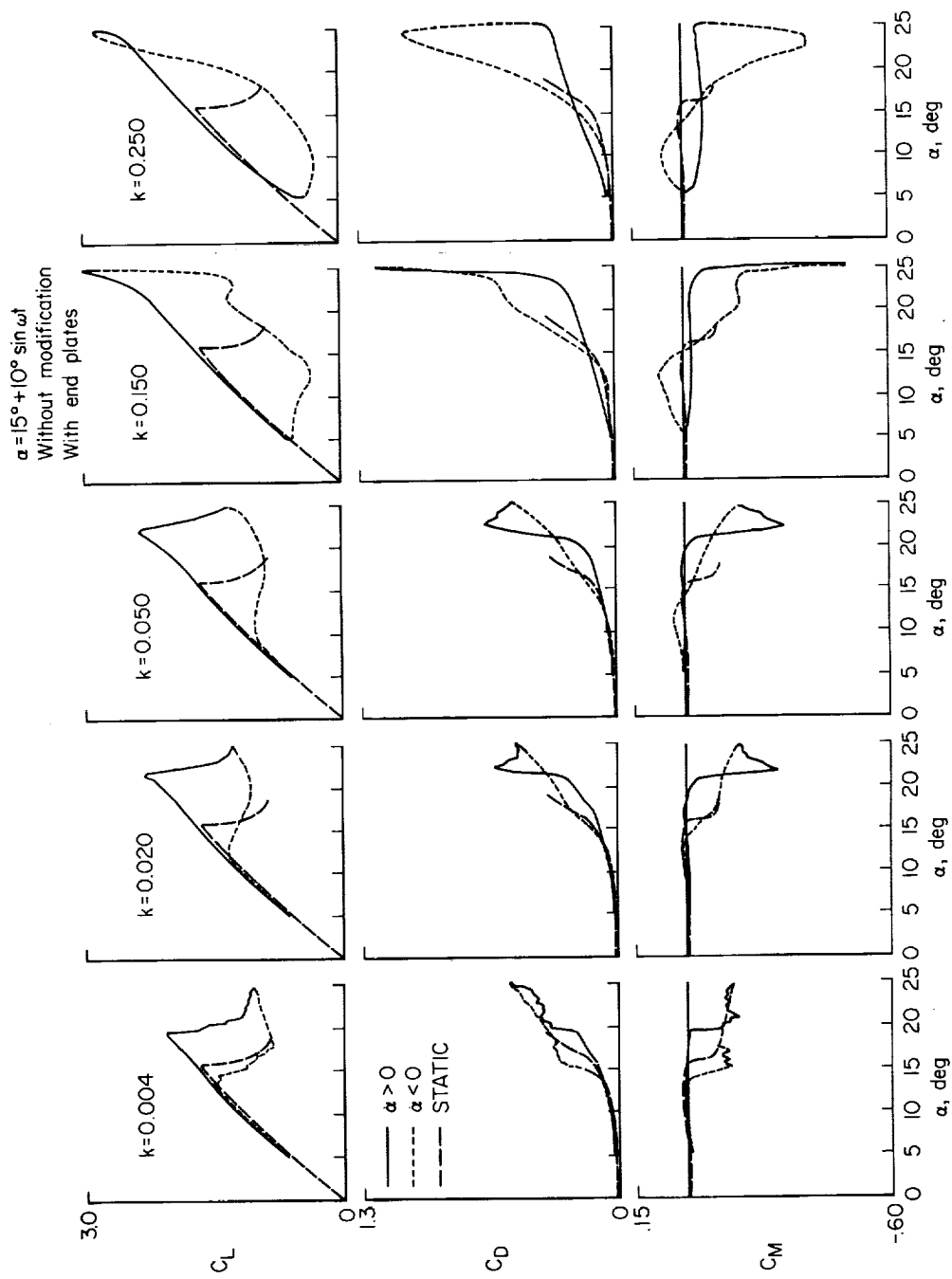
(b) With trip and without end plates.

Figure 30.— Continued.



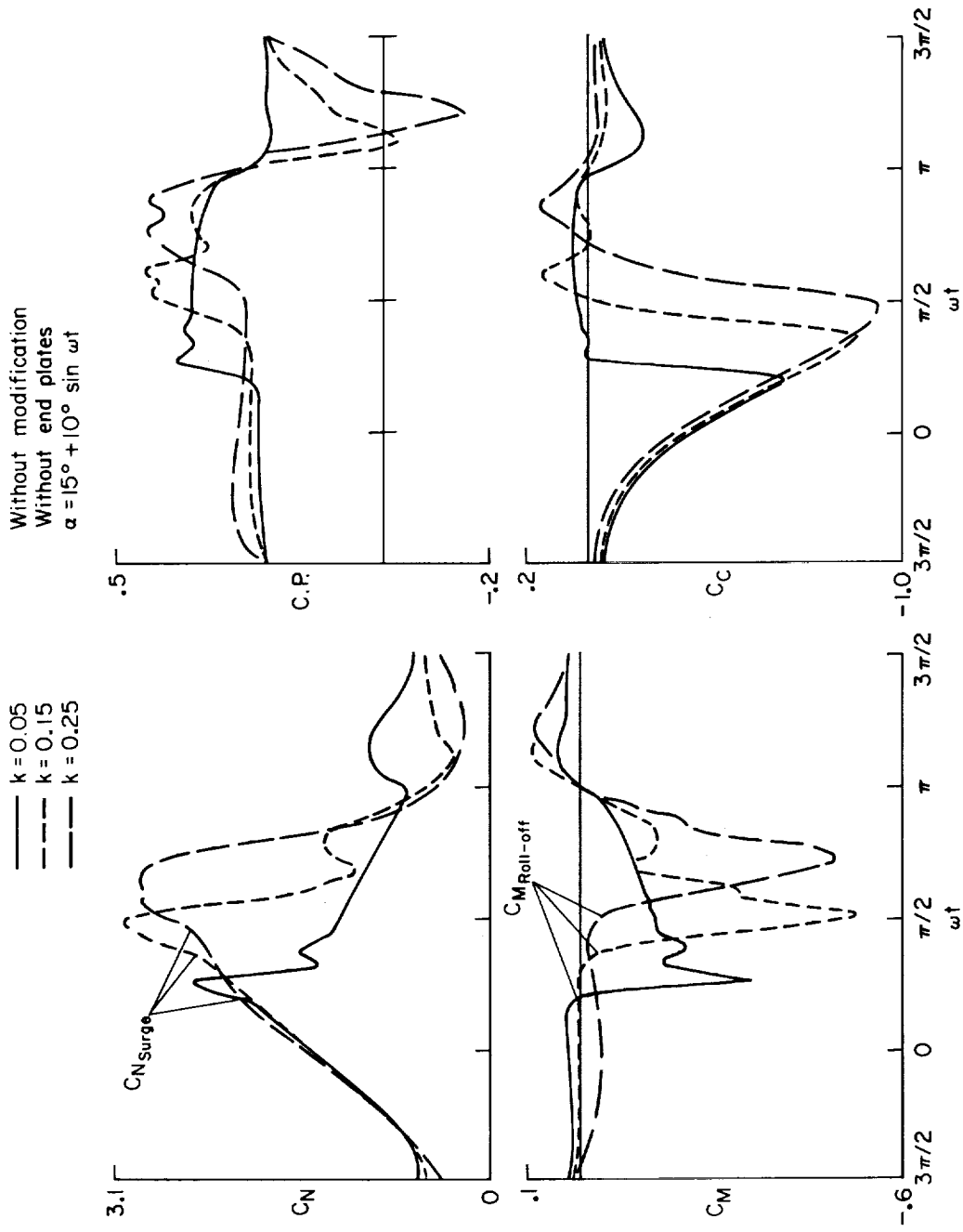
(c) With serrations and without end plates.

Figure 30.— Continued.



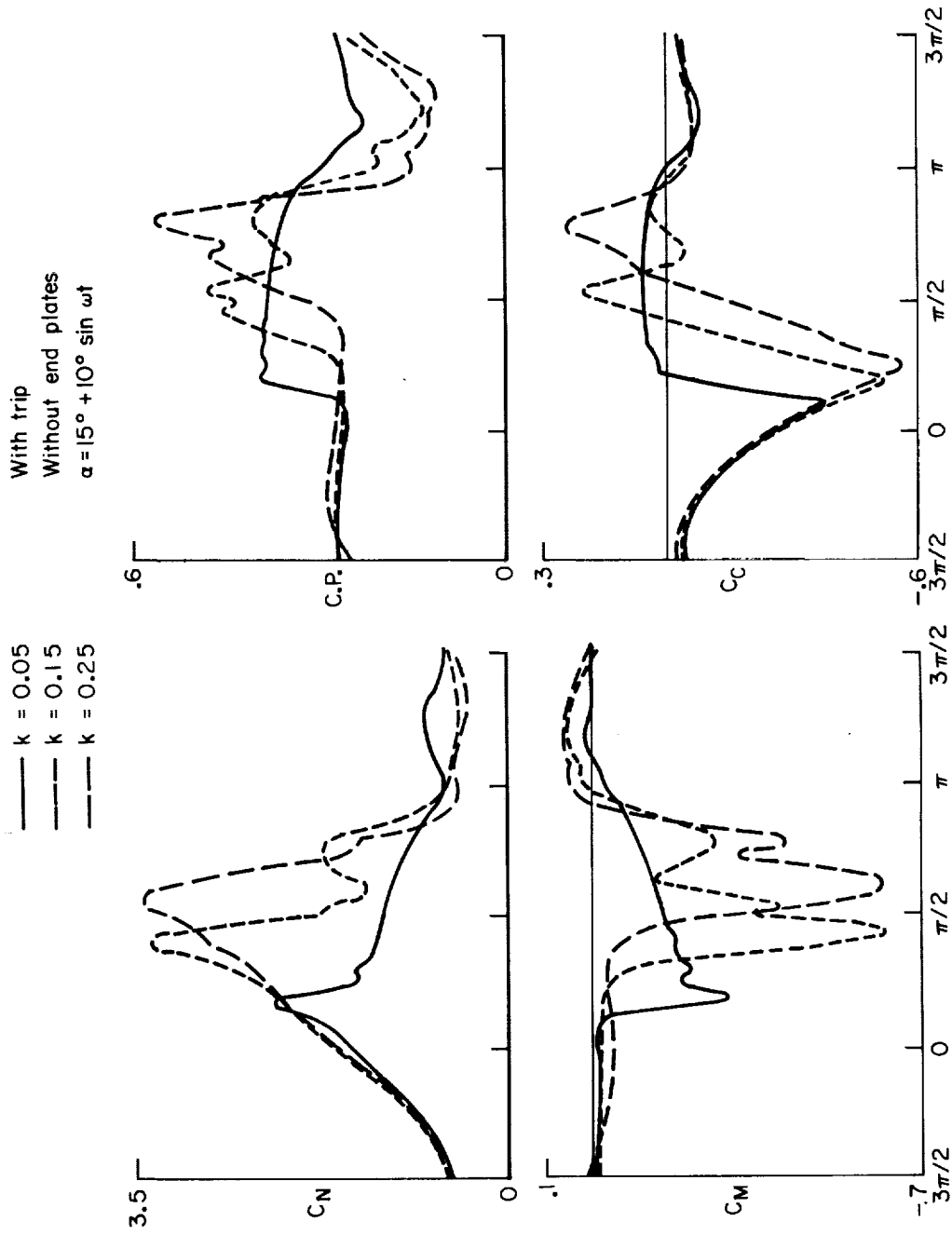
(d) Without modification and with end plates.

Figure 30.— Concluded.



(a) Without modification.

Figure 31.- Reduced frequency effect on integrated pressures without airfoil end plates.

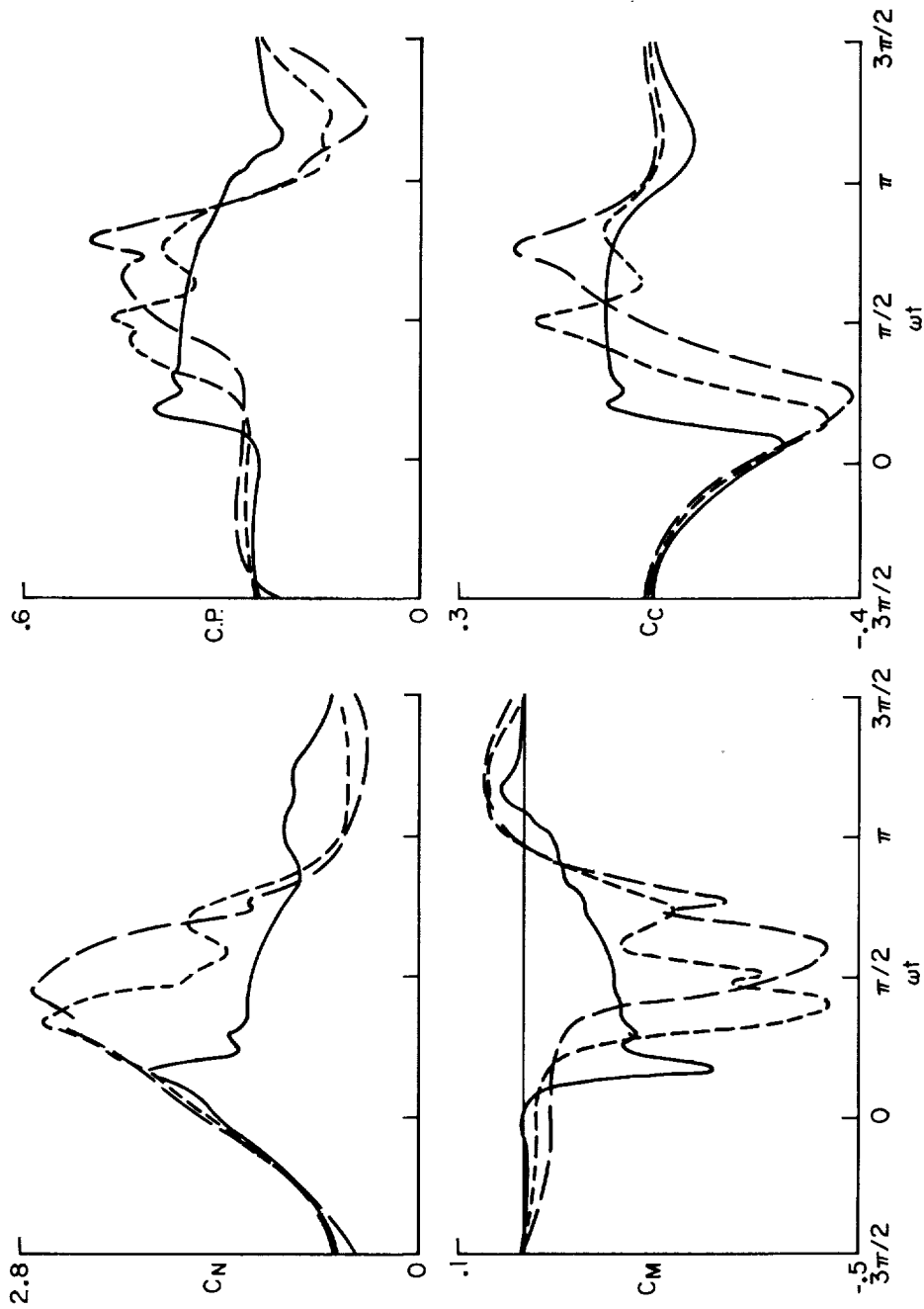


(b) With trip.

Figure 31.— Continued.

— k = 0.05
 - - - k = 0.15
 - - - k = 0.25

With serrations
 Without end plates
 $\alpha = 15^\circ + 10^\circ \sin \omega t$



(c) With serrations.

Figure 31.— Concluded.

$\alpha = 15^\circ + 10^\circ \sin \omega t$
 Without modification
 With end plates

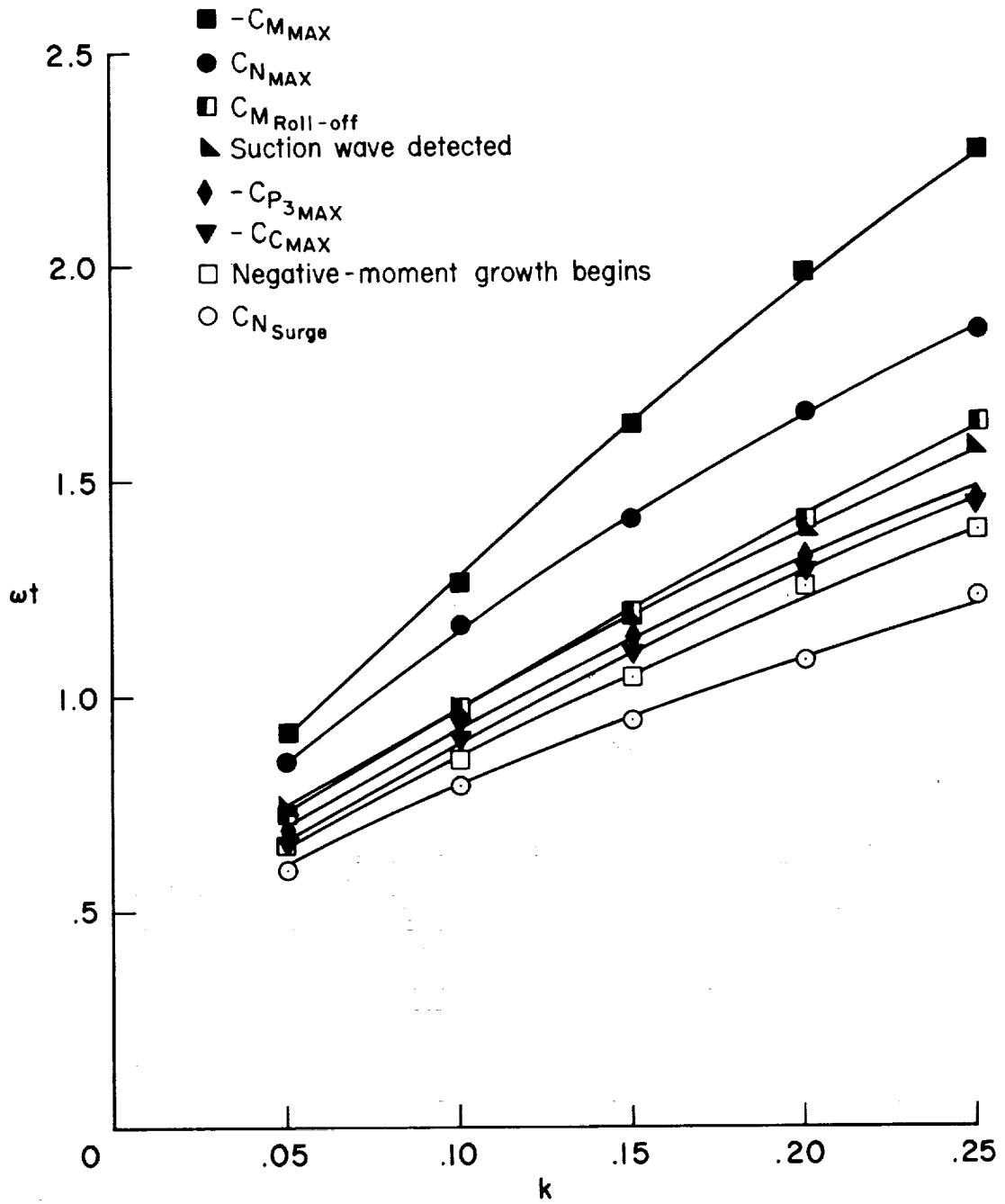
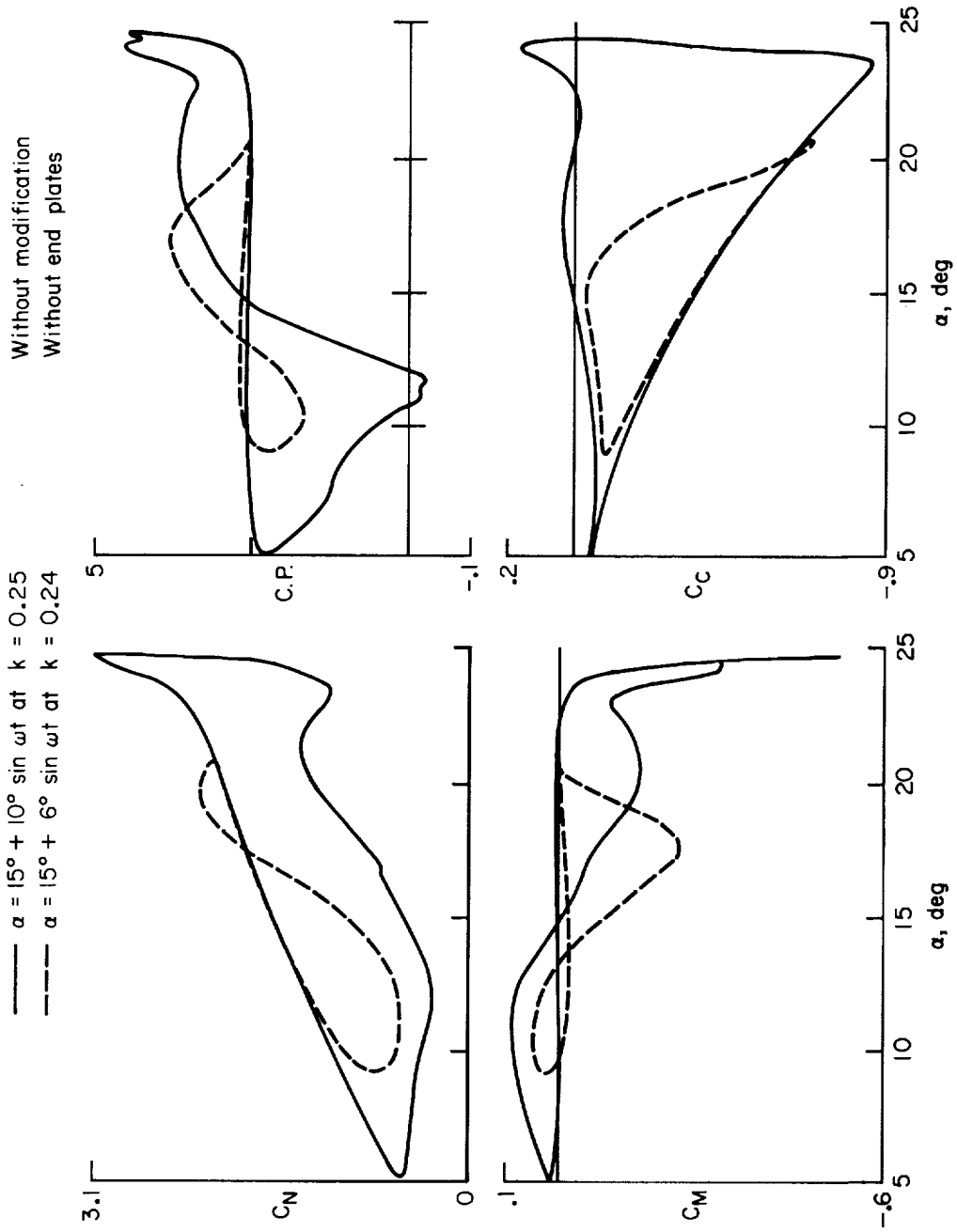
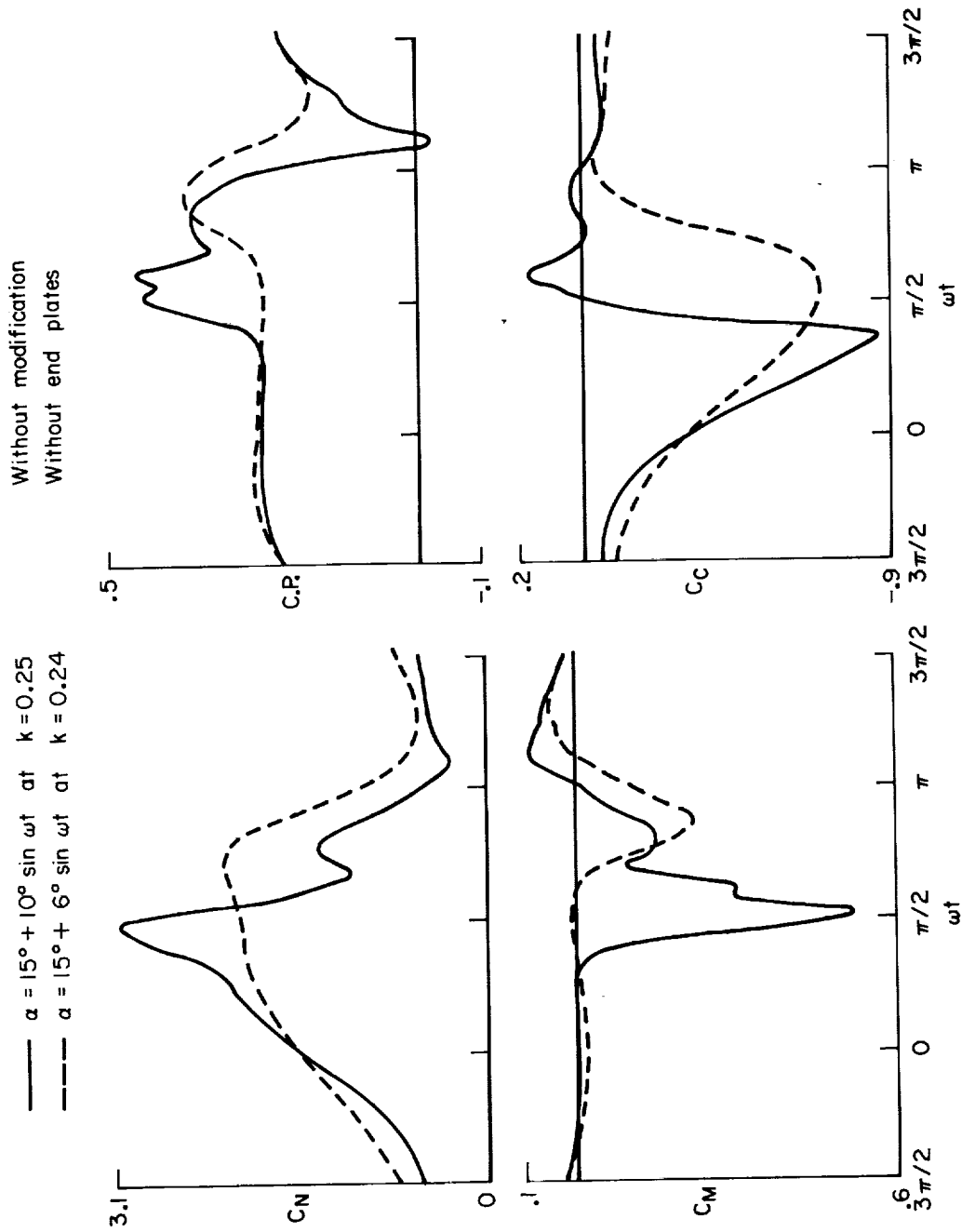


Figure 32.— Chronology of events associated with dynamic stall.



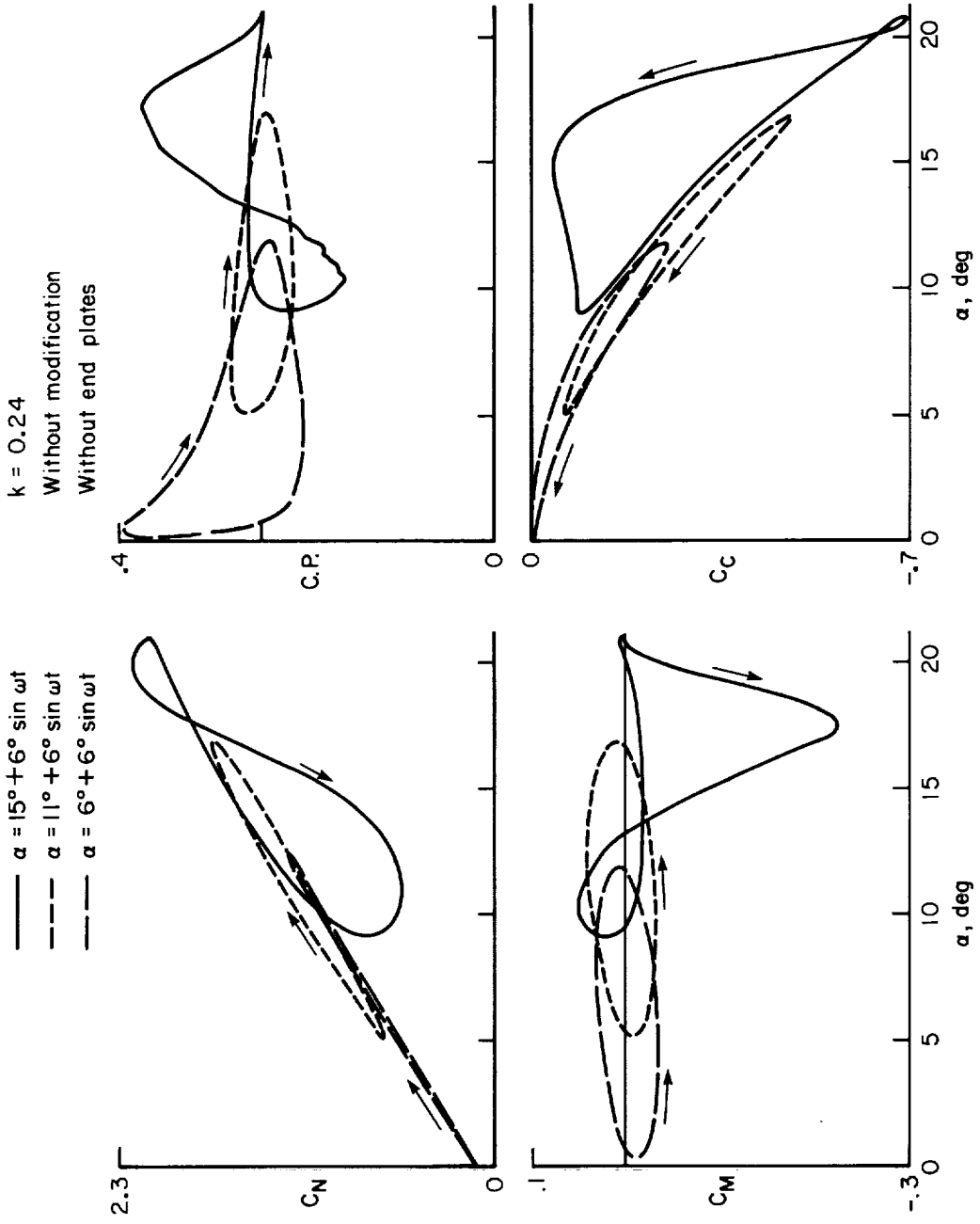
(a) Function of α .

Figure 33.— Effect of oscillation amplitude on integrated pressure without modification and without end plates.



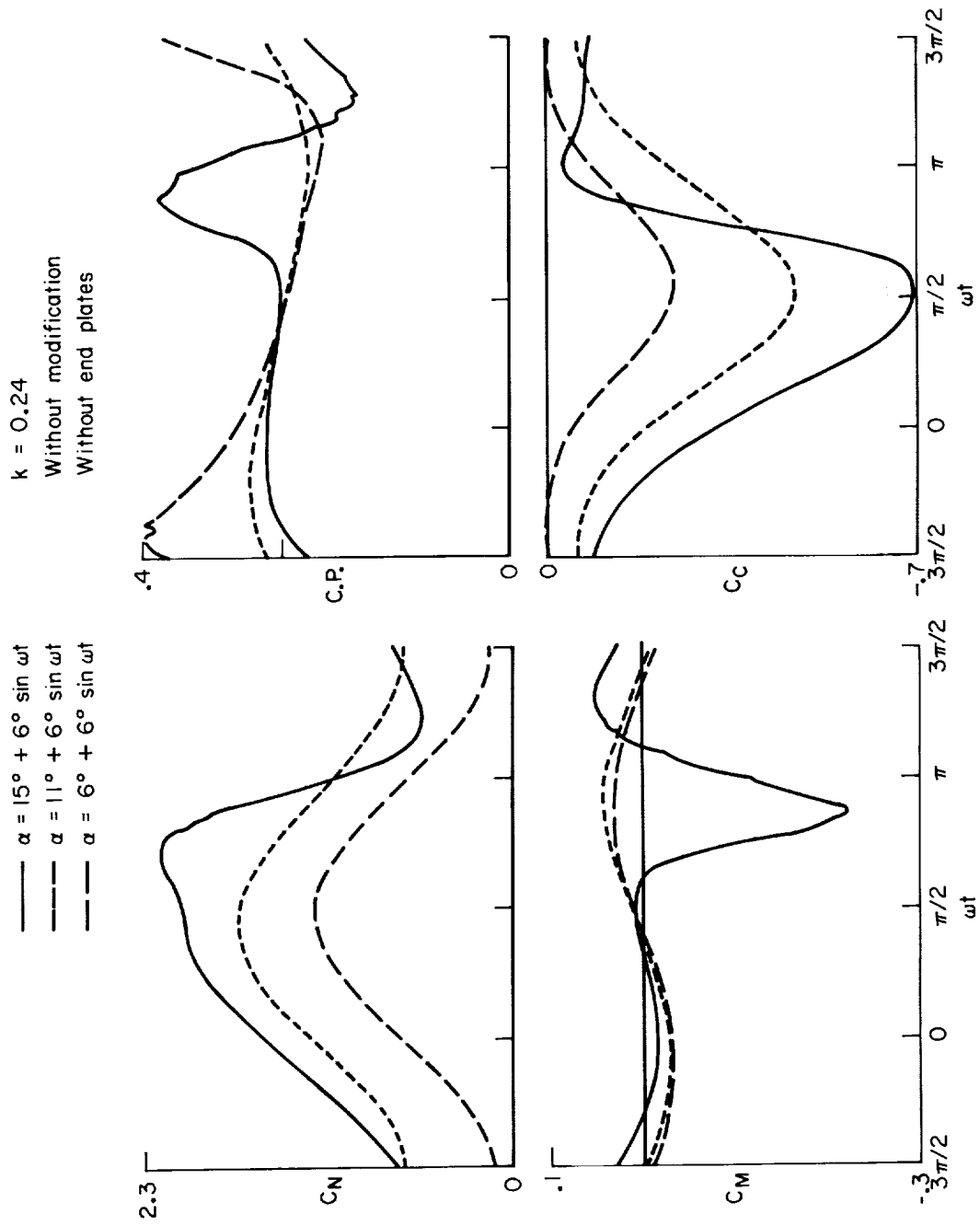
(b) Function of ωt .

Figure 33.— Concluded.



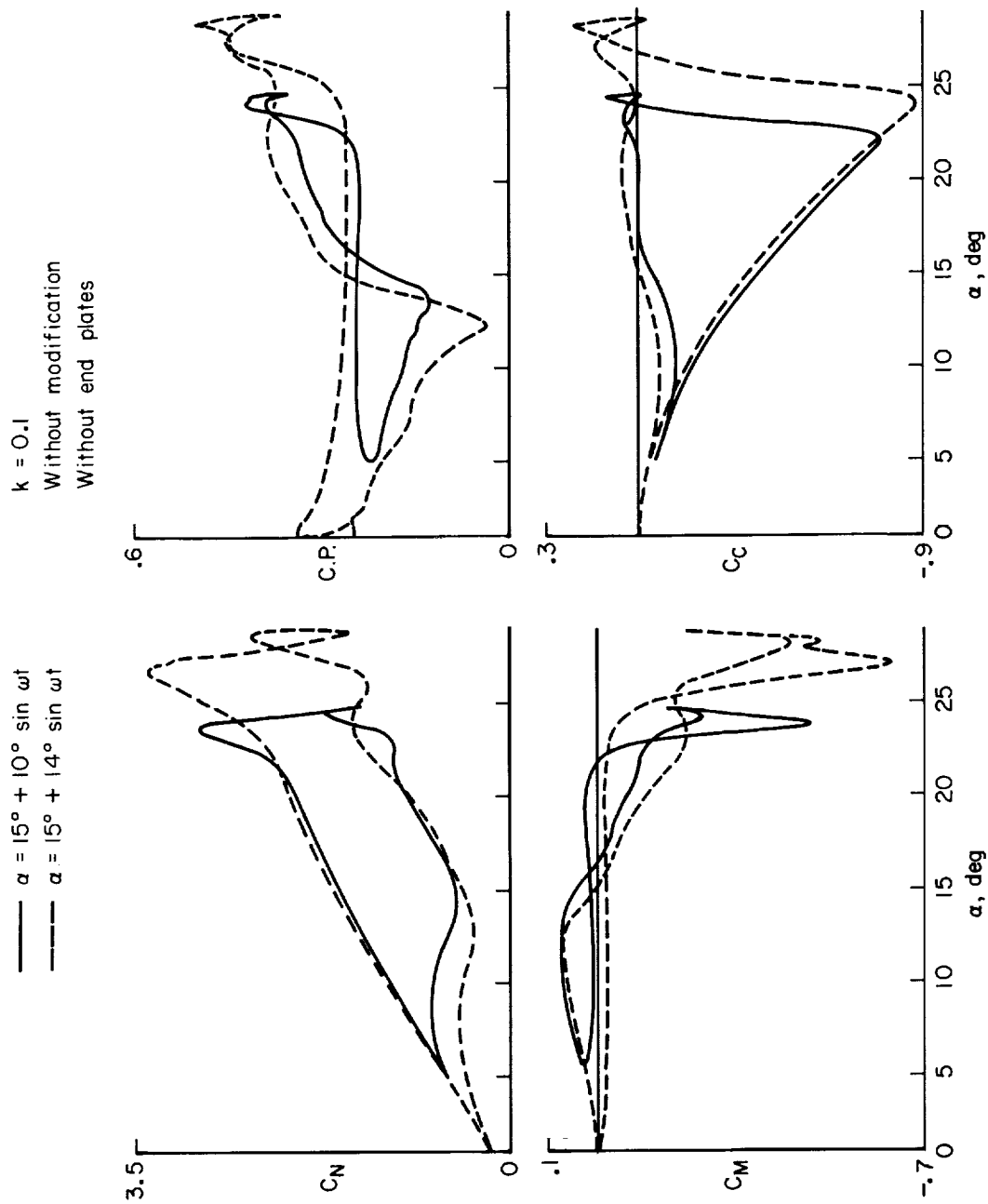
(a) Function of α .

Figure 34.— Effect of mean angle on integrated pressures without modification and without end plates.



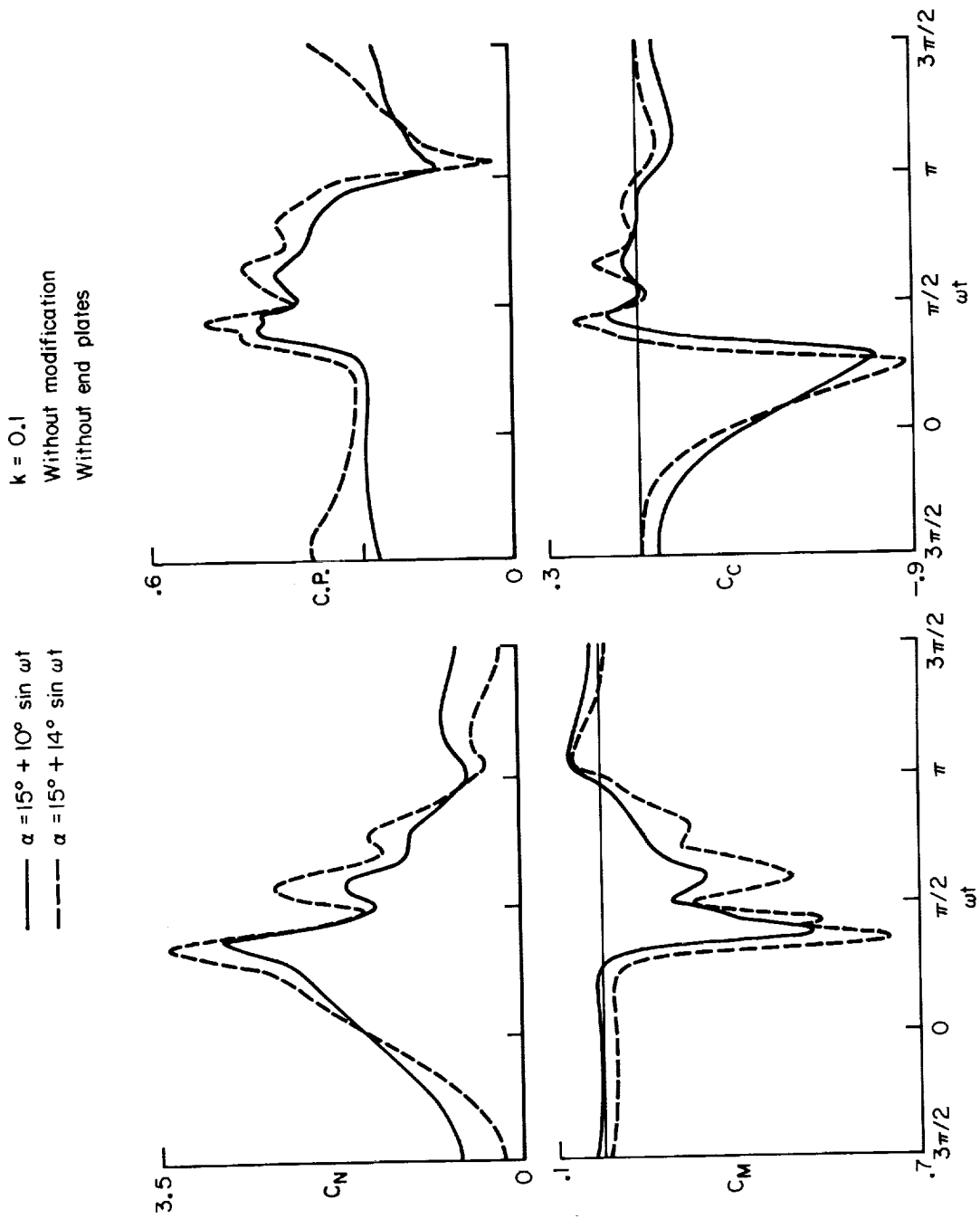
(b) Function of ωt .

Figure 34.— Concluded.



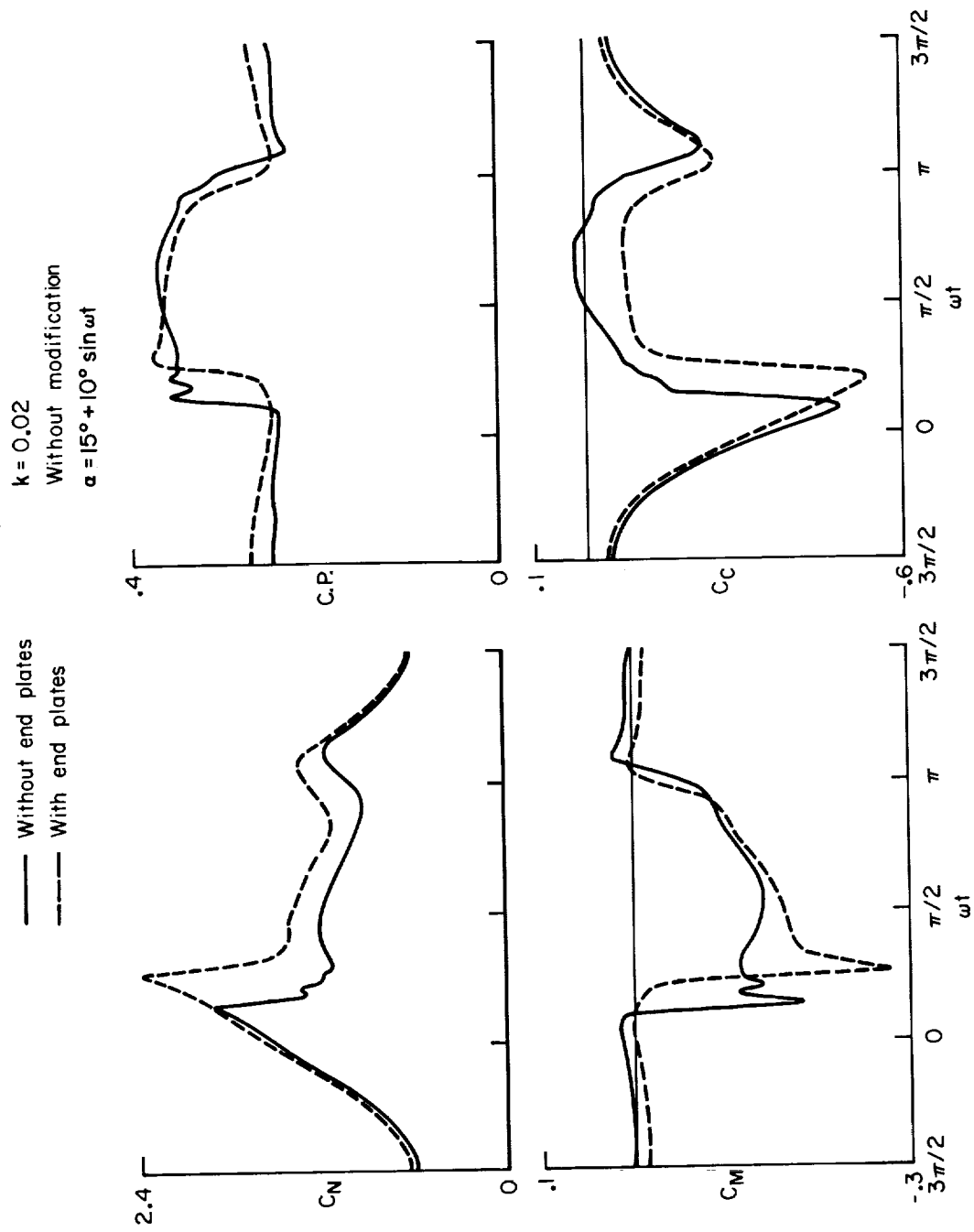
(a) Function of α .

Figure 35.— Effect of oscillation amplitude on integrated pressures without modification and without end plates.



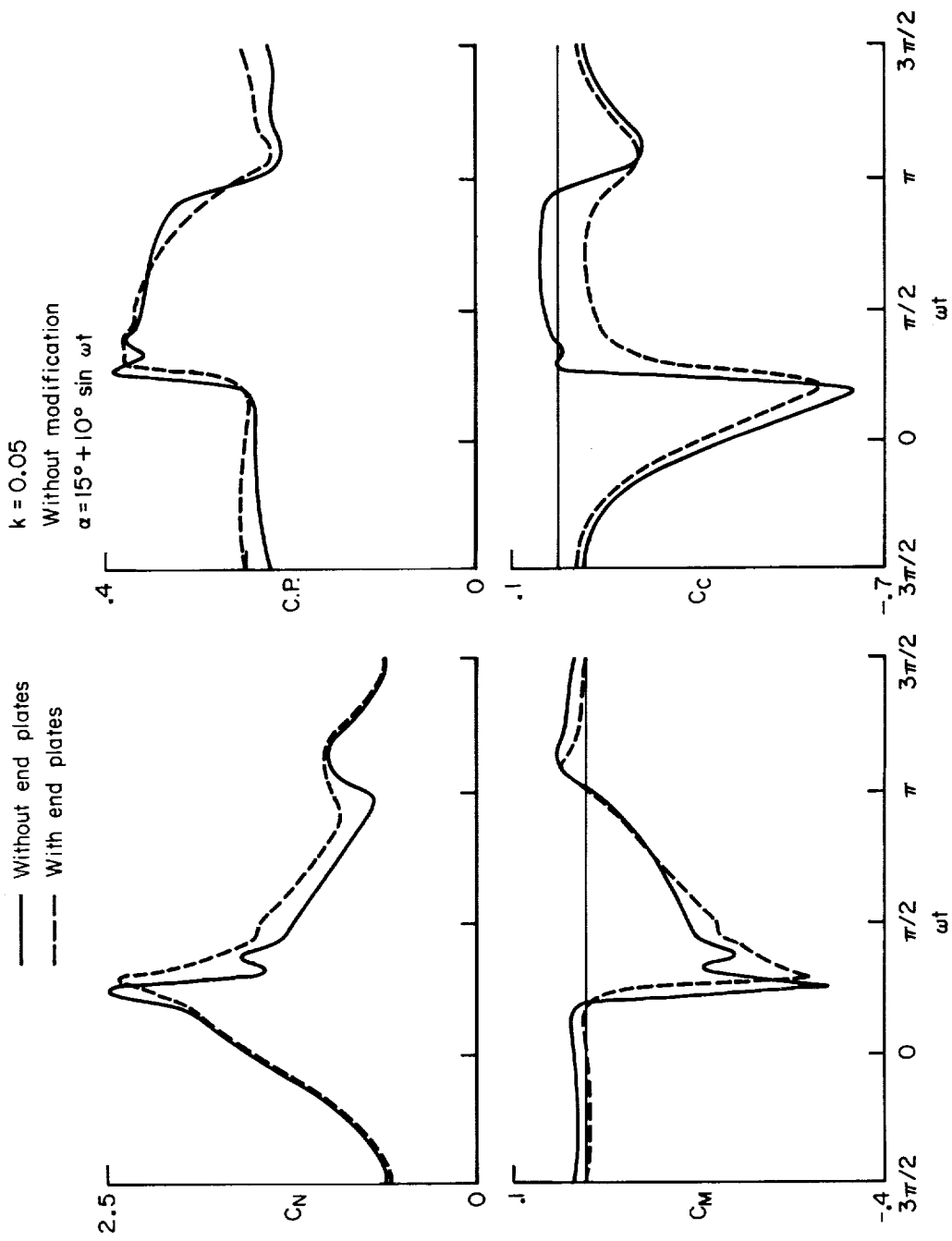
(b) Function of ωt .

Figure 35.— Concluded.



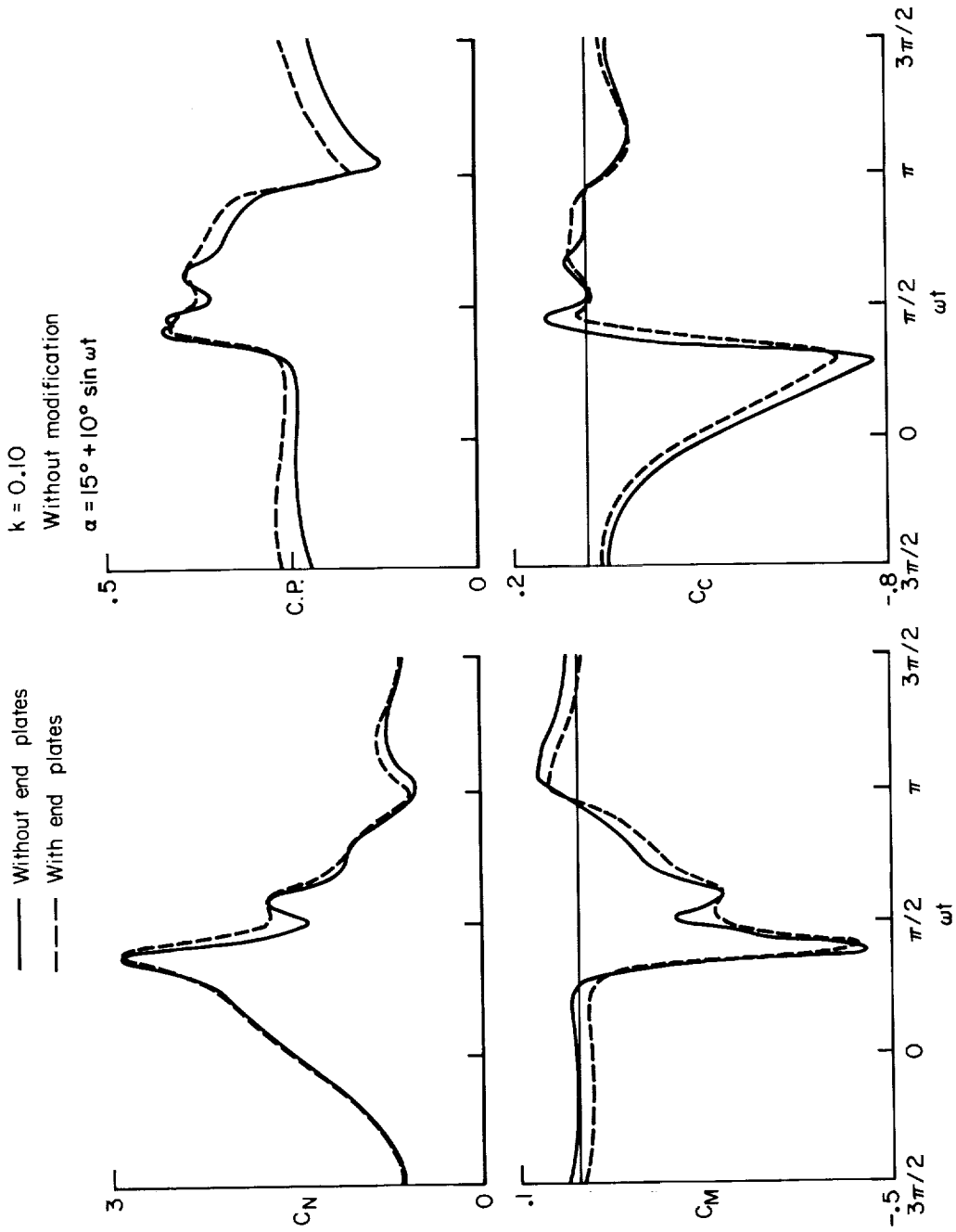
(a) $k = 0.02$.

Figure 36.— Effect of end plate on integrated pressures without airfoil modification.



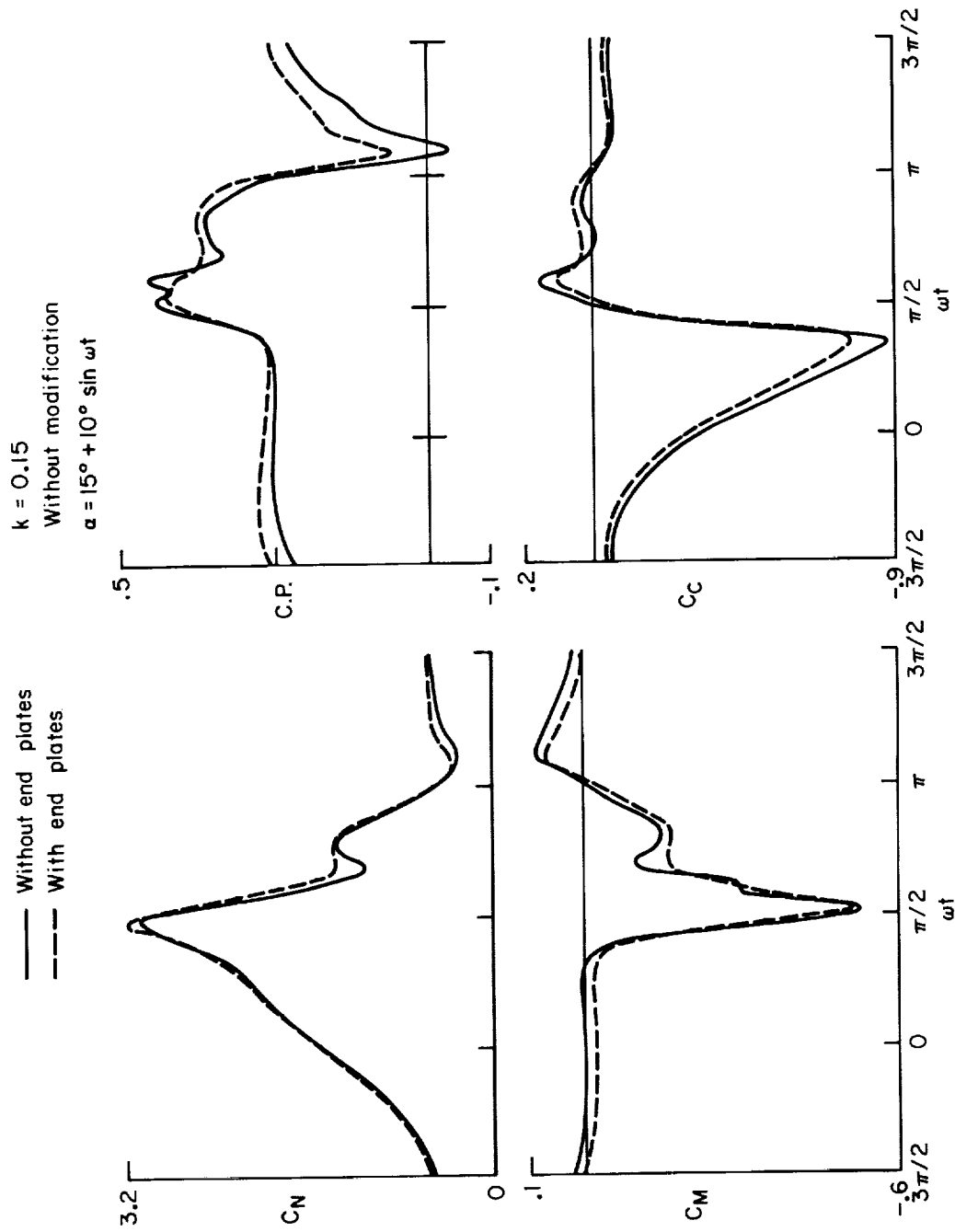
(b) $k = 0.05$.

Figure 36.— Continued.



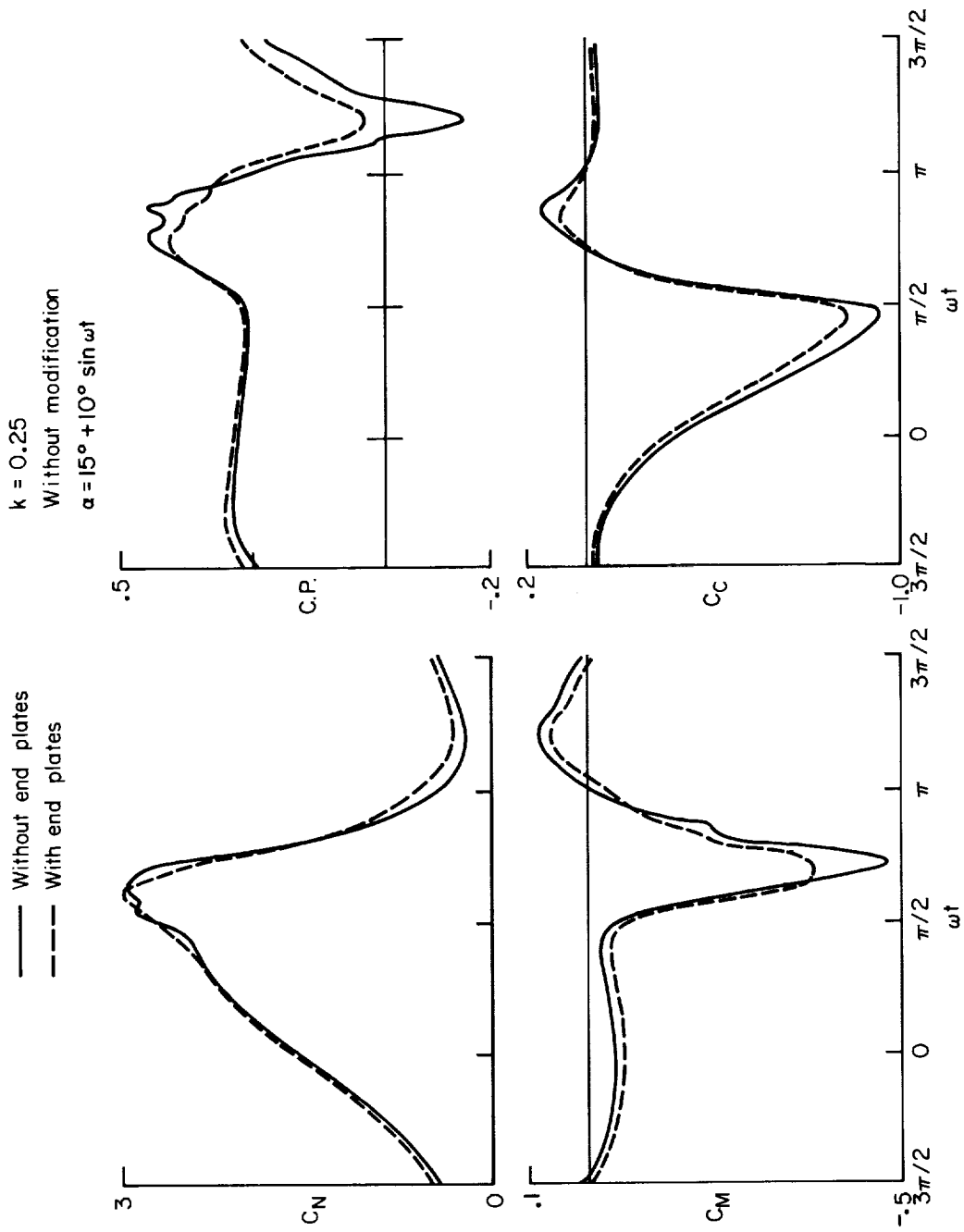
(c) $k = 0.10$.

Figure 36.-- Continued.



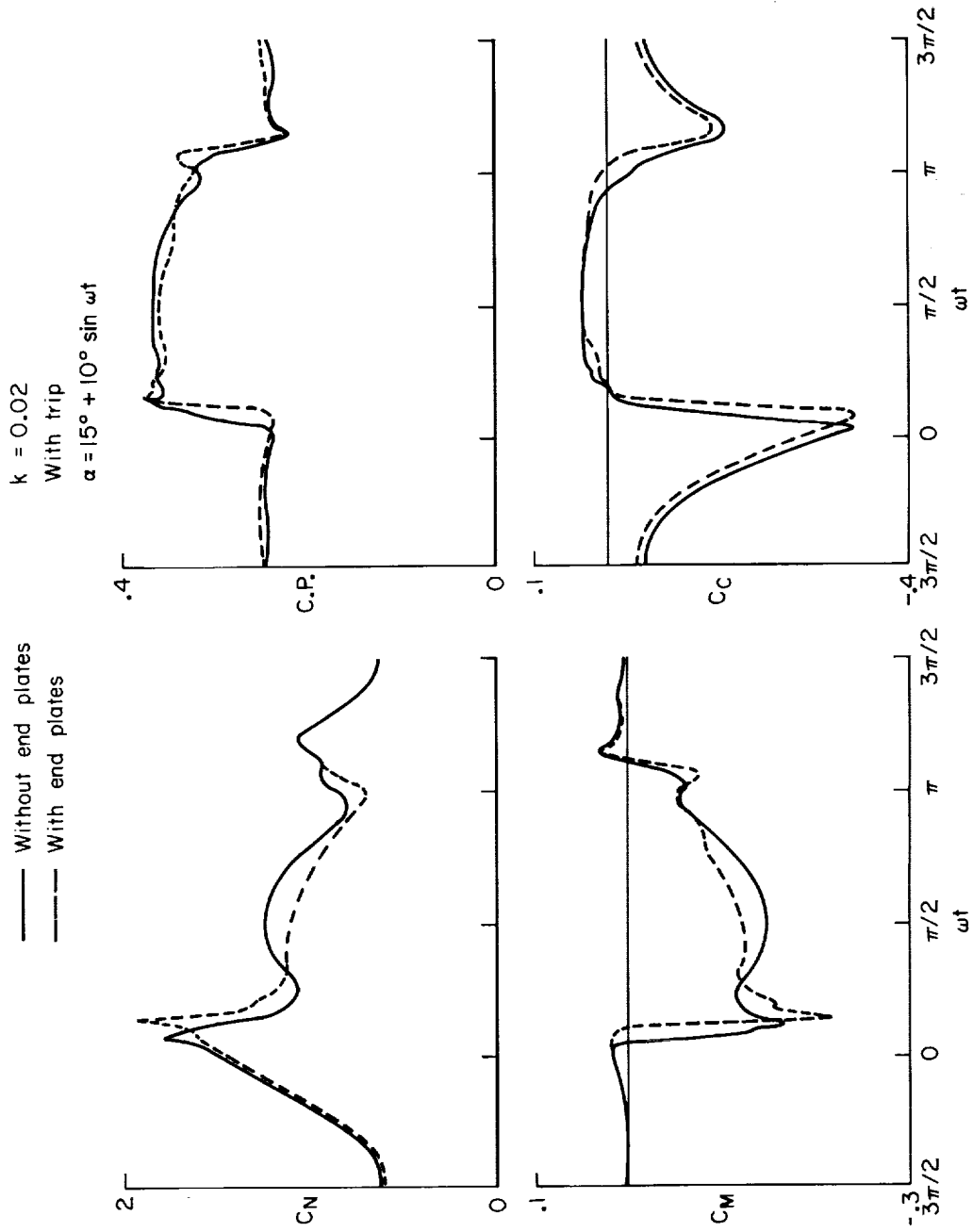
(d) $k = 0.15$.

Figure 36. — Continued.



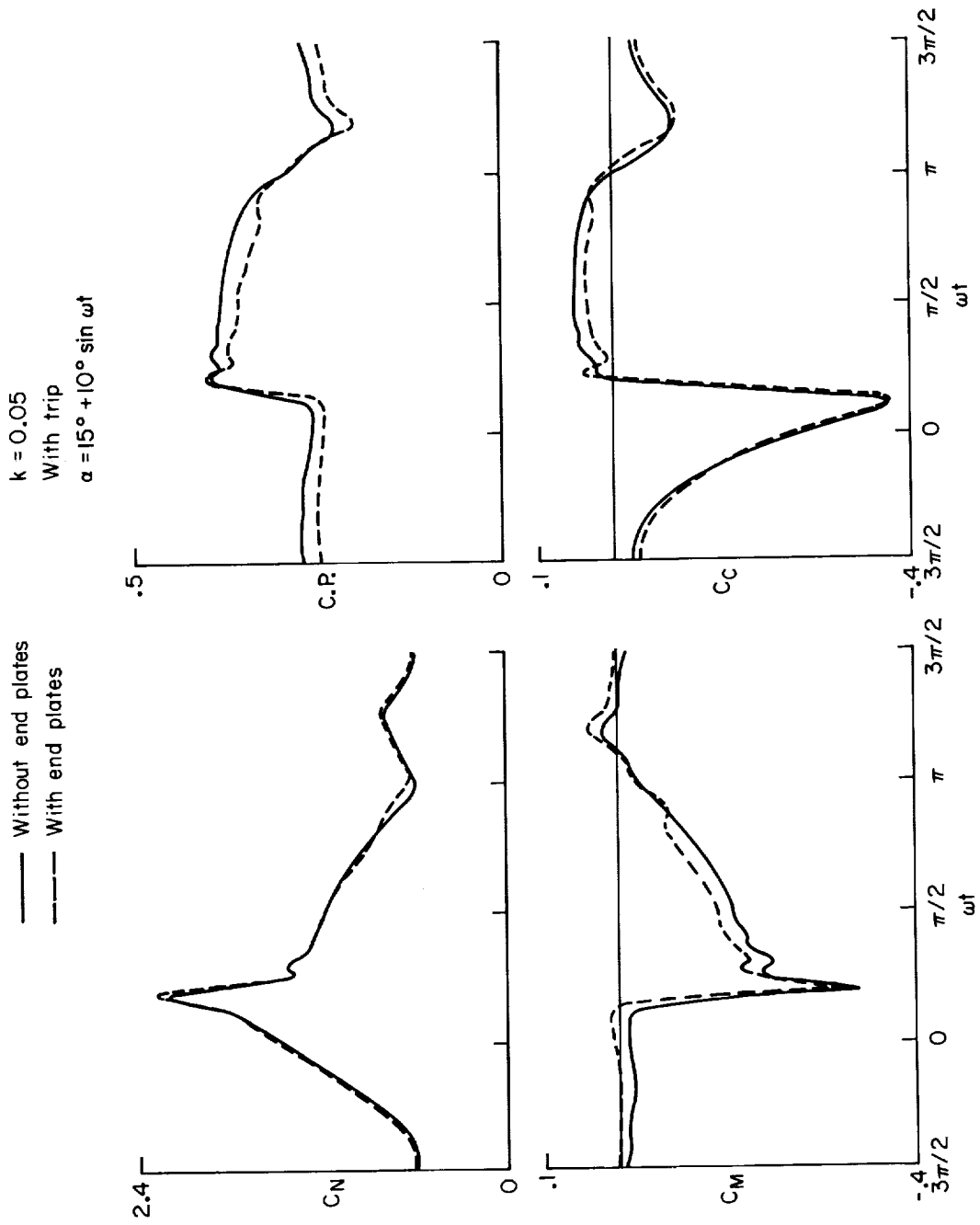
(e) $k = 0.25$.

Figure 36.— Concluded.



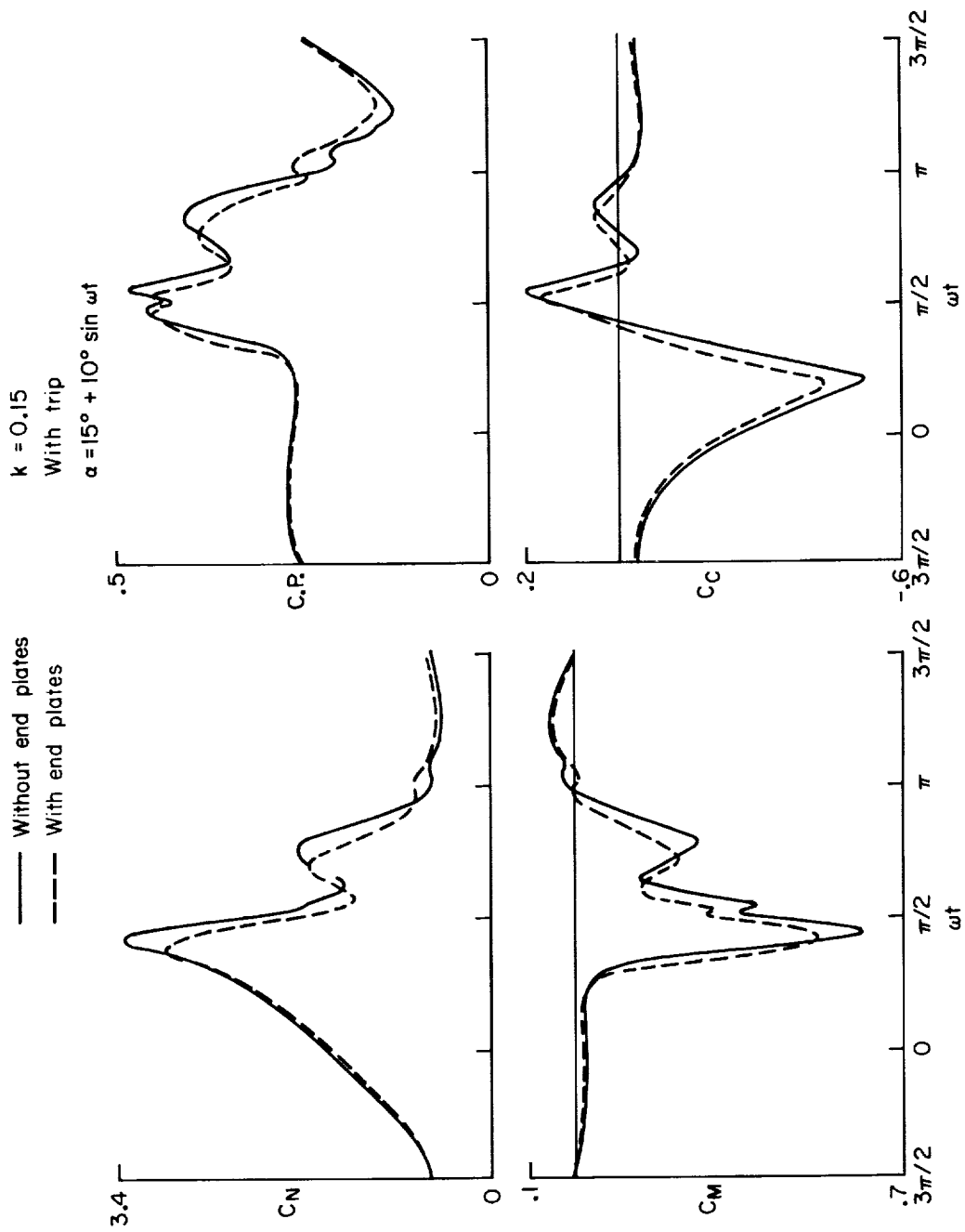
(a) $k = 0.02$.

Figure 37.— Effect of end plates on integrated pressures with trip.



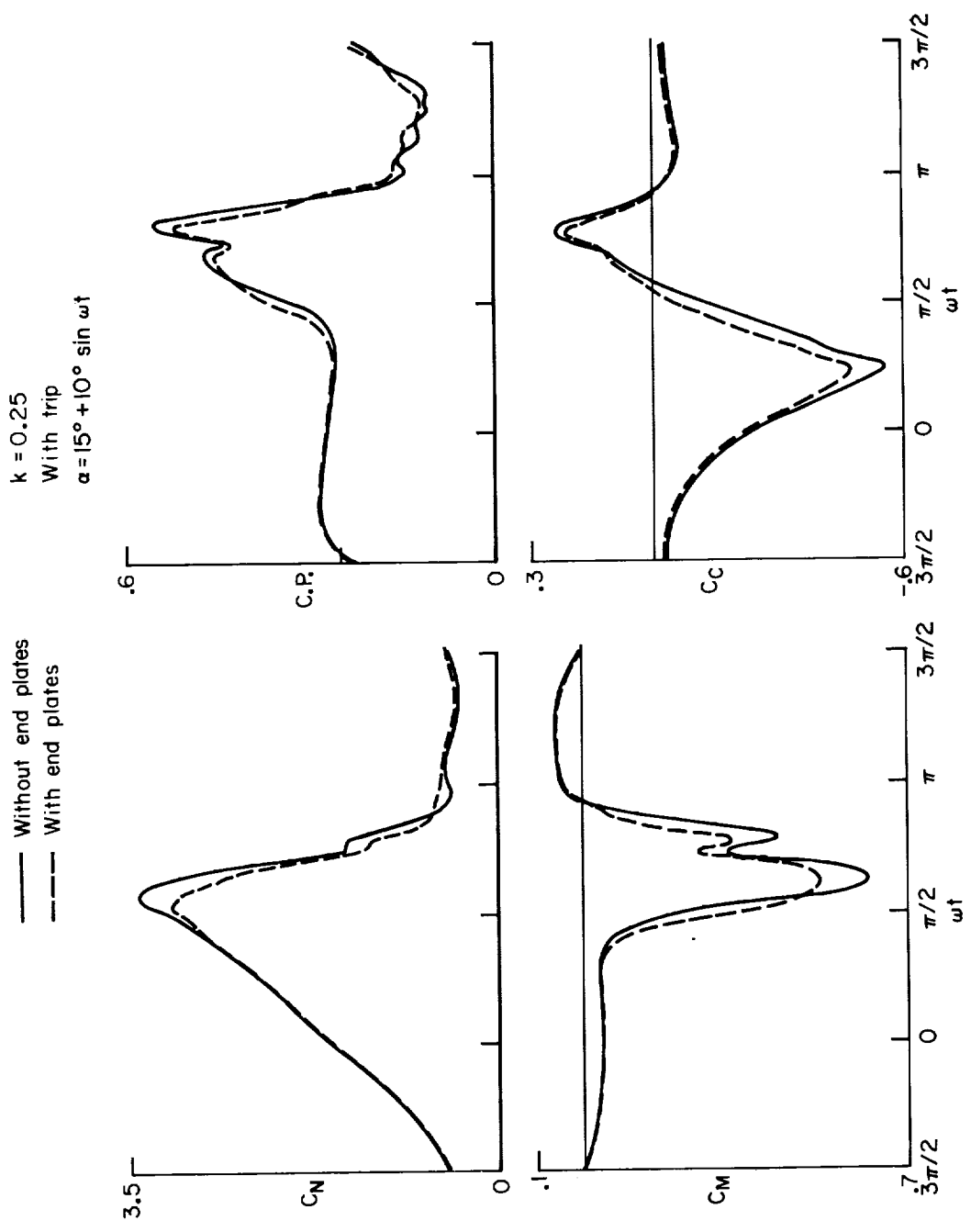
(b) $k = 0.05$.

Figure 37.— Continued.



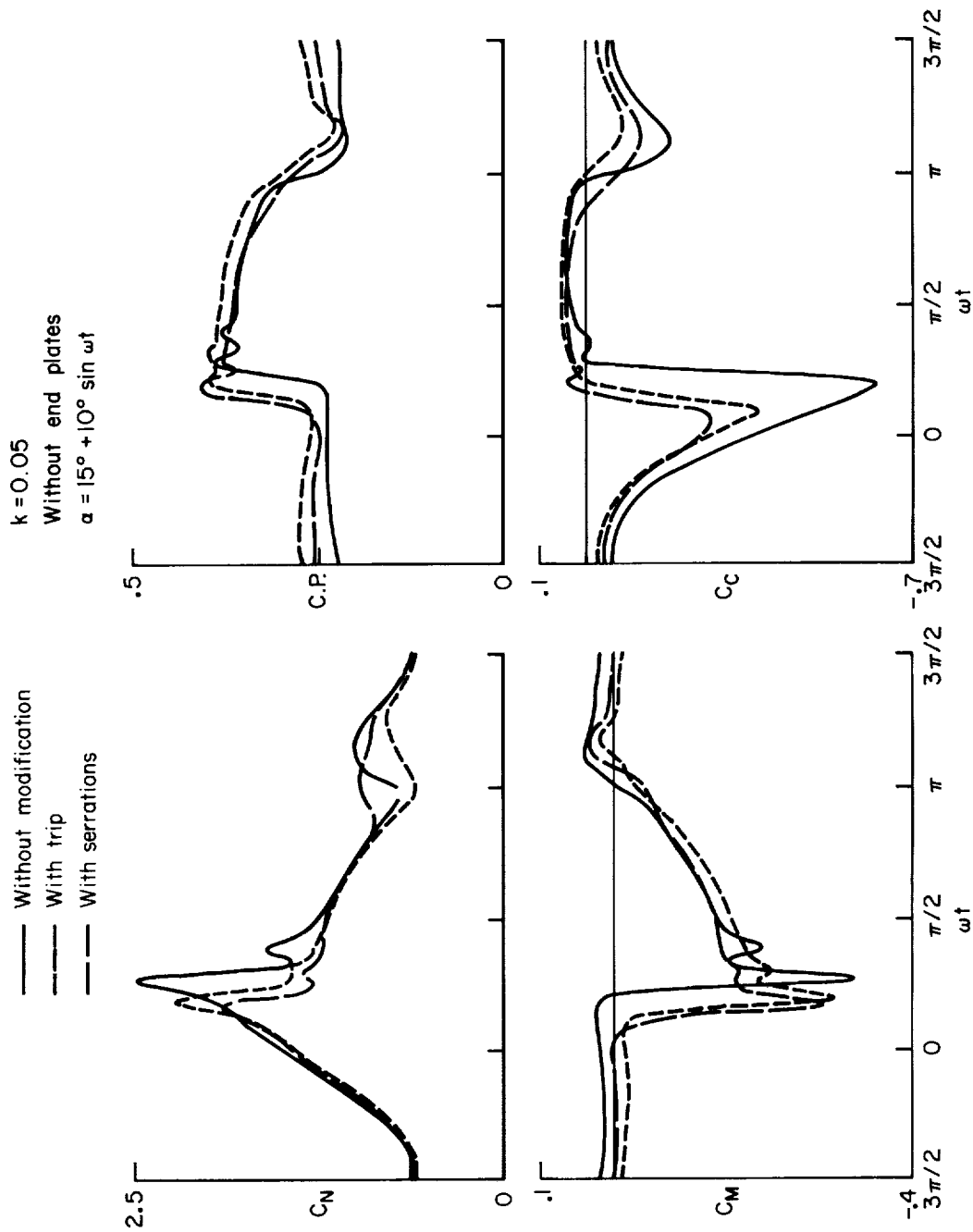
(c) $k = 0.15$.

Figure 37.— Continued.



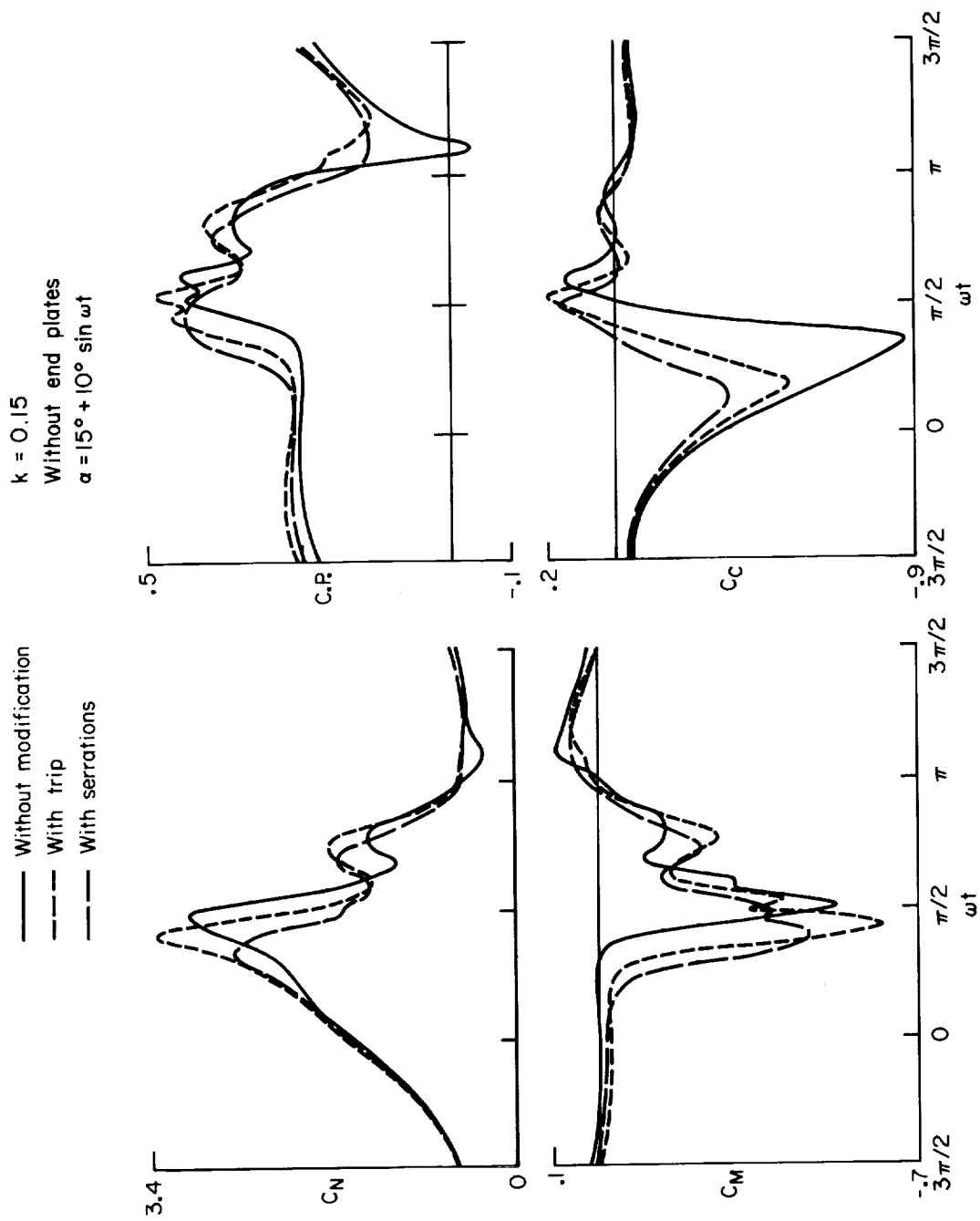
(d) $k = 0.25$.

Figure 37.— Concluded.



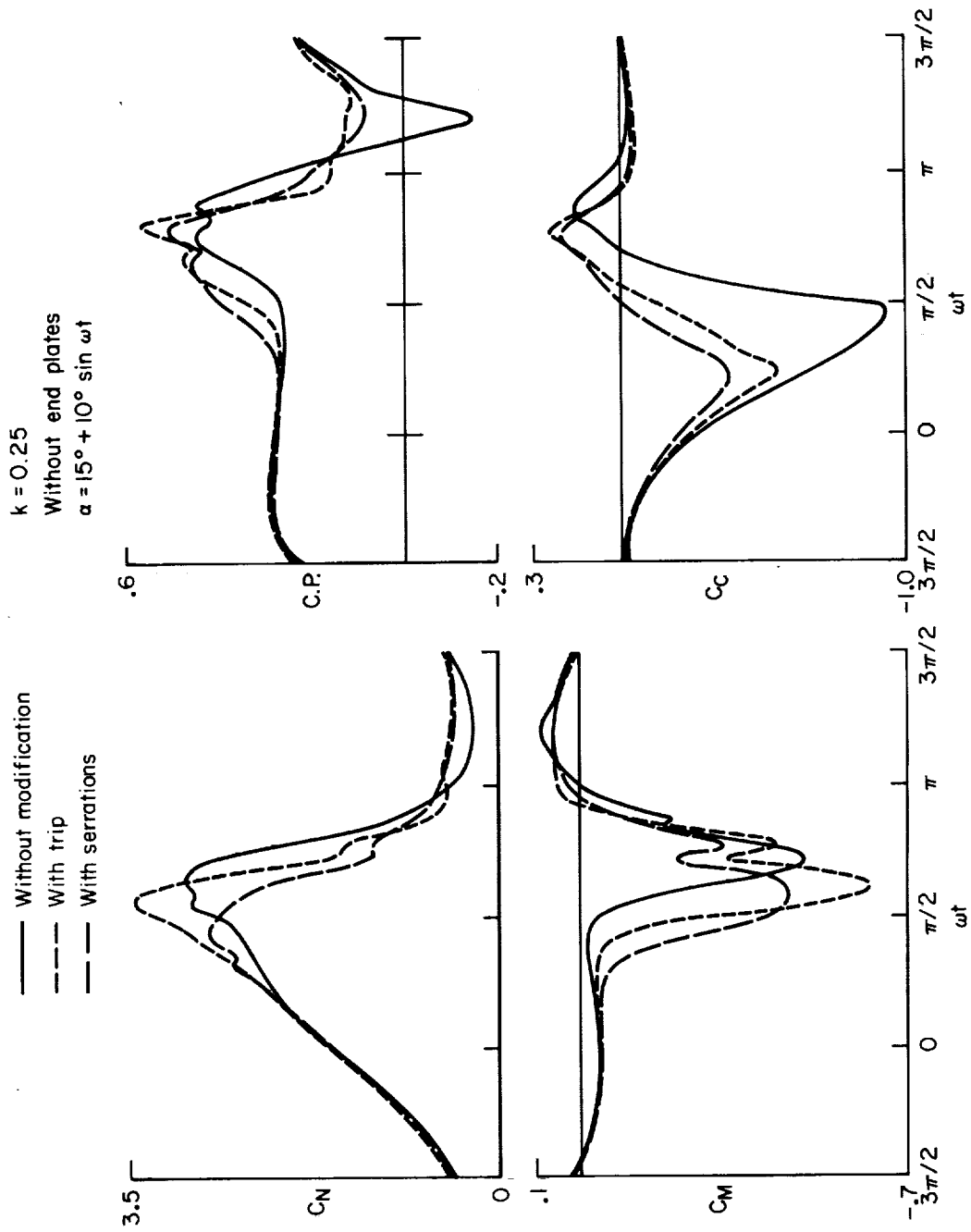
(a) $k = 0.05$.

Figure 38.— Effect of leading-edge modifications on integrated pressures without airfoil end plates.



(b) $k = 0.15$.

Figure 38.— Continued.



(c) $k = 0.25$.

Figure 38.— Concluded.

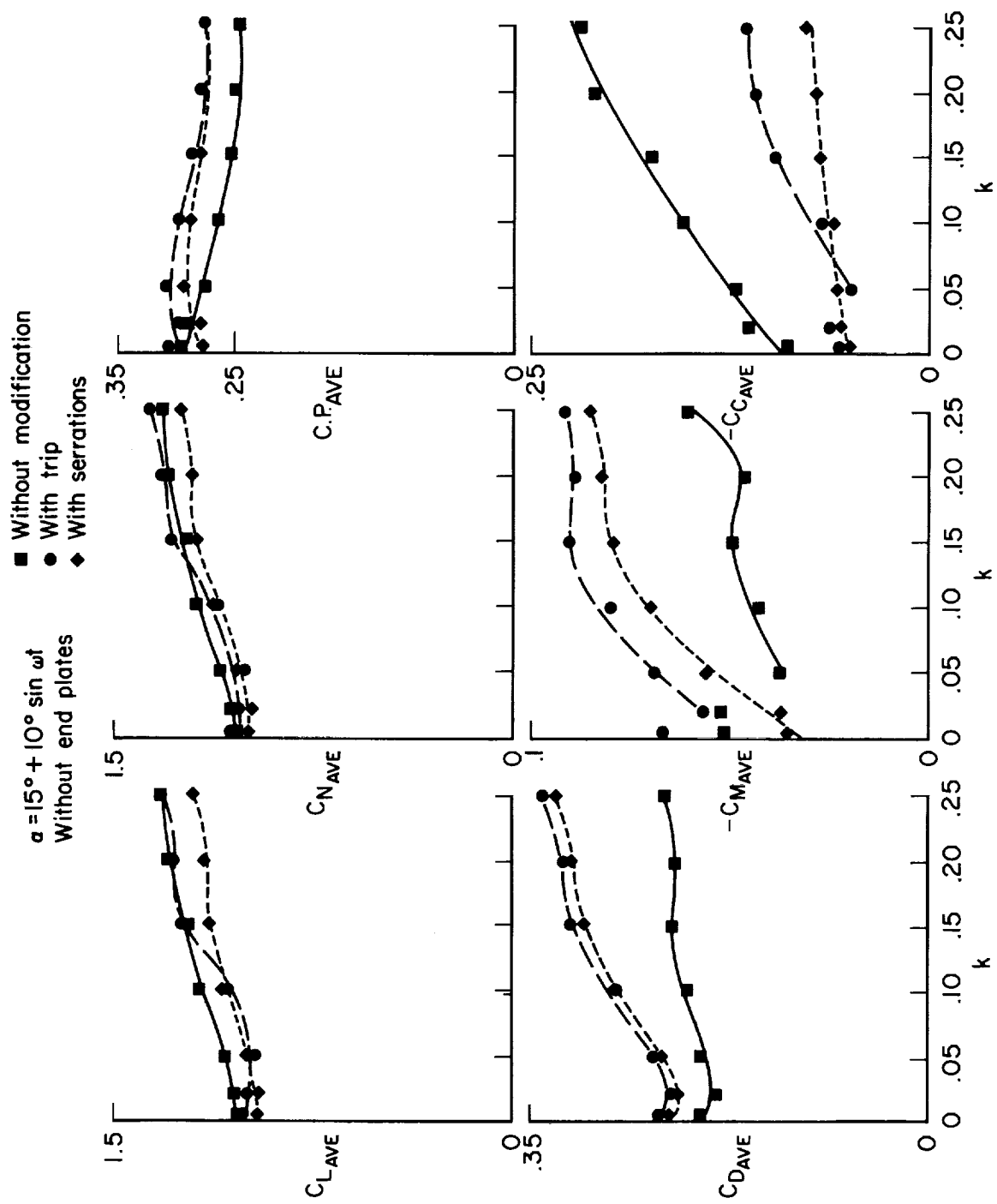


Figure 39.— Effect of leading-edge modifications on integrated pressure averages; without end plates.

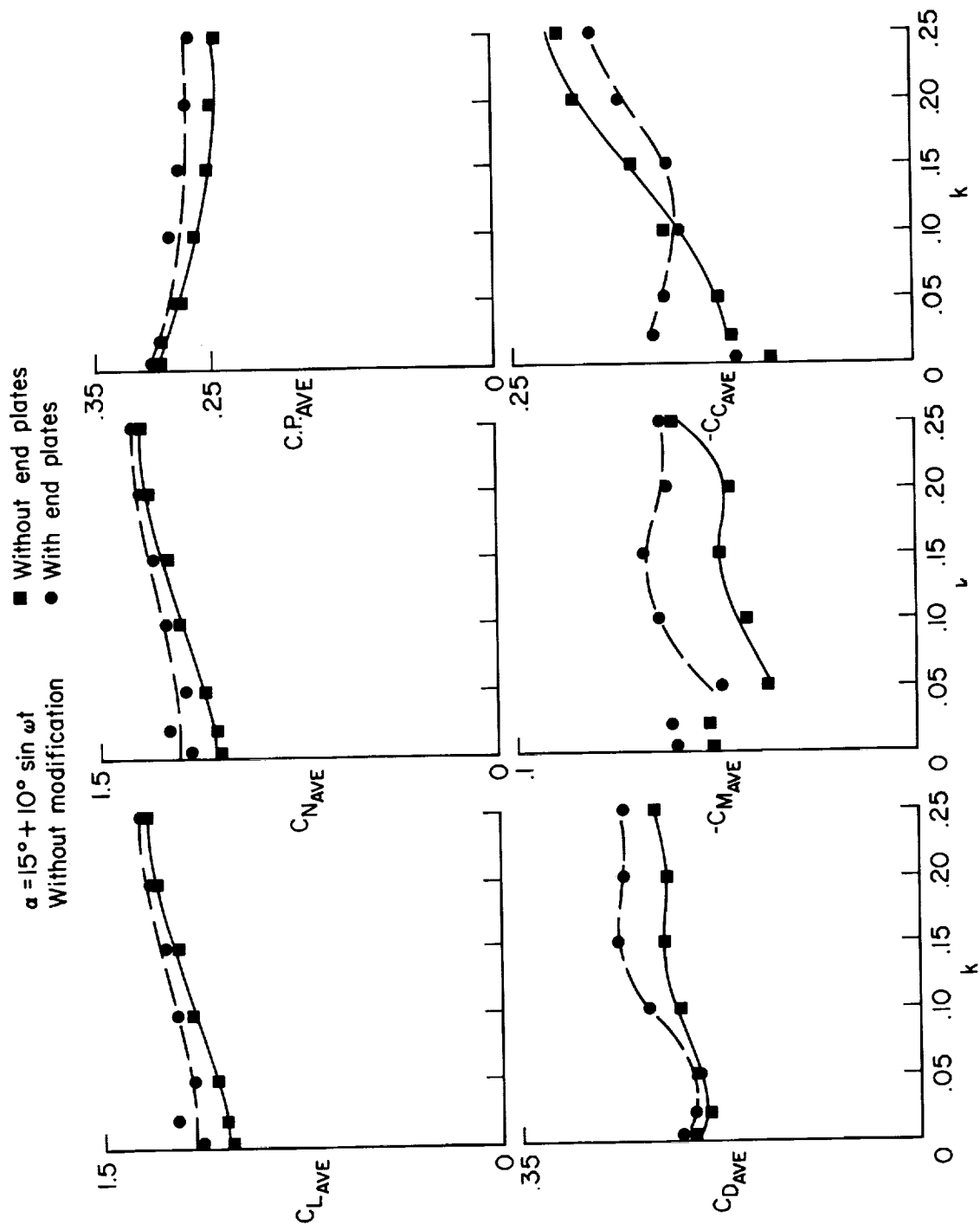


Figure 40.— Effect of end plates on integrated pressure averages; without airfoil modifications.

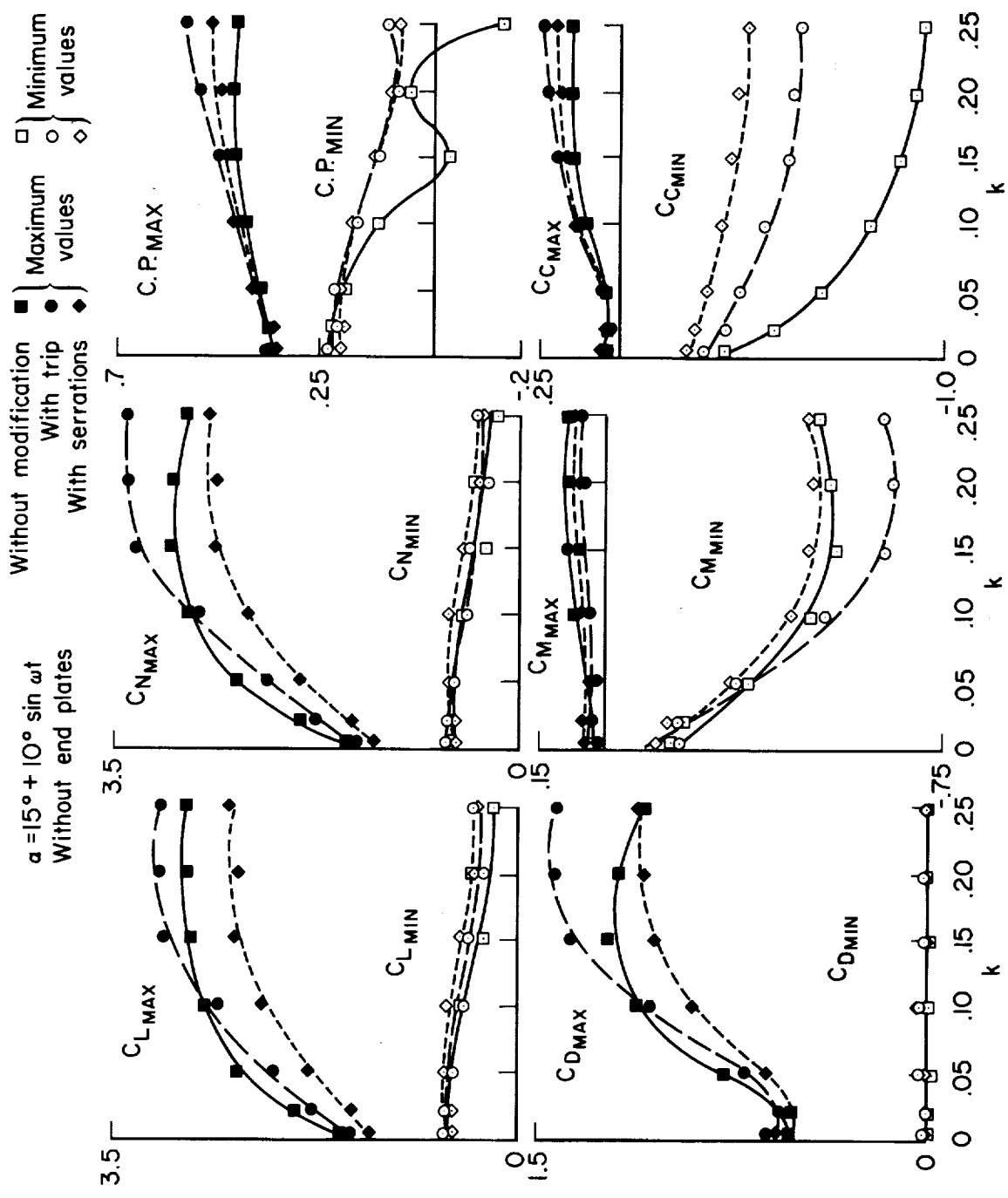


Figure 41.— Effect of leading-edge modifications on integrated pressure extrema; without end plates.

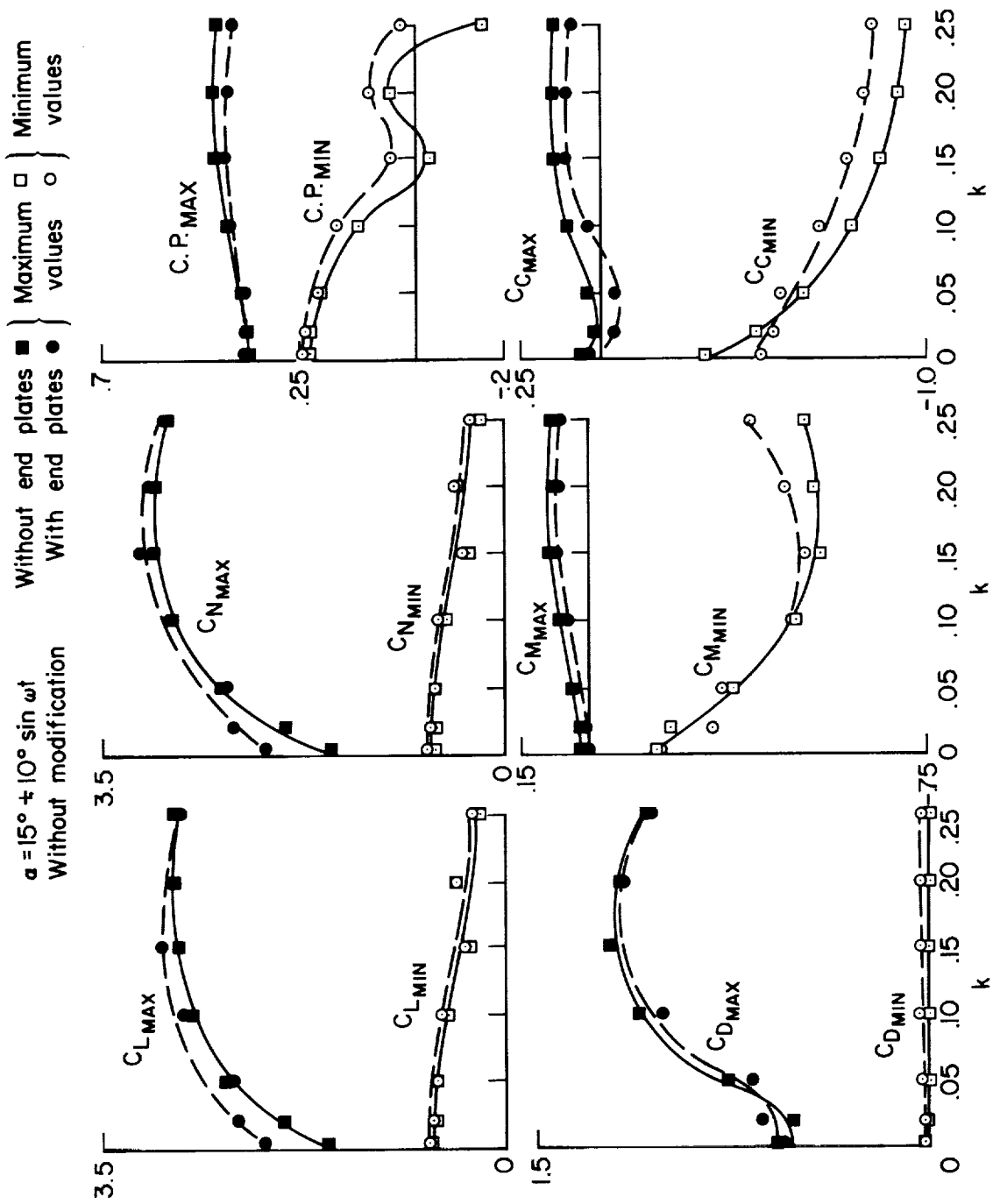


Figure 42.— Effect of end plates on integrated pressure extrema; without airfoil modification.

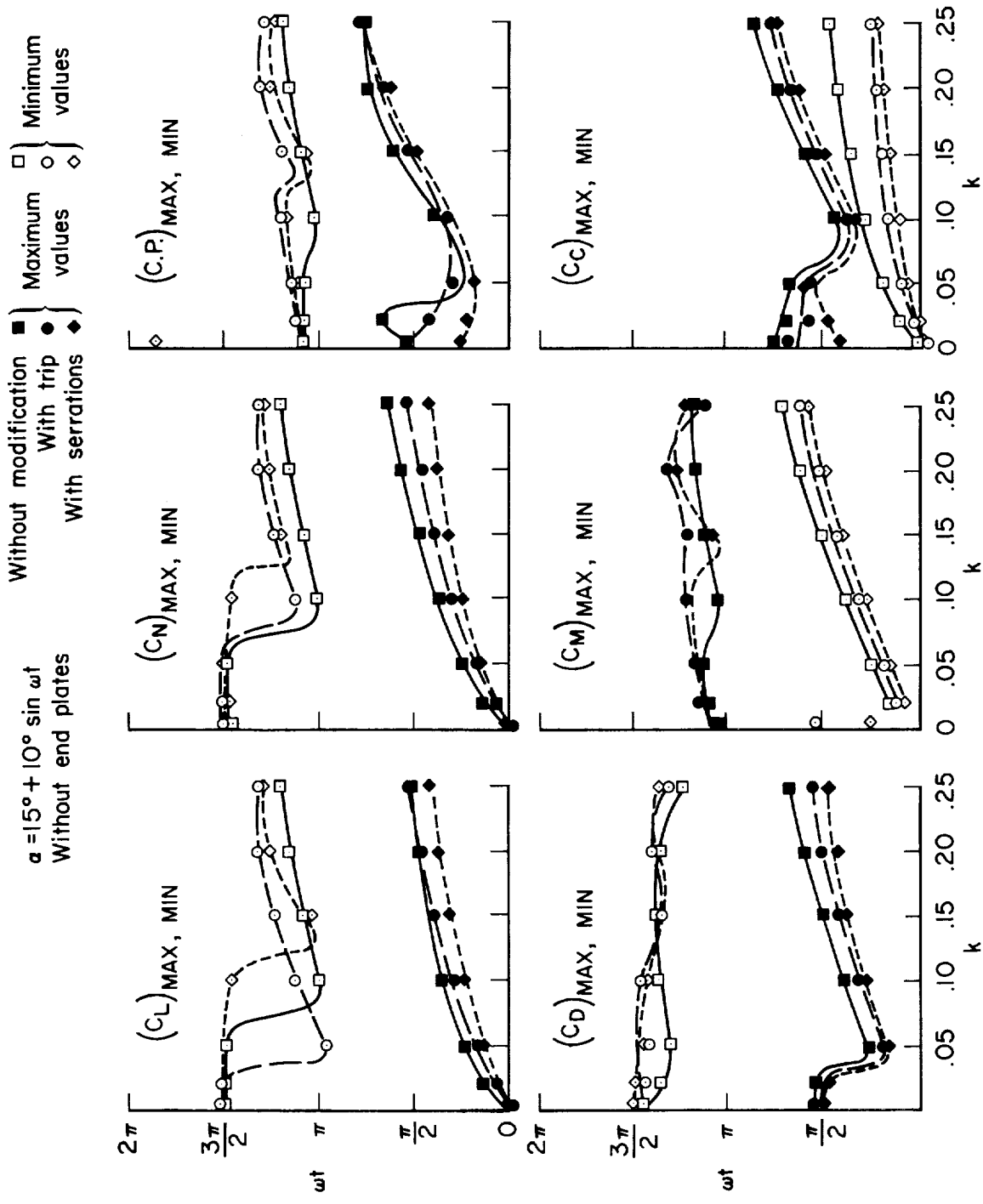


Figure 43.— Effect of leading-edge modifications on extremum phase angles; without end plates.

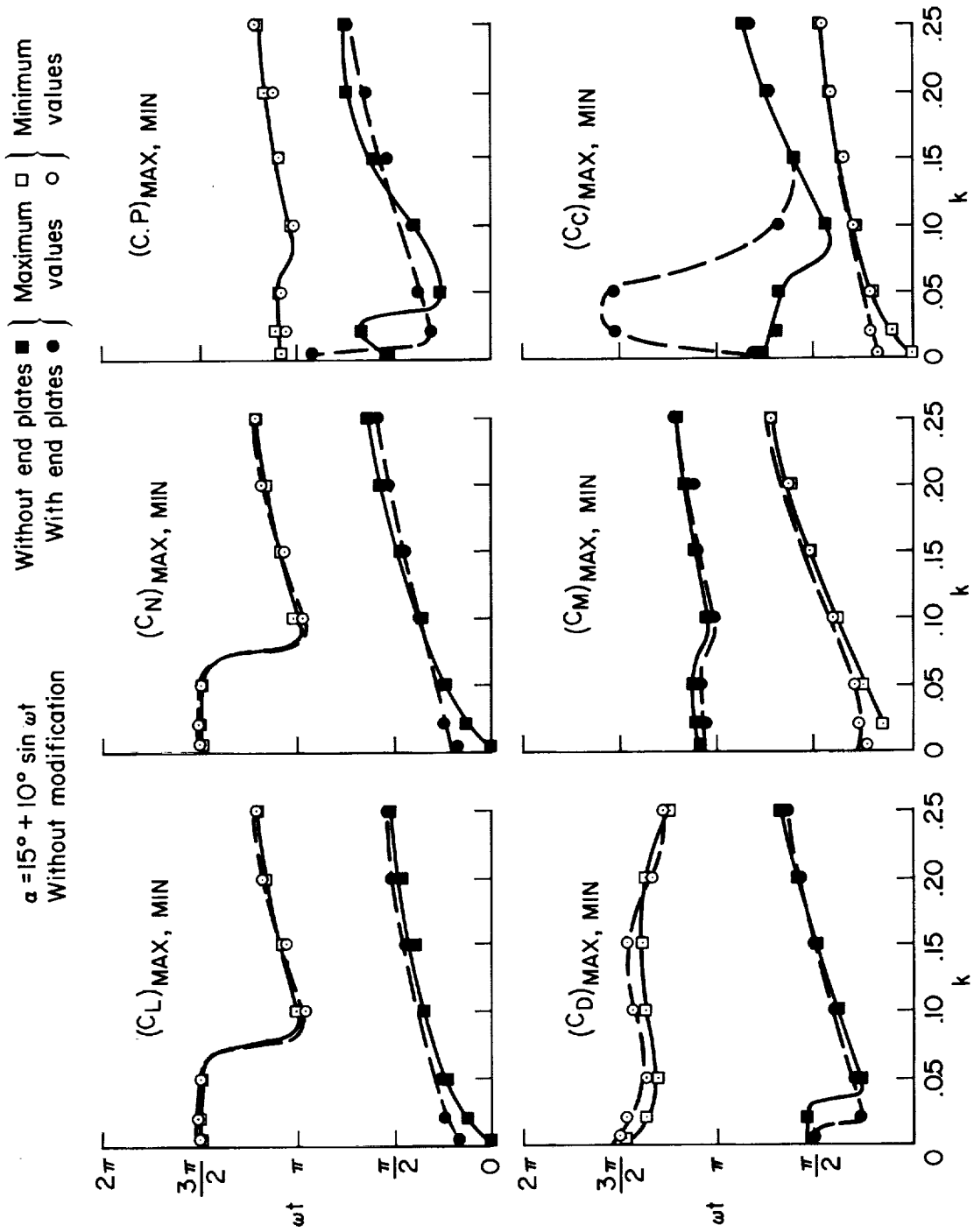


Figure 44.— Effect of end plates on extremum phase angles; without airfoil modification.

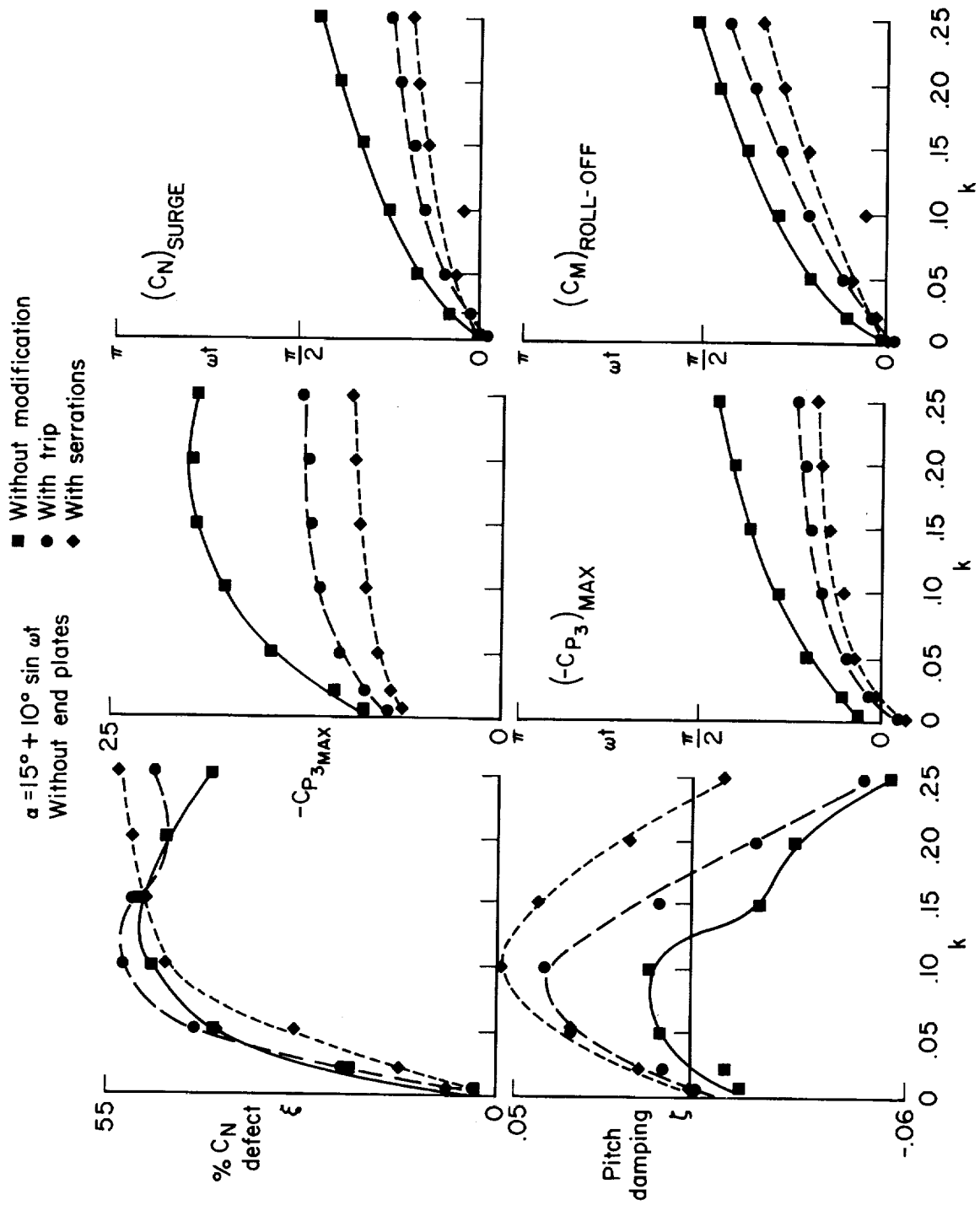


Figure 45.— Effect of leading-edge modifications on moment stall indicators; without end plates.

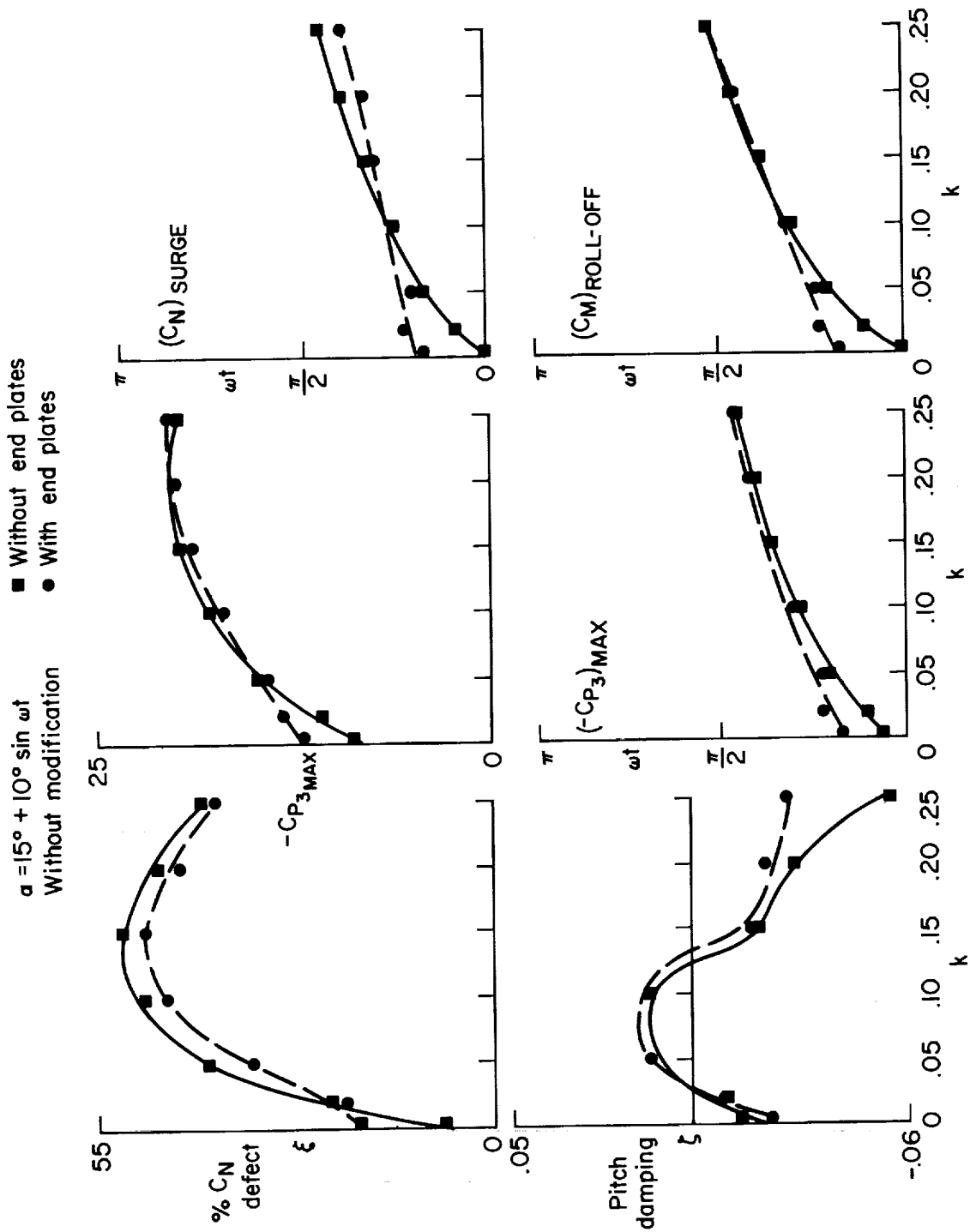


Figure 46.— Effect of end plates on moment stall indicators; without airfoil modification.

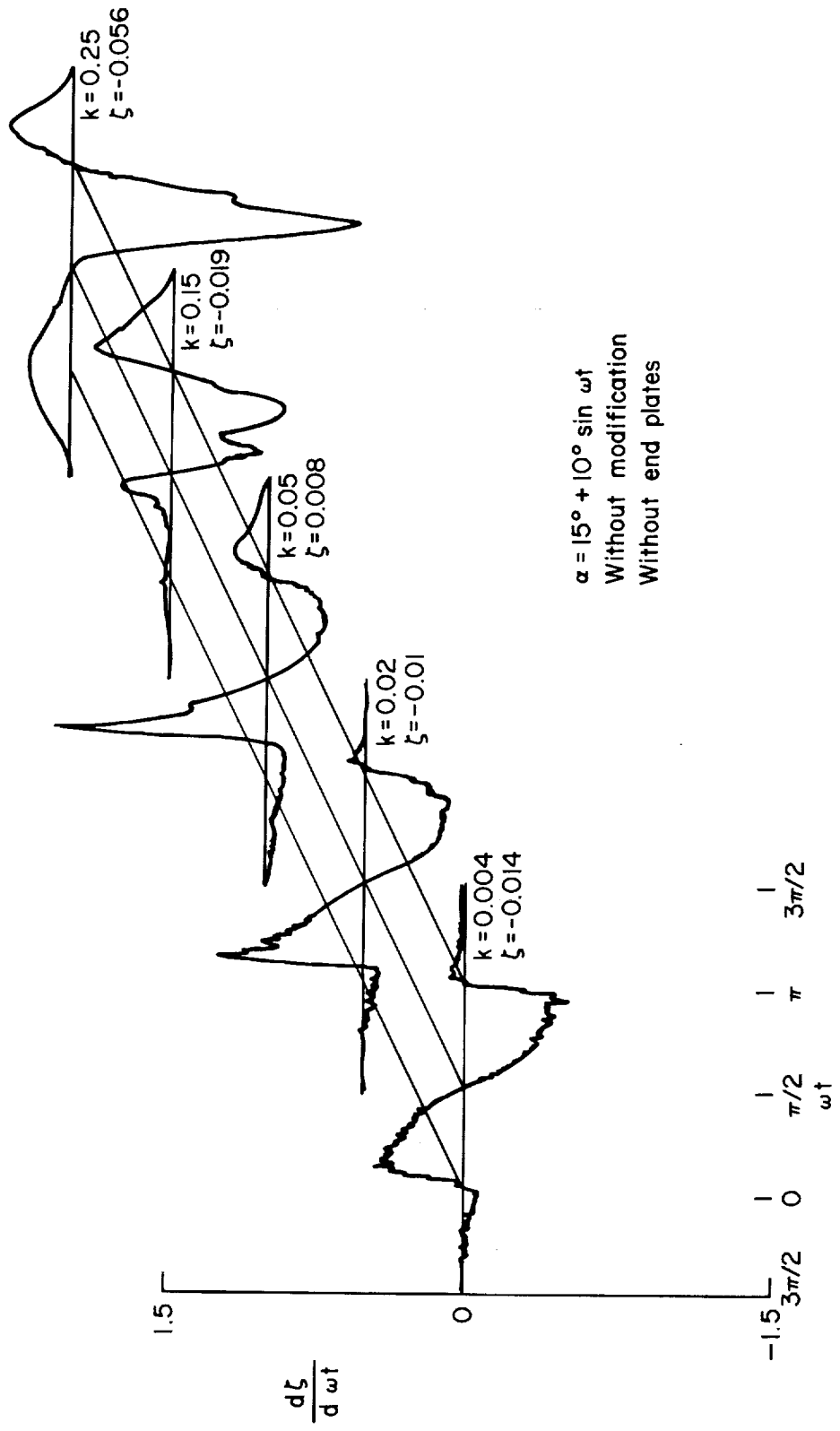
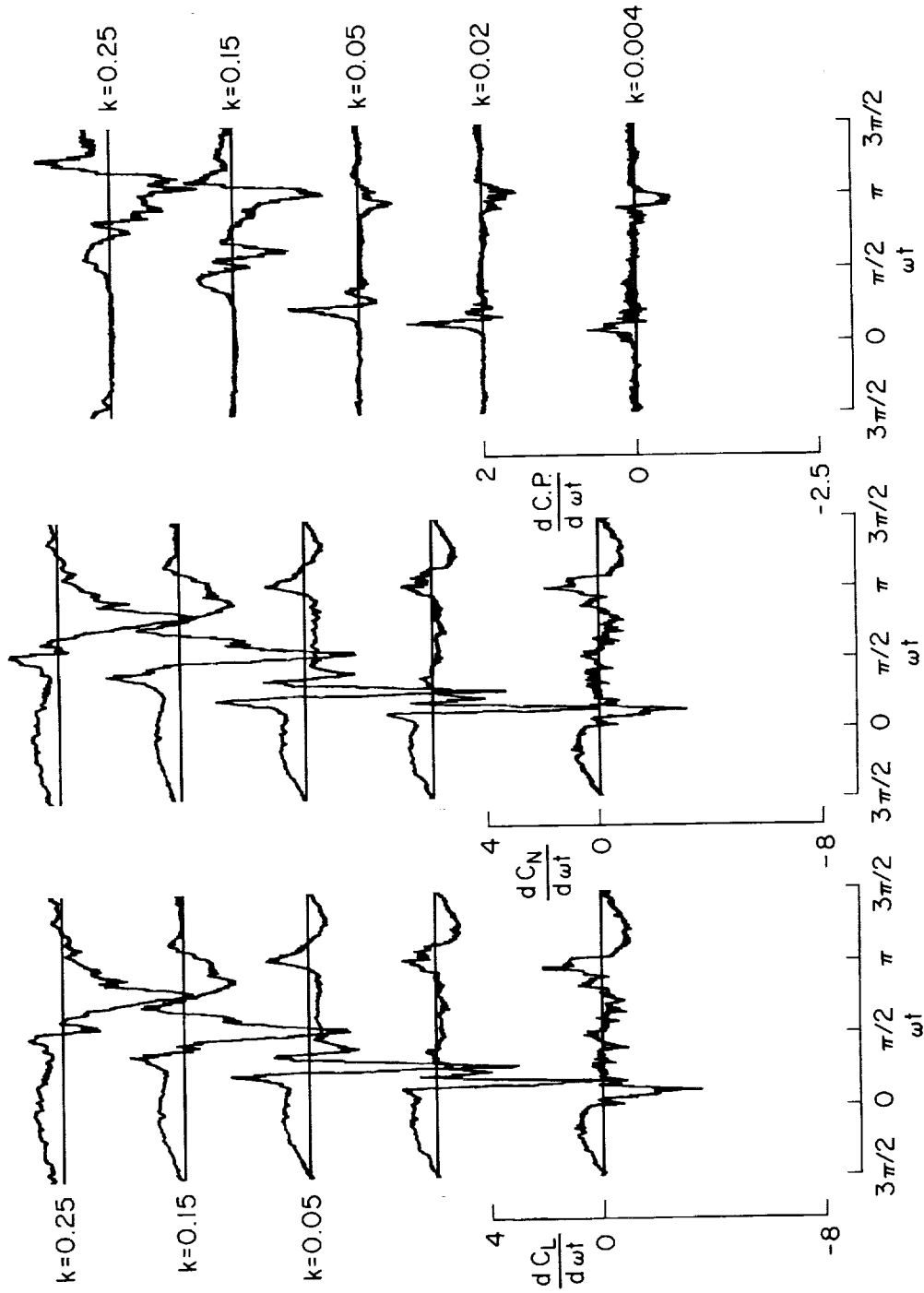


Figure 47.— Effect of reduced frequency on the azimuthal contributions to the pitch damping integral.

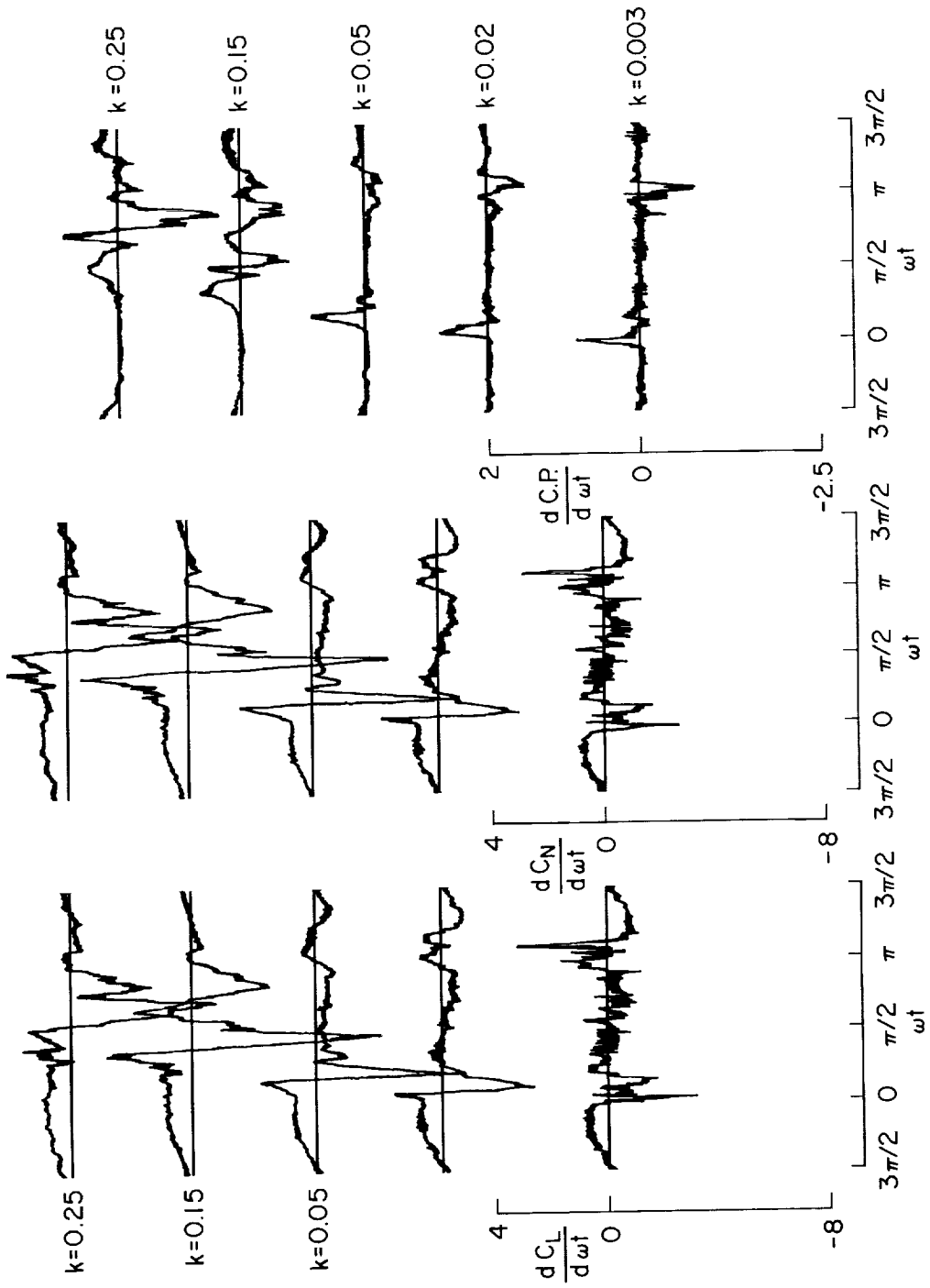
$\alpha = 15^\circ + 10^\circ \sin \omega t$
 Without modification
 Without end plates



(a) Without modification and without end plates.

Figure 48.— Azimuthal rate of change of lift, normal force, and center of pressure.

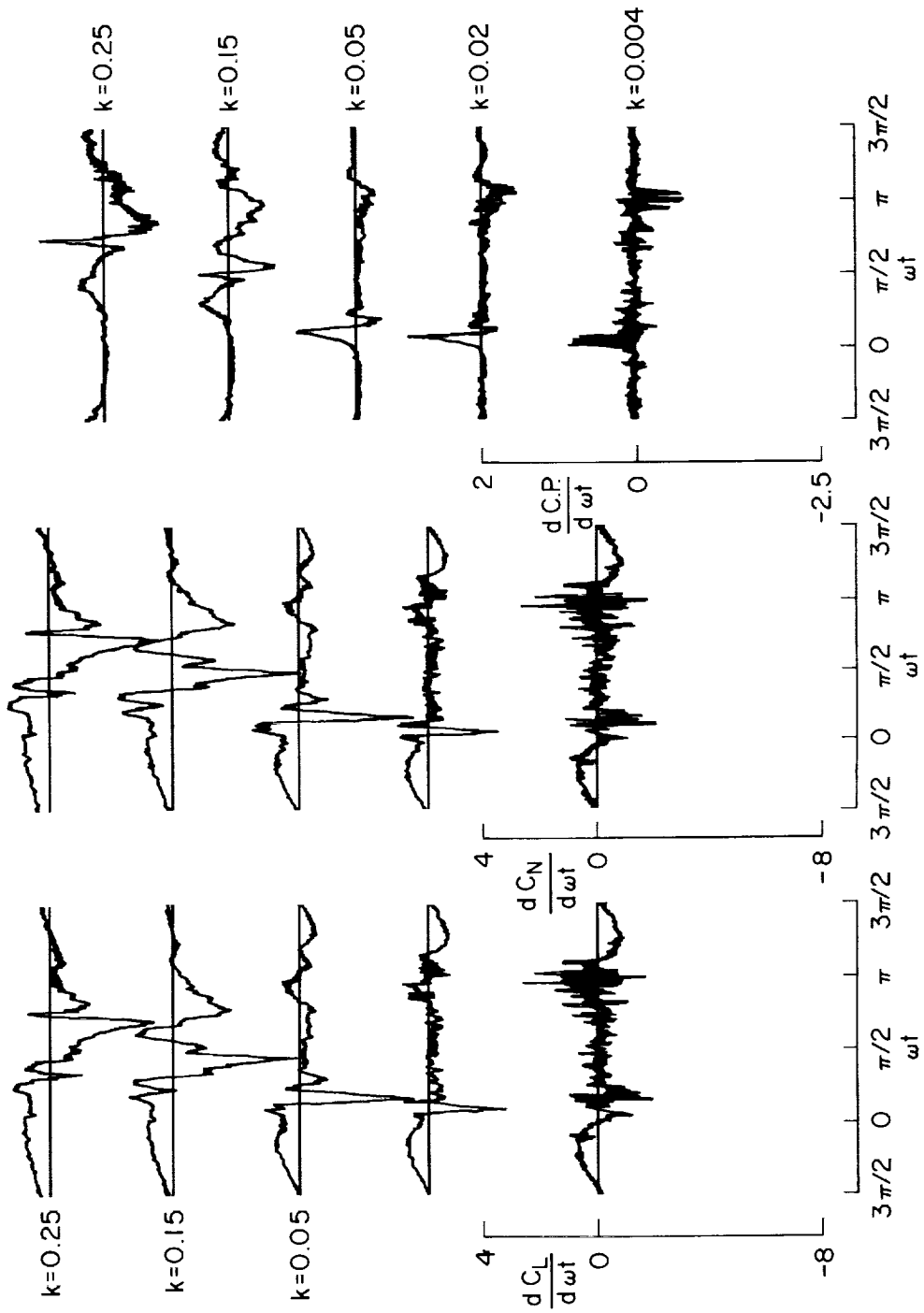
$\alpha = 15^\circ + 10^\circ \sin \omega t$
 With trip
 Without end plates



(b) With trip and without end plates.

Figure 48.— Continued.

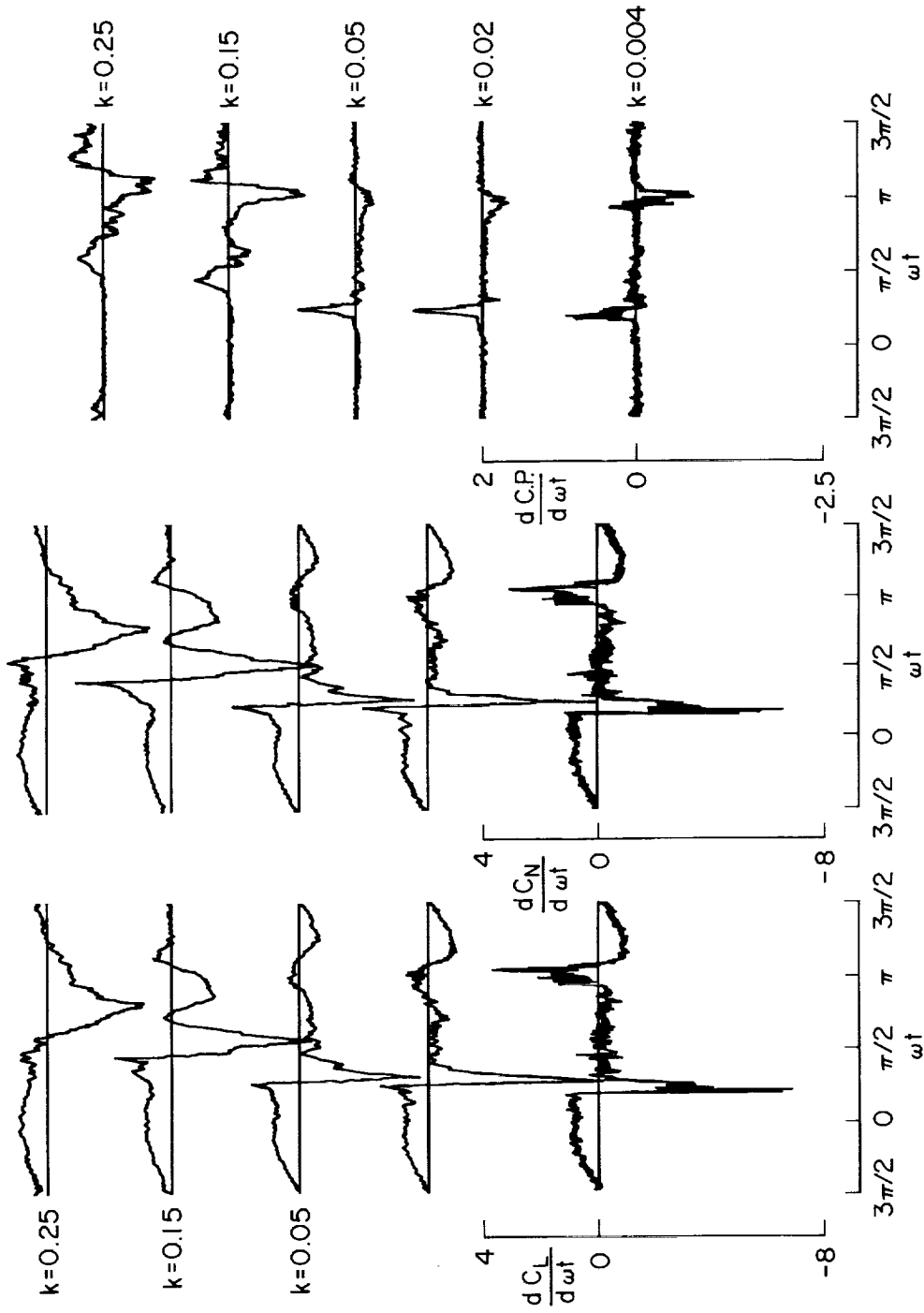
$\alpha = 15^\circ + 10^\circ \sin \omega t$
 With serrations
 Without end plates



(c) With serrations and without end plates.

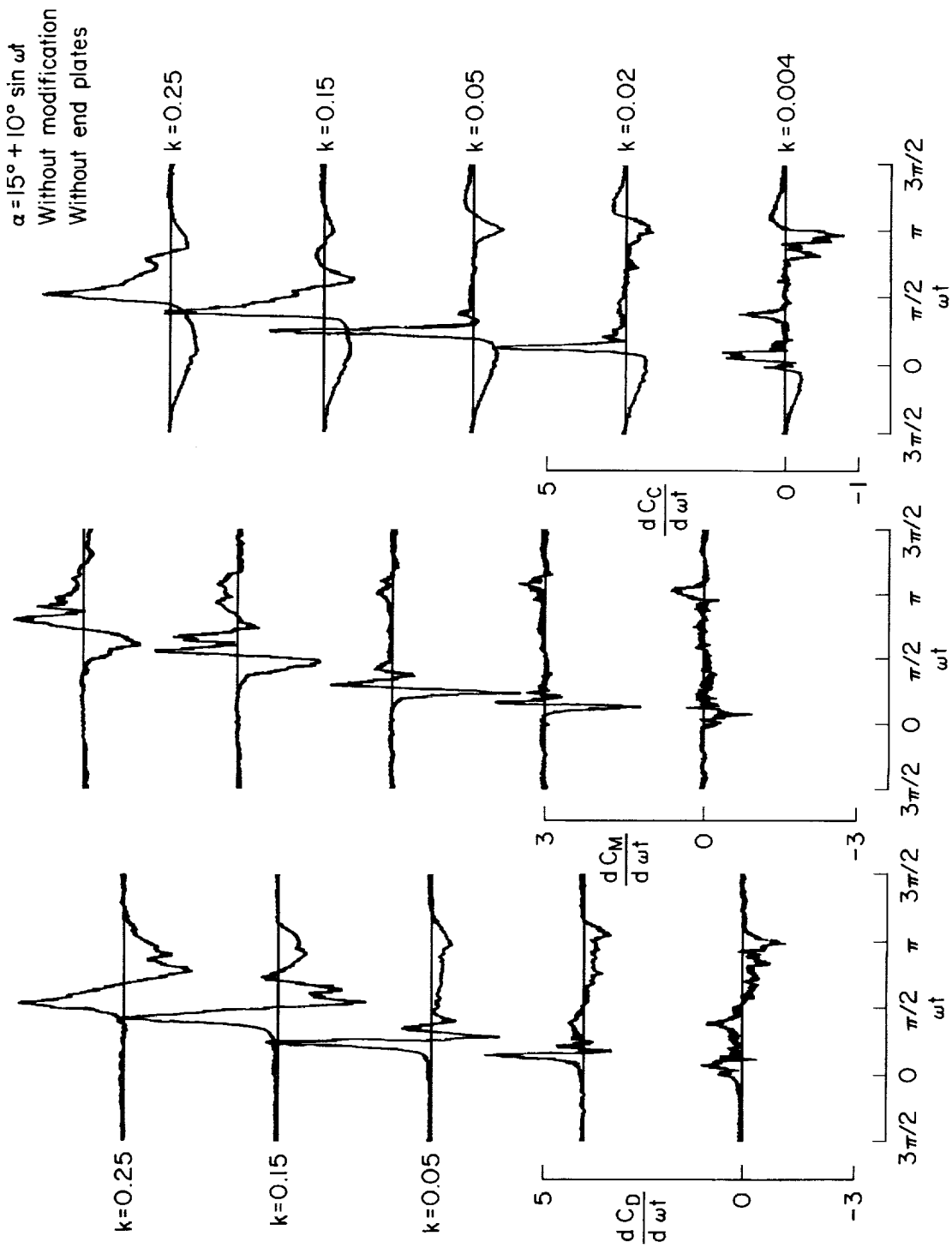
Figure 48.— Continued.

$\alpha = 15^\circ + 10^\circ \sin \omega t$
 Without modification
 With end plates



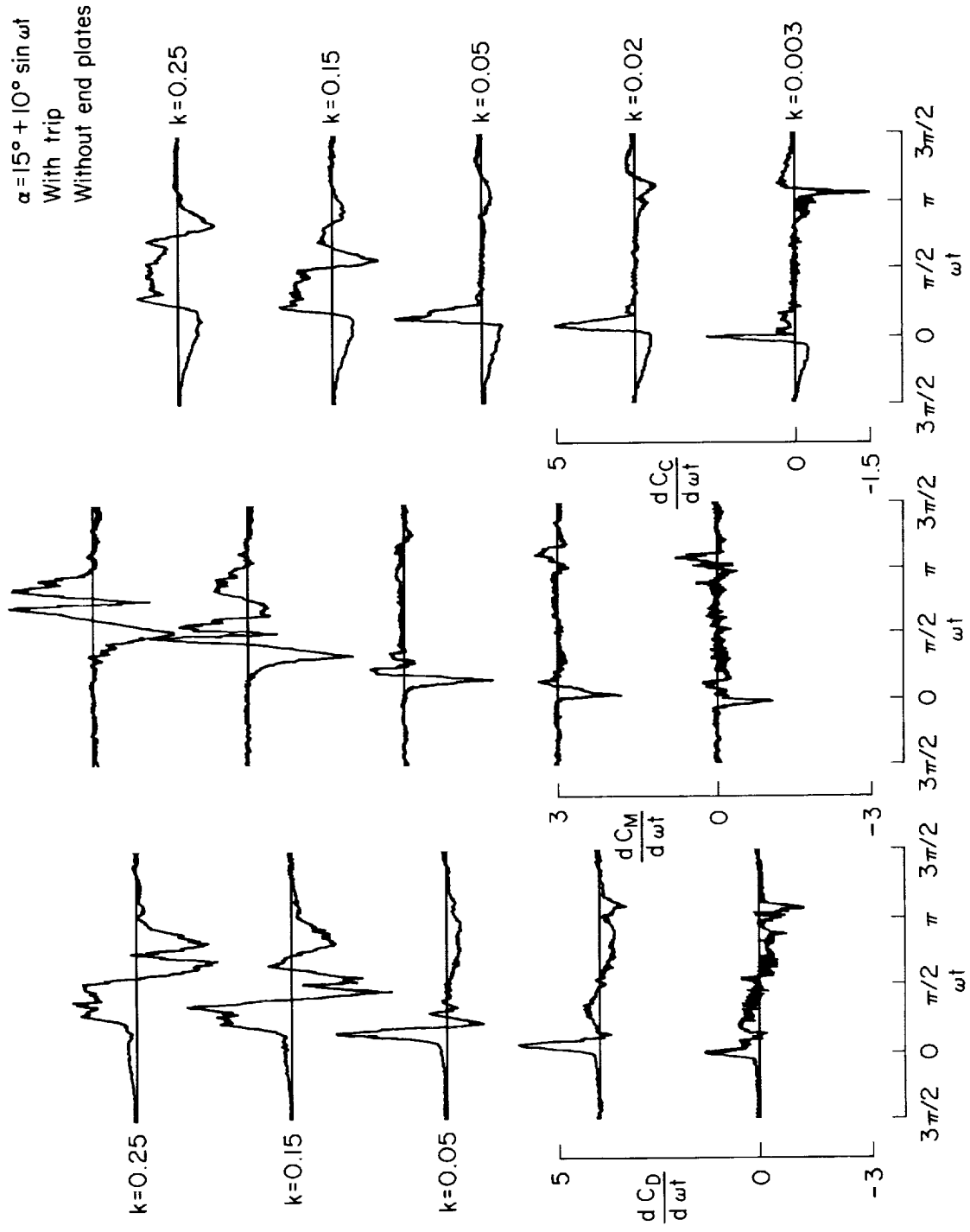
(d) Without modification and with end plates.

Figure 48. -- Concluded.



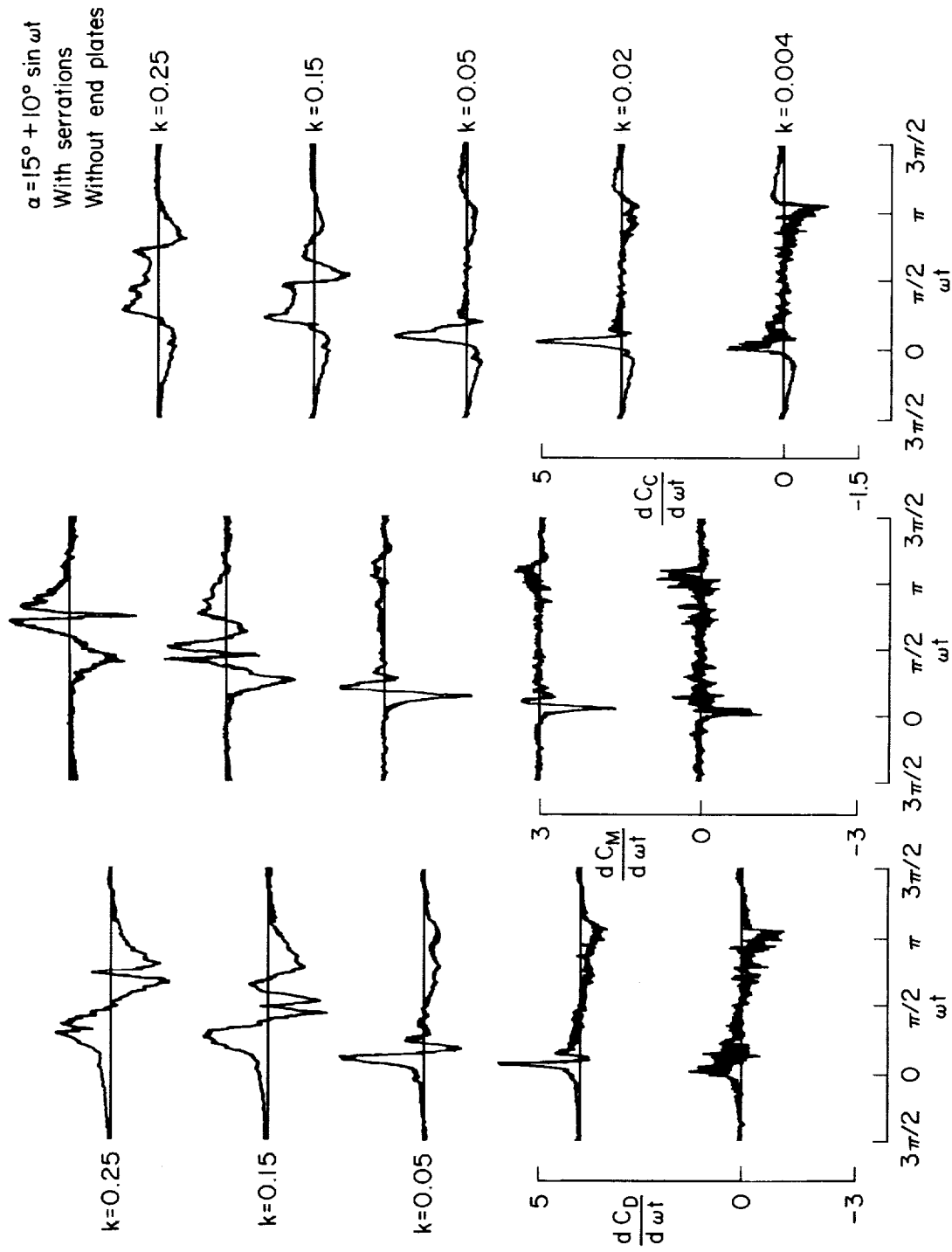
(a) Without modification and without end plates.

Figure 49.— Azimuthal rate of change of drag, pitching moment, and chord forces.



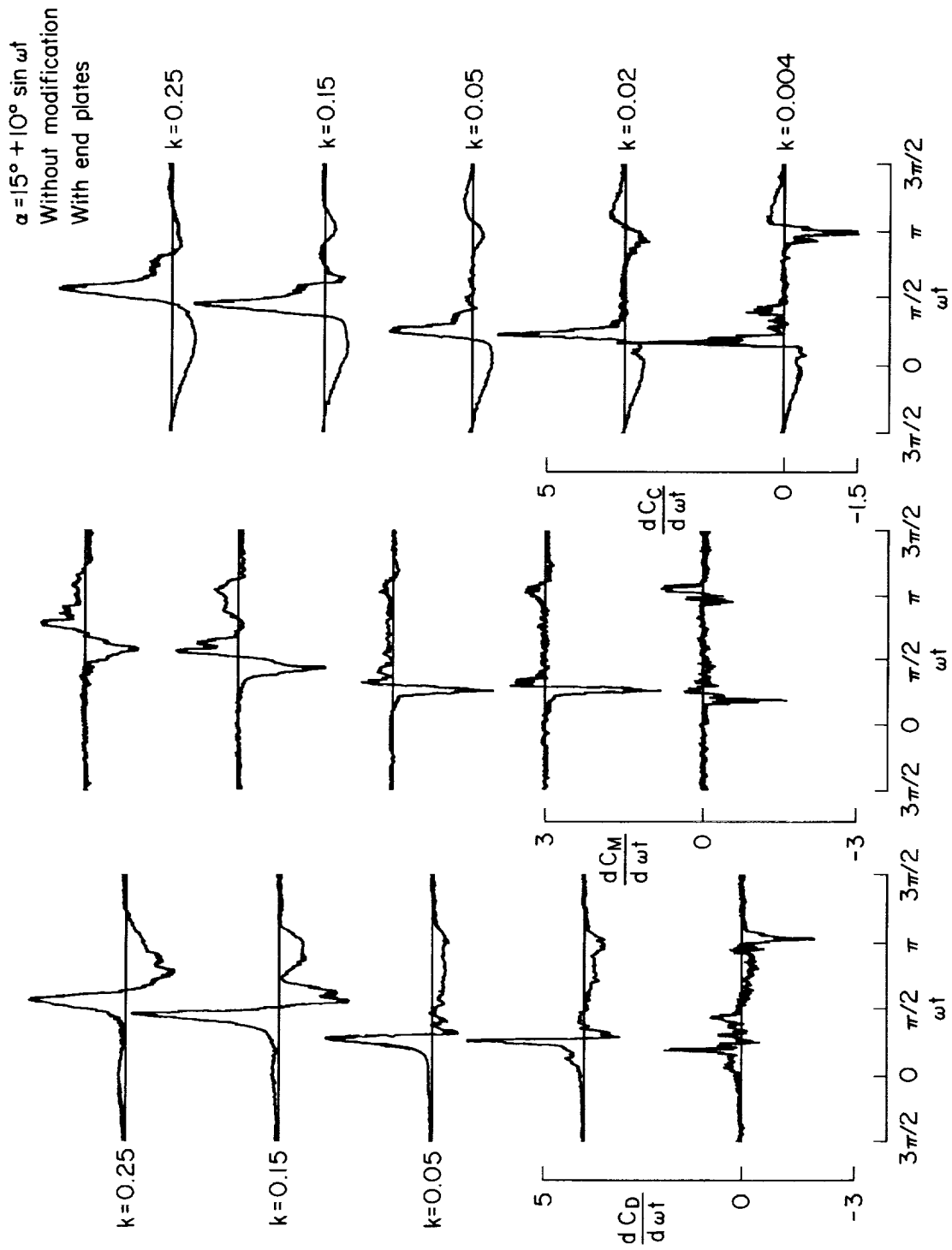
(b) With trip and without end plates.

Figure 49.— Continued.



(c) With serrations and without end plates.

Figure 49.— Continued.



(d) Without modification and with end plates.

Figure 49.— Concluded.

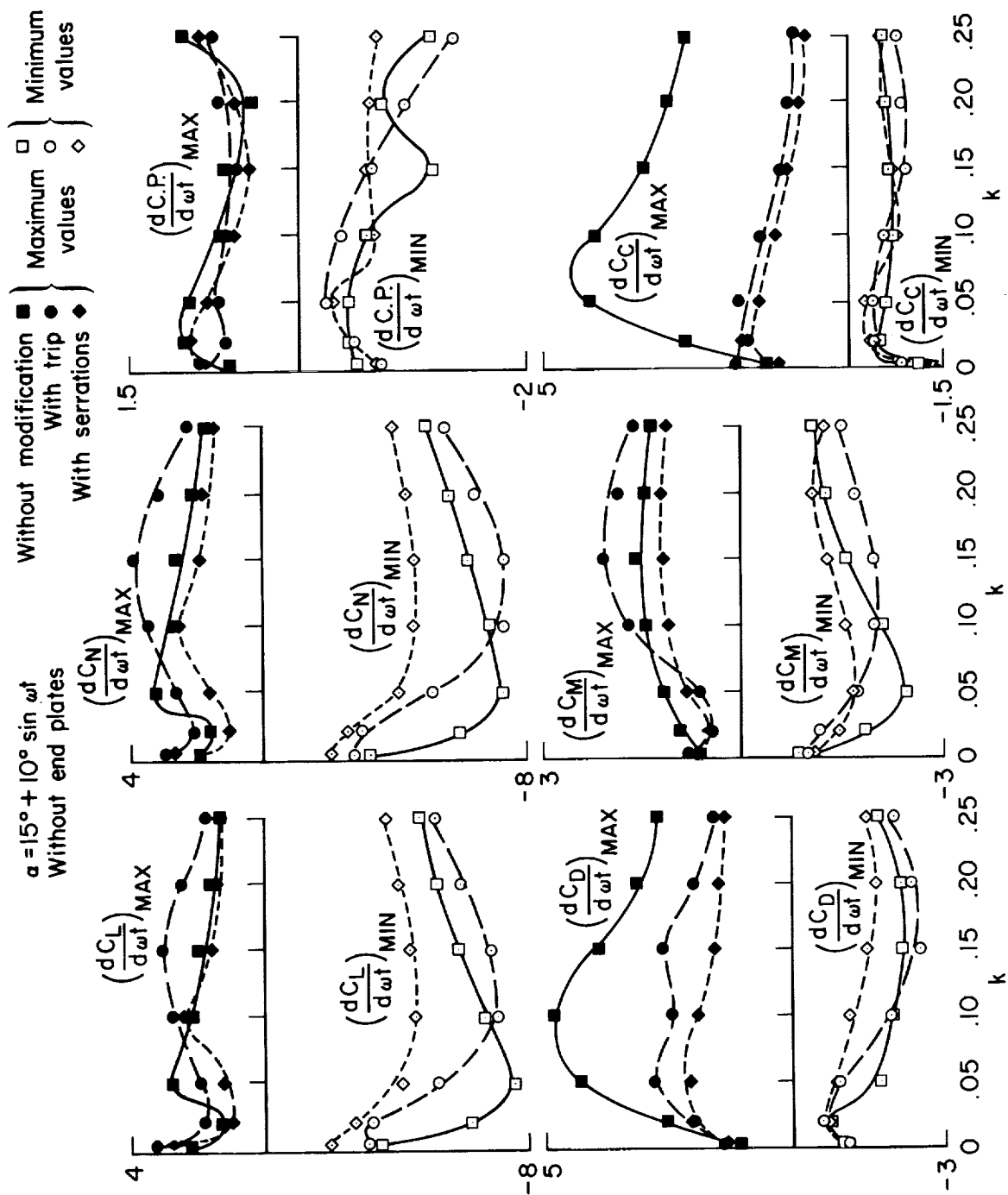


Figure 50.— Effect of leading-edge modifications on extrema of integrated pressure derivatives; without end plates.

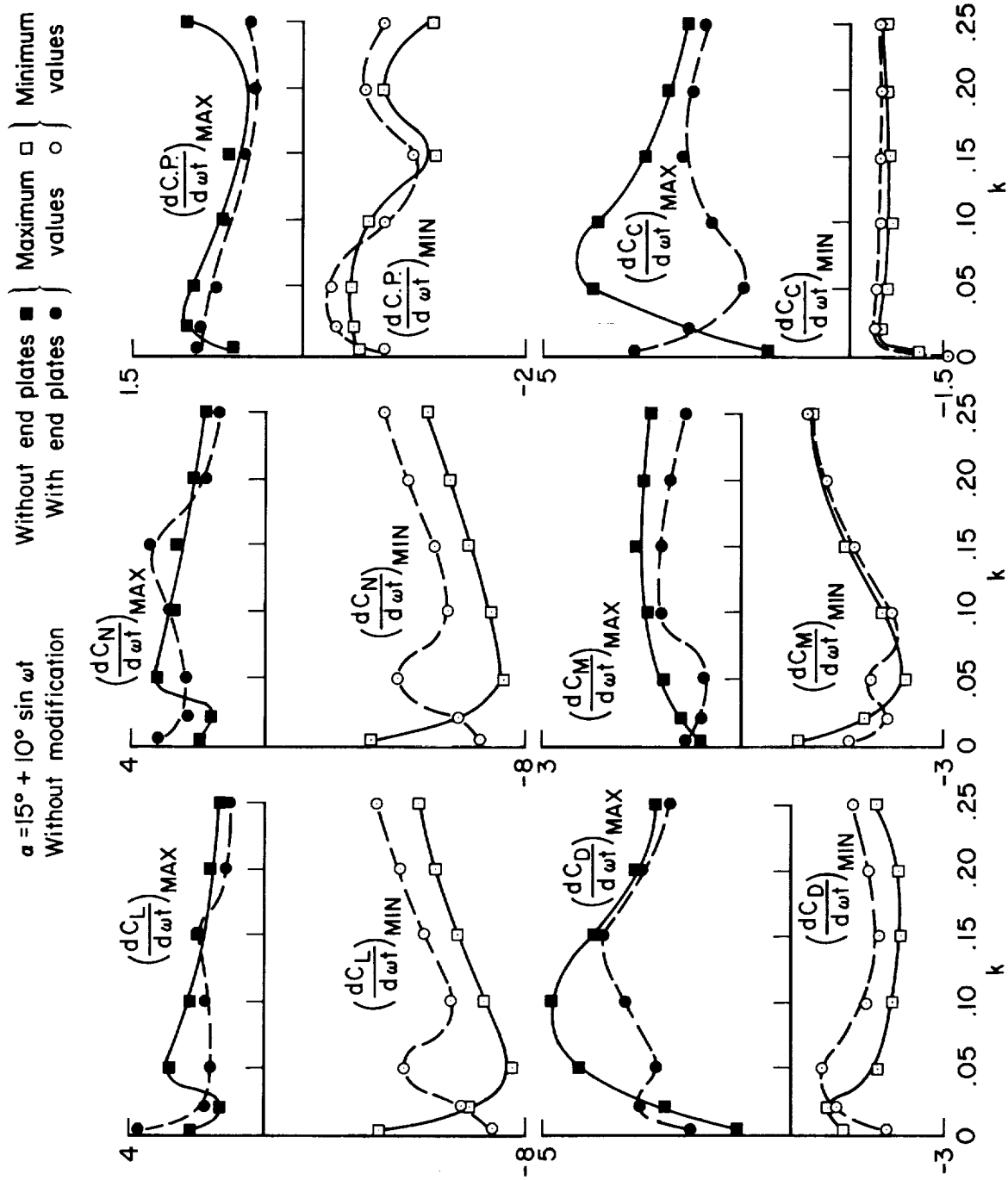


Figure 51.— Effect of end plates on extremums of integrated pressure derivatives; without modification.

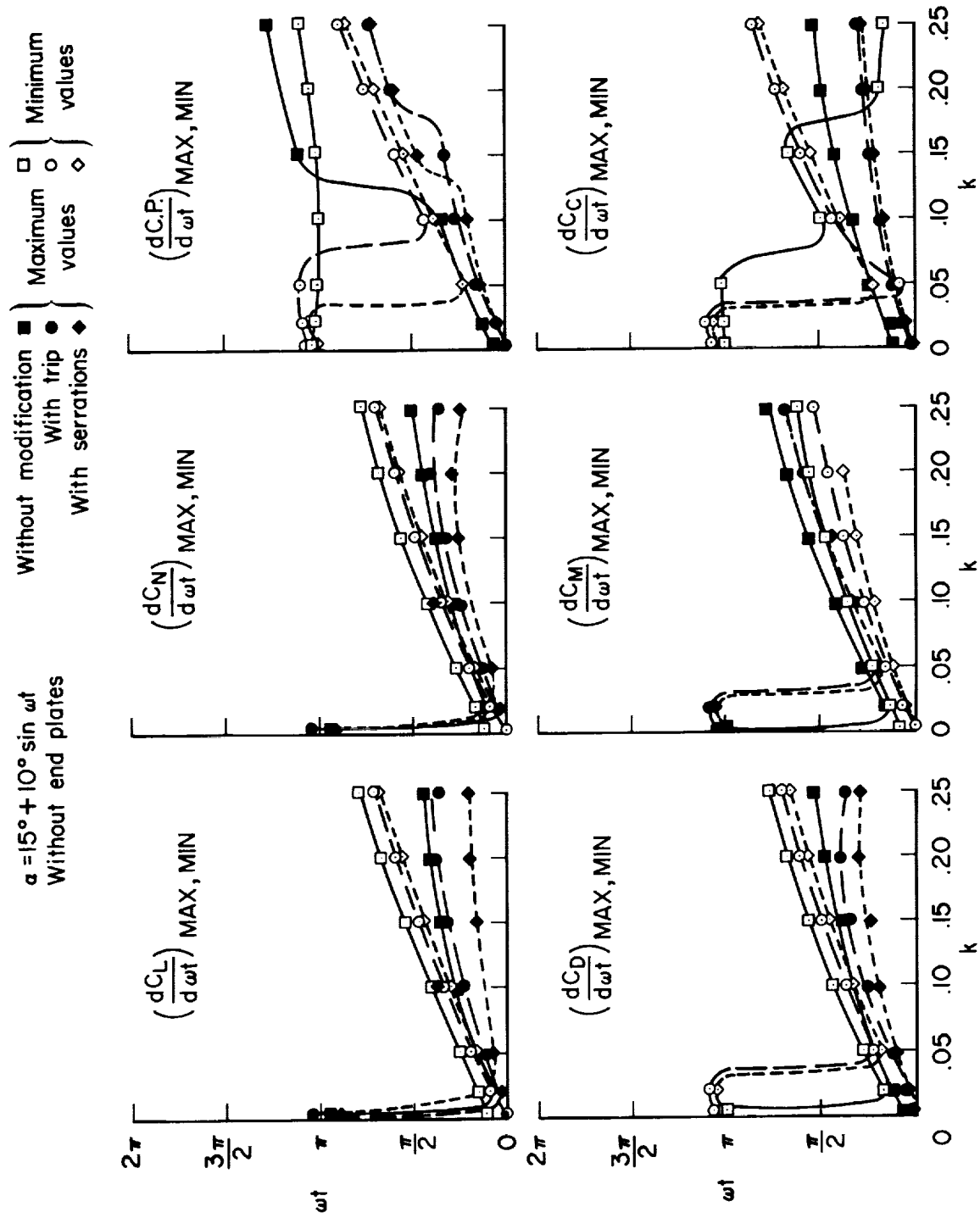


Figure 52.— Effect of leading-edge modifications on phase angles of integrated pressure derivative extrema; without end plates.

$\alpha = 15^\circ + 10^\circ \sin \omega t$

Without modification	Without end plates	Maximum values	Minimum values
		■	□
	With end plates	●	○

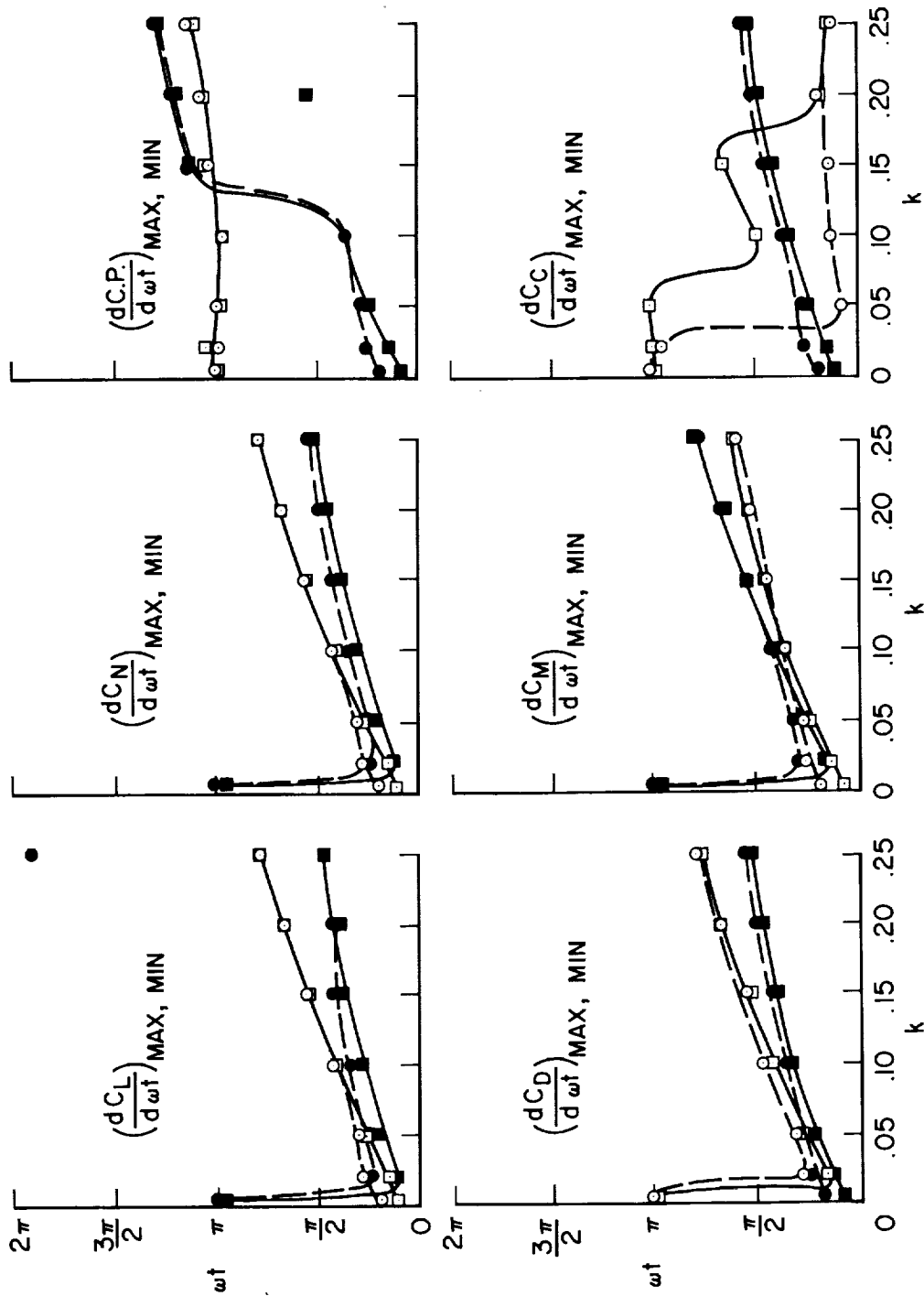
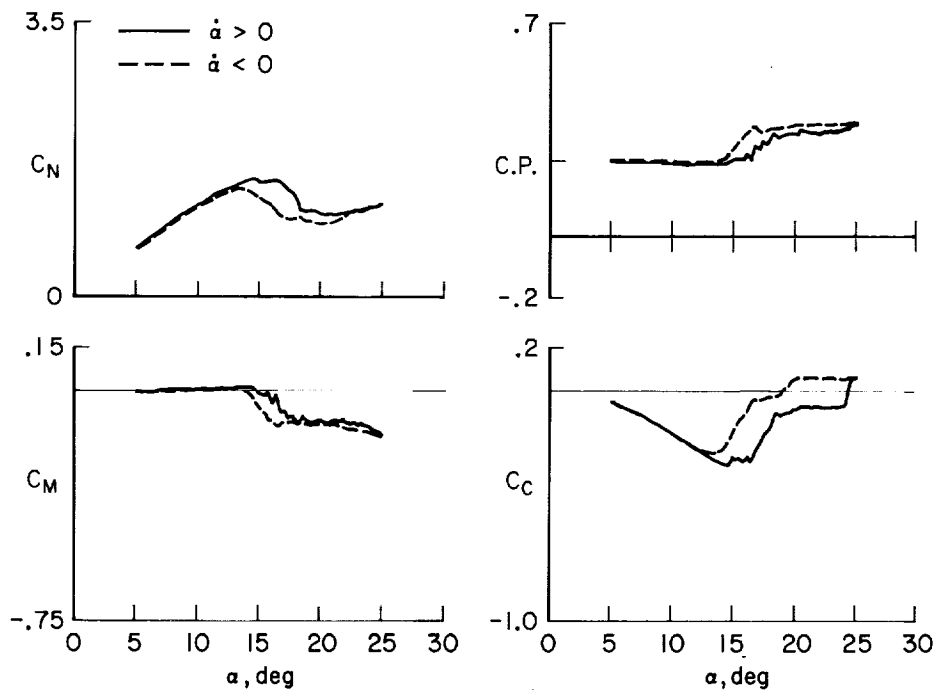
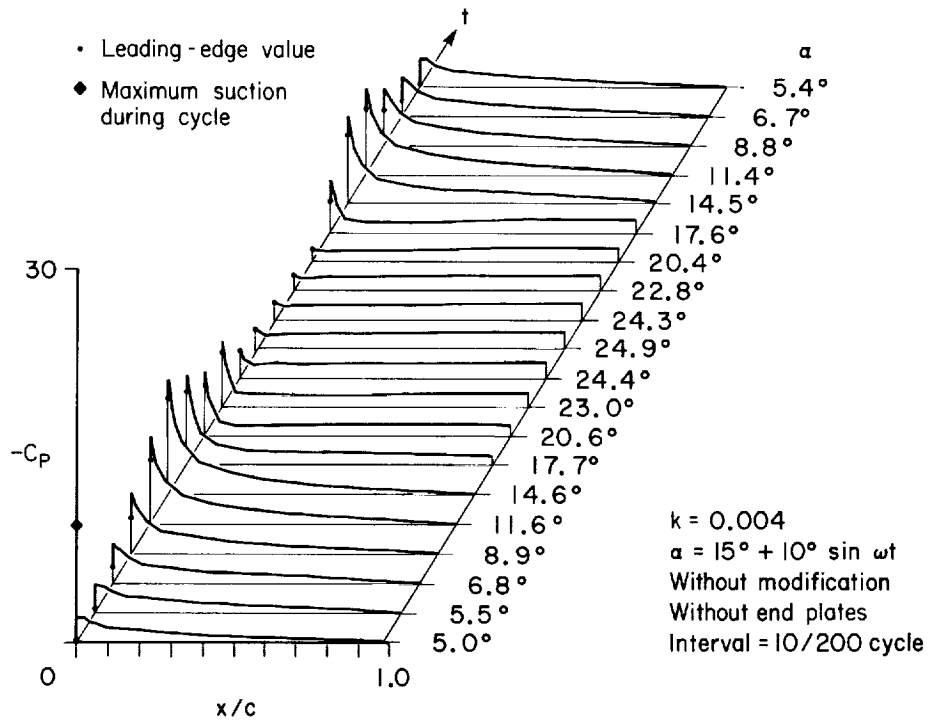


Figure 53.— Effect of end plates on phase angles of integrated pressure derivative extrema; without modification.

APPENDIX

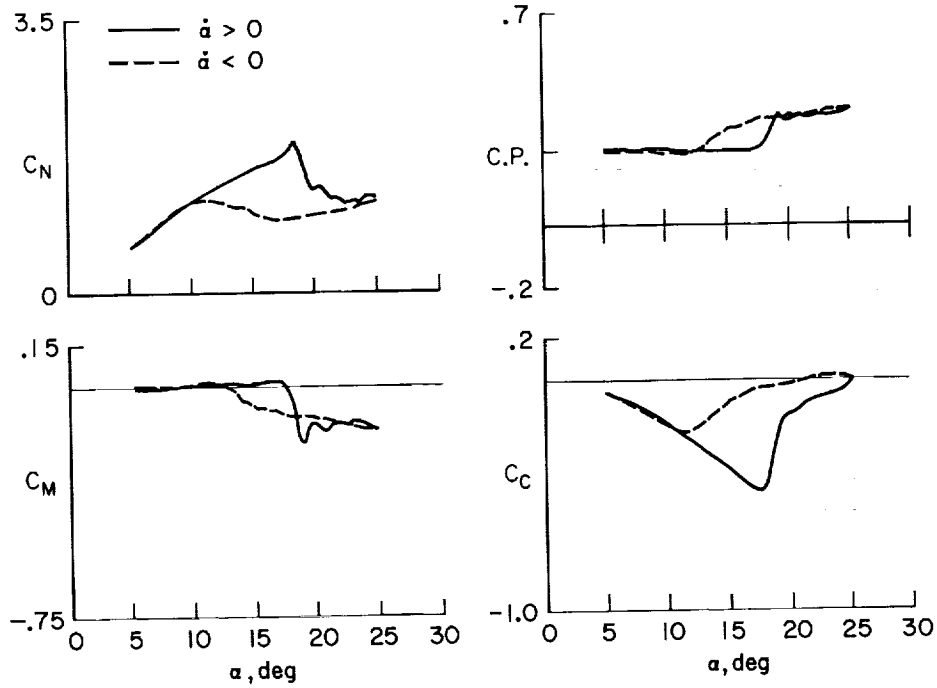
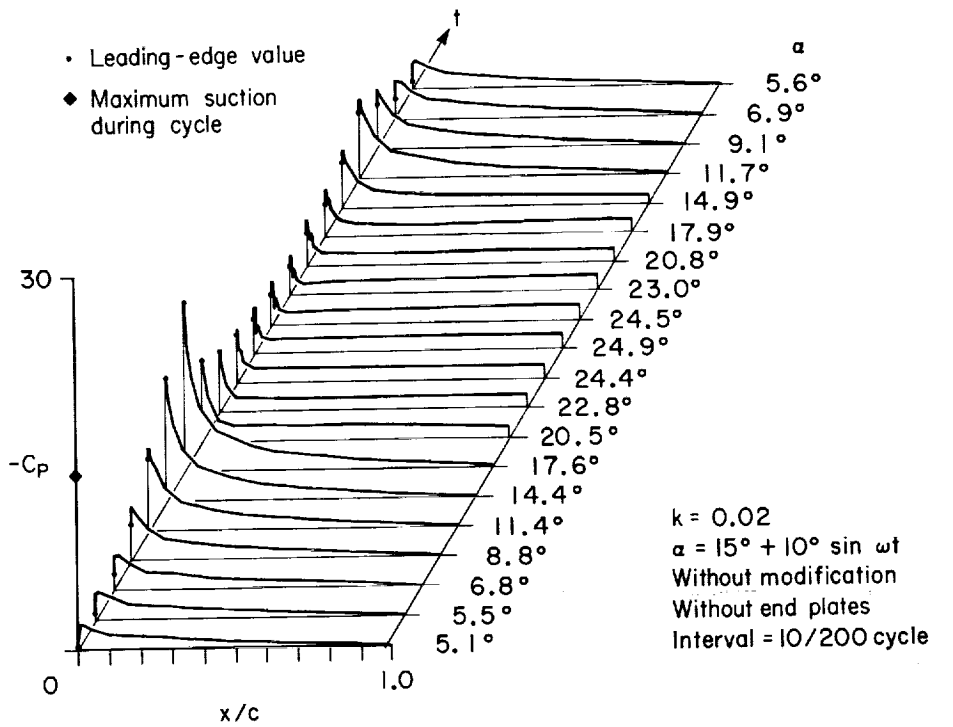
SUMMARY OF PRESSURE DISTRIBUTIONS AND INTEGRATIONS

The following figures represent a summary of the test program in terms of the upper surface pressure distribution over a complete cycle of oscillation along with the resultant pitching-moment coefficient, normal- and chord-force coefficients and the center of pressure. A common set of scales have been used to make comparisons more convenient. A detailed summary of these results is given in table 2.



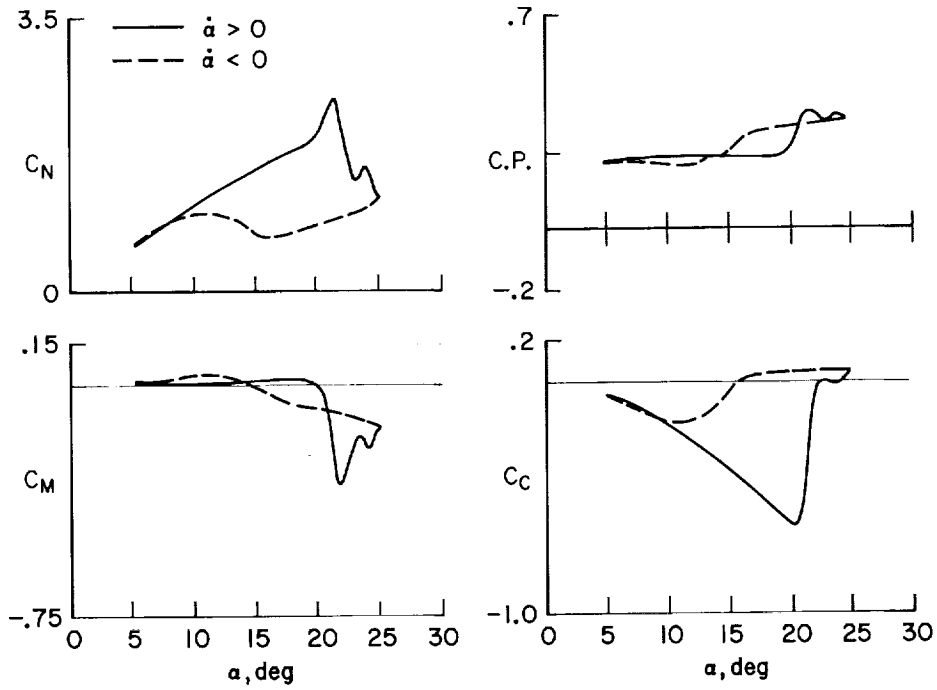
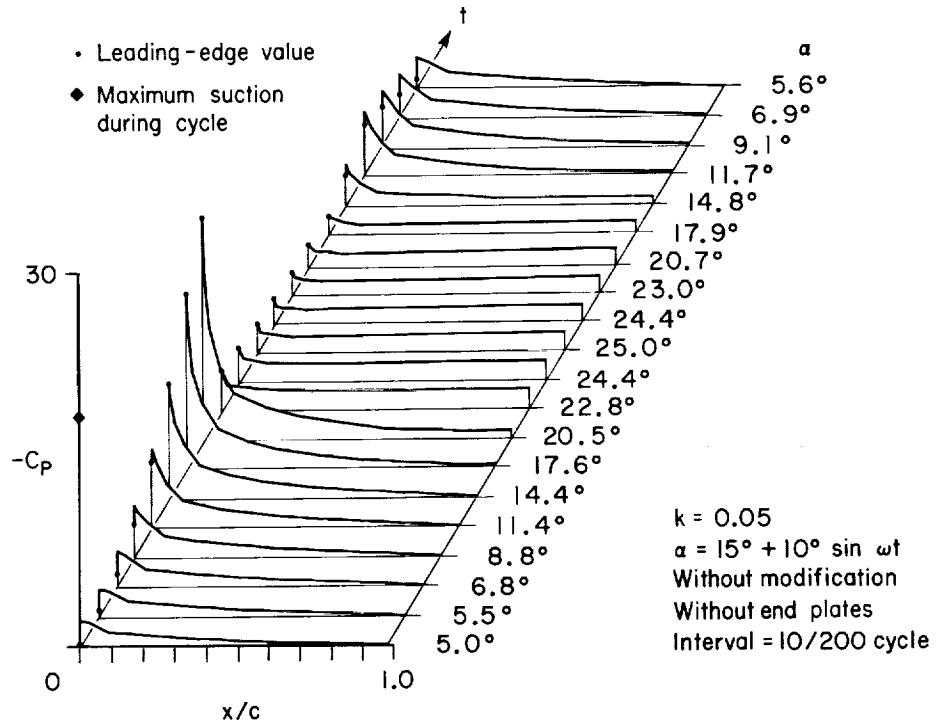
(a) $\alpha = 15^\circ + 10^\circ \sin \omega t, k = 0.004$.

Figure 54.— Aerodynamic loads on basic NACA 0012.



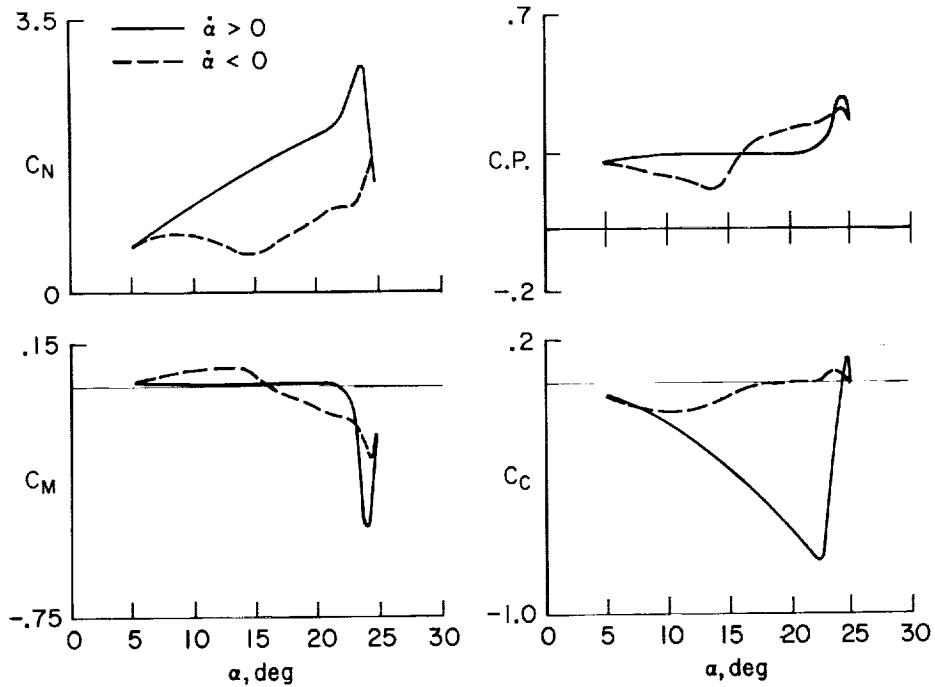
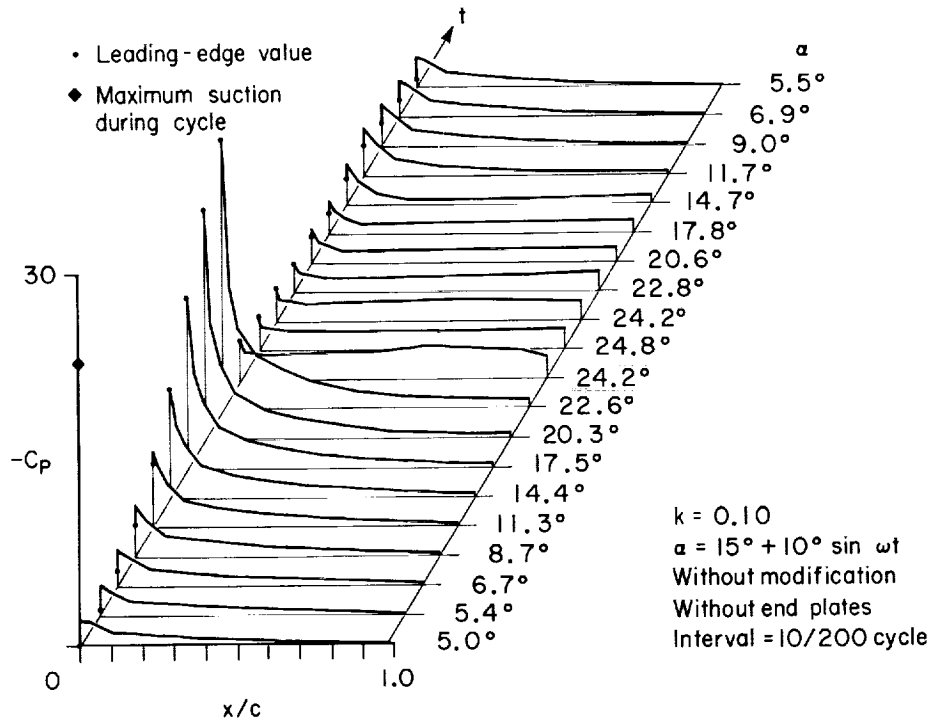
(b) $\alpha = 15^\circ + 10^\circ \sin \omega t$, $k = 0.020$.

Figure 54.— Continued.



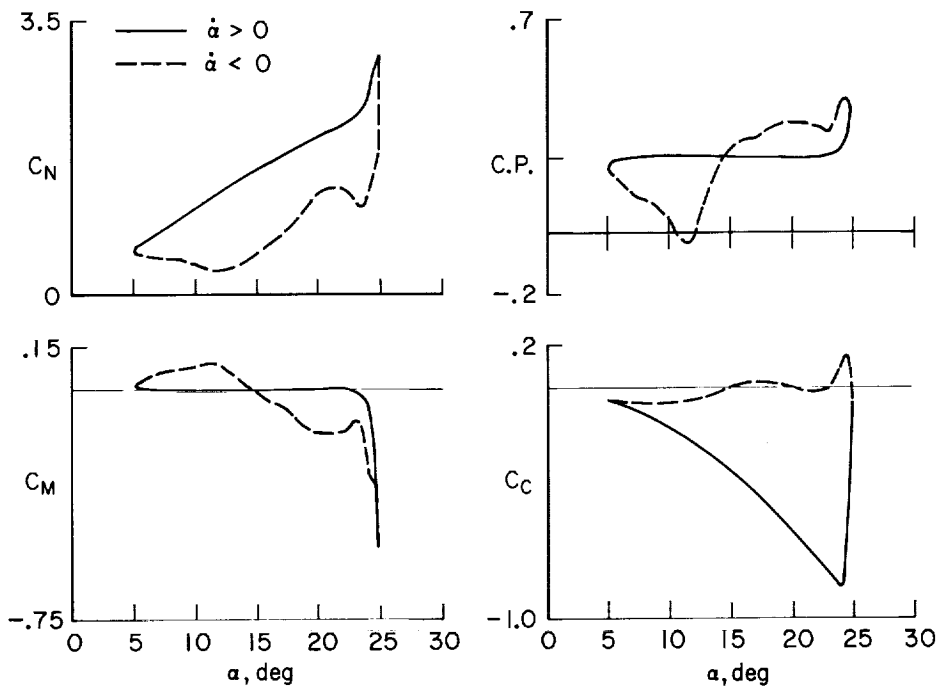
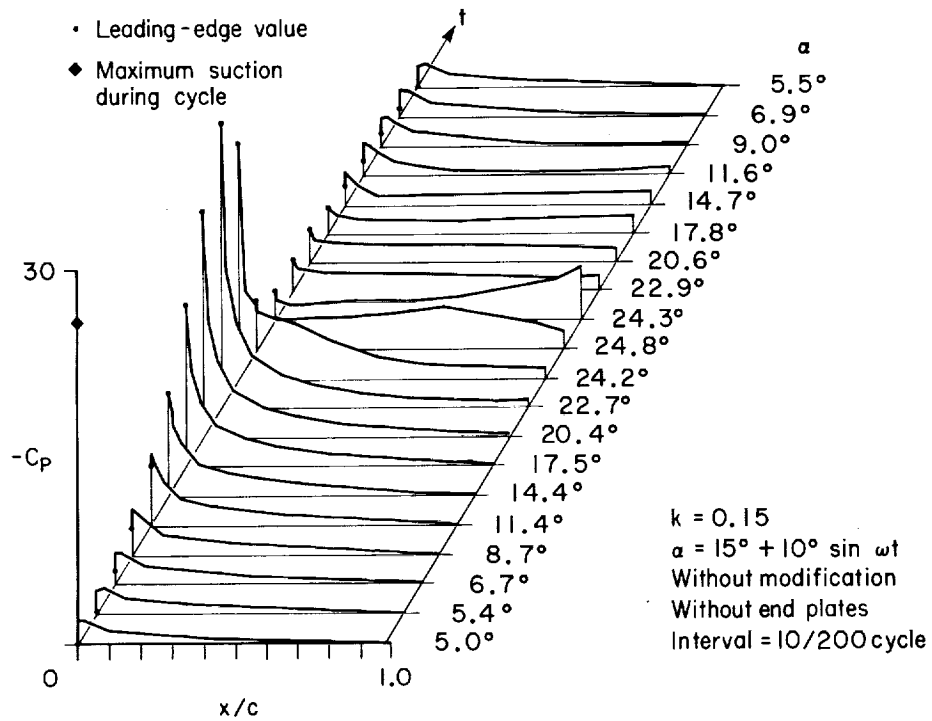
(c) $\alpha = 15^\circ + 10^\circ \sin \omega t, k = 0.050$.

Figure 54.— Continued.



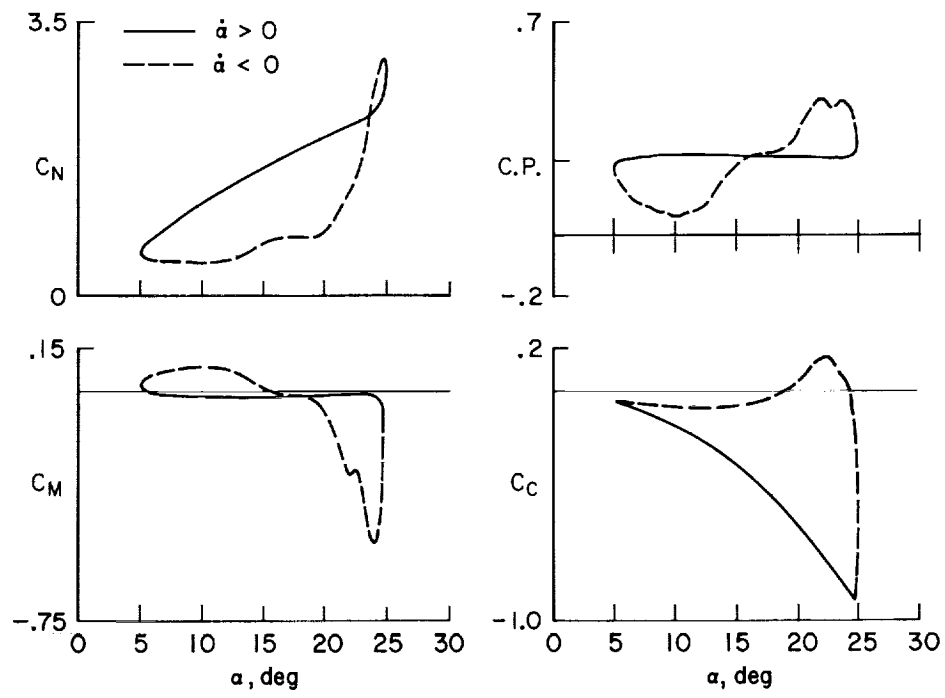
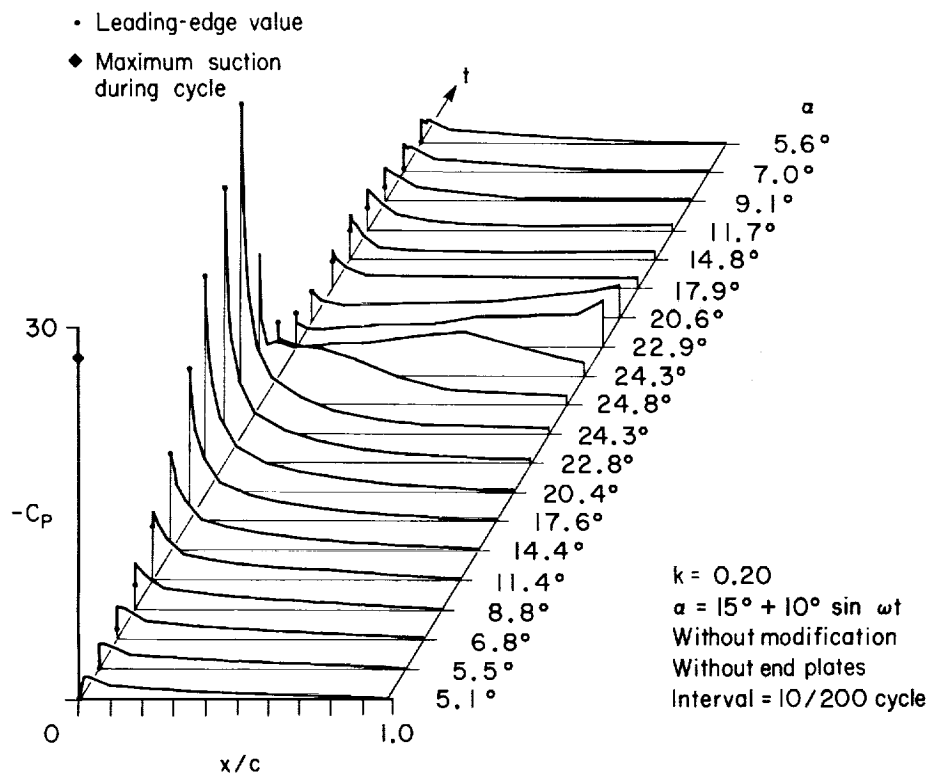
(d) $\alpha = 15^\circ + 10^\circ \sin \omega t, k = 0.100.$

Figure 54.— Continued.



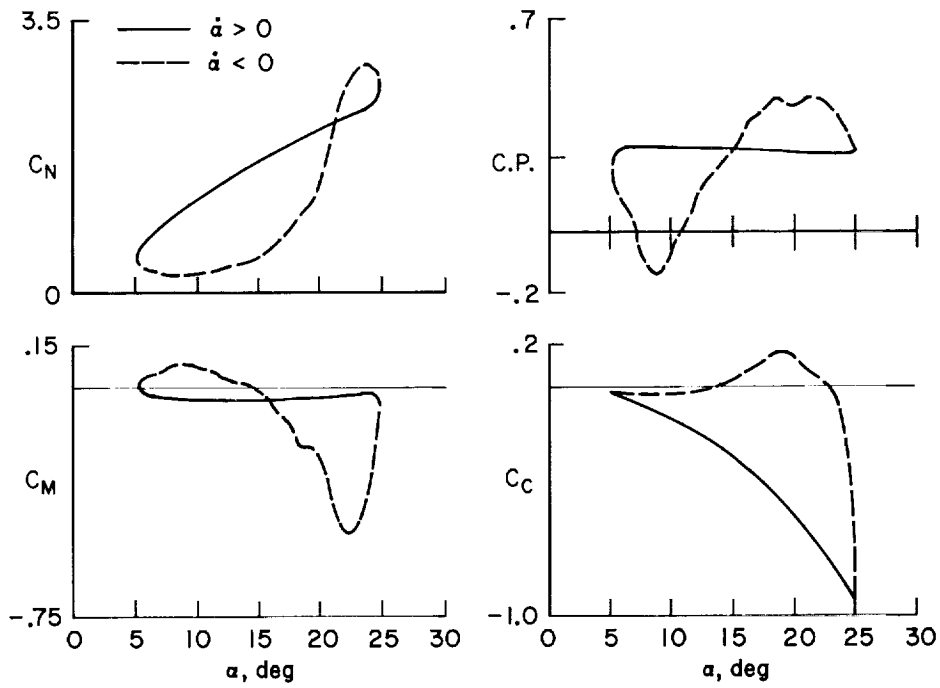
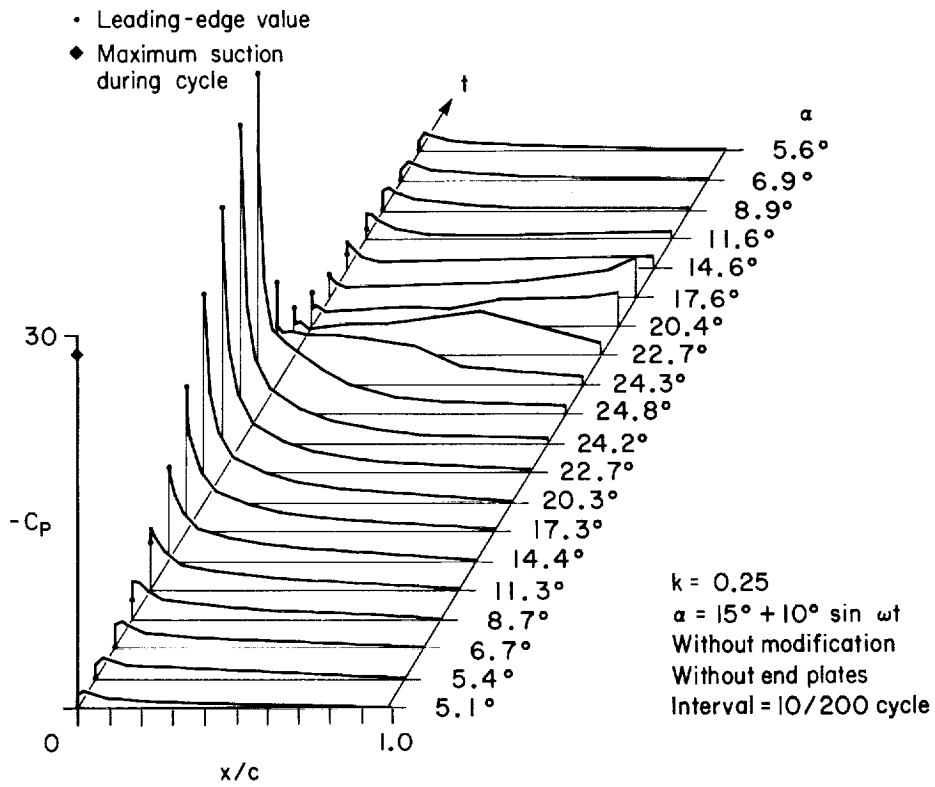
(e) $\alpha = 15^\circ + 10^\circ \sin \omega t, k = 0.150.$

Figure 54.— Continued.



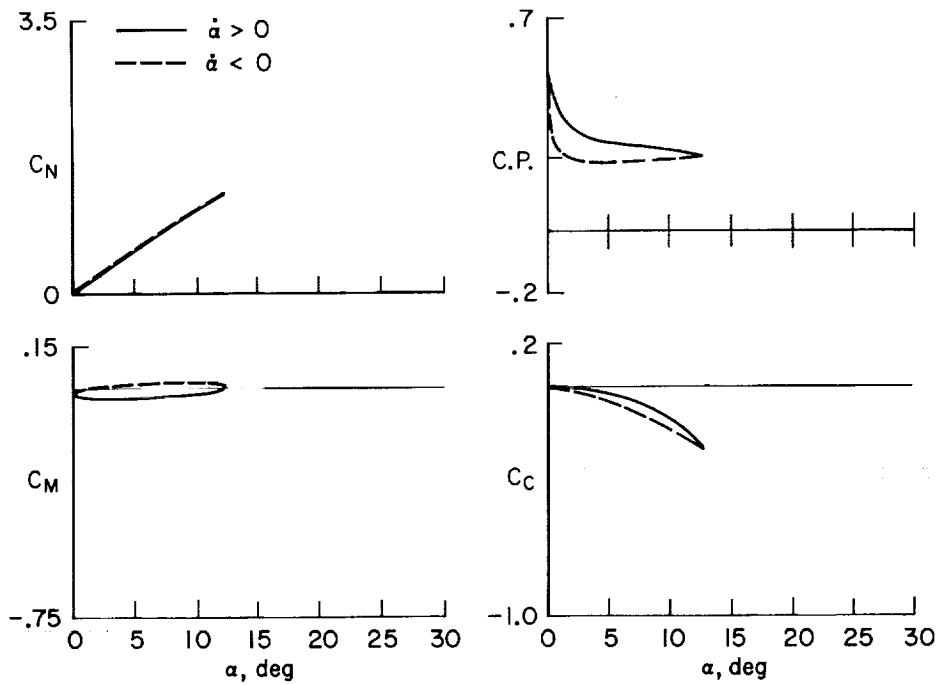
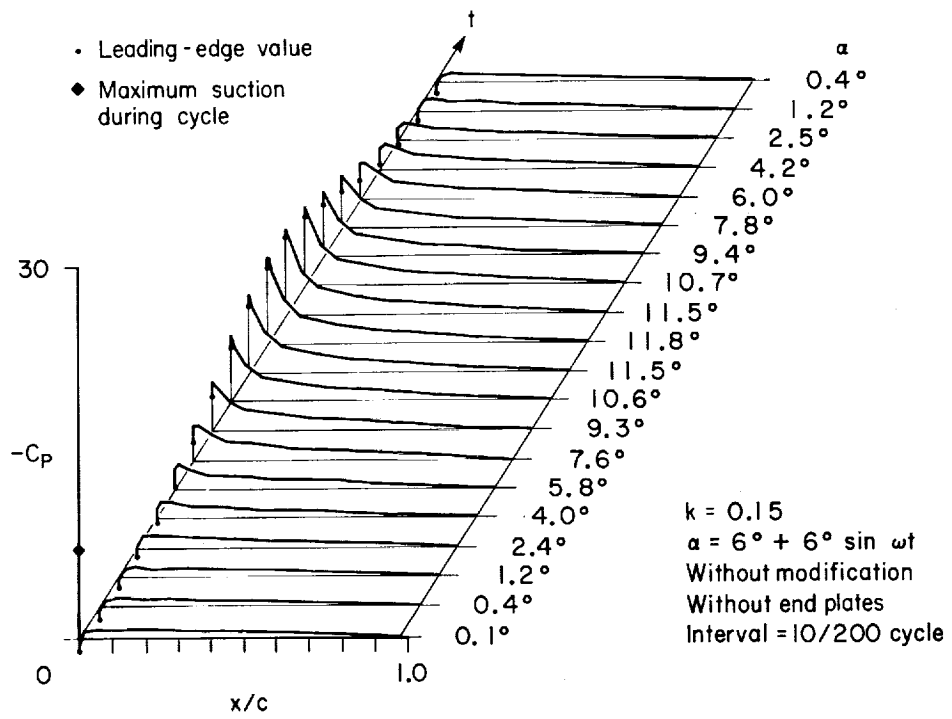
(f) $\alpha = 15^\circ + 10^\circ \sin \omega t, k = 0.200.$

Figure 54.— Continued.



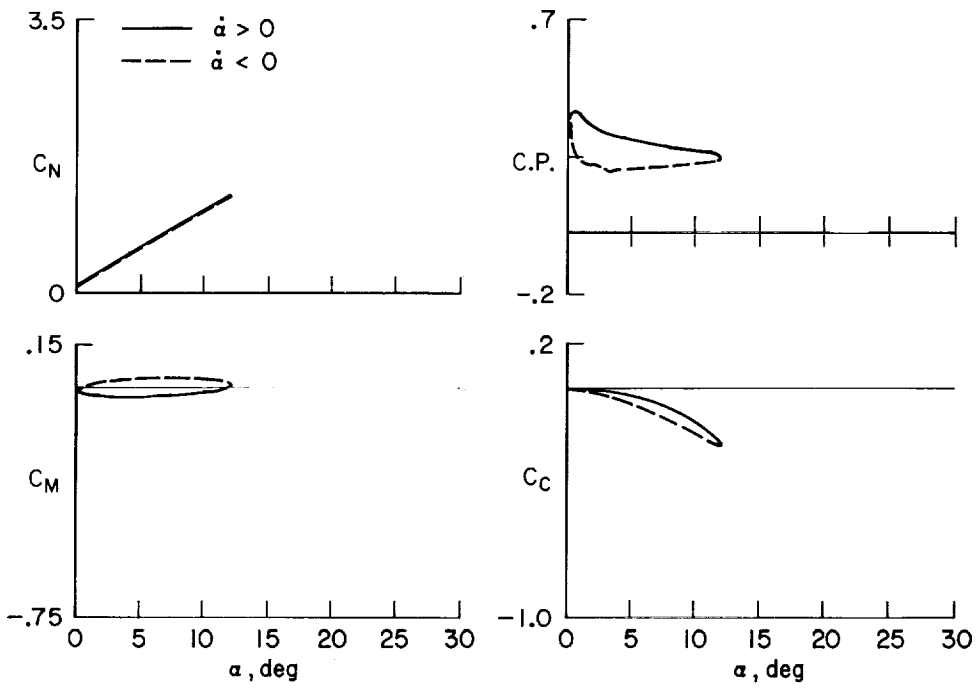
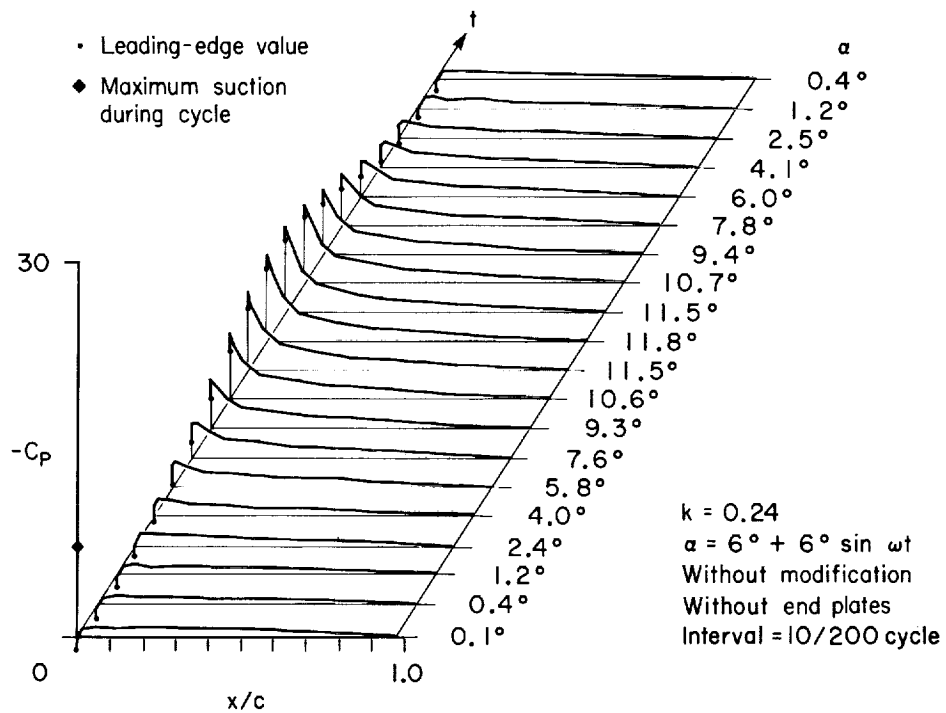
(g) $\alpha = 15^\circ + 10^\circ \sin \omega t, k = 0.250$.

Figure 54.— Continued.



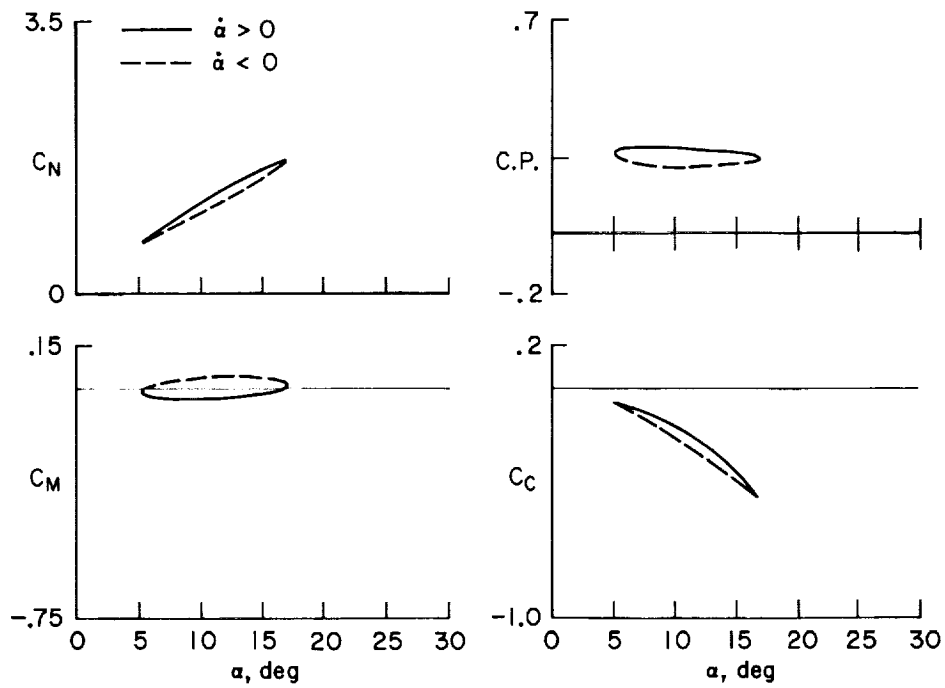
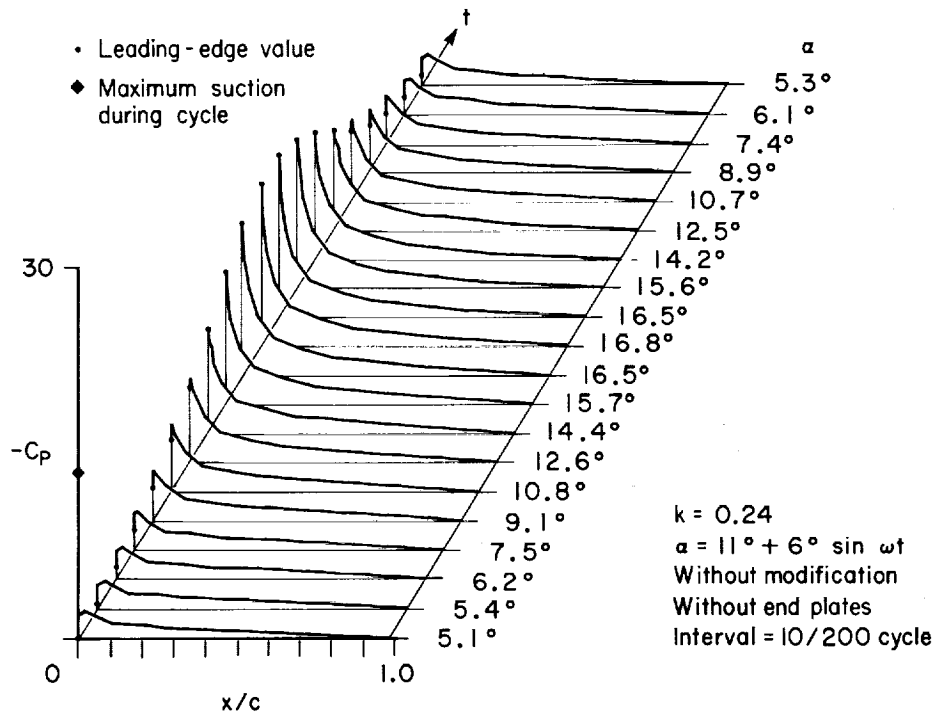
(h) $\alpha = 6^\circ + 6^\circ \sin \omega t, k = 0.150$.

Figure 54.— Continued.



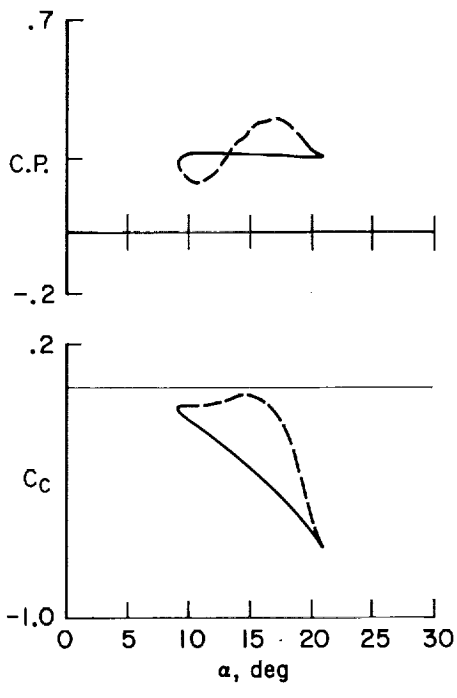
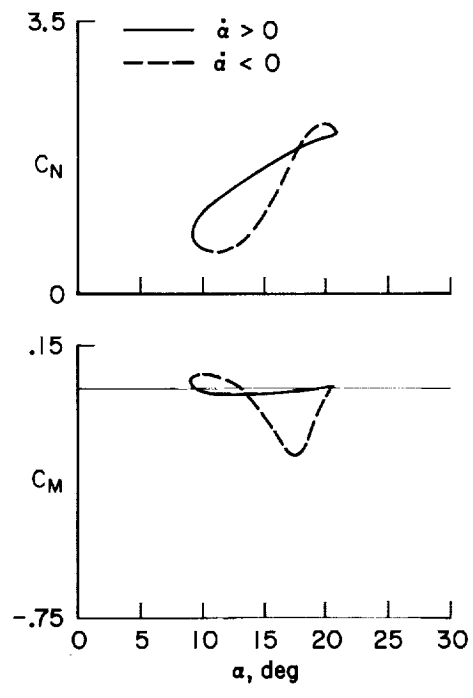
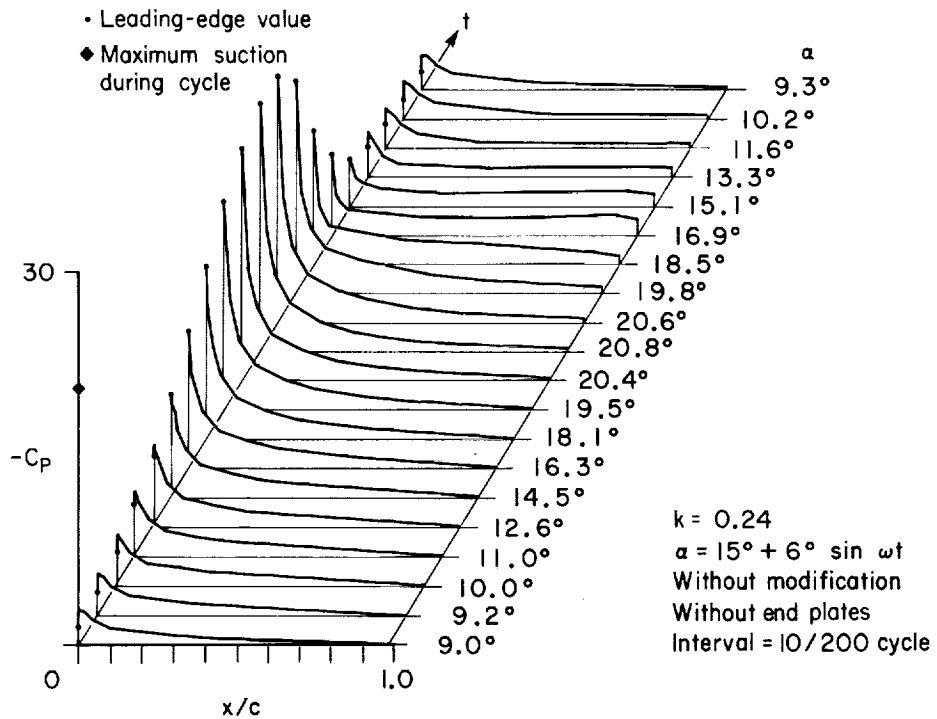
(i) $\alpha = 6^\circ + 6^\circ \sin \omega t, k = 0.240$.

Figure 54.— Continued.



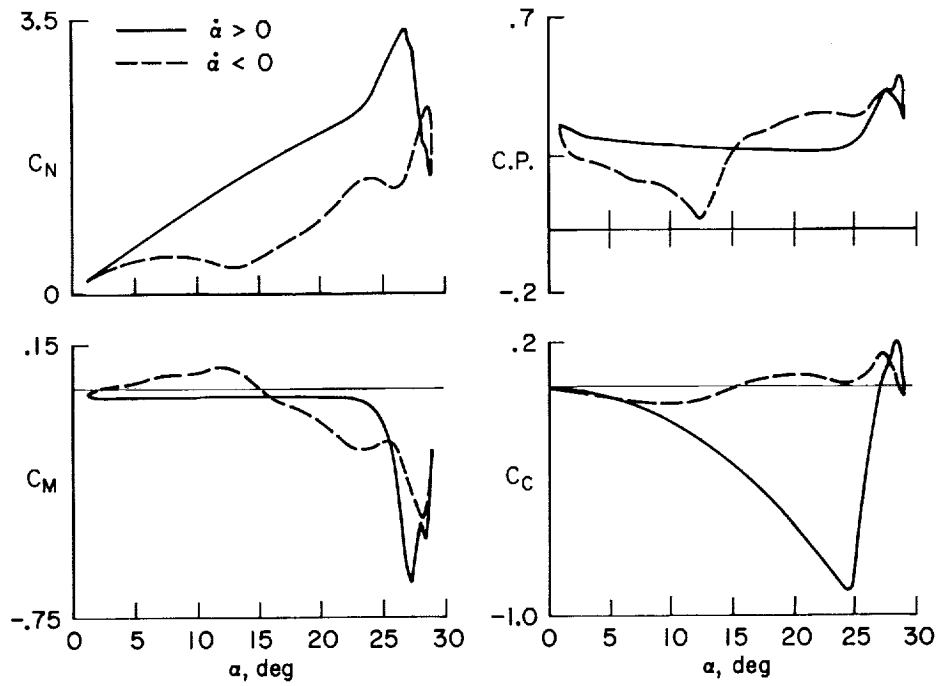
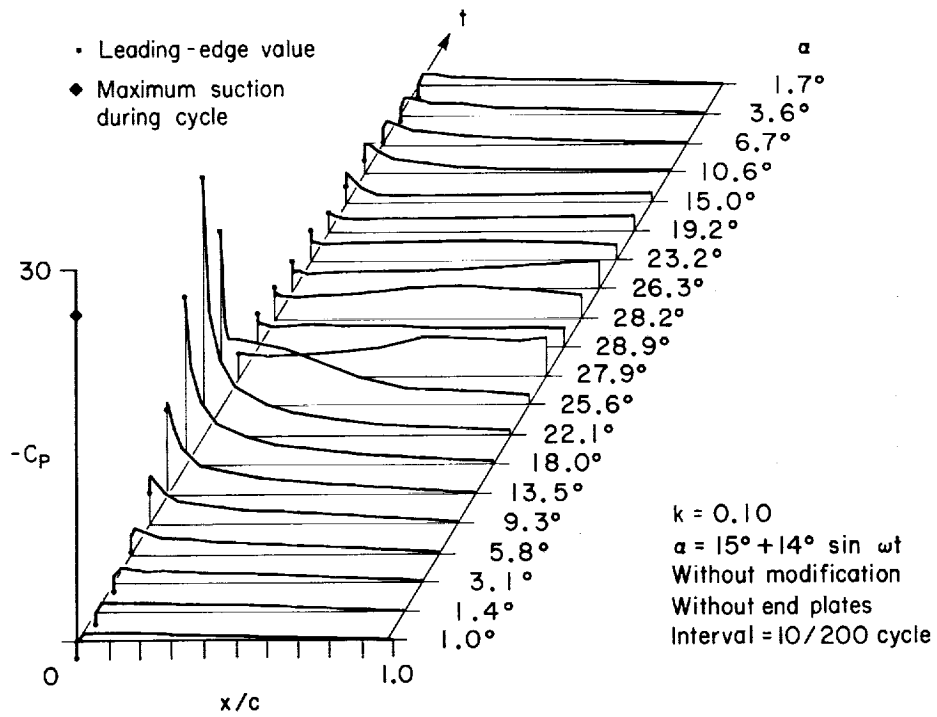
(j) $\alpha = 11^\circ + 6^\circ \sin \omega t, k = 0.240.$

Figure 54.— Continued.



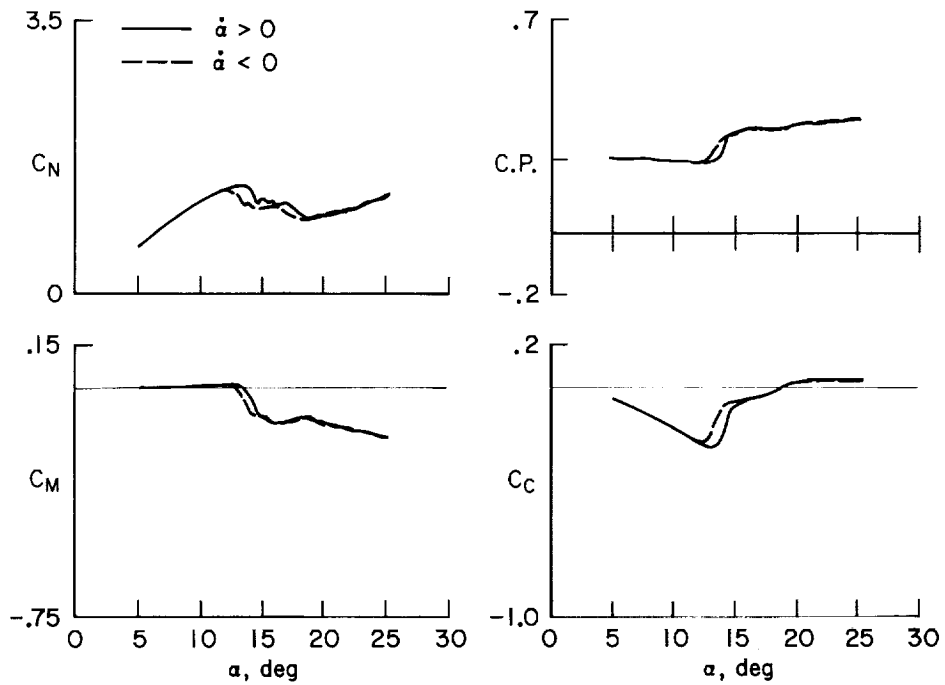
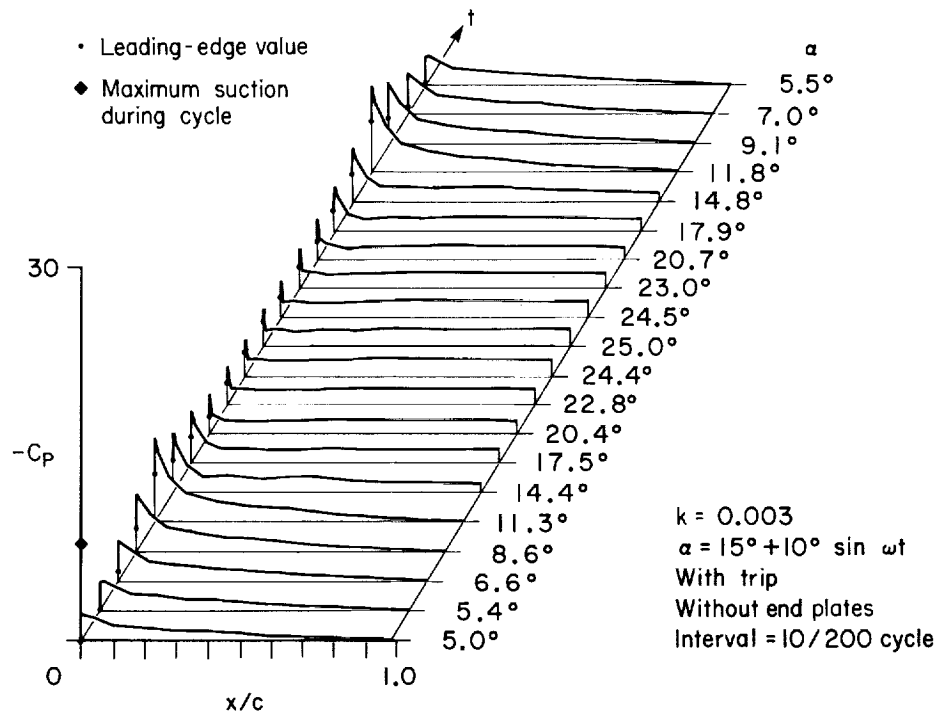
(k) $\alpha = 15^\circ + 6^\circ \sin \omega t, k = 0.240.$

Figure 54.- Continued.



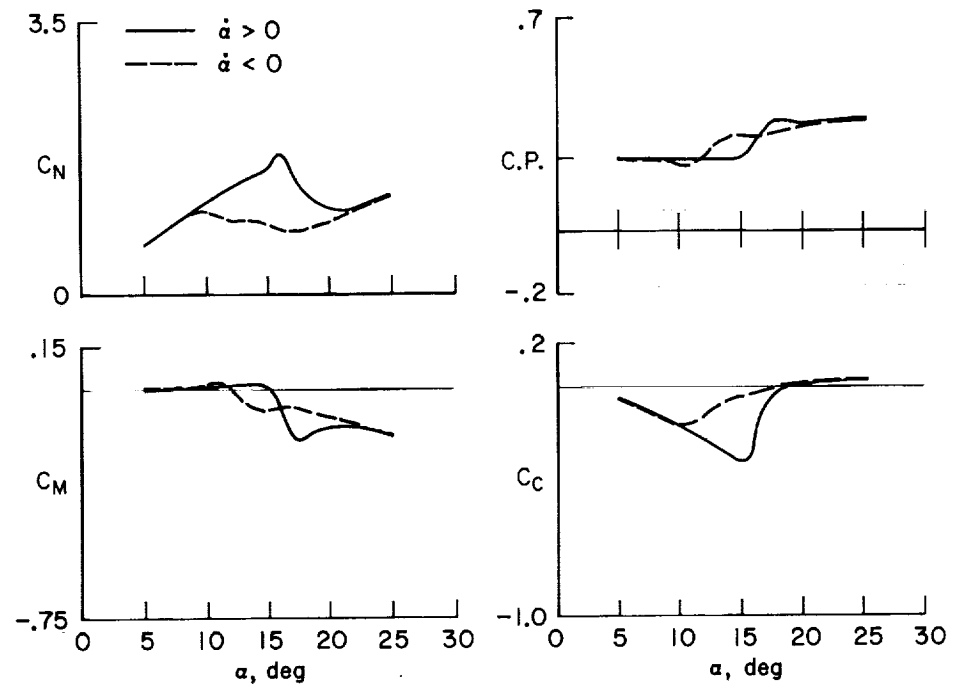
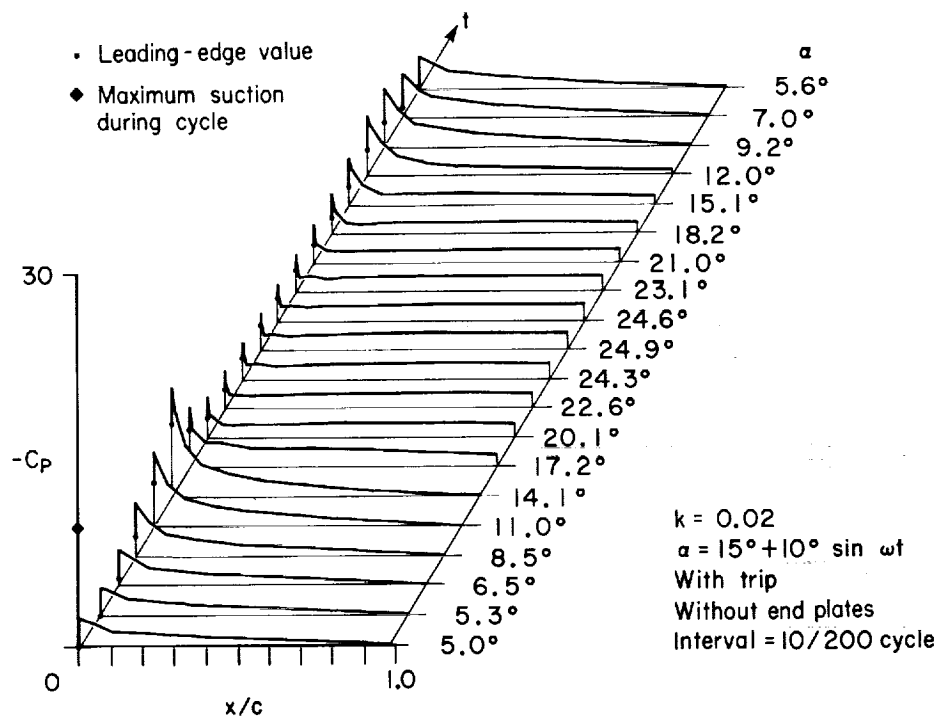
(I) $\alpha = 15^\circ + 14^\circ \sin \omega t, k = 0.100$.

Figure 54.— Concluded.



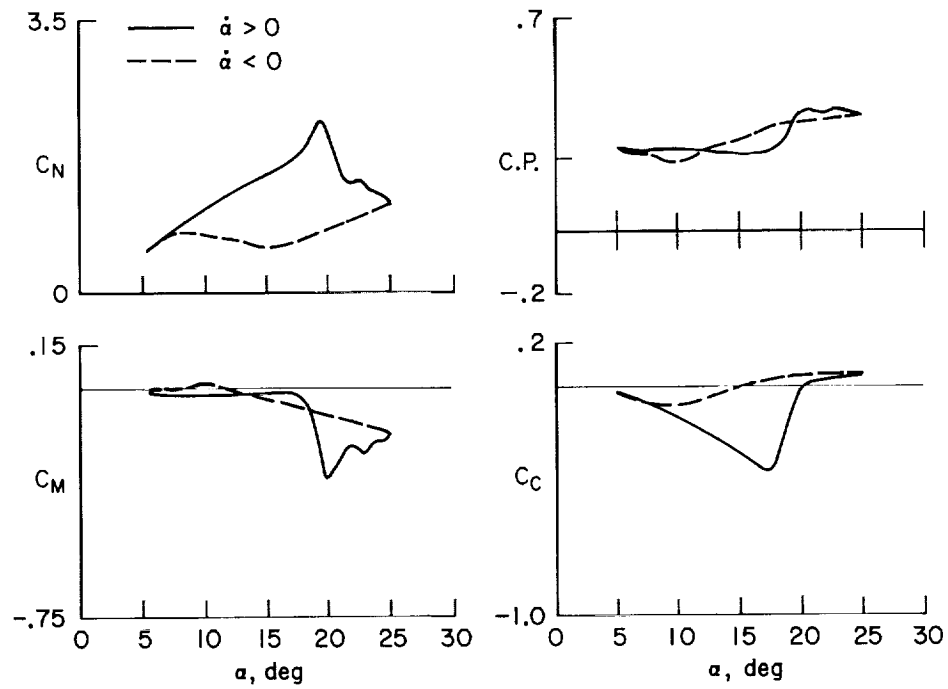
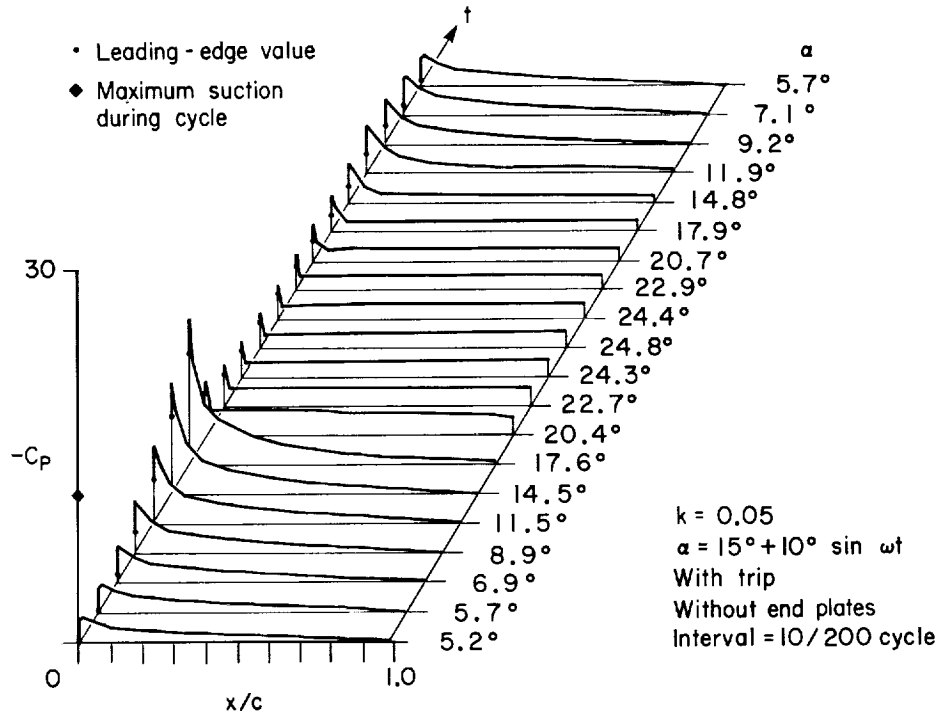
(a) $\alpha = 15^\circ + 10^\circ \sin \omega t, k = 0.003$.

Figure 55.— Aerodynamic loads on NACA 0012 with trip.



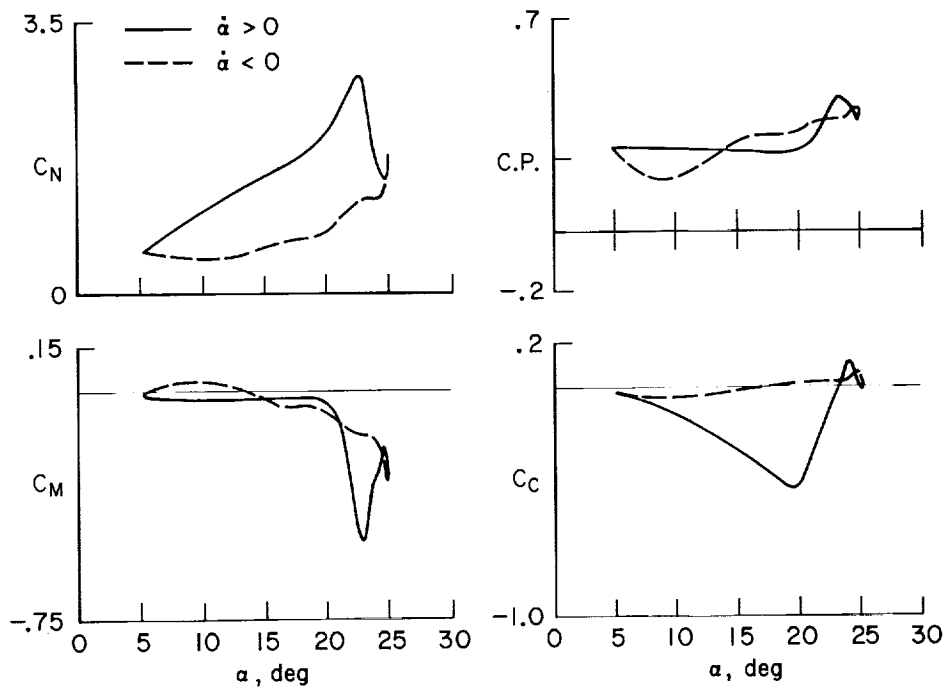
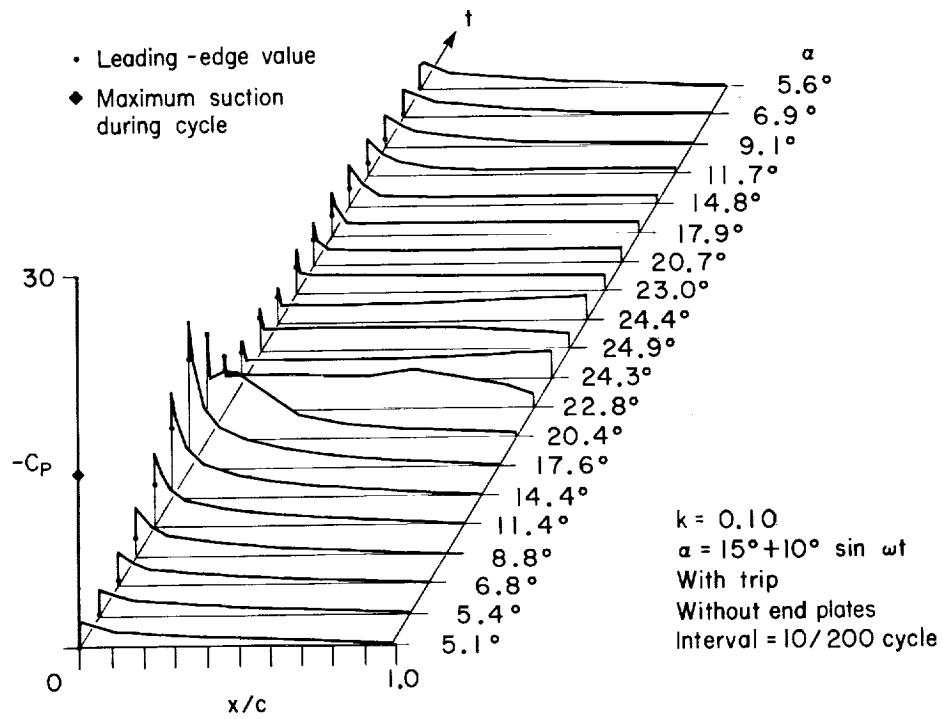
(b) $\alpha = 15^\circ + 10^\circ \sin \omega t, k = 0.020.$

Figure 55.— Continued.



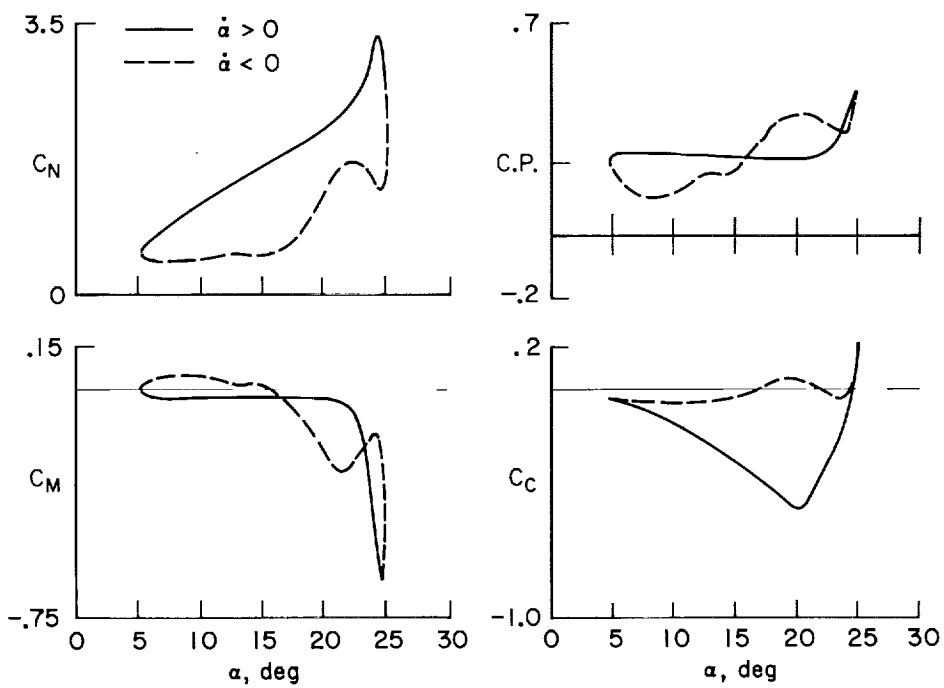
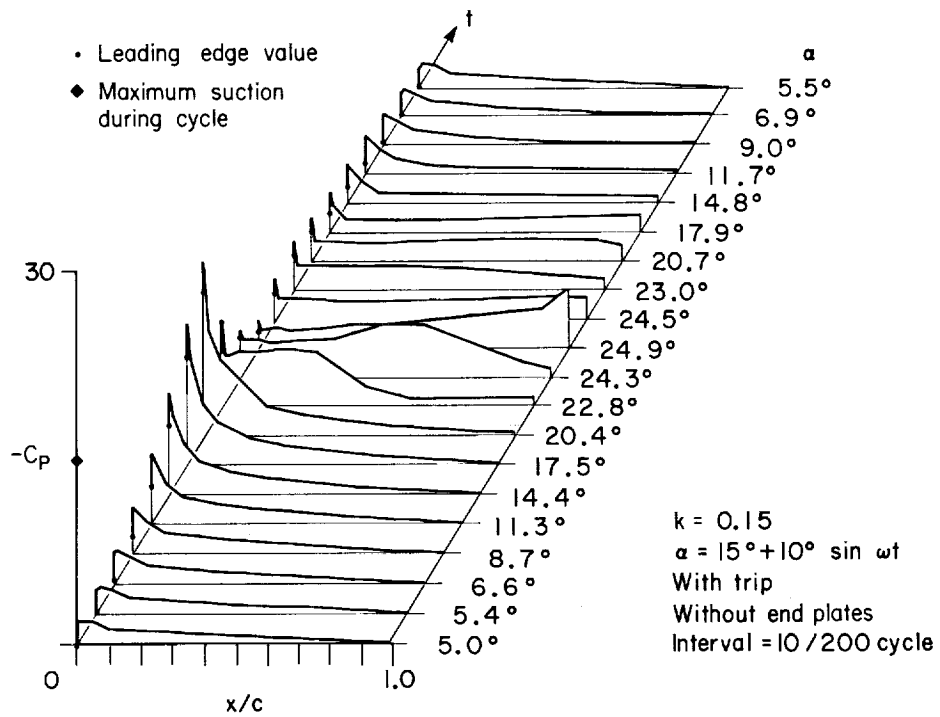
(c) $\alpha = 15^\circ + 10^\circ \sin \omega t, k = 0.050$.

Figure 55.— Continued.



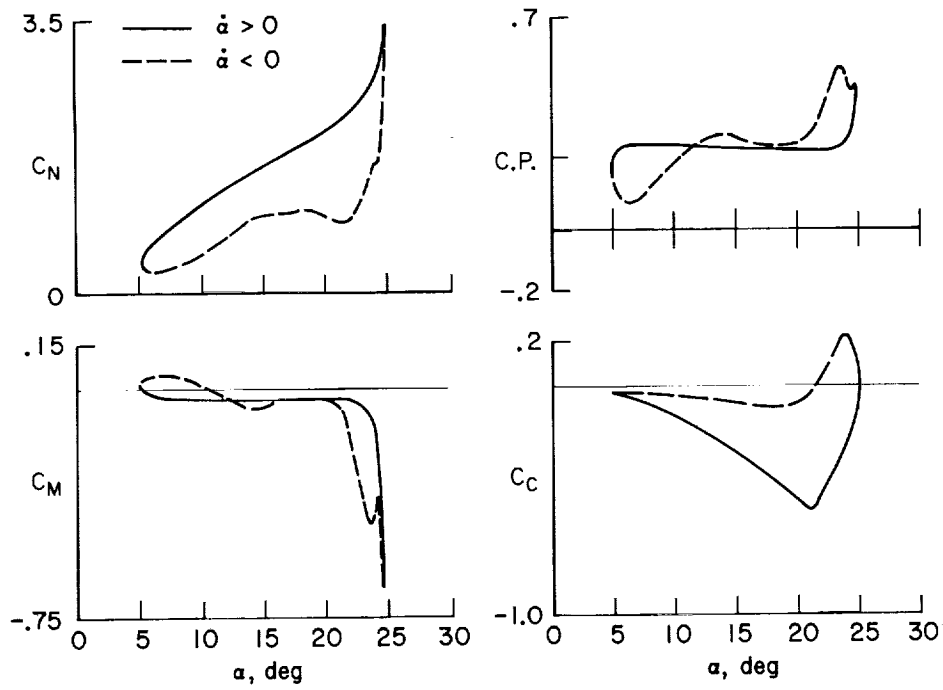
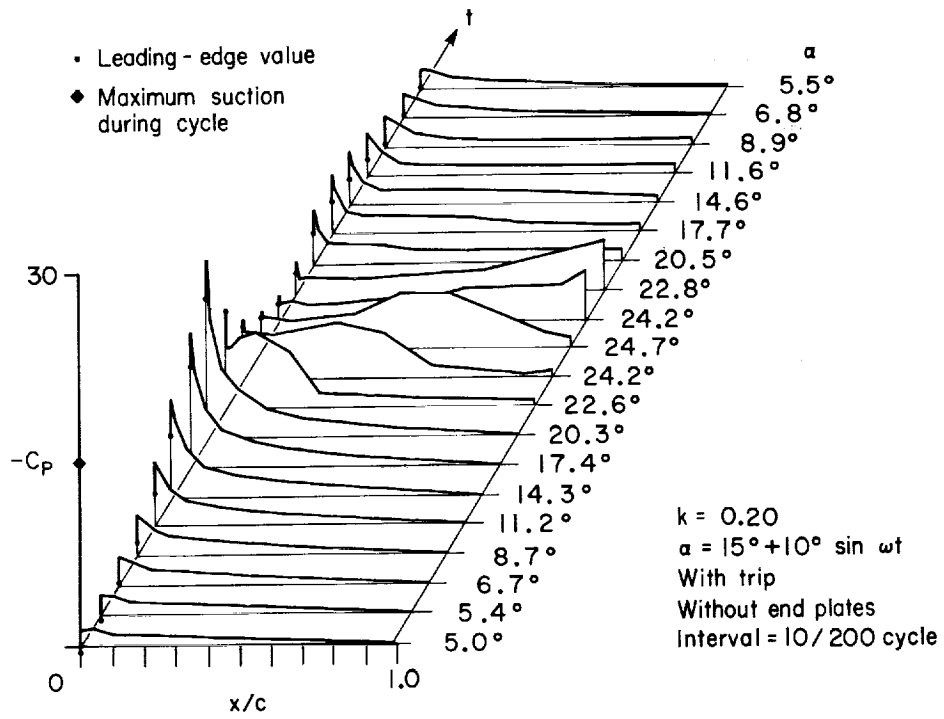
(d) $\alpha = 15^\circ + 10^\circ \sin \omega t, k = 0.100$.

Figure 55.— Continued.



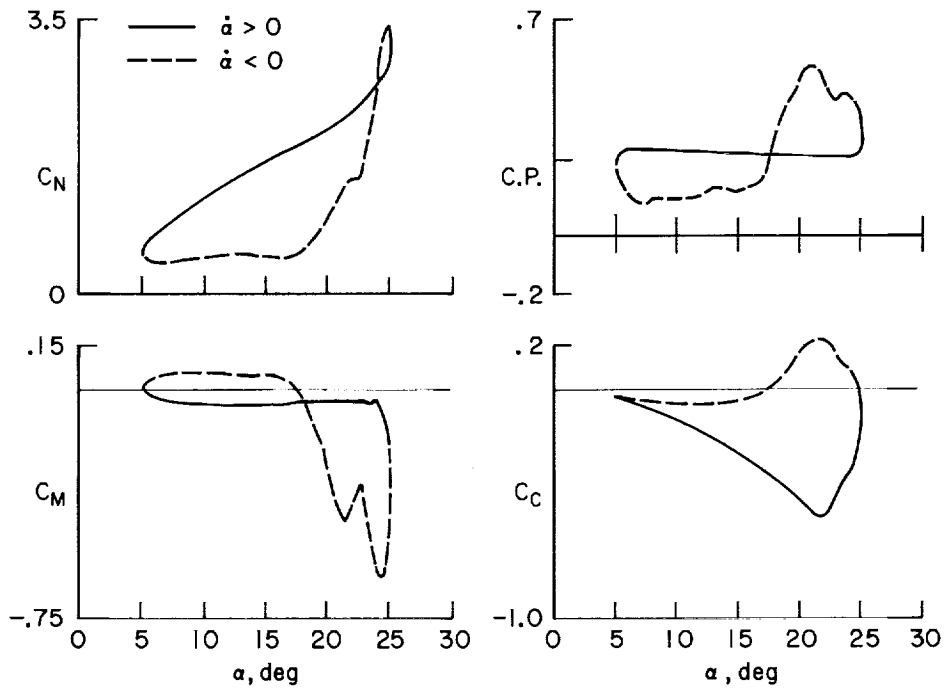
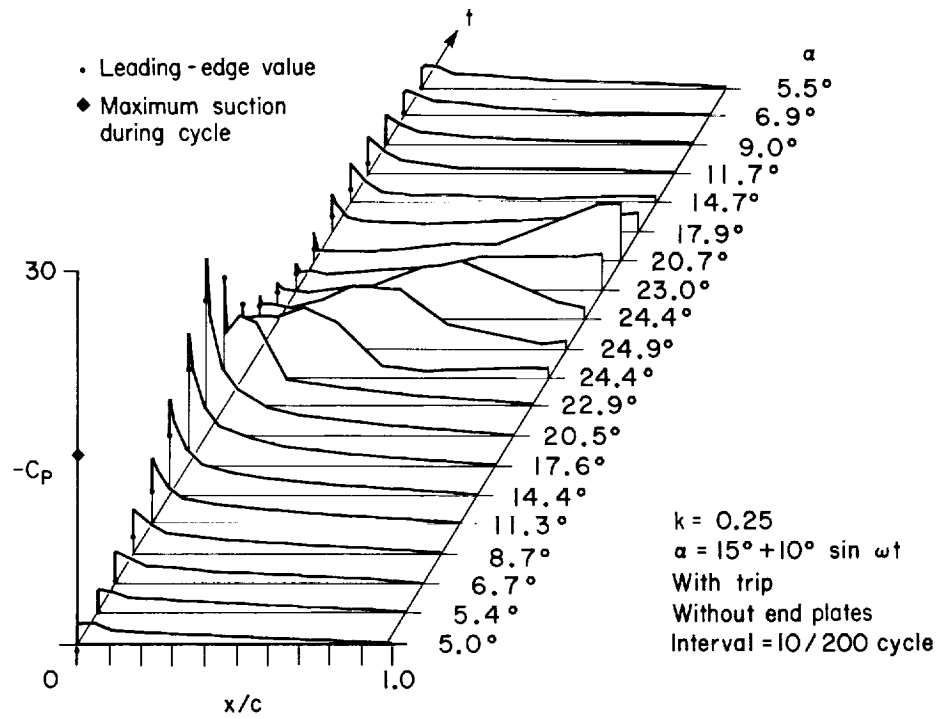
(e) $\alpha = 15^\circ + 10^\circ \sin \omega t, k = 0.150$.

Figure 55.— Continued.



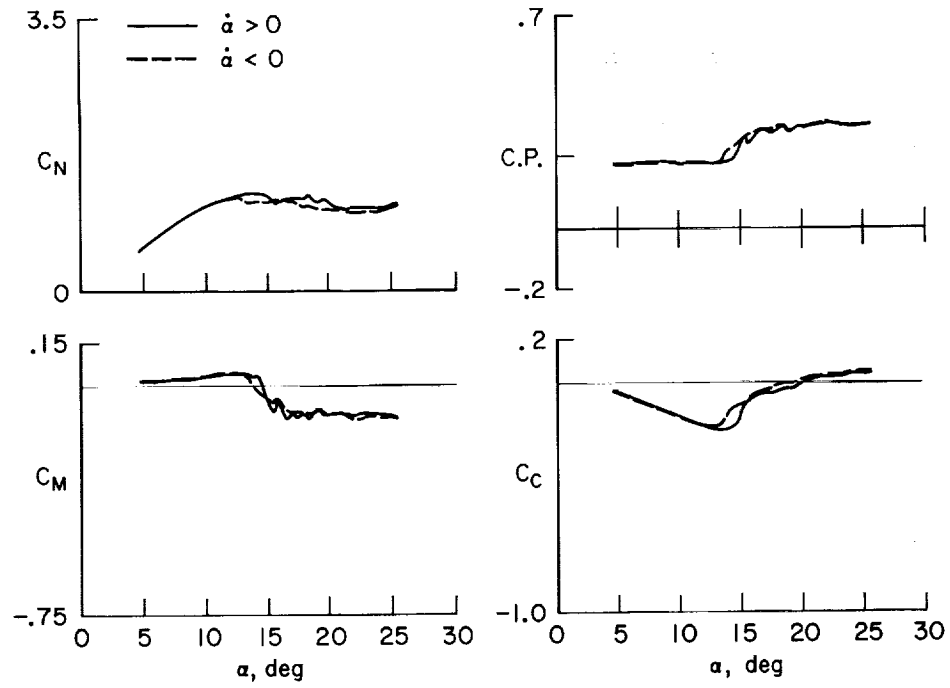
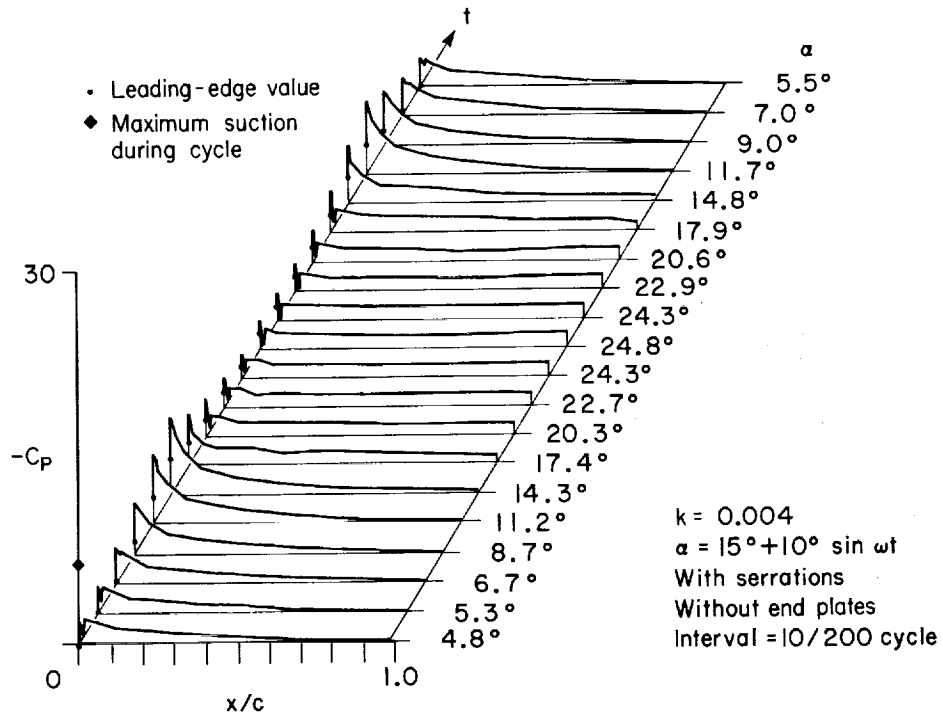
(f) $\alpha = 15^\circ + 10^\circ \sin \omega t, k = 0.200$.

Figure 55.— Continued.



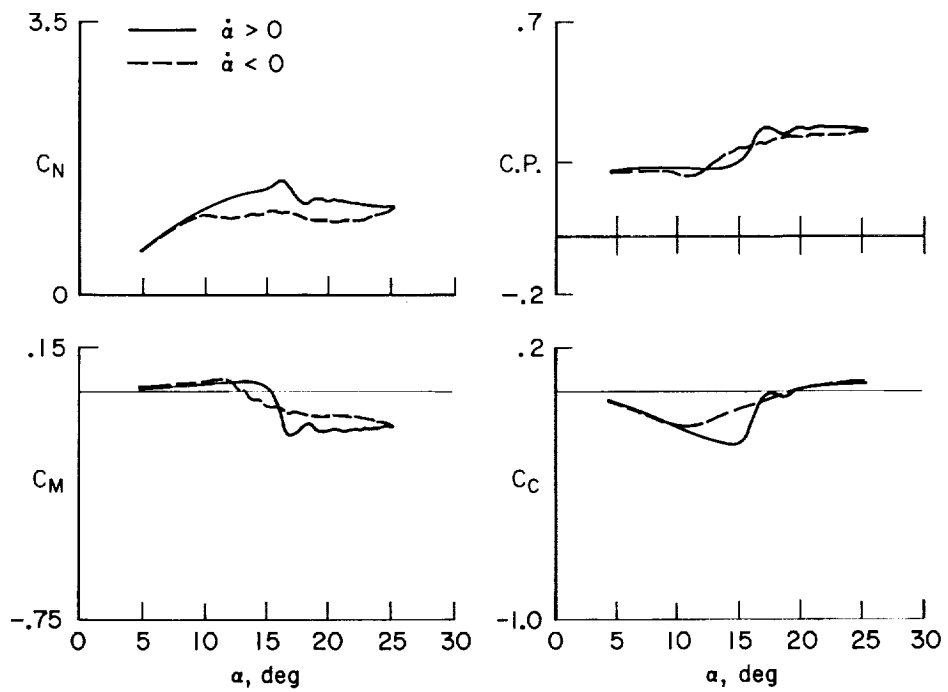
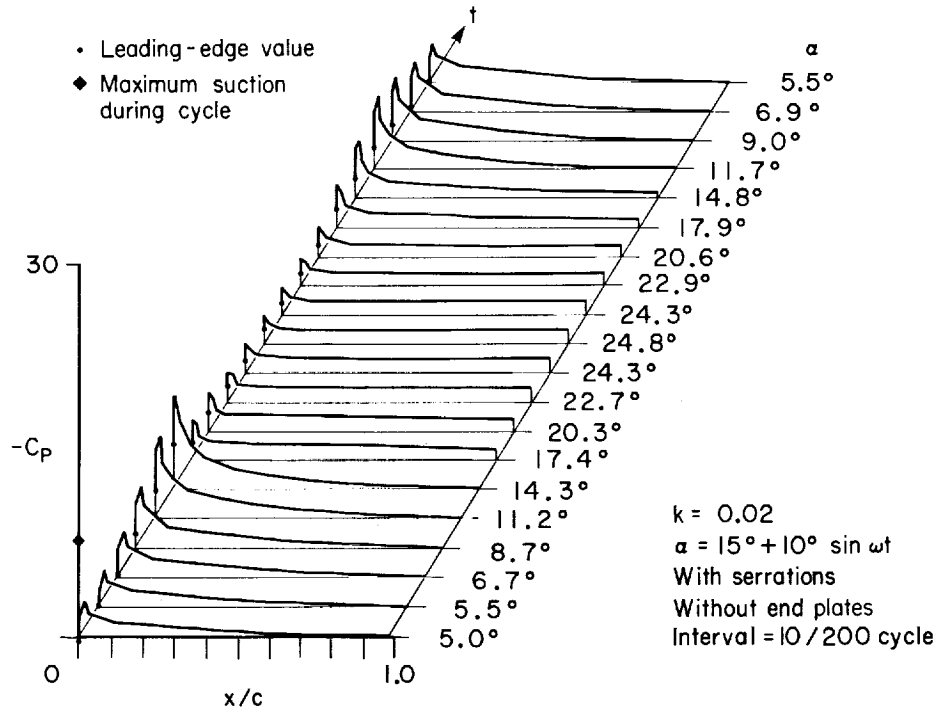
(g) $\alpha = 15^\circ + 10^\circ \sin \omega t, k = 0.250$.

Figure 55.— Concluded.



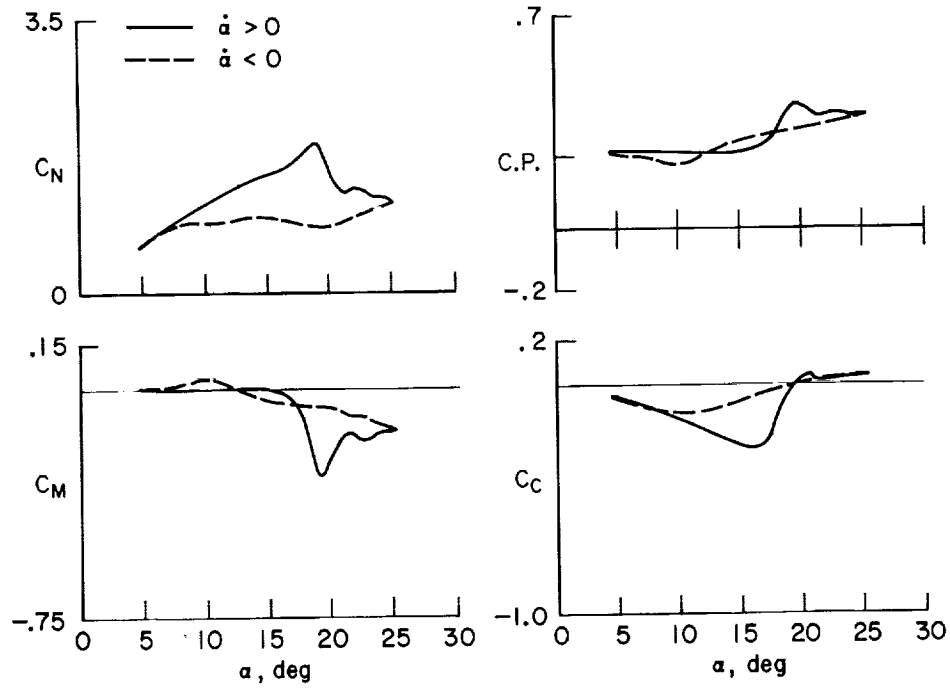
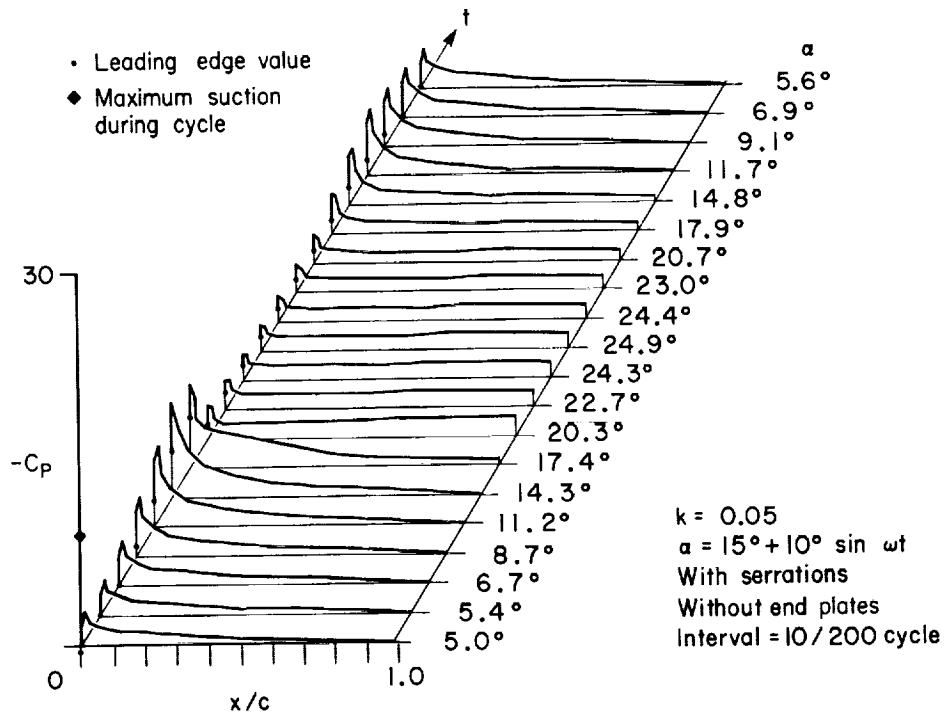
(a) $\alpha = 15^\circ + 10^\circ \sin \omega t, k = 0.004$.

Figure 56.— Aerodynamic loads on NACA 0012 with serrations.



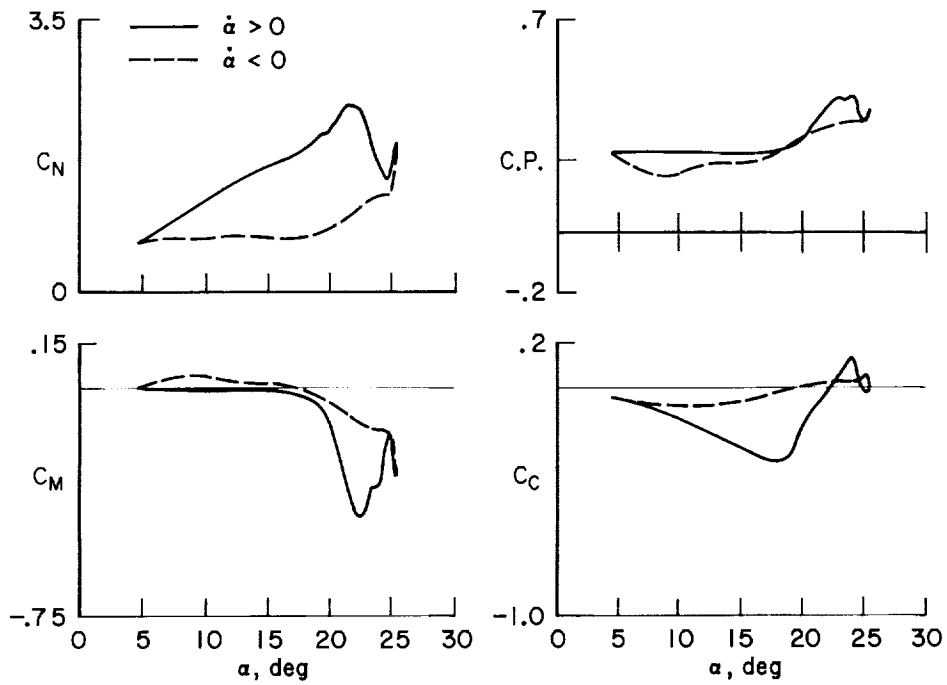
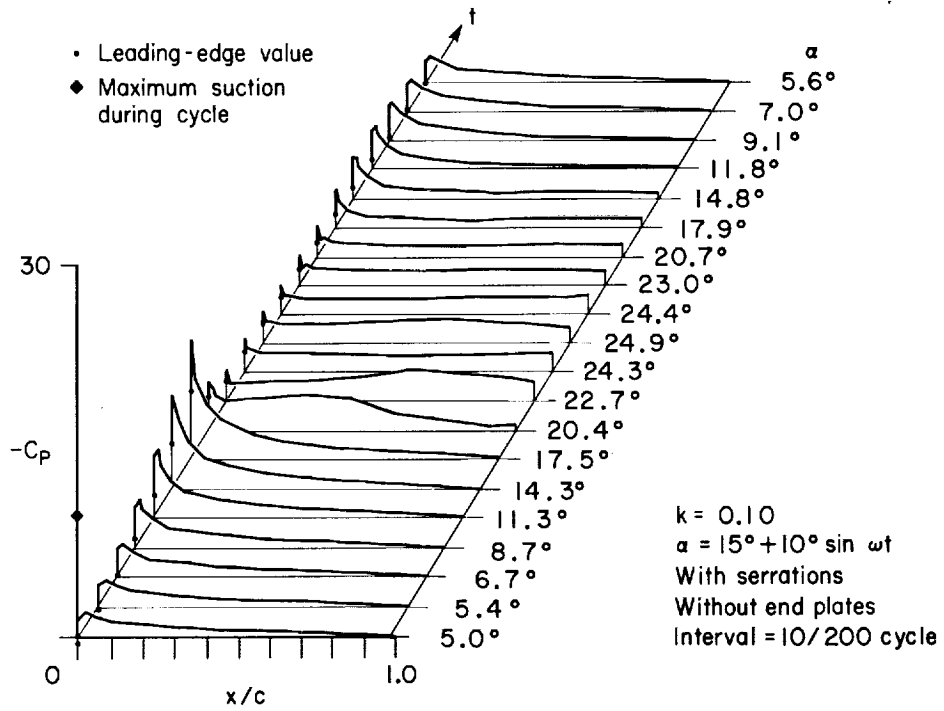
(b) $\alpha = 15^\circ + 10^\circ \sin \omega t, k = 0.020$.

Figure 56.— Continued.



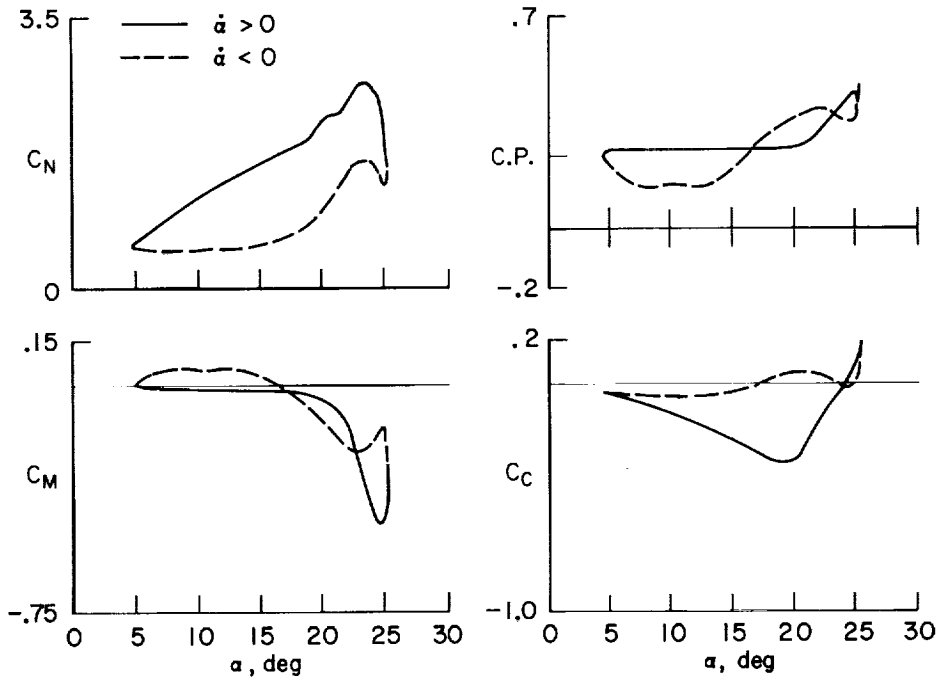
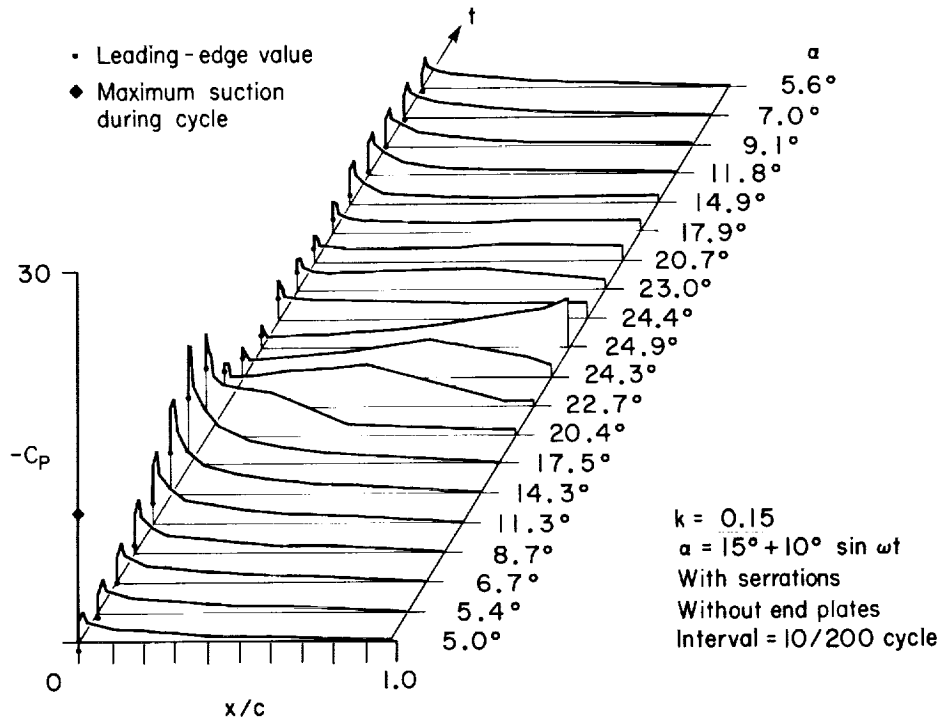
(c) $\alpha = 15^\circ + 10^\circ \sin \omega t, k = 0.050$.

Figure 56.— Continued.



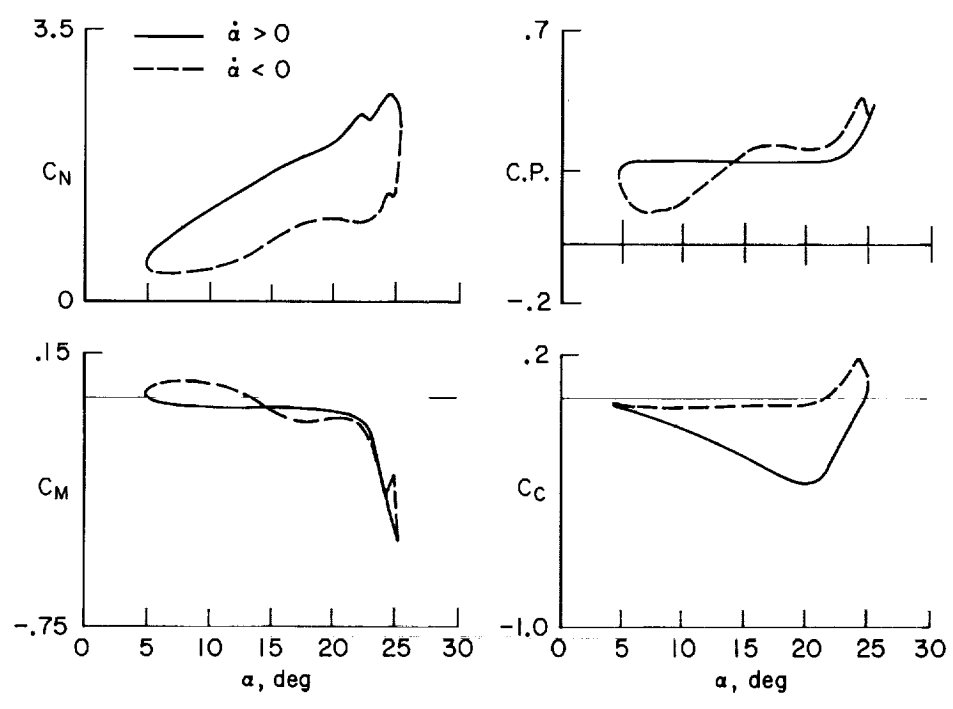
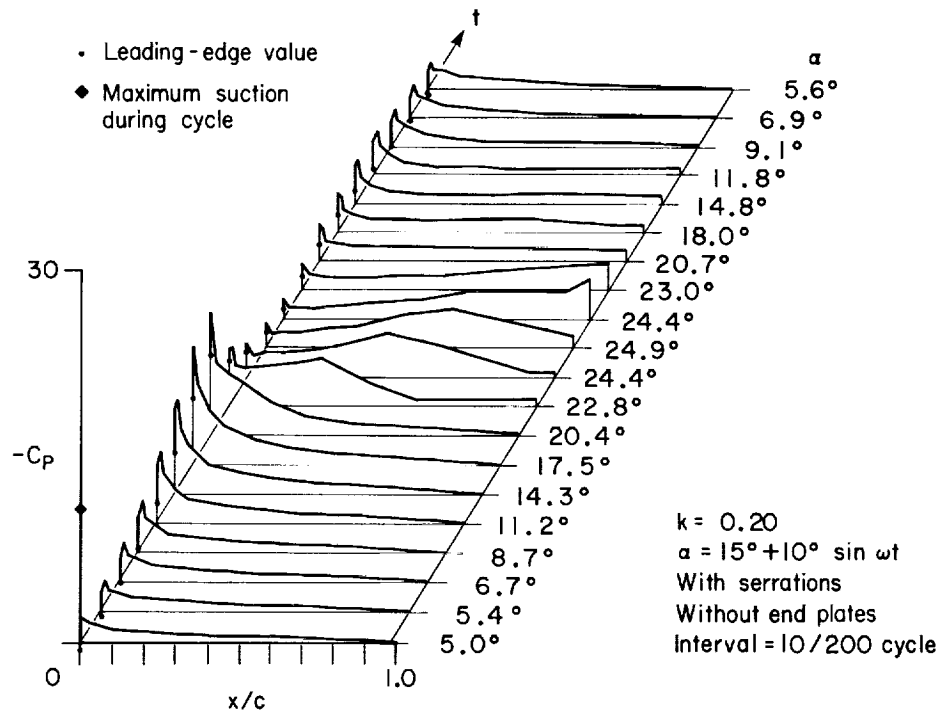
(d) $\alpha = 15^\circ + 10^\circ \sin \omega t$, $k = 0.100$.

Figure 56.— Continued.



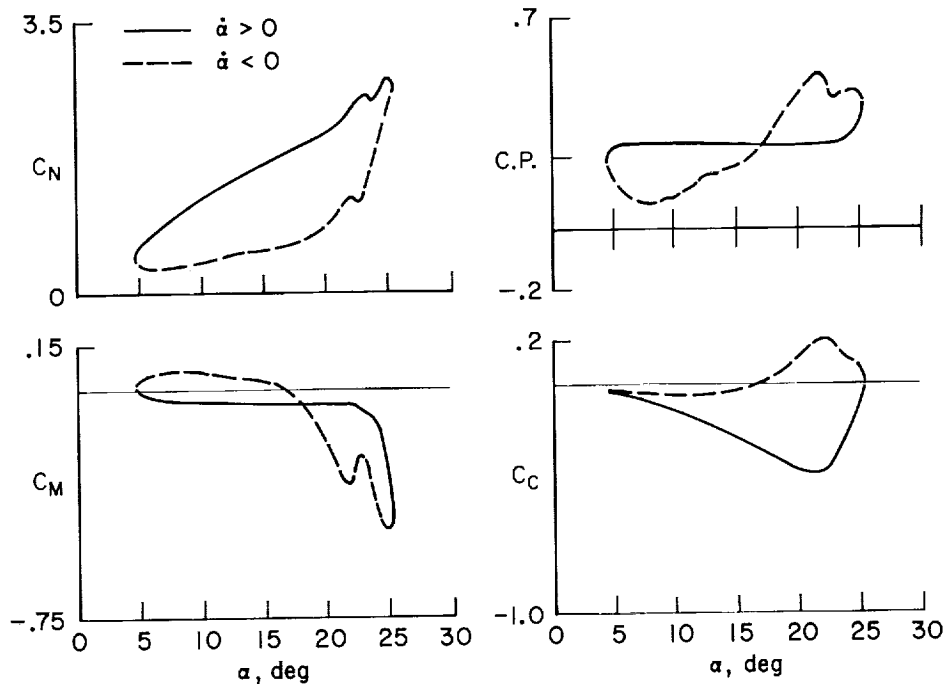
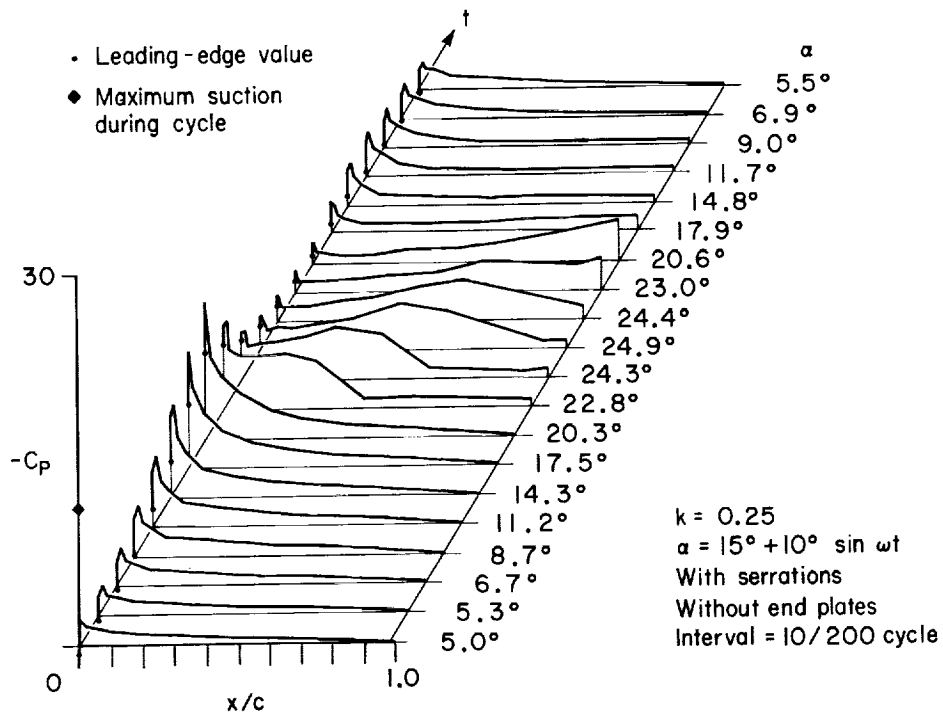
(e) $\alpha = 15^\circ + 10^\circ \sin \omega t, k = 0.150$.

Figure 56.— Continued.



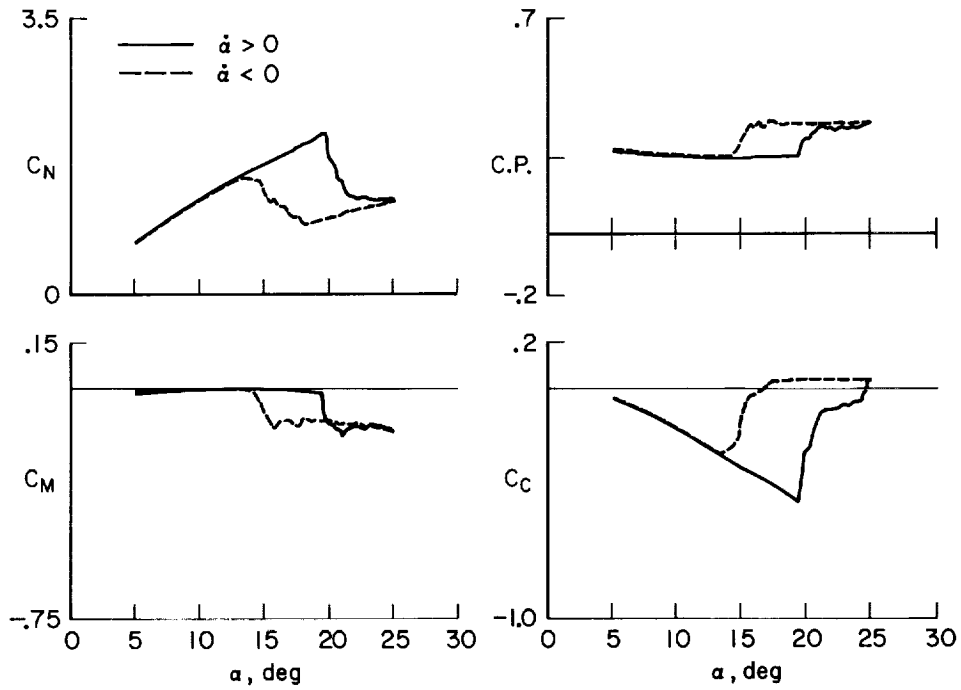
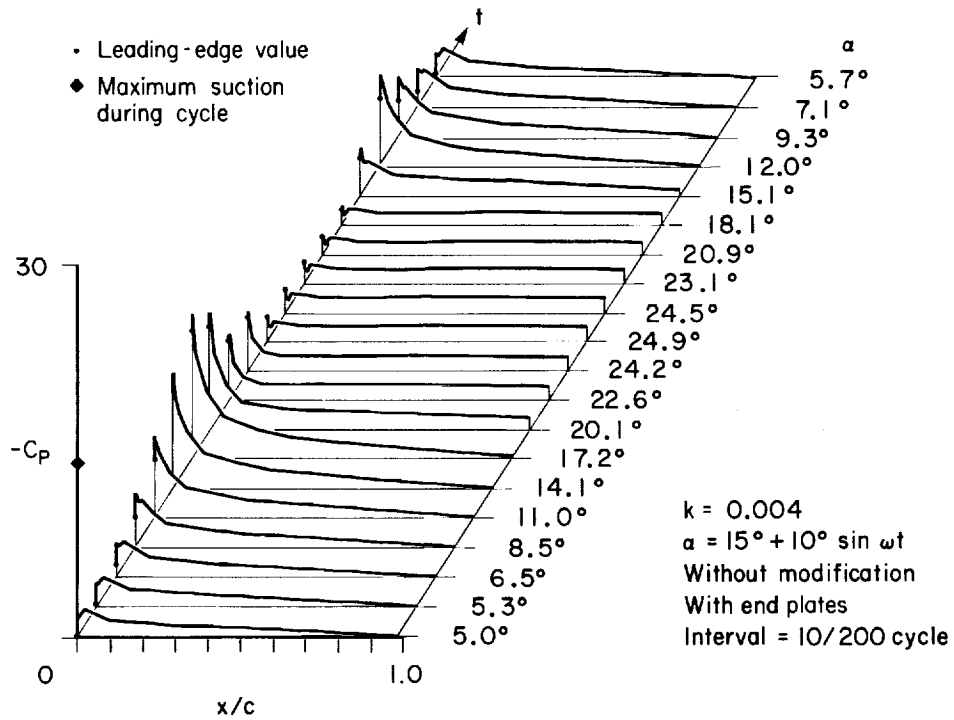
(f) $\alpha = 15^\circ + 10^\circ \sin \omega t, k = 0.200.$

Figure 56.— Continued.



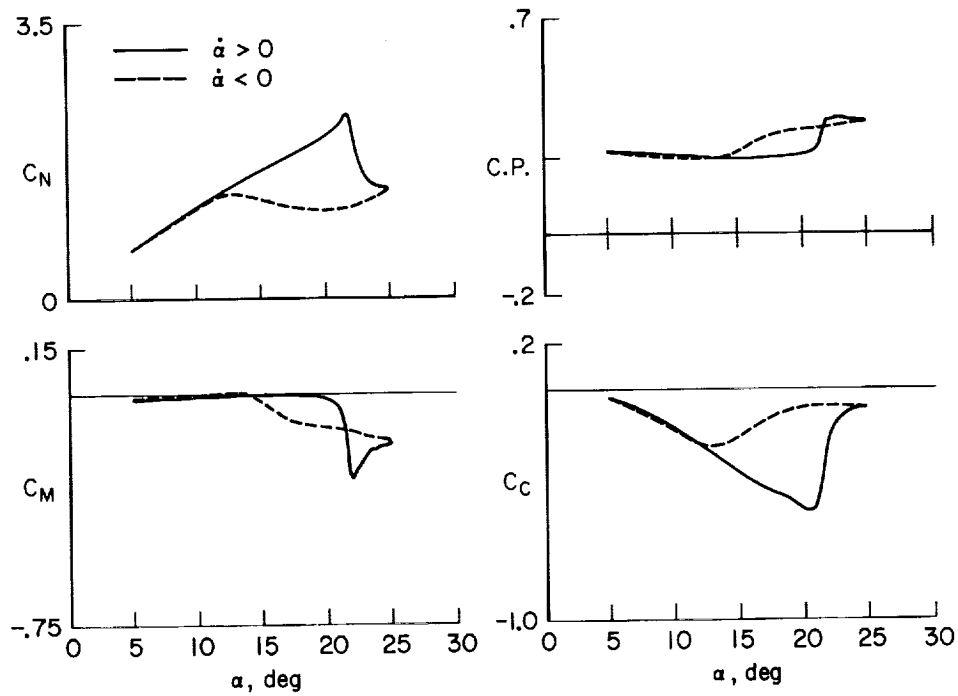
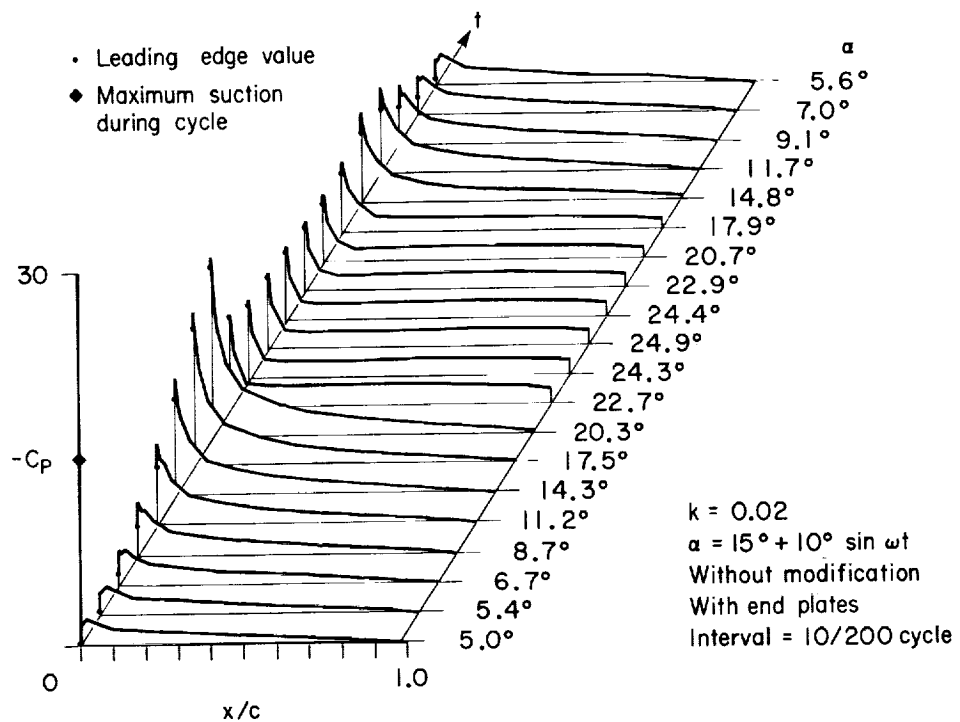
(g) $\alpha = 15^\circ + 10^\circ \sin \omega t$, $k = 0.250$.

Figure 56.— Concluded.



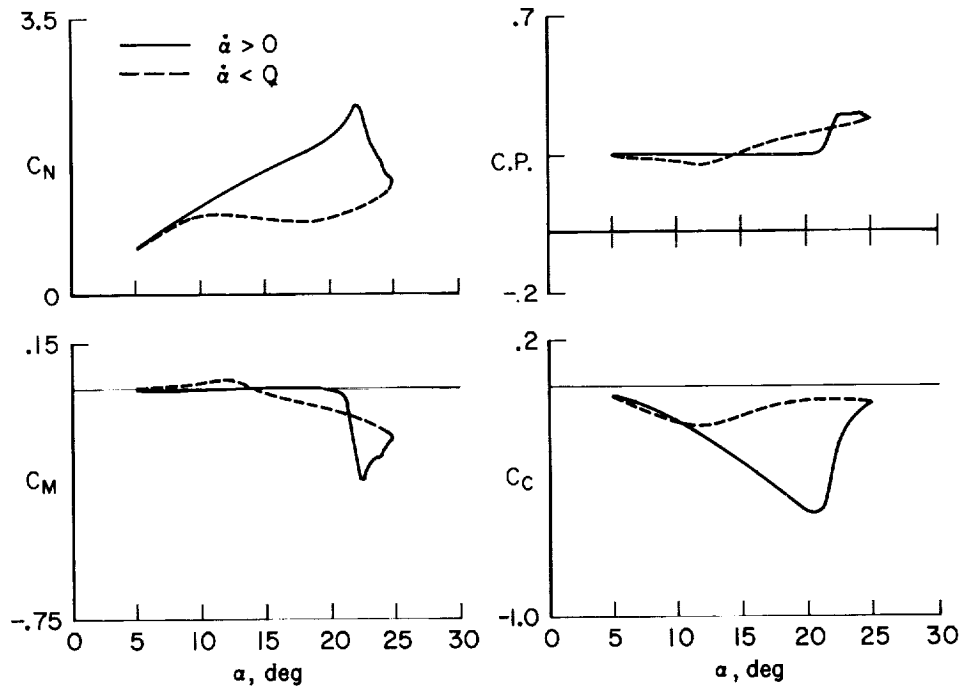
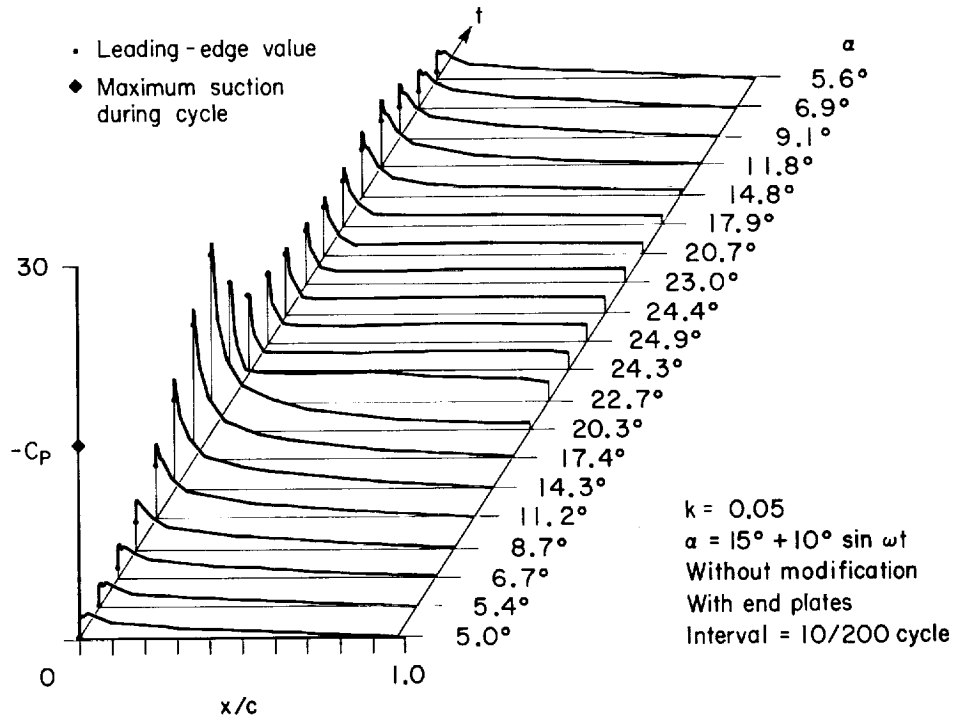
(a) $\alpha = 15^\circ + 10^\circ \sin \omega t, k = 0.004.$

Figure 57.— Aerodynamic loads on basic NACA 0012 with end plates.



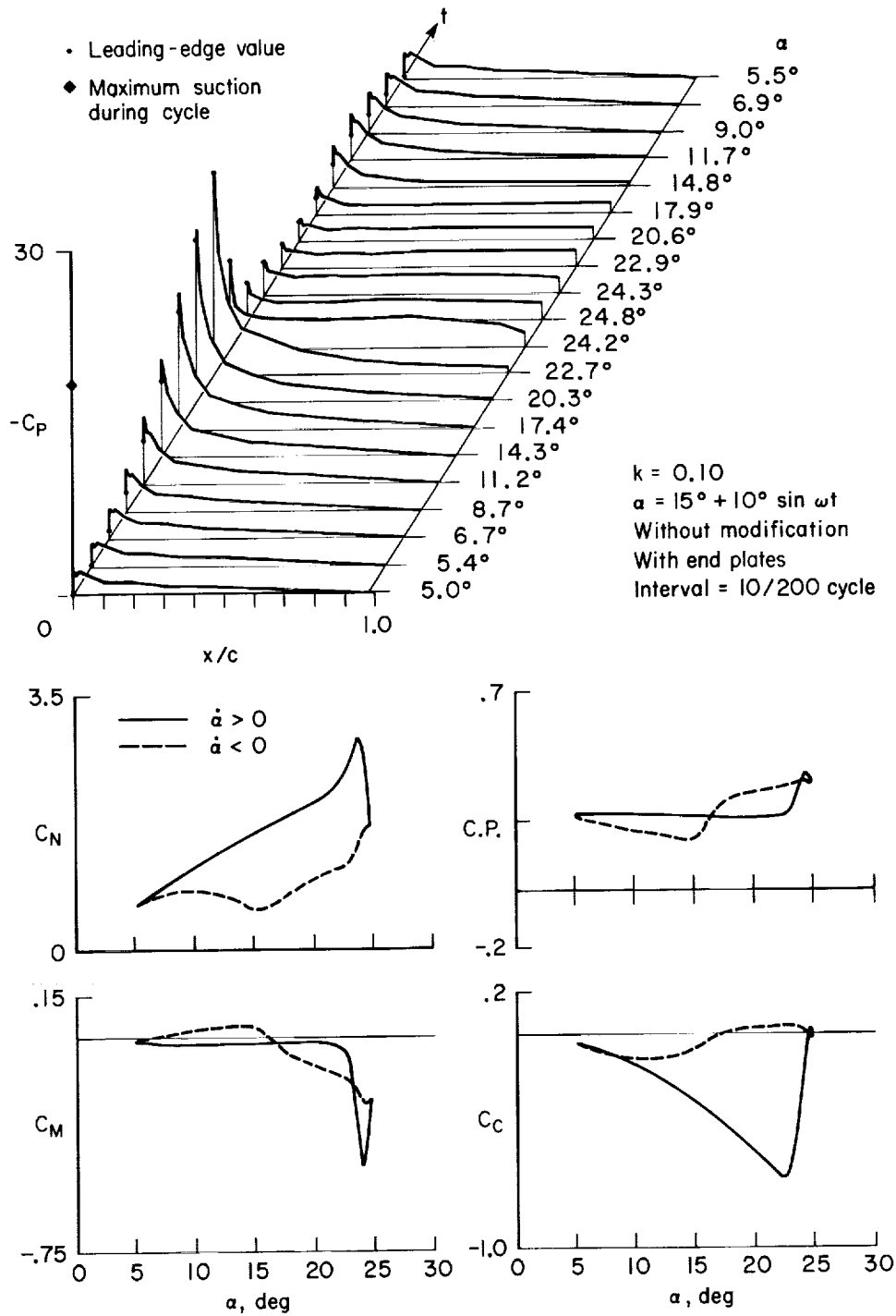
(b) $\alpha = 15^\circ + 10^\circ \sin \omega t, k = 0.020$.

Figure 57.— Continued.



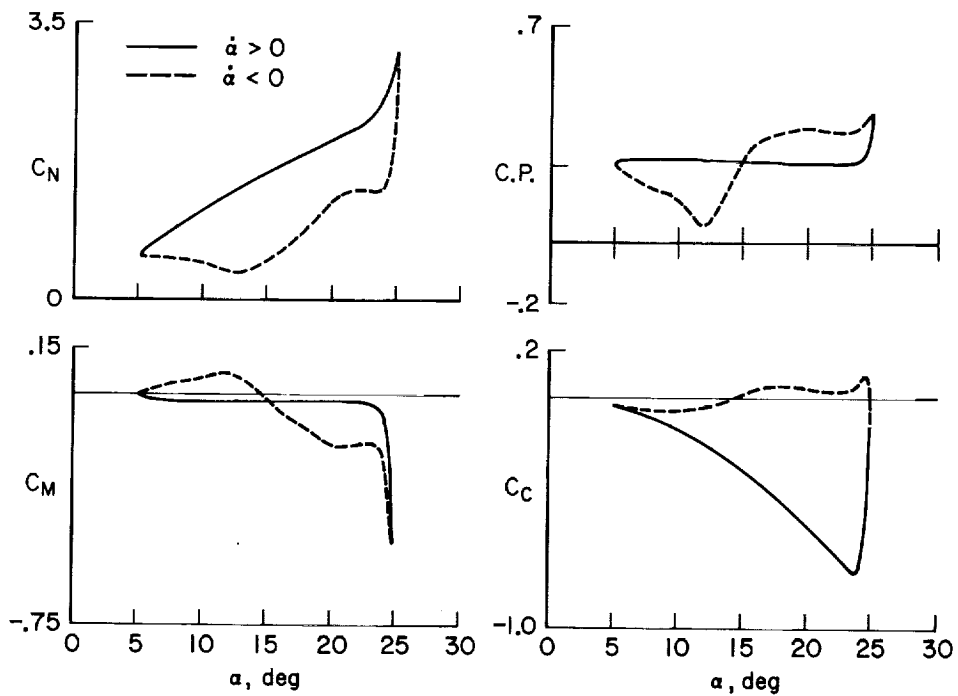
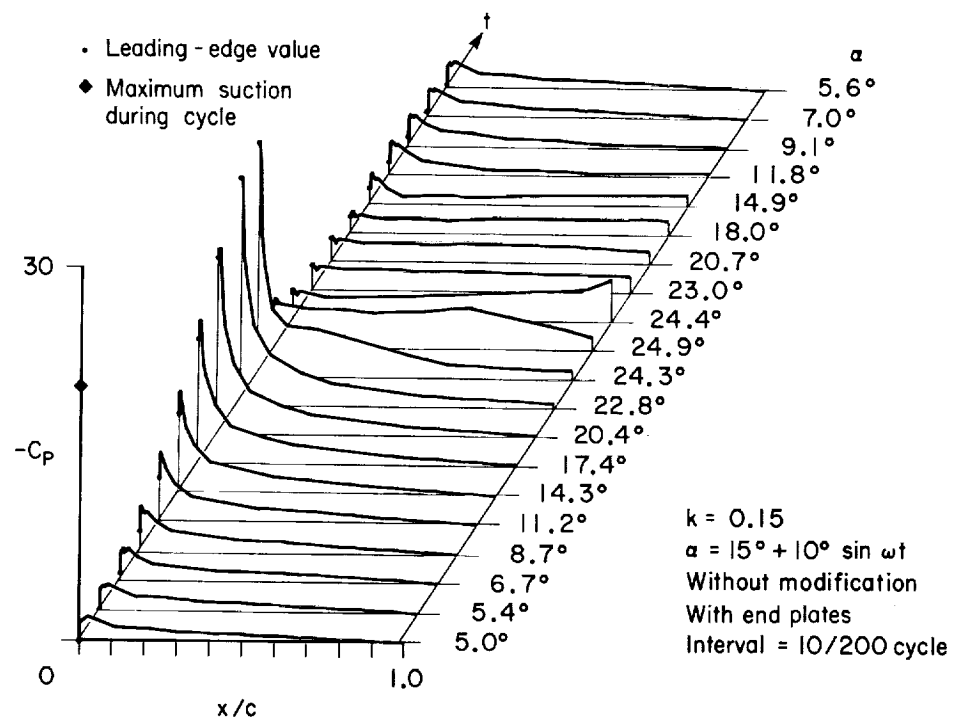
(c) $\alpha = 15^\circ + 10^\circ \sin \omega t, k = 0.050.$

Figure 57.— Continued.



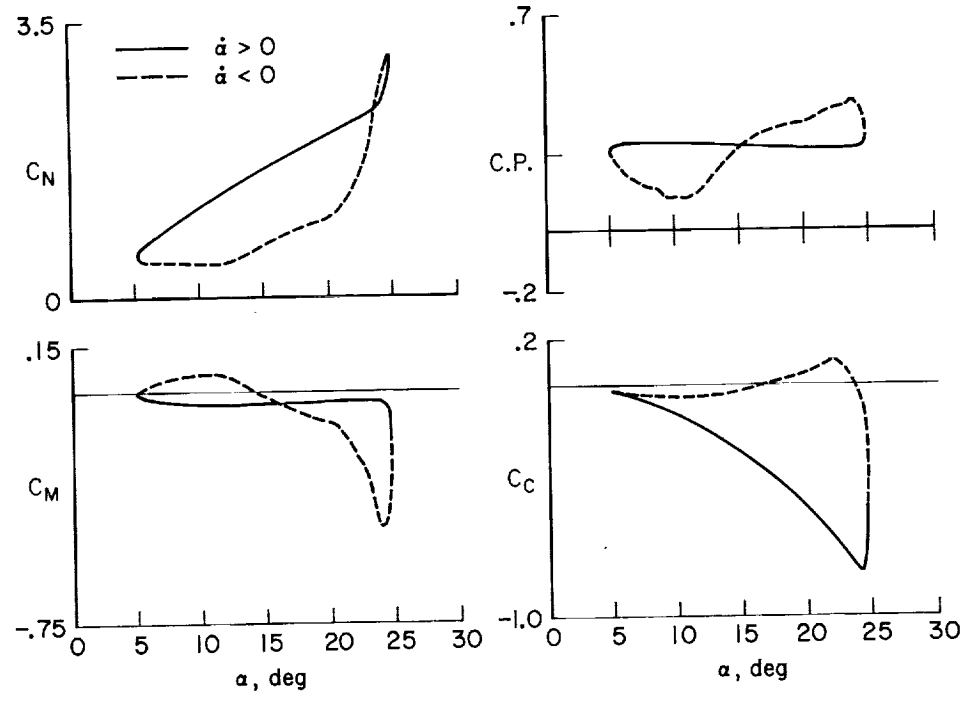
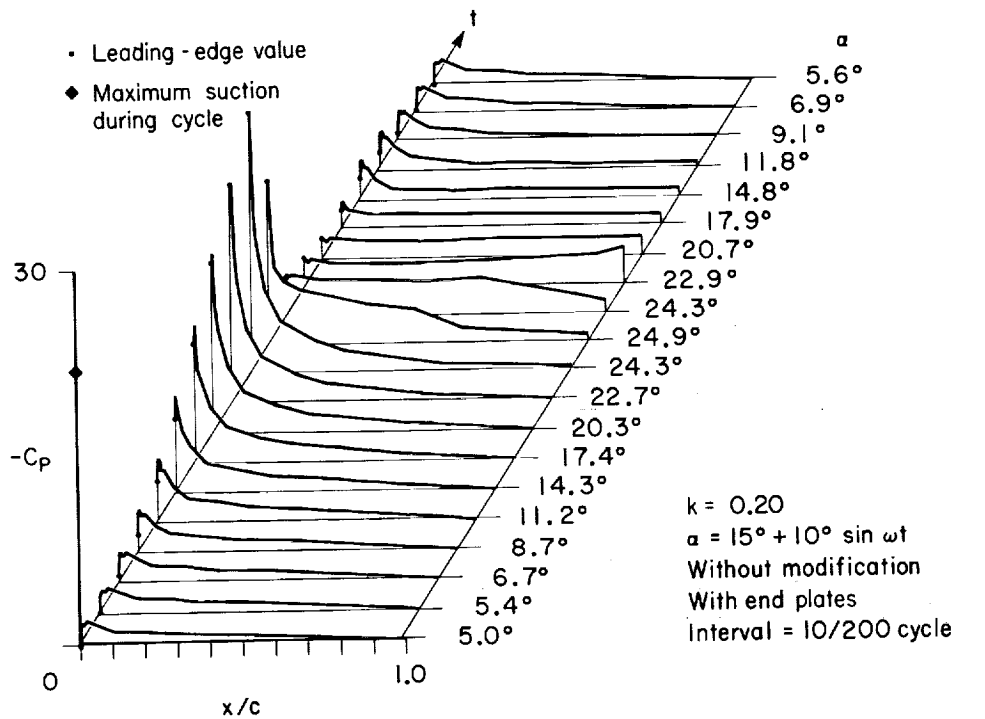
(d) $\alpha = 15^\circ + 10^\circ \sin \omega t, k = 0.100$.

Figure 57.— Continued.



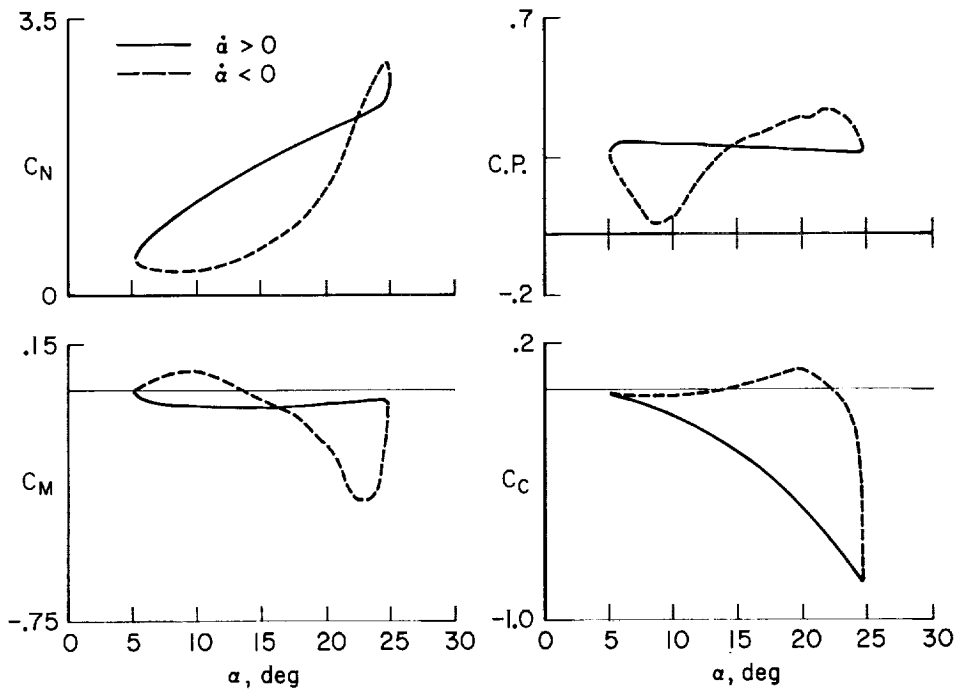
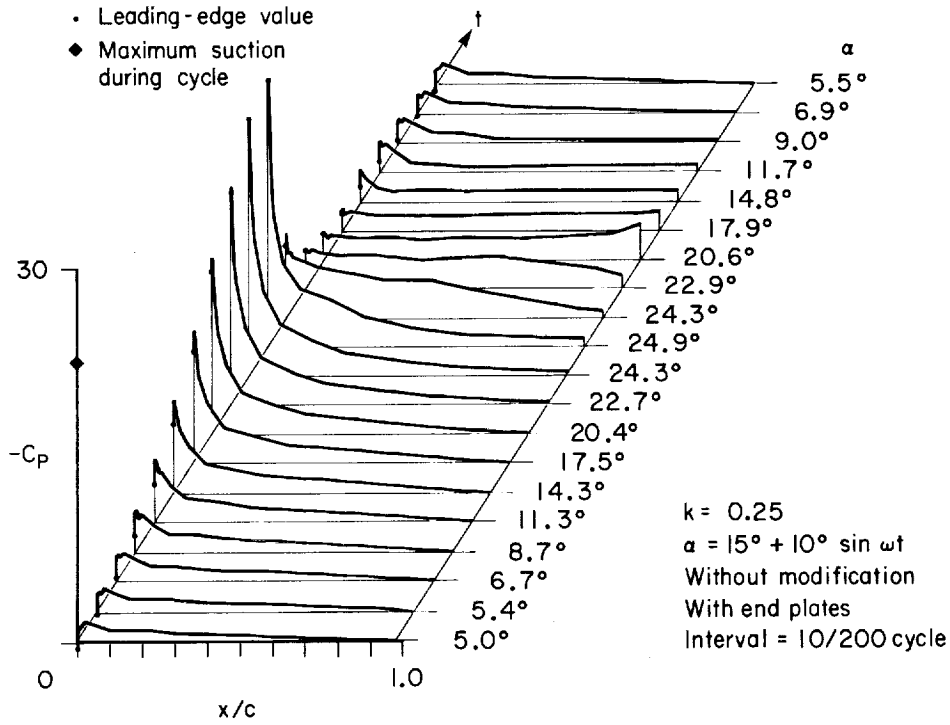
(e) $\alpha = 15^\circ + 10^\circ \sin \omega t, k = 0.150.$

Figure 57.— Continued.



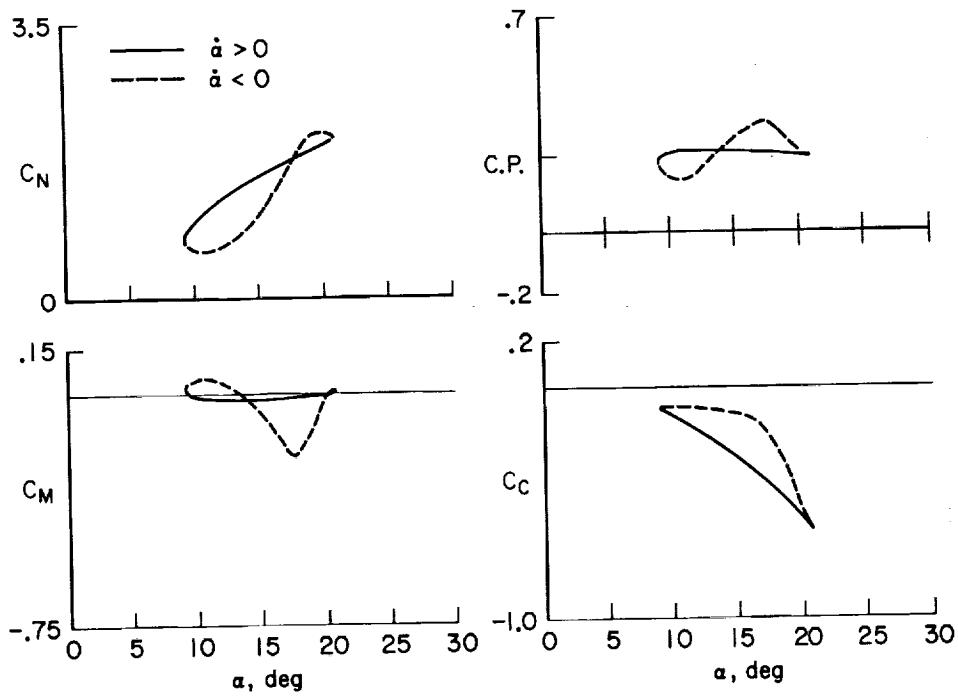
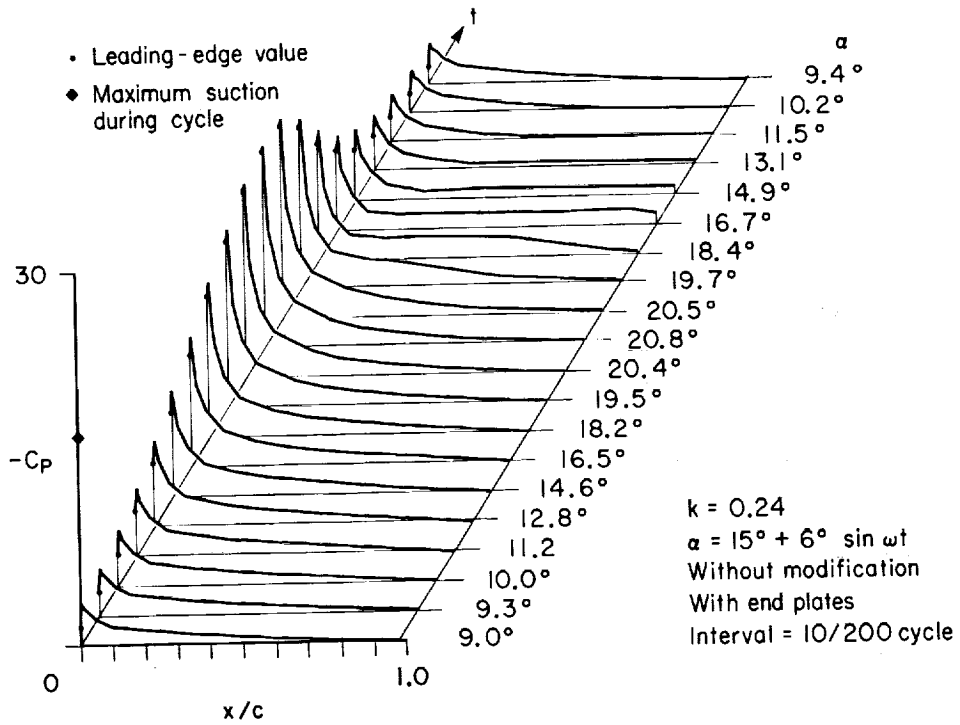
(f) $\alpha = 15^\circ + 10^\circ \sin \omega t, k = 0.200.$

Figure 57.— Continued.



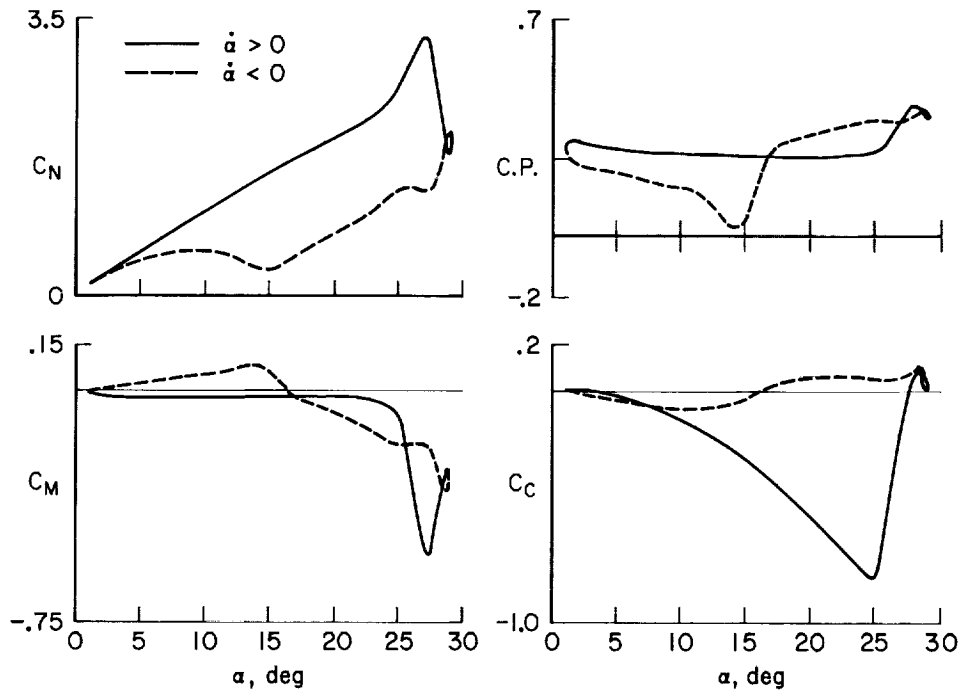
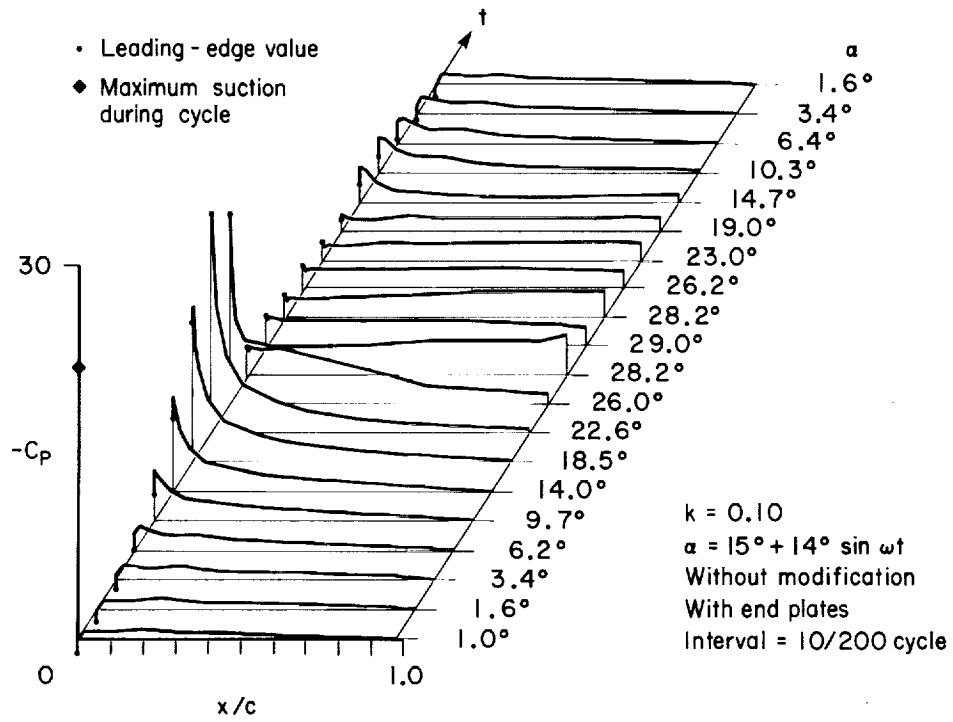
(g) $\alpha = 15^\circ + 10^\circ \sin \omega t, k = 0.250.$

Figure 57.— Continued.



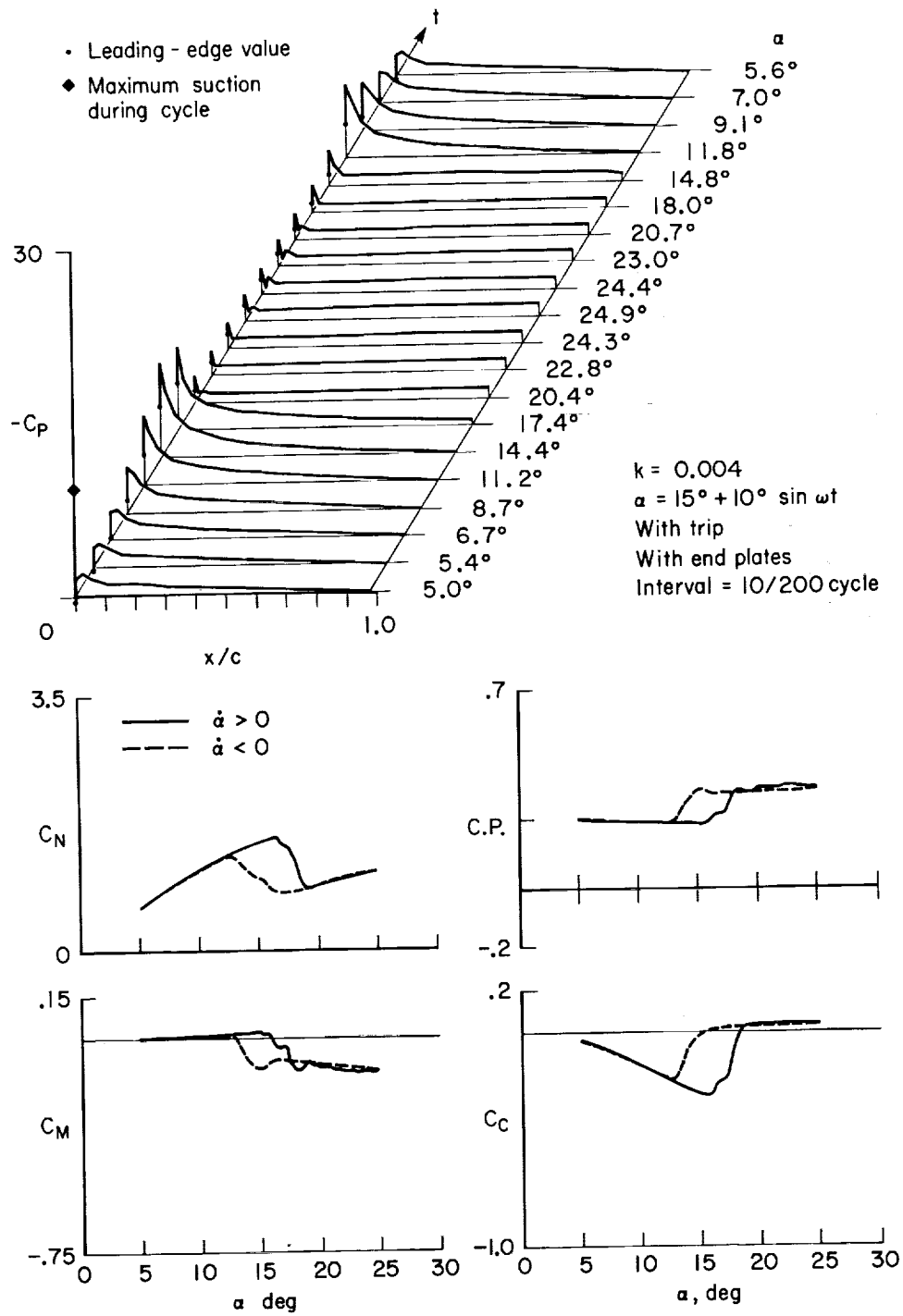
(h) $\alpha = 15^\circ + 6^\circ \sin \omega t$, $k = 0.240$.

Figure 57.— Continued.



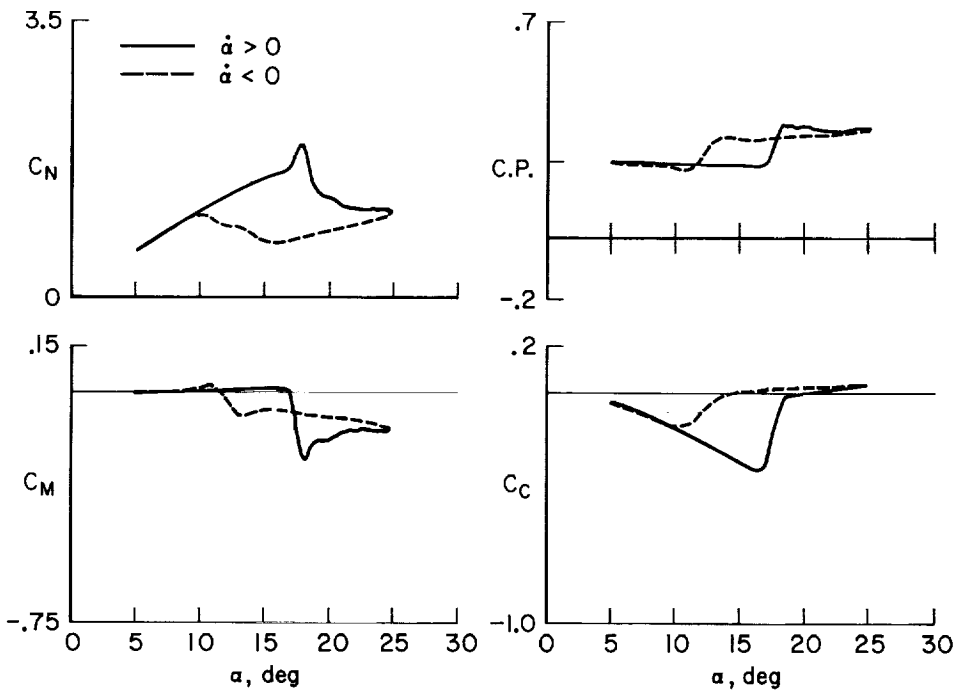
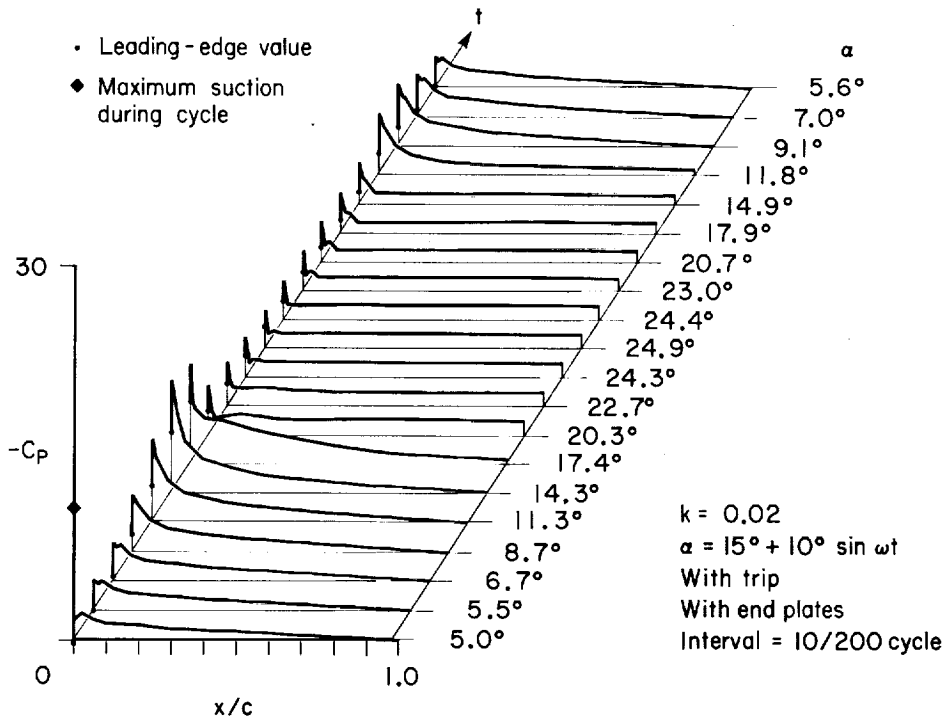
(i) $\alpha = 15^\circ + 14^\circ \sin \omega t$, $k = 0.100$.

Figure 57.— Concluded.



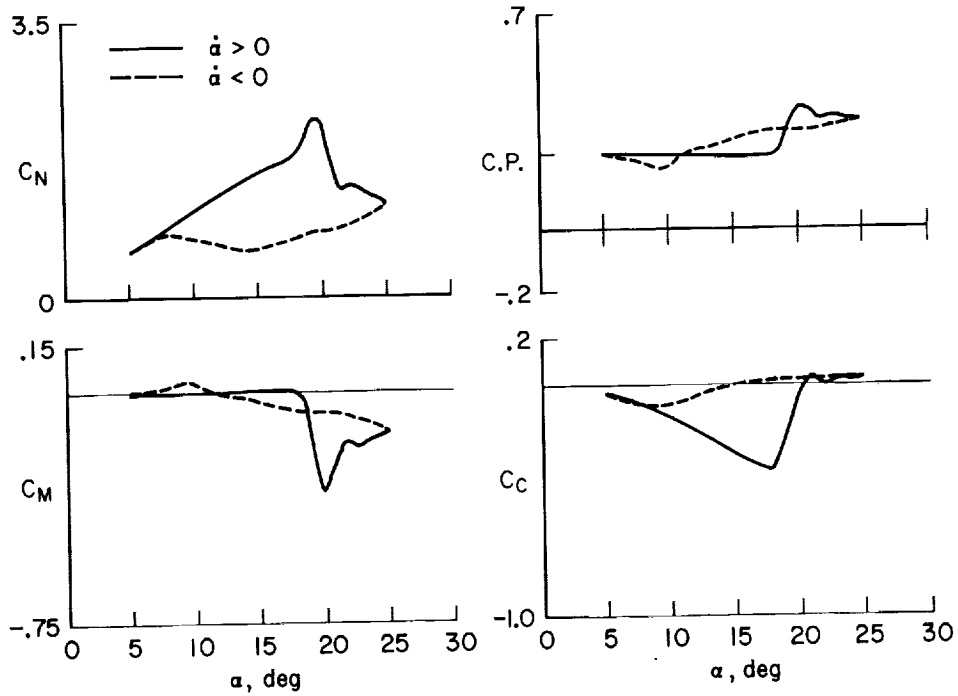
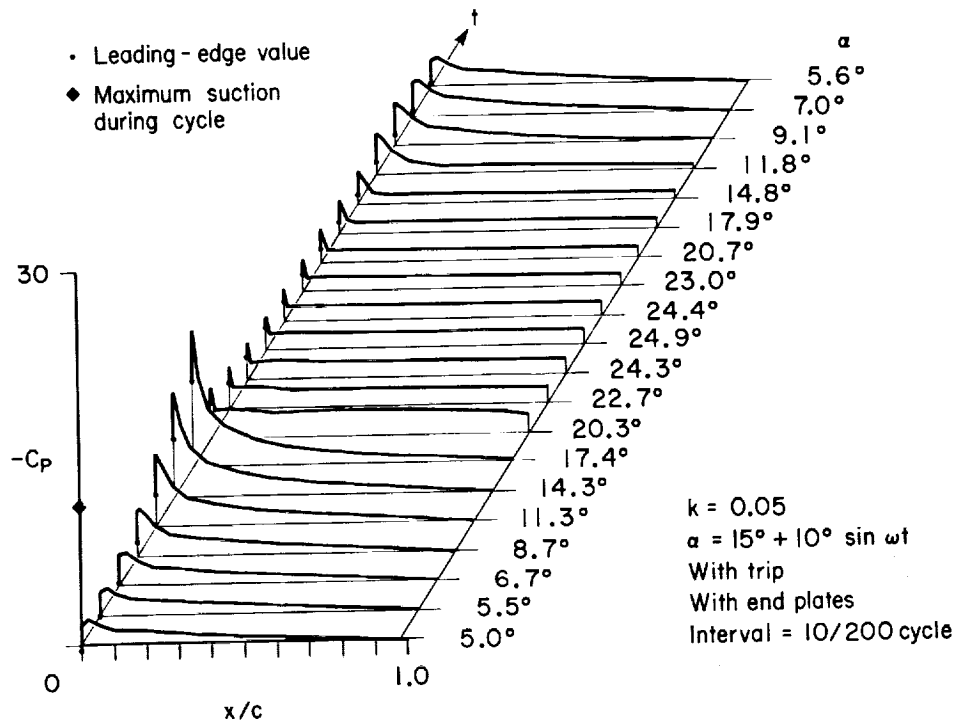
(a) $\alpha = 15^\circ + 10^\circ \sin \omega t$, $k = 0.004$.

Figure 58.— Aerodynamic loads on NACA 0012 with trip and end plates.



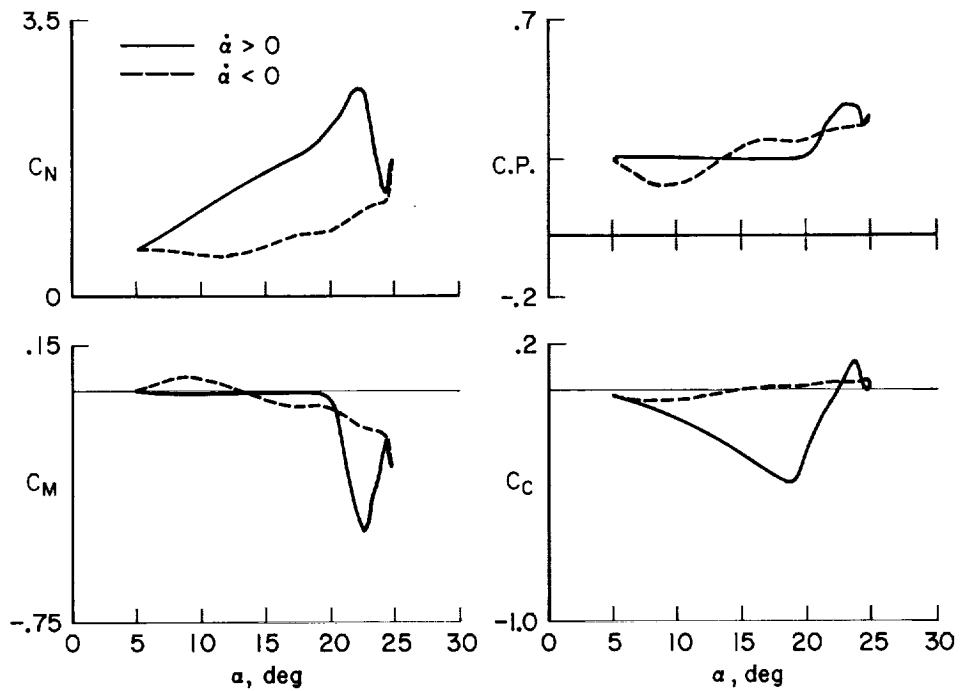
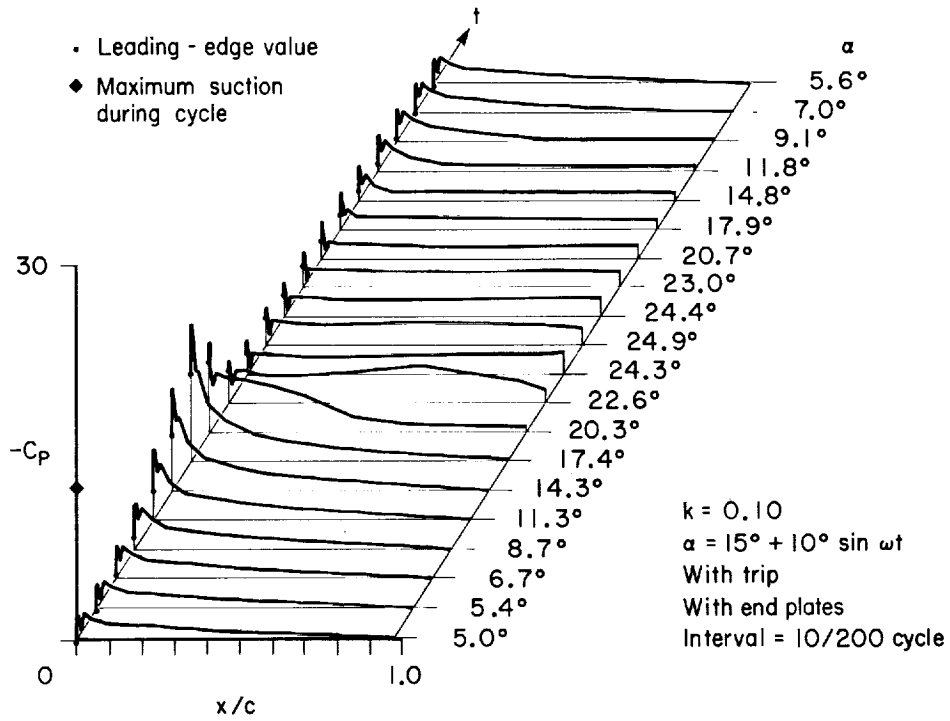
(b) $\alpha = 15^\circ + 10^\circ \sin \omega t, k = 0.020$.

Figure 58.— Continued.



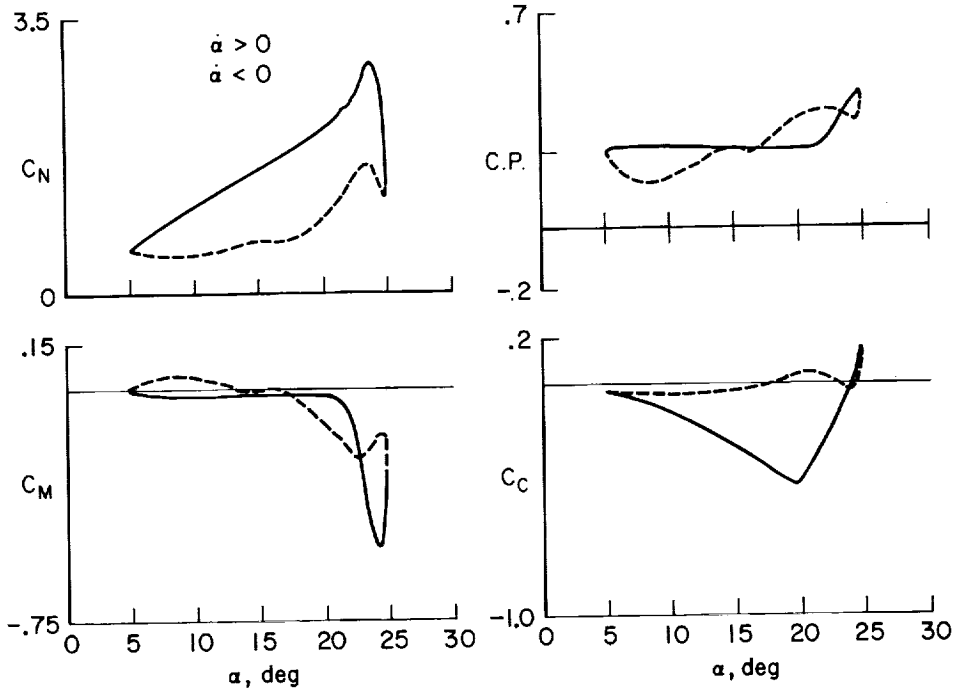
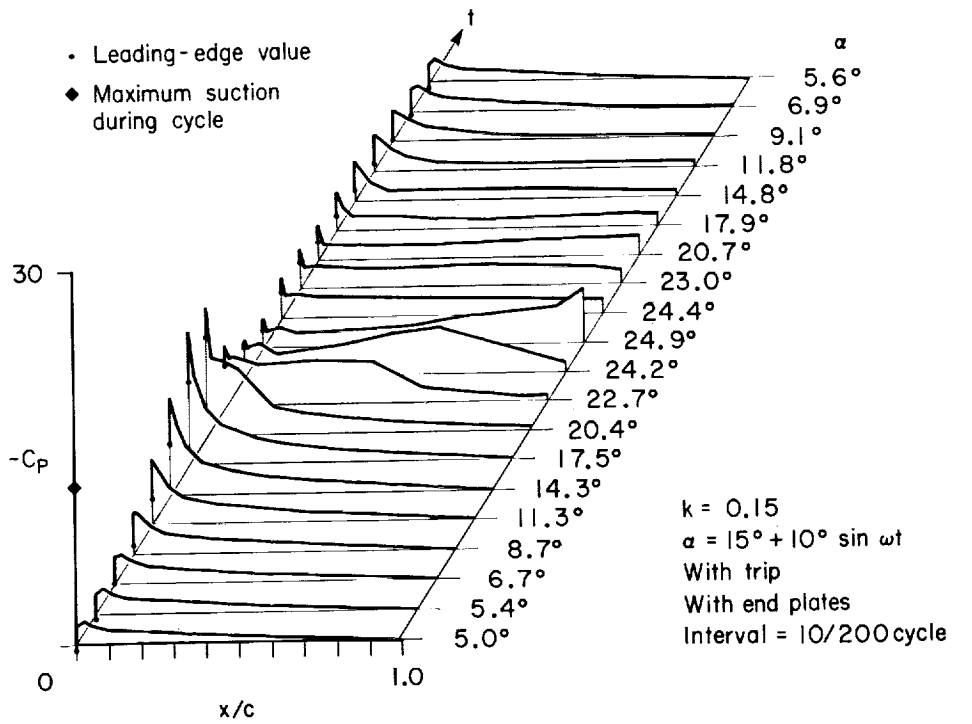
(c) $\alpha = 15^\circ + 10^\circ \sin \omega t$, $k = 0.050$.

Figure 58.— Continued.



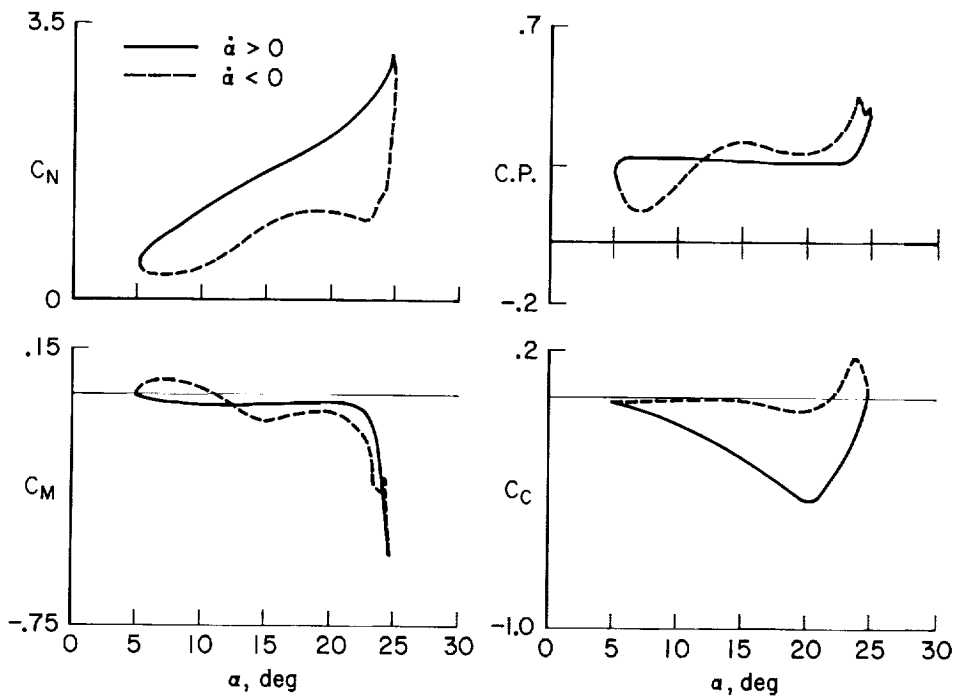
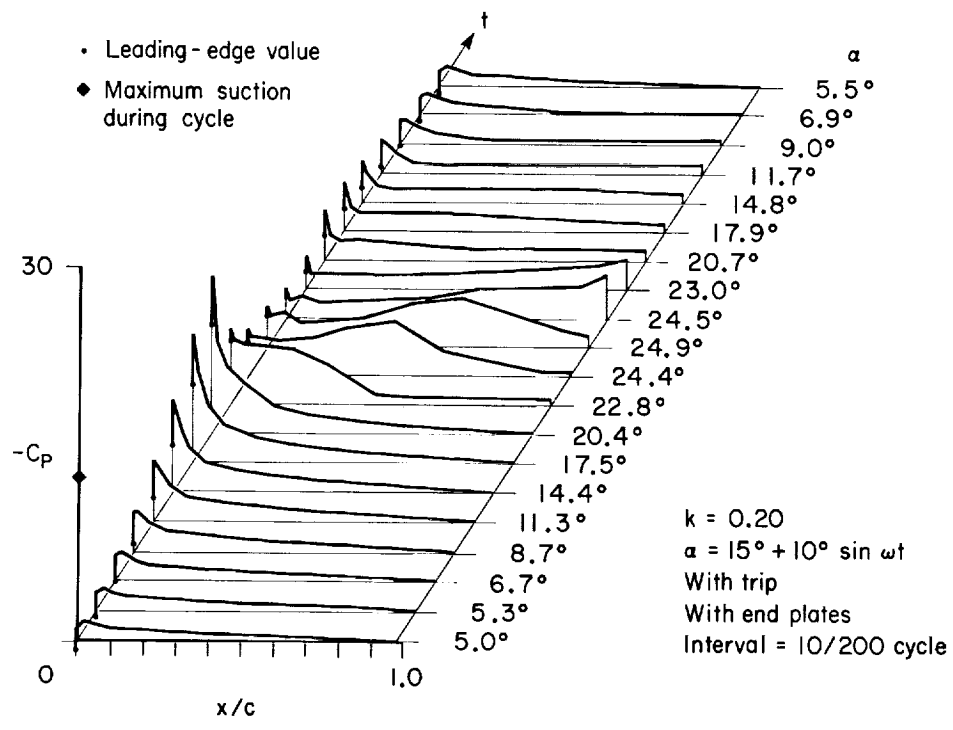
(d) $\alpha = 15^\circ + 10^\circ \sin \omega t$, $k = 0.100$.

Figure 58.— Continued.



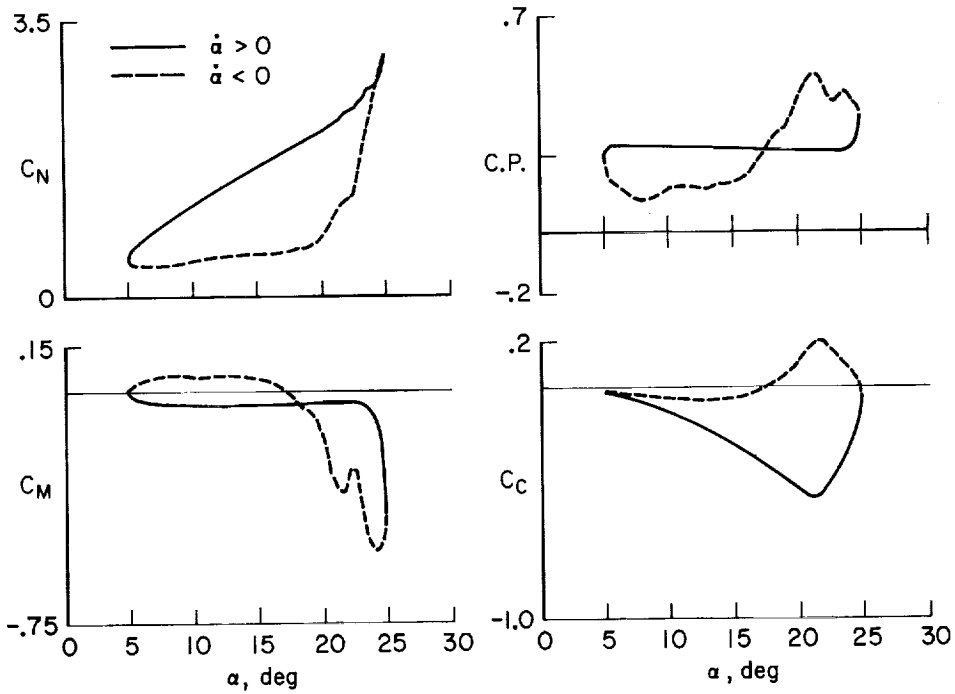
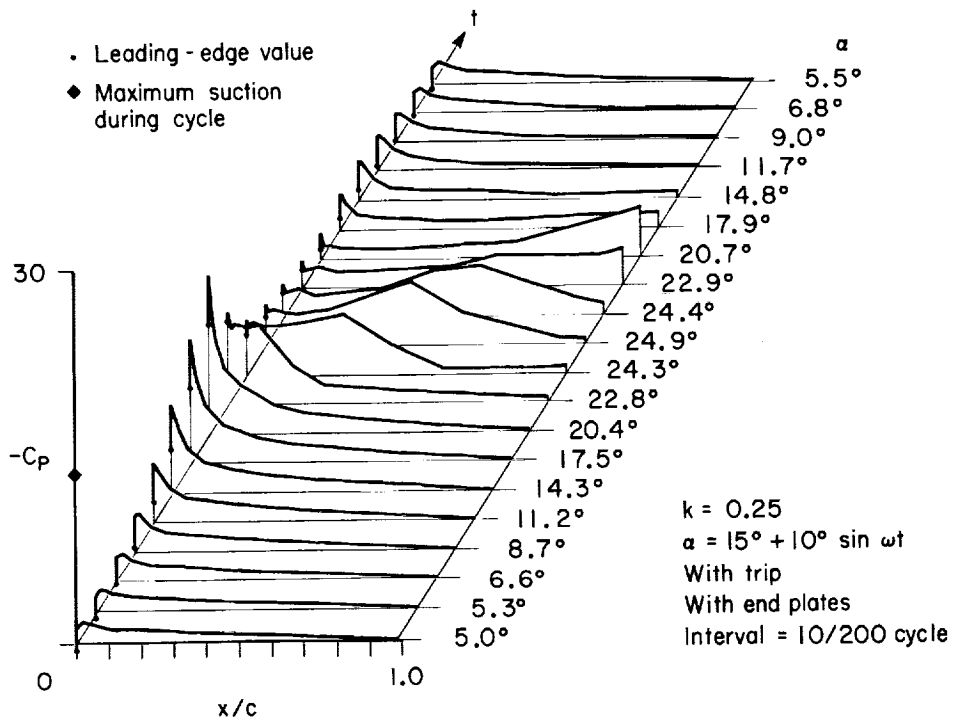
(e) $\alpha = 15^\circ + 10^\circ \sin \omega t, k = 0.150.$

Figure 58.— Continued.



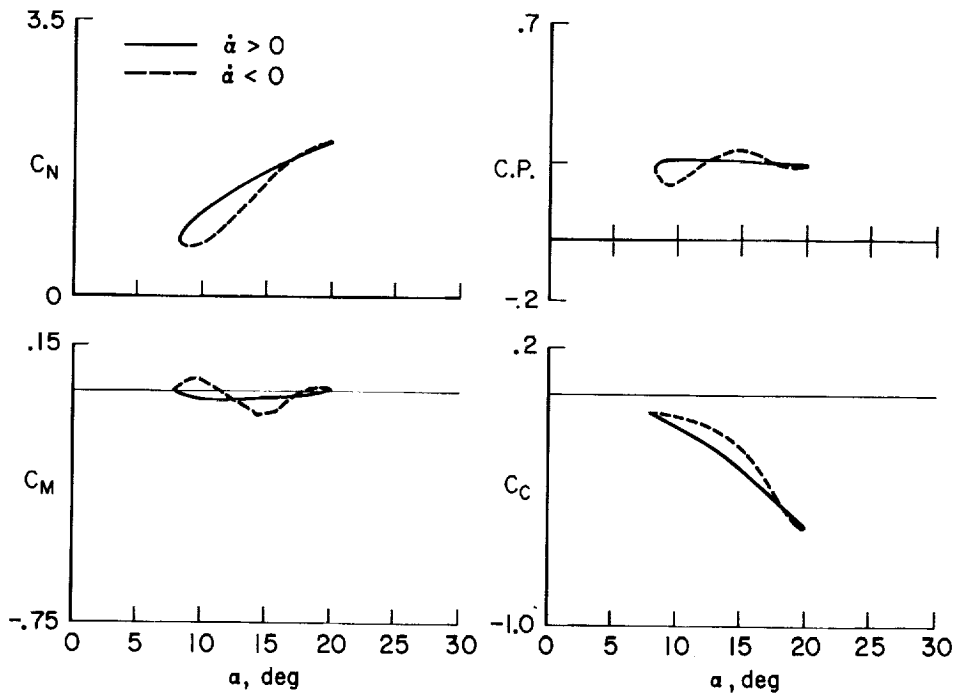
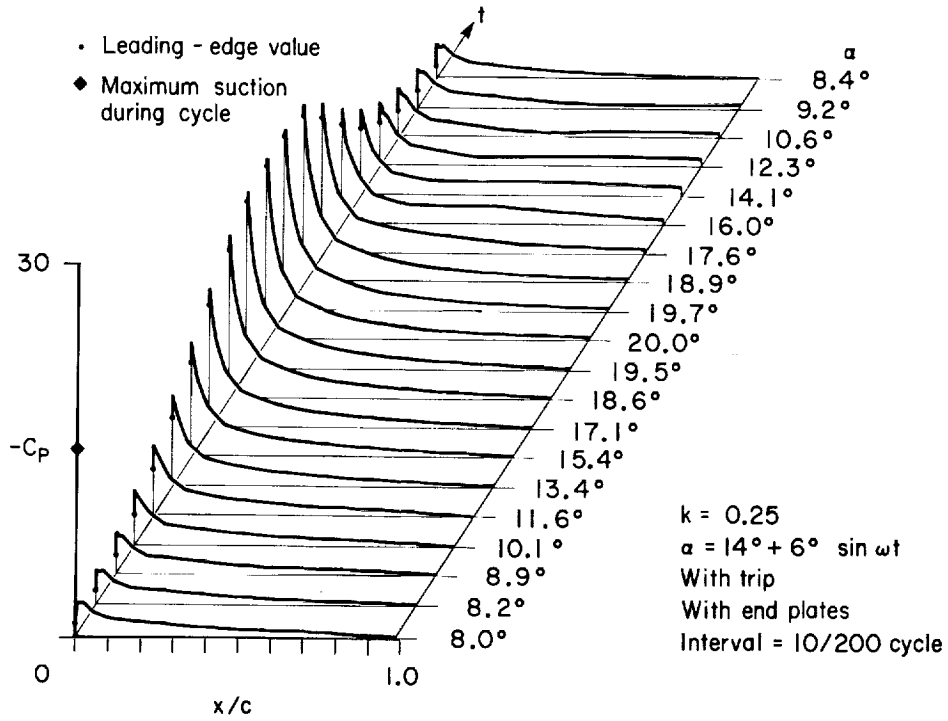
(f) $\alpha = 15^\circ + 10^\circ \sin \omega t, k = 0.200$.

Figure 58.— Continued.



(g) $\alpha = 15^\circ + 10^\circ \sin \omega t$, $k = 0.250$.

Figure 58.— Continued.



(h) $\alpha = 14^\circ + 6^\circ \sin \omega t, k = 0.250$.

Figure 58.— Concluded.

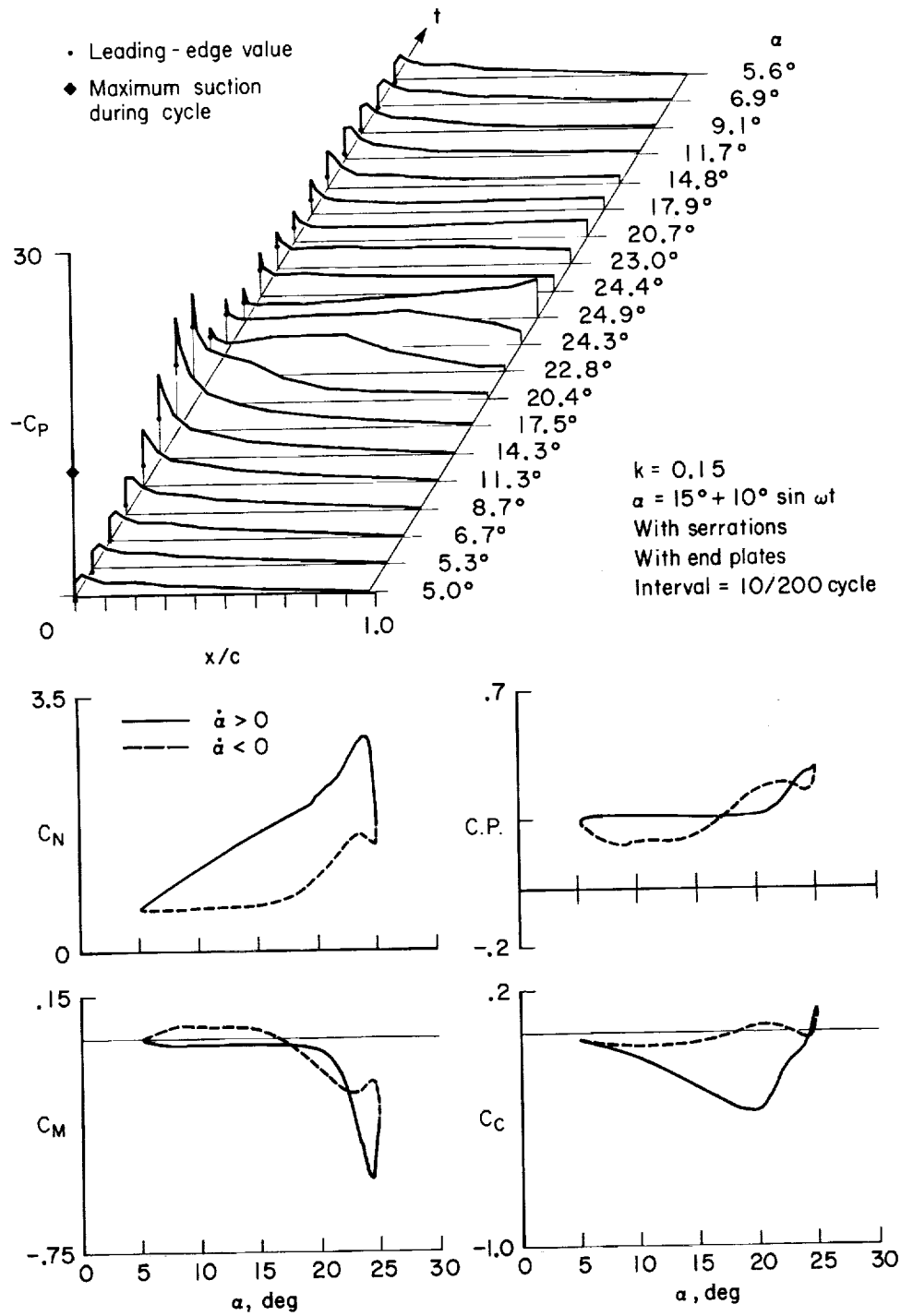


Figure 59.— Aerodynamic loads on NACA 0012 with serrations for $\alpha = 15^\circ + 10^\circ \sin \omega t$, $k = 0.150$ with end plates.

REFERENCES

1. Carr, Lawrence W.; McAlister, Kenneth W.; and McCroskey, William J.: Analysis of the Development of Dynamic Stall Based on Oscillating Airfoil Experiments. NASA TN D-8382, 1977.
2. Philippe, J. J.; and Sagner, M.: Aerodynamic Forces Computation and Measurement on an Oscillating Aerofoil Profile With and Without Stall. AGARD CP-111, September 1972.
3. Gregory, N.; and O'Reilly, C. L.: Low-Speed Aerodynamic Characteristics of NACA 0012 Aerofoil Section, Including the Effects of Upper-Surface Roughness Simulating Hoar Frost. NPL AERO Report 1308, January 1970.
4. Tanner, Watson H., "Charts for Estimating Rotary Wing Performance in Hover and at High Forward Speeds. NASA CR-114, 1964.
5. Abbott, Ira H.; and von Doenhoff, Albert E.: Theory of Wing Sections. Dover Publications, Inc., New York, 1959.
6. Dadone, L. U.: U.S. Army Helicopter Design Datcom. Volume I – Airfoils. USAAMRDL CR-76-2, May 1976.
7. Jacobs, Eastman N.; and Sherman, Albert: Airfoil Section Characteristics as Affected by Variations of the Reynolds Number. NACA Report 586, 1937.
8. Critzos, Chris C.; Heyson, Harry H.; and Boswinkle, Robert W. Jr.: Aerodynamic Characteristics of NACA 0012 Airfoil Section at Angles of Attack from 0° to 180° . NACA TN 3361, 1955.
9. Loftkin, Laurence K.; and Smith, Hamilton A.: Aerodynamic Characteristics of 15 NACA Airfoil Sections at Seven Reynolds Numbers from 0.7×10^6 to 9.0×10^6 . NACA TN 1945, 1949.
10. Pope, Alan; and Harper, John J.: Low-Speed Wind Tunnel Testing. John Wiley & Sons, 1966.
11. McCullough, George B.; and Gault, Donald E.: Examples of Three Representative Types of Airfoil-Section Stall at Low Speed. NACA TN 2502, 1951.
12. Martin, J. M.; Empey, R. W.; McCroskey, W. J.; and Caradonna, F. X.: An Experimental Analysis of Dynamic Stall on an Oscillating Airfoil. J. American Helicopter Soc., vol. 19, no. 1, 1974, pp. 26-32.
13. Ham, Norman D.; and Garelick, Melvin S.: Dynamic Stall Considerations in Helicopter Rotors. J. American Helicopter Soc., vol. 13, no. 2, 1968, pp. 49-55.
14. McCroskey, W. J.: Recent Developments in Dynamic Stall. Symposium on Unsteady Aerodynamics. Kinney, R. B., ed., University of Arizona, Tucson, Mar. 1975.

1. Report No. NASA TP-1100		2. Government Accession No.		3. Recipient's Catalog No.	
4. Title and Subtitle DYNAMIC STALL EXPERIMENTS ON THE NACA 0012 AIRFOIL				5. Report Date January 1978	
				6. Performing Organization Code	
7. Author(s) Kenneth W. McAlister, Lawrence W. Carr, and William J. McCroskey				8. Performing Organization Report No. A-7096	
9. Performing Organization Name and Address Ames Research Center, NASA and Aeromechanics Laboratory, U.S. Army Aviation R&D Command Ames Research Center, Moffett Field, Calif. 94035				10. Work Unit No.	
				11. Contract or Grant No.	
12. Sponsoring Agency Name and Address National Aeronautics and Space Administration, Washington, D.C. 20546 and U.S. Army Aviation R&D Command Ames Research Center, Moffett Field, Calif. 94035				13. Type of Report and Period Covered Technical Paper	
				14. Sponsoring Agency Code	
15. Supplementary Notes					
16. Abstract The flow over an NACA 0012 airfoil undergoing large oscillations in pitch was experimentally studied at a Reynolds number of 2.5×10^6 and over a range of frequencies and amplitudes. Hot-wire probes and surface-pressure transducers were used to clarify the role of the laminar separation bubble, to delineate the growth and shedding of the stall vortex, and to quantify the resultant aerodynamic loads. In addition to the pressure distributions and normal force and pitching moment data that have often been obtained in previous investigations, estimates of the unsteady drag force during dynamic stall have been derived from the surface pressure measurements. Special characteristics of the pressure response, which are symptomatic of the occurrence and relative severity of moment stall, have also been examined.					
17. Key Words (Suggested by Author(s)) Airfoil stall Vortex shedding Unsteady separation Oscillating NACA 0012			18. Distribution Statement Unlimited STAR Category - 02		
19. Security Classif. (of this report) Unclassified		20. Security Classif. (of this page) Unclassified		21. No. of Pages 165	22. Price* \$6.75

*For sale by the National Technical Information Service, Springfield, Virginia 22161

NASA-Langley, 1978